

## **Copyright Notices**

### **Notice 1**

Under the Copyright Act 1968, this thesis must be used only under the normal conditions of scholarly fair dealing. In particular no results or conclusions should be extracted from it, nor should it be copied or closely paraphrased in whole or in part without the written consent of the author. Proper written acknowledgement should be made for any assistance obtained from this thesis.

### **Notice 2**

I certify that I have made all reasonable efforts to secure copyright permissions for third-party content included in this thesis and have not knowingly added copyright content to my work without the owner's permission.

# Towards efficient hydrogen production using water splitting

Aleksey Izgorodin

A thesis submitted to the Faculty of Science, Monash University

in fulfillment of requirement for the Degree of

*“Doctor of Philosophy”*



“If a man does not know what port he is steering for,  
no wind is favorable to him.”

Seneca

# Contents

Contents.....	i
Abstract.....	vi
Declaration.....	viii
Acknowledgments.....	ix
Abbreviations.....	x

## Chapter 1                      General introduction

<b>1.1. Energy sources.....</b>	<b>1</b>
<b>1.2. Hydrogen production.....</b>	<b>4</b>
1.2.1. Electrolytic processes.....	5
1.2.2. Photolytic processes.....	8
<b>1.3. Semiconductors for water splitting.....</b>	<b>9</b>
1.3.1. General properties.....	9
1.3.2. Semiconductors in photo-electrochemical cells.....	10
1.3.3. Chemical stability.....	14
1.3.4. Synthesis of semiconductors for photolytic hydrogen production...	15
<b>1.4. State of the art in photolytic H<sub>2</sub> production.....</b>	<b>17</b>
<b>1.5. Aims of this project.....</b>	<b>20</b>
<b>1.6. Structure of thesis.....</b>	<b>21</b>
<b>References.....</b>	<b>22</b>

## Chapter 2      Electrical and optical properties of CdS nanoparticles

---

<b>Chapter overview .....</b>	<b>26</b>
<b>2.1. Introduction .....</b>	<b>26</b>
2.1.1. Reverse micelle method .....	27
2.1.2. Optical properties of semiconductors .....	29
2.1.3. Applications .....	30
<b>2.2. Aims of this work .....</b>	<b>31</b>
<b>2.3. Experimental .....</b>	<b>32</b>
2.3.1. Synthesis of nanoparticles .....	32
2.3.2. Characterization techniques .....	33
2.3.3. Quantum yield measurements .....	33
<b>2.4. Results and Discussion .....</b>	<b>34</b>
2.4.1. TEM and EDX results .....	34
2.4.2. Size characterization .....	37
2.4.3. Optical and electrical properties of CdS nanoparticles .....	39
2.4.4. “Core shell” structures based on cmCdS .....	46
<b>2.5. Conclusions .....</b>	<b>51</b>
<b>References .....</b>	<b>52</b>

## Chapter 3 Light harvesting semiconductor thin films for photo-electrochemical energy conversion

---

<b>Chapter overview .....</b>	<b>54</b>
<b>3.1. Introduction .....</b>	<b>54</b>
3.1.1. Deposition techniques .....	54
3.1.2. Substrates for CdS electrodeposition.....	57
3.1.3. Tuning electric properties of LHS .....	61
<b>3.2. Aims of this work .....</b>	<b>61</b>
<b>3.3. Experimental.....</b>	<b>63</b>
<b>3.4. Results and discussion .....</b>	<b>66</b>
3.4.1. Elemental sulfur as sulfide precursor and choice of IL .....	67
3.4.2. Sodium thiosulfate as sulfide precursor and choice of IL .....	79
3.4.3. Crystal structure of the CdS films .....	86
3.4.4. Thickness of films .....	87
3.4.5. Electric properties of CdS films.....	90
3.4.6. Mechanism of growth.....	95
3.4.7. Electrodeposition of CdS on metals, semiconductors, and polymers .....	96
3.4.8. Towards mixed metal sulfides .....	102
<b>3.5. Conclusions.....</b>	<b>107</b>
<b>References.....</b>	<b>109</b>

## Chapter 4 Photo-electrochemical water splitting

<b>Chapter overview .....</b>	<b>112</b>
<b>4.1. Introduction.....</b>	<b>112</b>
4.1.1. Semiconductor electrolyte interface.....	112
4.1.2. Hole conductors and catalysts for water oxidation.....	115
4.1.3. Self-repair agents.....	119
<b>4.2. Aims of this work .....</b>	<b>121</b>
<b>4.3. Experimental.....</b>	<b>123</b>
<b>4.4. MnO<sub>2</sub> hole conductor/catalyst deposition.....</b>	<b>127</b>
4.4.1. Electrodeposition of MnO <sub>2</sub> from ILs .....	127
4.4.2. Chemical composition and surface morphology .....	130
4.4.3. Electric properties of MnO <sub>2</sub> thin films.....	134
4.4.4. UV-vis spectroscopy.....	137
4.4.5. Catalytic activity and electrochemical stability.....	138
4.4.6. Photo-driven electrodeposition of MnO <sub>2</sub> .....	142
<b>4.5. Self-repair agents .....</b>	<b>146</b>
4.5.1. Electrodeposition of self-repair agent .....	146
4.5.2. Photo-driven electrochemical deposition of self-repair agents.....	149
<b>4.6. Performance of the water splitting cell.....</b>	<b>151</b>
4.6.1. Stability of water splitting cells in the presence of a strong oxidizing agent.....	152
4.6.2. Photo-electrochemical test of the water splitting cell.....	154
<b>4.7. Conclusions.....</b>	<b>156</b>
<b>References.....</b>	<b>158</b>

**Chapter 5      General conclusions and future work**

---

**5.1.General conclusions ..... 161**

**5.2.Future work..... 164**

**Chapter 6      Appendix**

---

**6.1.Publications..... 166**

# Abstract

Although there is no shortage of supply of fossil fuels at the moment, the necessity to reduce green house gas emission and growing difficulties in fossil fuel recovery raise great challenges for the scientific community to develop efficient, low cost alternative energy sources. Hydrogen is sought by many as a way to store and transport energy produced from renewable sources and as a fuel hydrogen produces only water on burning and is not toxic in any way.

The main pathways to produce hydrogen can be classified as thermal, electrolytic, and photolytic processes. Most of the hydrogen is currently produced *via* thermal processes, which use the energy from fossil fuels stored in natural gas, coal or biomass to release hydrogen. Although photolytic processes are very attractive due to the zero greenhouse gas emissions, they can be used for commercial hydrogen production only if limitations related to low efficiency and poor stability can be resolved.

State-of-the-art hydrogen producing photoelectrochemical cells have 12.4% efficiency under visible light irradiation and combine several semiconducting materials in a monolithic device. Although efficient, this cell is able to split water only for a few days, making the possibility of commercial application daunting. Thus, the general aim of the project is to develop a novel structure for a stable photo-electrochemical device for water splitting applications. Having high efficiencies for photo electrochemical energy conversion, metal sulfides are promising candidates for use in commercial water splitting systems if their long-term stability can be improved. Cadmium sulfide was chosen for our investigations as a representative of the metal sulfide family, due to its well known properties. In the photo-electrochemical cell developed in this work the light harvester is separated from the electrooxidation and reduction processes that occur in the water splitting cell.

The quantum confinement effect observed for semiconducting nanoparticles significantly alters electrical properties of materials that allow for engineering of the desired electrical properties. A range of nanoparticles and nanostructures were prepared in this work in order to investigate the influence of dopant and quantum size effects in

nanoparticles on the energy structure of the material and their potential to be utilized in the water splitting and electroluminescent applications.

In order to address the high costs of production of thin film semiconductors, in this work we have developed a novel method for low cost, efficient deposition of high quality metal sulfide semiconductors and their alloys utilizing electrodeposition from ionic liquids at high temperatures.

The structure of the proposed photoelectrochemical cell was created using electrochemical deposition as well as photo-driven electrochemical deposition, which allows in situ deposition of catalyst for water oxidation. It was shown that a multilayered structure of the device based on metal sulfides provides high corrosion resistance of the cell during photo-electrochemical water splitting leading to significant extension of the cell lifetime.

# Declaration

This thesis, composed by myself, is submitted to Monash University for fulfillment of the requirements for a Doctor in Philosophy in Chemistry at Monash University. The research was carried out by myself, except where acknowledged, in the School of Chemistry (Monash University). It is wholly original except where due reference is given, and has not been submitted for any previous degree.

.....

Aleksey Izgorodin

03 / 09 / 2010

# Acknowledgments

I would like to take this opportunity to thank my research supervisor Prof. Doug MacFarlane for suggesting this project and inviting me to undertake Ph.D. studies in his group. I am indebted to him for his role in facilitating the progress of this project as well as my personal development. His kindness and fairness relating to matters both scientific and personal will never be forgotten. I would also like to thank Prof. Bjorn Winther-Jensen for many stimulating conversations. His willingness to share his scientific wisdom is much appreciated.

I am very happy to thank all of the members of the MacFarlane and Forsyth groups for ensuring that the memory of my years at Monash will never leave me.

It is a pleasure to acknowledge Dr Orawan Winther-Jensen for much help in SEM measurements, Prof Joanne Etheridge and Miss Hadas Katz for help with HRTEM measurements and Mr Finlay Shanks for help with Raman measurements.

Special thanks go to my family, my parents Natalya and Ivan, my sister Katya and brother-in-law Steve and my best friend Ilya. I would also like to thank Steve for his help with preparation of this thesis and for proof reading of this work. Their enormous love, belief in me and bountiful support have been invaluable through all the years of my studies. They have always been there for me during good as well as bad times. This work is dedicated to them.

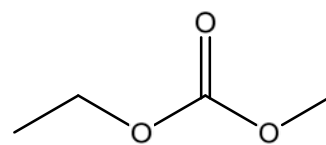
# Abbreviations

Abbreviation (instrumental):	Full name:
DLS	Dynamic light scattering
EDX	Energy-dispersive X-ray spectroscopy
FS	Fluorescence spectroscopy
HRTEM	High resolution transmission electron microscopy
IS	Impedance Spectroscopy
SAD	Selected area electron diffraction
SEM	Scanning electron microscopy
TEM	Transmission electron microscopy
UV-vis	Ultraviolet – visible spectroscopy
XRD	X-ray diffraction

Abbreviation:	Full name:	Structure:
AOT	Diethyl sulfosuccinate sodium salt	
EC	Ethylene carbonate	

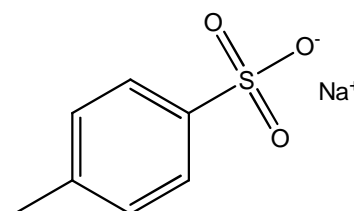
MEC

methyl-ethyl carbonate



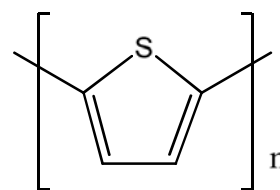
NaPTS

Sodium p-toluene sulfonate



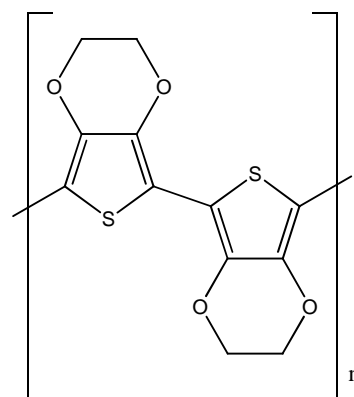
PBTh

PolyBiThiophene



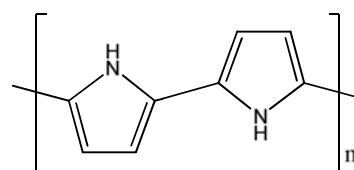
PEDOT

Poly(3,4-ethylenedioxythiophene)



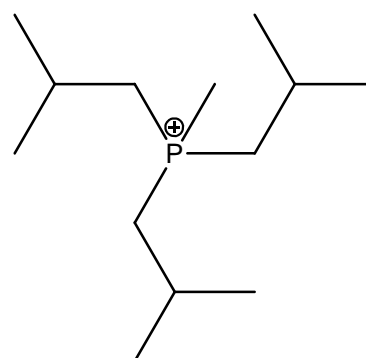
PPy

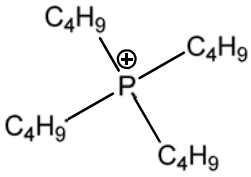
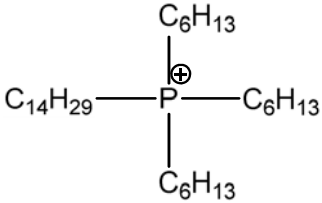
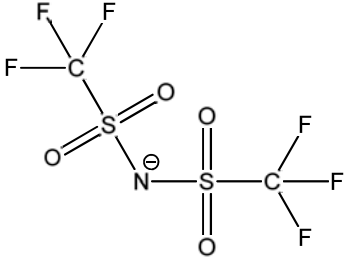
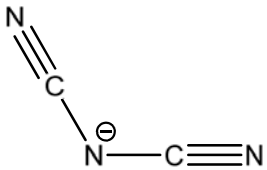
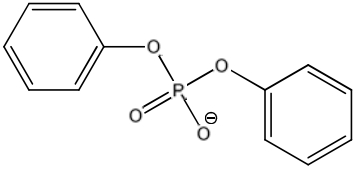
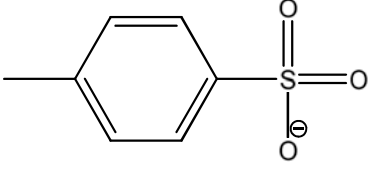
PolyPyrrole



[P<sub>1444</sub>]<sup>+</sup>

Methyl-triisobutyl phosphonium



[P <sub>4444</sub> ] <sup>+</sup>	Tetrabutyl phosphonium	
[P <sub>66614</sub> ] <sup>+</sup>	Tetradecyl(trihexyl) phosphonium	
[NTf <sub>2</sub> ] <sup>-</sup>	Bis(trifluoromethylsulfonyl)imide	
[DCA] <sup>-</sup>	Dicyanamide	
[DPP] <sup>-</sup>	Diphenylphosphate	
[Tosylate] <sup>-</sup>	Tosylate	
EAN	Ethyl ammonium nitrate	

**Abbreviation (other):**

CB	conduction band
CBD	chemical bath deposition
CIE	International Commission on Illumination
cmCdS	chemically modified CdS
CVD	chemical vapor deposition
ECALE	electrochemical atomic layer epitaxy
FTO	fluorine-doped tin oxide
HC	hole conductor
IL	Ionic liquid
LED	light emitting diode
LHS	light harvesting semiconductor
MOCVD	metal organic chemical vapor deposition
NHE	normal hydrogen electrode
PdED	photo-driven electrochemical deposition
PEC	photo-electrochemical
PL	photoluminescent
PV	photo-voltaic
RTIL	room temperature ionic liquid
SCE	standard calomel electrode
UV-LED	ultraviolet light emitting diode
VB	valence band
VPP	vapor phase polymerization
W	water to surfactant mole ratio
(aq)	aqueous

(g)	gaseous
<i>e.g.</i>	<i>exempli gratia</i>
$E_{cb}$	energy of the conduction band edge
$E_F$	Fermi level
$E_g$	band gap energy
<i>et al.</i>	<i>et alii</i>
<i>etc.</i>	<i>et cetera</i>
$E_{vb}$	energy of the valence band edge
<i>i.e.</i>	<i>id est</i>
<i>vs</i>	<i>versus</i>

# Chapter 1

## General introduction

### *1.1. Energy sources*

The modern technological era relies on a steady, reliable supply of energy, which is used in all aspects of everyday life: from transport systems to material production. Several main groups of energy sources can be distinguished:<sup>[1]</sup>

- Thermo-mechanical energy, which is based on wind, water, or geological sources of steam or hot water.
- Nuclear energy, which is released either by splitting heavy nuclei or by fusing light nuclei. The energy is about  $10^6$  eV per nuclear reaction.
- Chemical or photo-physical energy, which is based on the energy liberated from chemical reactions or generated from light absorption in the form of heat or electricity. The energy thus produced is proportional to the energy of chemical bond and is of the order of several electron volts.

The use of each of the mentioned energy sources has some disadvantages. For example, fossil fuels produce carbon dioxide, while nuclear plants produce radioactive fission products. Even renewable energy sources have limitations through the geographical availability of natural resources, such as dams and lakes for hydroelectric plants or large areas of land for solar and wind energy plants.

The world consumption of energy from all fuel sources is expected to significantly increase, based on the IEO2010 reference case,<sup>[2]</sup> as seen in Figure 1.1.

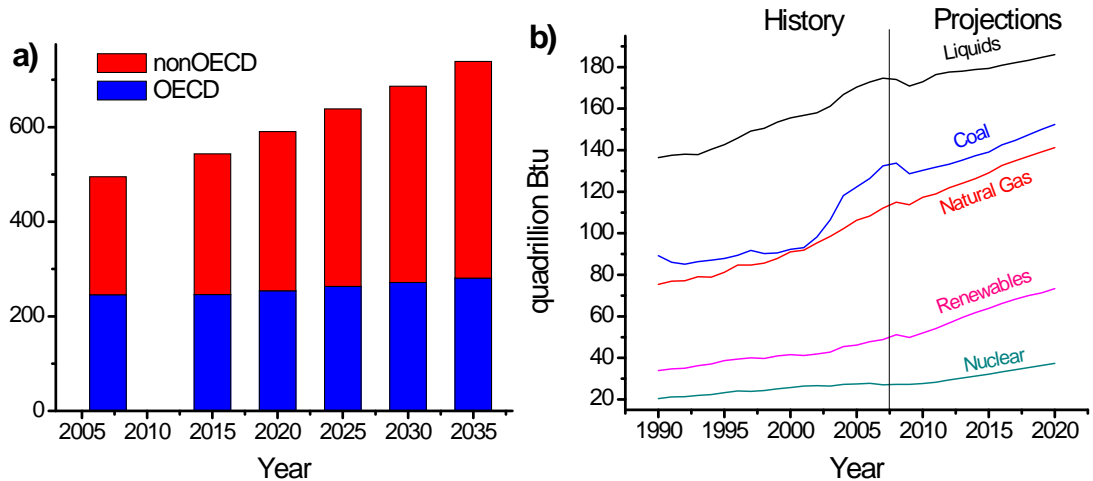


**Figure 1.1:** The world consumption of energy from fuel sources by the countries members of Organization for Economic Cooperation and Development (OECD) and nonOECD countries (left). Energy consumption for different types of fuel sources (right), where Btu is British thermal unit (equivalent to 1.06 kJ).

Following the data reported in the IEO2010 reference case, only wind and hydropower will be able to increase capacity as rapidly as fossil fuels, corresponding to 26 and 54 percent of total increase in energy production from renewable sources by the 2035. Solar, geothermal, biomass, waste, and tidal/wave/oceanic energy will continue to increase over the projection period, see Figure 1.2. It can be seen however, that they will maintain only a small fraction compared to the total energy produced worldwide.

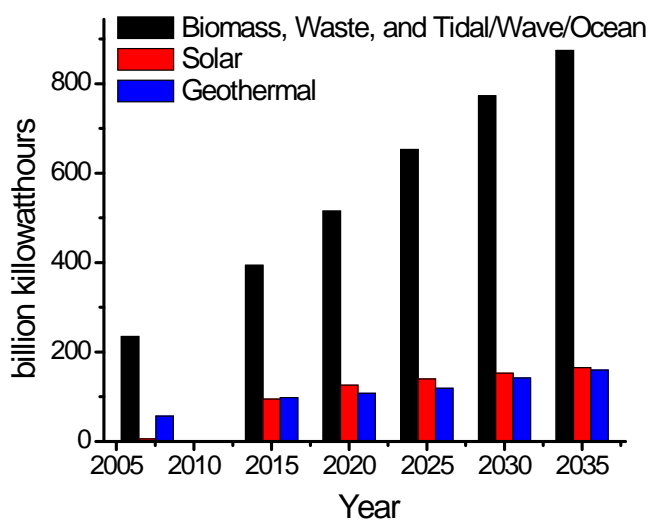


**Figure 1.2:** World renewable electricity generation by energy source, excluding wind and hydropower.

Liquid fuels, natural gas, and coal will supply much of the energy used worldwide in the near future. It is predicted that the use of liquid fuels will continue to increase only in transportation, mainly due to the absence of significant technological advancement in

this area. As a result of the rapid increase in world energy prices in the recent years, long-term prospects continue to improve for generation from both nuclear and renewable energy sources. Another important issue that has to be addressed is reduction in carbon dioxide production and its influence on the global climate. The idea of carbon dioxide sequestration by storing the gas underground or in Deep Ocean has significant costs involved and liable to potential risks of sudden emission of sequestered carbon dioxide.<sup>[1]</sup> In order to meet increasing global demands for energy without relying on the finite amount of fossil fuels and address the issue of carbon dioxide sequestration, renewable energy sources must be developed.

Hydrogen is seen by many as a way to store and transport energy produced from renewable sources.<sup>[1, 3-5]</sup> It is the most abundant element in the universe, which upon oxidation produces only heat and pure water.<sup>[3]</sup> As a gas it can be transported in pipelines and supply decentralized “micropower” plants. When used in the vehicles based on fuel cells, hydrogen would dramatically cut down emissions of air pollutants in big cities. In a perfect hydrogen cycle, renewable energy is used to split water into oxygen and hydrogen, which is ultimately used in fuel cells to produce electricity and water.<sup>[3]</sup>

The chemical energy per mass of hydrogen is 142 MJ/kg, which is much larger compared to that of hydrocarbons (47 MJ/kg); however, the storage of hydrogen remains a big problem. When used as a fuel in cars, tank capacity of around 200 L would be required to store 4 kg of hydrogen (400 km car range).<sup>[4]</sup> Carbon nanotubes were proposed as a storage medium due to their high surface area and light weight, however, it is doubtful that reversible hydrogen storage can be achieved in carbon nanotubes under reasonable operating conditions. Metal hydrides on the other hand are seen as the most promising materials for hydrogen storage, as seen in the review by Schlapbach *et al.*<sup>[1]</sup>

There are several ways in which hydrogen can be used to produce energy. One of these ways is to use hydrogen in an internal combustion engine, where, combined with oxygen from air, chemical energy is converted into mechanical energy. The efficiency of such energy transformation is limited by the Carnot efficiency and is around 25%.<sup>[1]</sup> In another method, hydrogen is combined with oxygen from air in a fuel cell, in which chemical energy is converted into electricity and heat. The efficiency of such transformation can reach 50–60%, which is much higher compared to the thermal process.<sup>[1]</sup>

Hydrogen does not exist naturally, but chemically bound as hydrocarbons, carbohydrates and water. Thus, techniques for efficient hydrogen production are described below.

### ***1.2. Hydrogen production***

The main pathways to produce hydrogen,<sup>[5]</sup> can be classified as thermal, electrolytic, and photolytic processes (Figure 1.3). Most hydrogen is currently produced *via* thermal processes, which use energy from fossil fuels stored in natural gas, coal, or biomass to release hydrogen. In electrolytic processes, electricity mainly produced from fossil fuels is used as the energy source to split water, whereas in photolytic processes the energy of the sunlight is used to drive the reaction. Hydrogen produced *via* electrolysis could become very attractive if it results in zero greenhouse gas emissions. This may be achieved if the electricity used is based on renewable (wind, solar, *etc.*) or nuclear energy sources.

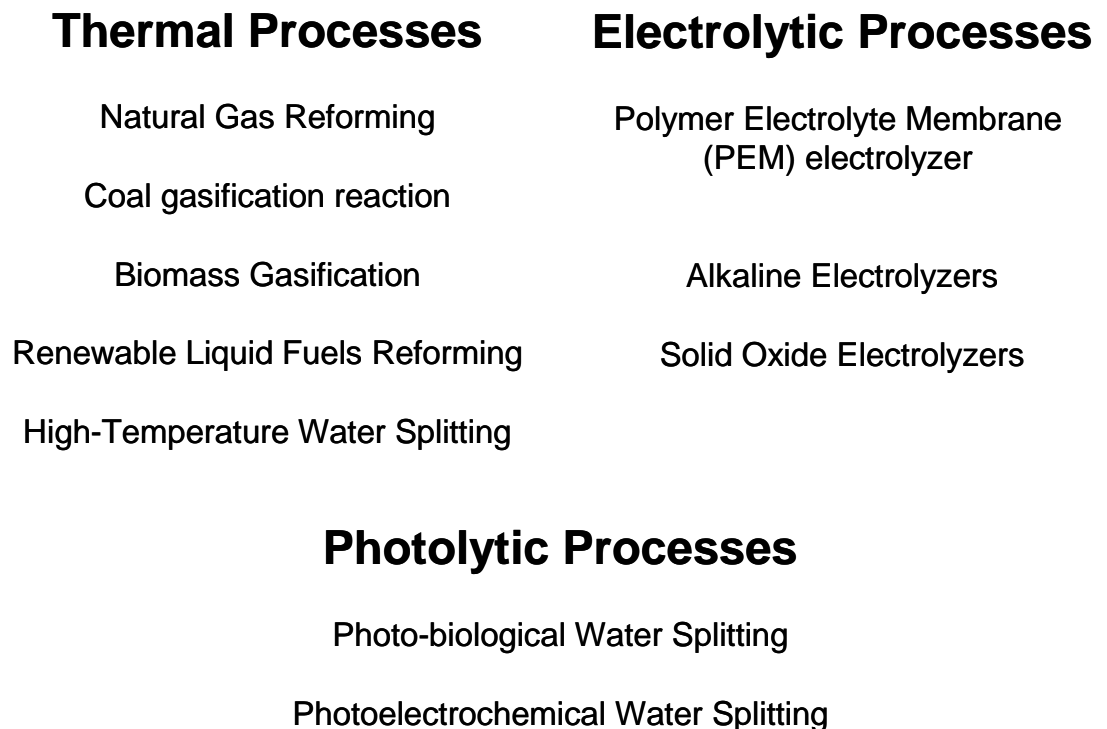


**Figure 1.3:** Current technologies available for hydrogen production.<sup>[6, 8, 9]</sup>

Photolytic processes allow for direct water splitting using sun light illumination. In photo-biological water splitting, hydrogen is produced using specialized microorganisms (*e.g.* green algae and cyanobacteria), while in photo-electrochemical (PEC) water splitting

this function is carried out by semiconductor materials. These methods can be used for commercial hydrogen production only if limitations related to low efficiency and poor stability can be resolved.<sup>[1, 9]</sup>

### 1.2.1. Electrolytic processes

The electrochemical decomposition of water into hydrogen and oxygen is one of the simplest ways to produce high purity hydrogen. Although the efficiency of water electrolysis lies in the range of 50-70%, the cost of hydrogen produced by this method is in the range of \$20-30/GJ (assuming \$0.05/kWh), compared to \$6-12/GJ produced *via* natural gas reforming and coal gasification.<sup>[5]</sup> Despite high production costs, hydrogen produced from water electrolysis is seen as one of the important means to store and transport the energy produced from renewable sources like wind and photo-voltaics.<sup>[8, 9]</sup>

Nernstian potentials for the  $\text{H}_2\text{O}/\text{O}_2$  and  $\text{H}_2\text{O}/\text{H}_2$  half cell reactions are pH dependant and can be calculated as follows  $E(\text{H}_2\text{O}/\text{O}_2) = 1.23 - 0.059(\text{pH})$  versus normal hydrogen electrode (NHE) and  $E(\text{H}_2\text{O}/\text{H}_2) = 0 - 0.059(\text{pH})$  vs NHE. Thus, it is expected that an efficient water catalyst will be able to oxidize and reduce water in neutral solutions close to 0.817 and -0.413 V vs NHE, respectively. Due to the high over-potentials actually needed in order to drive this reaction at a reasonable rate, current commercial electrolyzers operate at 1.7– 1.9 V (see Figure 1.4). This directly reduces efficiency of the energy conversion, because only 1.23 V is required for ideal electrochemical water splitting.

One of the main obstacles to improved efficiency of the water splitting processes lies in development of catalysts that meet the broad requirements of practical applications. Ideally the catalyst should be based on abundant, low cost materials, have high turnover frequencies, remain active over prolong periods of time and be able to regenerate itself.<sup>[6]</sup> The latter is particularly important as the four-electron, four-proton exchange must be mediated by the catalyst under highly oxidizing conditions.

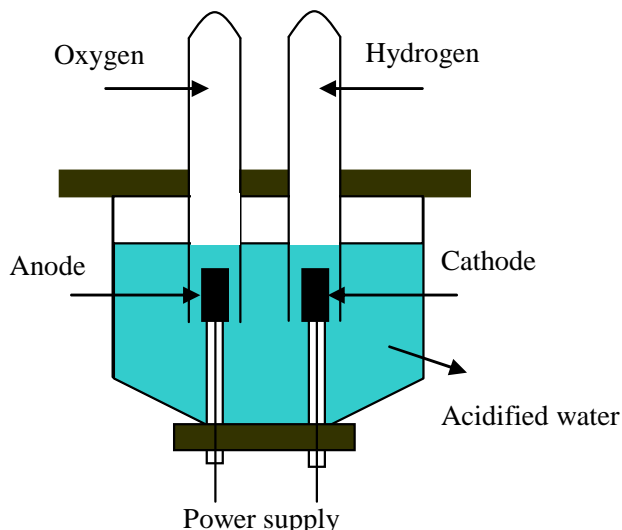


**Figure 1.4:** Schematic representation of water electrolysis.

Two types of catalysts can be distinguished based on their interaction with electrolytes:

- 1) Homogeneous catalysts, which are molecules dissolved in the electrolyte
- 2) Heterogeneous catalysts, which are solid materials in contact with the electrolyte

Homogeneous catalysts are seen as promising materials due to their high reactivity. However, most of homogeneous catalysts developed so far rapidly lose their catalytic capabilities due to the degeneration of organic ligands in the aggressive conditions.<sup>[11, 12]</sup> Heterogeneous catalysts, on the other hand, have lower costs and show better stability and regeneration capabilities.<sup>[13, 14]</sup> Despite these they are less adjustable in device fabrication and are prone to deactivation by surface poisoning.<sup>[7]</sup>

### Water oxidation catalysts



The broad range of water oxidation catalysts developed so far allows for water oxidation in concentrated basic solutions ( $\text{pH} > 13$ ) by materials based on the perovskite metal oxides ( $\text{RuO}_2$ ,  $\text{IrO}_2$ ,  $\text{Co}_3\text{O}_4$ ,  $\text{MnO}_2$  etc.),<sup>[13, 16-18]</sup> and under neutral or acidic conditions ( $\text{pH} < 1$ ) by precious metals and their oxides (e.g. Pt,  $\text{PtO}_2$ ).<sup>[19, 20]</sup> The overpotentials achieved by noble metal catalysts are around 320 mV.<sup>[8]</sup>

Among heterogeneous oxygen-evolving catalysts, one of the highest activities was produced from material formed upon anodic polarization in phosphate solutions containing Co(II).<sup>[7]</sup> Here, the natural formation of the catalyst under an applied potential of 1.3V vs NHE (pH=7) gives a viable mechanism for catalyst self-repair. In a typical procedure, Co<sup>2+</sup> is oxidized to Co<sup>3+</sup> in the presence of phosphate, leading to the formation of amorphous deposits that incorporate the phosphate anion as a major constituent. It was shown that presence of the phosphate is crucial in establishing the self-repair mechanism, which was not achieved using other suitable electrolytes (*e.g.* borate, methylphosphonate).<sup>[9]</sup> Although the catalyst is able to oxidize water in neutral pH and at room temperature water oxidation occurred at potential around 1.2V vs NHE which corresponds to about 400 mV of overpotential, indicating that improvements are needed before this catalyst will be energetically efficient.

Recent work on homogeneous inorganic water oxidation catalysts<sup>[23, 24]</sup> explored the use of polyoxometalate stabilized complexes. The aim of the study was to combine stability, durability, and accessibility of heterogeneous metal oxide catalysts with the activity, selectivity, and tunability of homogeneous catalysts. Among the range of cobalt-based complexes, only [Co<sub>4</sub>(H<sub>2</sub>O)<sub>2</sub>(PW<sub>9</sub>O<sub>34</sub>)<sub>2</sub>]<sup>10-</sup>, which self-assembles in water from salts of Co, W, and P, was shown to be hydrolytically and oxidatively stable with overpotentials for water oxidation around 300 mV.

### Water reduction catalysts



It is well known that Pt has superior catalytic abilities for the hydrogen evolution reaction and hence, is commonly used in various applications.<sup>[25, 26]</sup> The high cost of Pt electrodes and their tendency to become deactivated through the interaction with carbon monoxide<sup>[27]</sup> has led to ever growing interest in developing alternative solutions for hydrogen production.

Much progress was made in development of composite materials based on nanoparticles<sup>[10]</sup> and conducting polymers<sup>[11]</sup> for electrocatalytic reactions of this type. Recently, novel composite materials based on the conducting polymer poly(3,4-ethylenedioxythiophene) (PEDOT) and a non-conducting polymer of the polyethylene glycol (PEG), was shown to have high catalytic activity for the hydrogen evolution

reaction in acidic solutions.<sup>[12]</sup> It was demonstrated that such materials were not subjected to carbon monoxide poisoning common for Pt electrodes and were stable for more than 1900 hours of continuous operation without deterioration of activity.

### 1.2.2. Photolytic processes

The energy of the sun is one of the most promising alternatives to traditional fossil fuels. The typical solar spectrum is shown in Figure 1.5. When the sun is directly overhead, radiation on a horizontal surface can be as high as  $1000 \text{ W/m}^2$ .

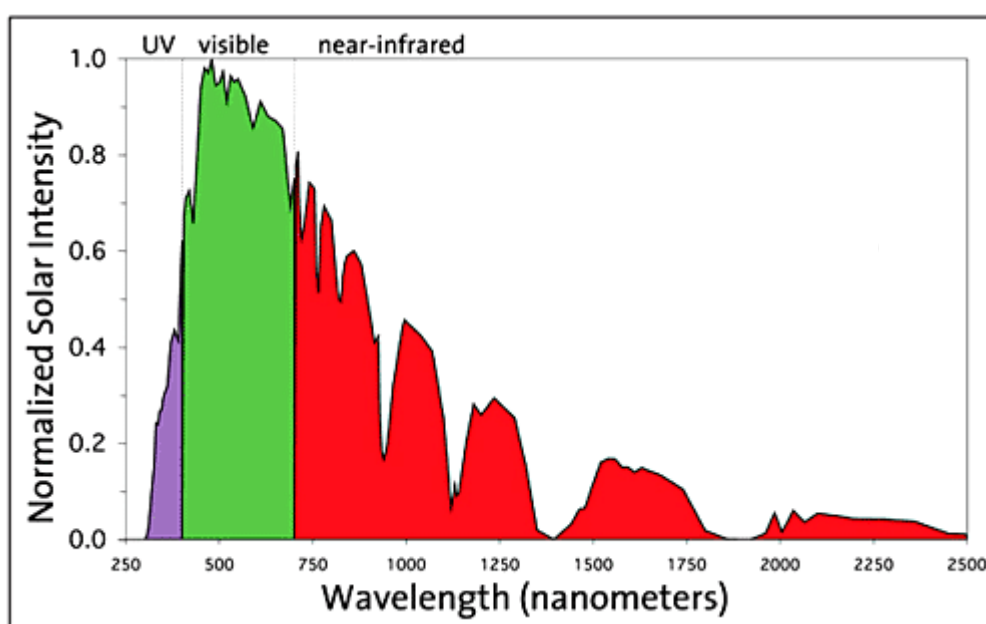


**Figure 1.5:** The typical solar spectrum that reaches the Earth's surface.<sup>[13]</sup>

As was mentioned in the previous section, the potential at which most existing electrolyzers operate does not exceed 1.9 V. The wavelength of the photon in solar spectrum that has similar energy corresponds to 650 nm (red light). Thus, the energy of the entire visible spectra (46% of the total solar energy) can potentially be used to drive the water splitting reaction.<sup>[31]</sup>

A number of general strategies that can be employed in the development of water splitting systems can be defined. Among the most promising are powdered photo-catalyst systems and photo-electrochemical (PEC) devices. The former strategy is based on the use of semiconducting microparticles that can be uniformly dispersed in aqueous electrolytes. The necessity of further separation between hydrogen and oxygen evolved from electrolysis is counterbalanced by the simplicity and adaptability of such systems for large

scale applications. By controlling the concentration of the dispersed photo-catalyst in solution, it becomes possible to utilize materials with low extinction coefficients (*e.g.* Si) and to maintain high levels of light absorption. Another important advantage arises when the size of the semiconducting particles is significantly reduced (*e.g.* in nanoparticles). The distance that photo-generated electrons and holes have to traverse before reaching the surface is smaller, thus reducing internal recombination rate on defects in the crystal structure and increasing efficiency.<sup>[14]</sup>

In PEC devices light is absorbed by the semiconductor film, which, when coupled with a counter electrode in the electrolyte solution, acts as photo-anode or photo-cathode. Although this method allows for effective separation of gaseous products forming on the electrode surface, thick films of good quality have to be used to achieve high levels of light absorption and hence, efficiency.<sup>[15]</sup>

### ***1.3. Semiconductors for water splitting***

Semiconductors are one of the most important classes of materials that have revolutionized the computer industry in the 20<sup>th</sup> century. Today they find immense number of applications, from microelectronics and energy conversion<sup>[34, 35]</sup> to biological labeling<sup>[36, 37]</sup> and organic synthesis.<sup>[16]</sup>

#### **1.3.1. General properties**

By the type of band gap all semiconductors can be divided into direct and indirect band gap materials. In a direct band gap semiconductor, the top of the valence band and the bottom of the conduction band are located at the same value of electron momentum, while in an indirect band gap semiconductor, their positions in respect to electron momentum are shifted with relation to each other. The properties of common semiconductors<sup>[17, 18]</sup> are summarized in Table 1.1.

The values of light absorbance is much higher in direct band gap semiconductors compared to indirect ones, with the absorption coefficient reaching values as high as  $10^4$ - $10^5$   $\text{cm}^{-1}$ . In indirect semiconductors, however, the lowest energy electronic transition is formally optically forbidden. This fact significantly reduces the probability for photon absorption and typical absorption coefficient values for such materials are several orders of magnitude lower.<sup>[19]</sup>

**Table 1.1:** Properties of common semiconductors at 300K.<sup>[17, 18]</sup>

Semiconductor	Crystal structure	Band gap, eV	Type of band gap
Si	Diamond	1.12	Indirect
Si	Amorphous	1.7	-
Ge	Diamond	0.66	Indirect
GaAs	Zinc blende	1.42	Direct
ZnS	Zinc blende	3.58	Direct
CdS	Wurtzite	2.42	Direct
TiO <sub>2</sub>	Rutile	3.02	Indirect
TiO <sub>2</sub>	Brookite	1.9	Indirect

In order to be successfully applied in photo-voltaic energy conversion, a semiconductor needs to be thick enough to absorb all incident photons. In the case of Si (an indirect band gap material), which has the absorption coefficient near the band gap about  $10^2 \text{ cm}^{-1}$ ,  $d \sim 100 \text{ }\mu\text{m}$  thick film is required for high light absorption. Because of the relatively high thickness of the absorbing layer, materials with a high level of crystallinity have to be used in order to reduce the amount of defect sites present and ultimately produce high efficiency energy conversion rates. GaAs (a direct band gap semiconductor) has an absorption coefficient near the band gap energy several orders of magnitude higher compared to silicon, which allows even  $\sim 1 \text{ }\mu\text{m}$  thick film to be sufficient for effective light absorption. Thus, being direct band gap semiconductors, metal sulfides are promising materials for efficient energy conversion in thin films.

### 1.3.2. Semiconductors in photo-electrochemical cells

In direct photo-electrochemical (PEC) water splitting, a semiconductor is immersed in aqueous solution where, upon illumination, it can decompose water directly as shown in Figure 1.6. The semiconductor in this case acts as a light harvester and may be coupled with a surface layer of catalyst to improve its electrocatalytic performance. In order to be successfully used in such systems, materials must be stable in the aqueous environment; generate sufficient voltage (band gap greater than 1.9 eV for a single semiconductor); straddle the redox potentials of the hydrogen and oxygen half-reactions with its conduction

and valence band edges; be composed of earth abundant elements and have a low-cost synthesis procedure.<sup>[9]</sup>



**Figure 1.6:** Photo-electrolysis occurring in a multi-junction cell.<sup>[20]</sup>

Upon illumination by solar light of the semiconductor-electrolyte interface for materials that are able to split water directly, generated electrons and holes have sufficient energy to drive the respective electrochemical reactions. Based on the type of majority carriers in the semiconductor two types of electrochemical cells may be distinguished (where the semiconductor acts as a photo-anode or photo-cathode) as shown in Figure 1.7.<sup>[9, 32]</sup> Minority charge carriers in such cells are injected into the electrolyte while majority charge carriers, whose potential energy is represented by the Fermi level, are transferred to a metal counter electrode.

The basic difference between a photo-voltaic and a photo-electrolysis cell is that in the former a well-defined external photo-voltage is generated.<sup>[15]</sup> A photo-electrolysis cell operates at short circuit; the voltage that can be measured in the open circuit mode is determined by the difference between Fermi energy level in semiconductor and electrolyte as shown in Figure 1.8.

$E_g \sim 1.6 - 1.7 \text{ eV}$  (1.23 eV required)

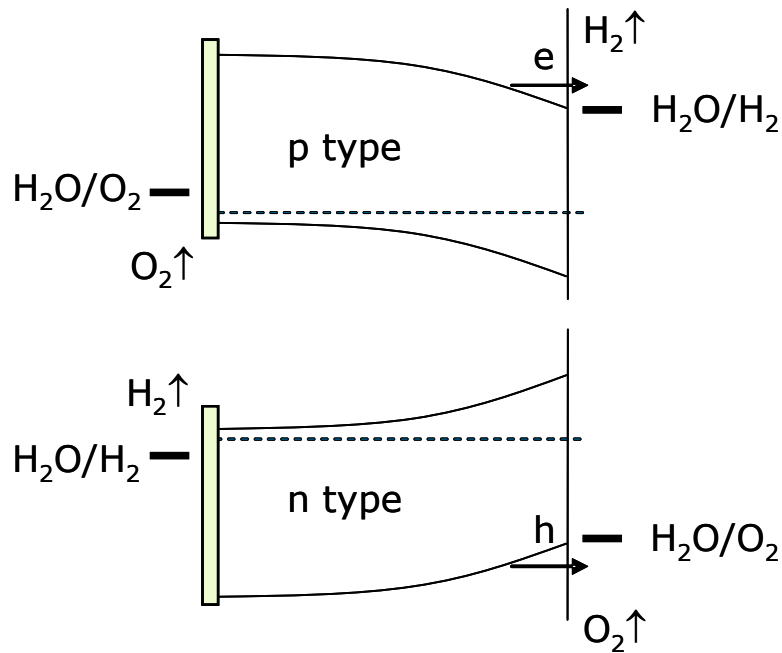


**Figure 1.7:** Energy level diagrams of the semiconductor-electrolyte interface, in which semiconductor is used as a) photo-anode (p-type, top) or b) photo-cathode (n-type, bottom).

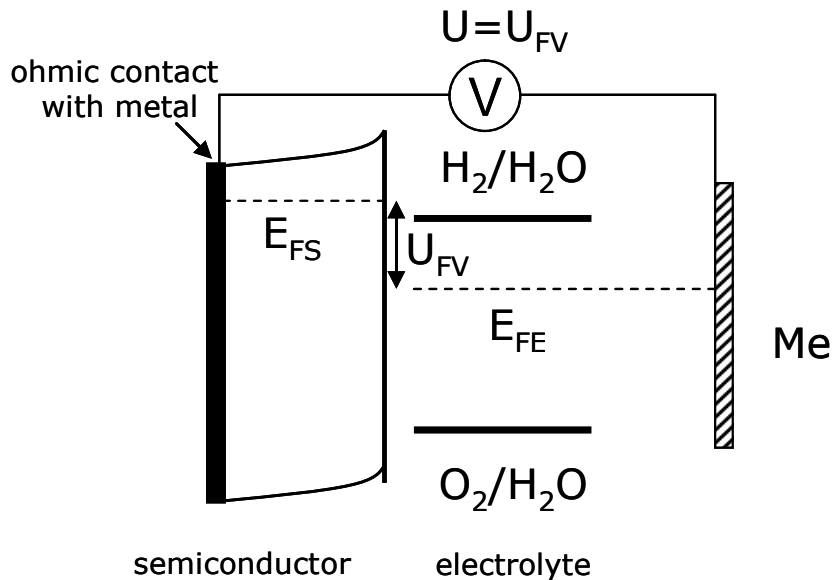


**Figure 1.8:** Energy level diagram of n-type semiconductor and aqueous electrolyte. Where  $E_{FS}$  and  $E_{FE}$  are positions of the Fermi level in semiconductor and electrolyte respectively,  $U_{FV}$  is the photo-voltage that can be measured in the external circuit.

The values of band gap energies and positions of conduction and valence band edges of selected semiconductors in relation to the water redox potentials at  $\text{pH}=0$  are shown in Figure 1.9.<sup>[21]</sup> There are not many materials that meet the prerequisites for direct

water splitting. This may be not only because of the low values of band gap energies, but also the relative positions of conduction and valence band edges with regard to water oxidation and reduction potentials.

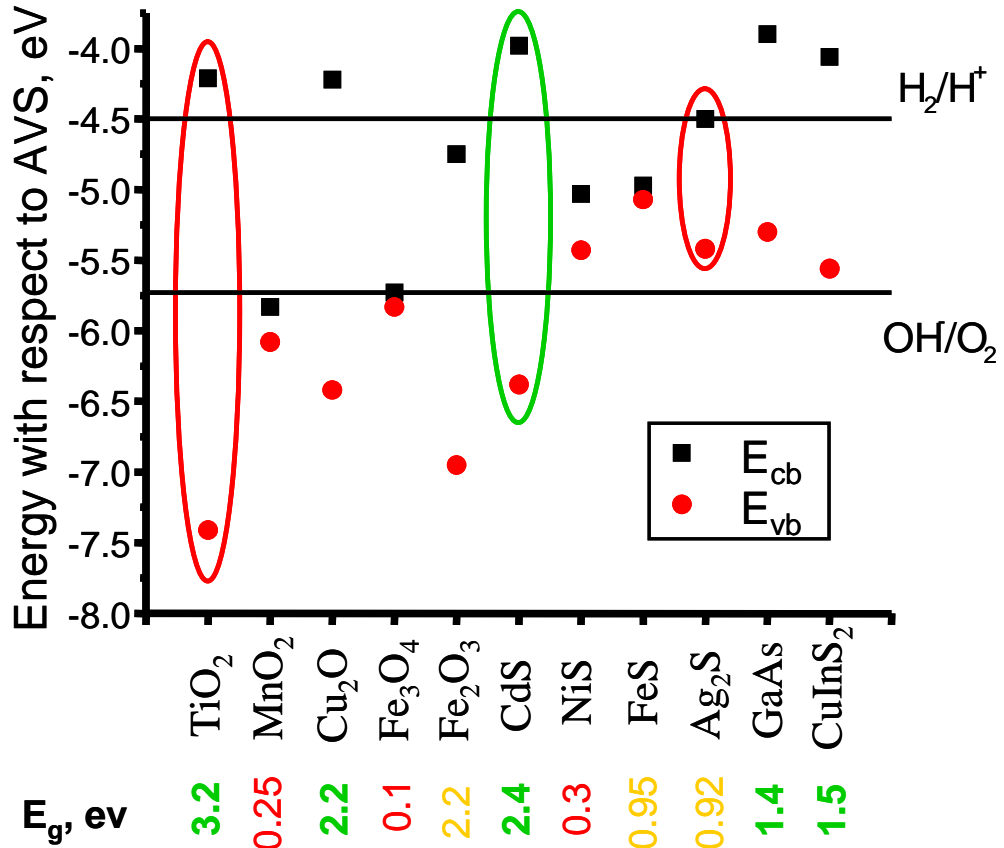


**Figure 1.9:** Conduction band edges and valence band edges of selected semiconductors in relation to water reduction and oxidation potentials at pH = 0.<sup>[21]</sup>

Three main strategies exist to provide overall water splitting with materials such as that presented in Figure 1.10:<sup>[9, 32, 43]</sup>

1. tandem configuration of several low band gap semiconductors.
2. p-n type photo-electrolysis cell, where two separate semiconductors are used as photo-anode and photo-cathode.
3. if the value of the band gap is appropriate (1.6-1.7 eV), the relative positions of conduction and valence band edges can be shifted by surface modification.

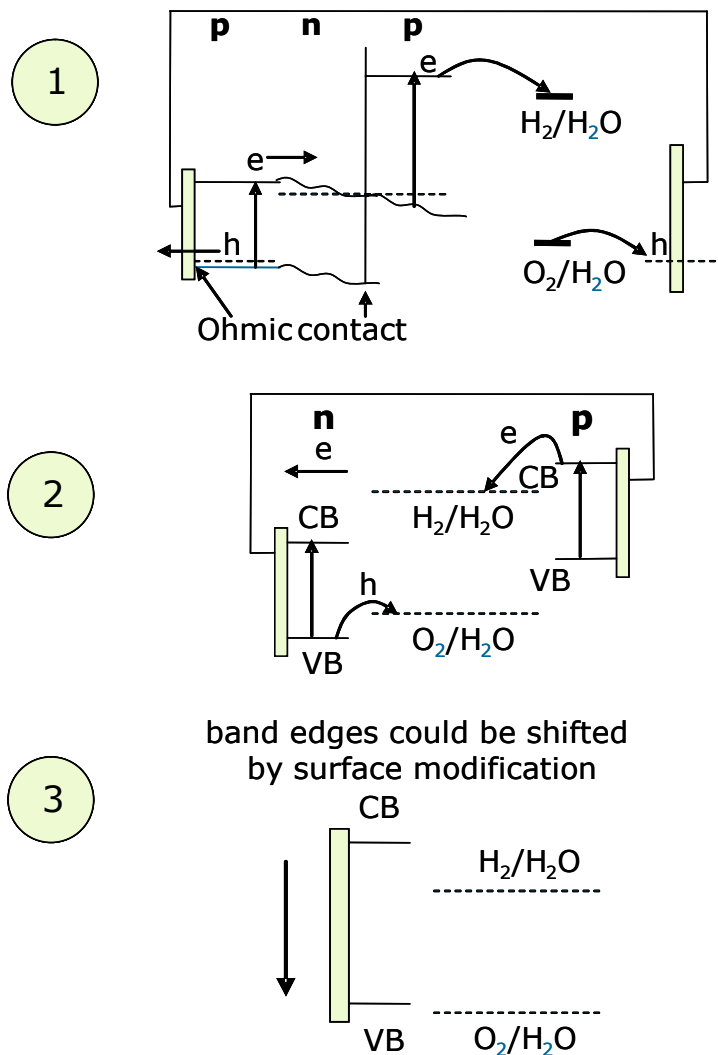


**Figure 1.10:** Strategies for overall water splitting from semiconductors that cannot meet requirements for direct water splitting.

### 1.3.3. Chemical stability

Chemical reactivity of semiconductors is significantly affected by their structure and relative positions of the valence and conduction bands. Metal oxide semiconductors are generally more stable towards corrosion and passivation than covalent semiconductors. It is generally accepted that chemical reactivities can be determined through the value of the band gap.<sup>[22]</sup> Thus, covalent semiconductors, in which orbitals of the valence and conduction bands are relatively close in energy, are expected to be more reactive, while semiconductors that have wide band gaps (*e.g.*  $\text{TiO}_2$ ) are more stable.<sup>[22]</sup>

In covalent crystals, such as Si, the valence and conduction bands are formed by the combination of Si molecular orbitals. However, in metal oxides, such as  $\text{TiO}_2$ , the valence band consists of orbitals from the filled  $\text{O}^{2-}$  2p orbitals, while the conduction band is

comprised of the empty 3d orbitals of  $Ti^{4+}$ .<sup>[23]</sup> It is important to note, that in most metal oxides the energy of the valence band edge is quite similar and does not depend on the metal type. This can be explained by the fact that the valence band in these materials is comprised predominantly of the 2p orbitals of oxygen and thus, retains its energy value for the different types of metal oxides. The type of metal cation mostly affects the energy of the conduction band edge. This theory has been generalized over most compound semiconductors, where the valence band character is dominated by the atomic orbitals of the anion in the crystal structure.<sup>[24]</sup> Although this theory is not expected to be valid for a wide range of materials with different crystal structures and chemical compositions, it allows for rough estimation of chemical and electronic properties.

Similar approaches can be used to estimate reactivity of excited states. It was suggested that covalent semiconductors should be more stable towards oxidation than II-VI group semiconductors,<sup>[25]</sup> based on the character of conduction and valence bands in these materials. In  $MoS_2$ , for example, both bands are composed of 3d Mo energy levels, so that there is no deterioration during excitation. In CdS, however, the valence band is  $S^{2-}$  in character. During excitation the electron is removed from the  $S^{2-}$  orbitals and this process subsequently leads to dissolution of the anion as  $S^0$ .<sup>[26]</sup>

### 1.3.4. Synthesis of semiconductors for photolytic hydrogen production

The vast majority of applications require high quality semiconductor films to be created at low cost. High quality is a significant performance parameter, since defect sites present in the lattice act as centers of recombination, decreasing charge carrier mobility and carrier separation efficiency. Thus, the overall efficiency of thin film device is significantly affected.<sup>[27]</sup> Sputter deposition,<sup>[28]</sup> spray pyrolysis,<sup>[29]</sup> and photo-chemical deposition<sup>[30]</sup> can be used to create metal sulfide films, but high roughness and poor crystal structure are among disadvantages of these techniques. Although films deposited *via* vacuum evaporation,<sup>[31, 32]</sup> chemical vapor deposition (CVD),<sup>[33]</sup> metal organic chemical vapor deposition (MOCVD),<sup>[34]</sup> and electrochemical atomic layer epitaxy (ECALE)<sup>[27, 35]</sup> are of better quality, the costs involved limit their wider application. One of the most widely used methods to deposit CdS is chemical bath deposition (CBD).<sup>[36]</sup> Although significant improvement of film quality was achieved in the recent years, the method produces very low yield (~2%), resulting in copious amounts of toxic waste.<sup>[37]</sup>

Electrodeposition is a promising technique for deposition of metal sulfides. It is fairly simple, has low cost and produces films at very high yield. In the recent years ionic liquids (ILs) have attracted significant interest as electrolytes for electrodeposition. The high temperature at which the deposition in an IL can, in principle, be conducted allows for atom diffusion on the surface during growth, which has a major positive influence on the quality of the films.<sup>[38]</sup> One of the key advantages of ionic liquids in this context is their combination, in some cases, of thermal and electrochemical stability that allows the electrodeposition process to be carried even at elevated temperatures with minimal interference from solvent chemical or electrochemical breakdown.<sup>[61-63]</sup>

### **Ionic liquids as electrolytes for electrodeposition of semiconductors**

Ionic liquids are low-melting salts that are comprised entirely of cations and anions. Conventionally, salt melting below the boiling point of water is known as an ionic liquid.<sup>[39]</sup> The main difference between ILs and molten salts is that the former consist mainly of organic cations rather than inorganic ones present in molten salts. One of the main advantages in using ILs, over common solvents and electrolytes, is their negligible vapor pressure. The range of possible and potential applications for such materials is enormous, ranging from solvents and electrolytes to lubricants.<sup>[40]</sup>

The number of possible combinations between available anions and cations implies more than  $10^{12}$  different ILs may be possible.<sup>[41]</sup> With such a wide range of possible combinations it becomes possible to design an IL that interacts with a solute in a specific fashion. For example, with the use of specific functional groups that affect certain properties or reactivities it is possible to synthesize “task-specific ionic liquids”.<sup>[40]</sup> Some of the common anions and cations used in ILs are shown in Figure 1.11.

Ionic liquids are seen as a potential replacement for traditional organic solvents and are generally considered as polar solvents, with polarity ranging between that of water and chlorinated organic solvents.<sup>[42]</sup> The viscosity of ILs is generally higher than of water, but decreases rapidly with an increase in temperature. ILs generally have a very broad liquid range, which in some cases is as large as 300° C. Across such a vast range of temperatures they maintain their volume and fluidity allowing vast kinetic control of chemical processes.<sup>[39]</sup>

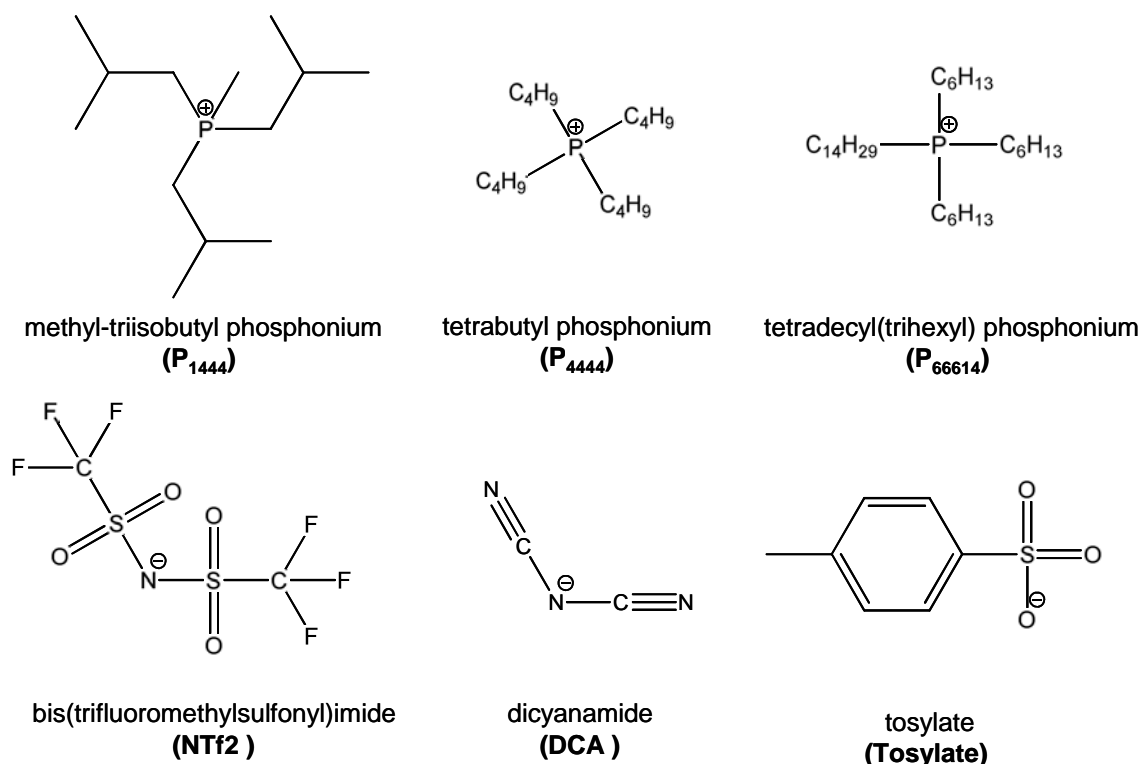


**Figure 1.11:** Examples of cations and anions used in ILs relevant for the present work.

In the electrochemistry of transition metal catalysts it is important to provide sufficient solubility of simple metal salts as well as metal coordination complexes in the ILs. As a general rule, simple ionic compounds are not very soluble in most ILs, while ionic complexes have better solubility.

The electrochemical window is one of the most important properties of an IL, which is used to describe its electrochemical stability. It defines the range of potentials over which the solvent is electrochemically inert and can be used for electrodeposition. The value is mainly determined by the stability of the cation towards reduction and the anion towards oxidation.<sup>[43]</sup>

#### 1.4. State of the art in photolytic H<sub>2</sub> production

Metal sulfides and oxides are the main group of materials that have been investigated for water splitting applications. Narrow band gap metal sulfides are able to absorb light in the visible region, however, such materials are not stable and undergo photo-corrosion:  $\text{MeS} + 2\text{h}^+ \rightarrow \text{Me}^{2+} + \text{S}$ , where “h<sup>+</sup>” represents a hole generated in the semiconductor. Presence of a hole scavenger (*e.g.* S<sup>2-</sup>, EDTA) allow metal sulfides to be studied as water reduction catalysts. In particular CdS (absorption edge at around 520nm)

and  $\text{Cd}_{0.85}\text{Zn}_{0.15}\text{S}$  with a Pt co-catalyst showed excellent performance for hydrogen evolution under visible light irradiation.<sup>[44]</sup> The efficiencies towards water splitting under irradiation with light of wavelength more than 300nm are as high as 37%, which is one of the highest obtained from powder photo-catalytic systems.<sup>[44]</sup> The problem of poor corrosion resistance of these materials and hence, the necessity to use electron scavengers still stands.<sup>[44]</sup>

Among metal oxides and nitrides,  $\text{Ga}_{1-x}\text{Zn}_x\text{N}_{1-y}\text{O}_y$  modified with nanoparticles of a mixed oxide of rhodium and chromium (absorption edge at about 510 nm), was found to become catalytically active with efficiency of overall water splitting equal to 2.5% under 420–440 nm illumination.<sup>[45]</sup> In other work, nitrogen doping of  $\text{TiO}_2$  was used to reduce the wide band gap of the material and shift the absorption edge to 500nm.<sup>[46]</sup> The  $\text{TiO}_{2-x}\text{N}_x$  films, prepared by this method, were studied for oxidation of various organic compounds under solar illumination.

Stoichiometric amounts of oxygen and hydrogen under visible light irradiation have also been produced from nickel doped indium-tantalum-oxides (absorption band at 420–520 nm).<sup>[47]</sup> The efficiency of water splitting for  $\text{In}_{0.9}\text{Ni}_{0.1}\text{TaO}_4$  at 402 nm was estimated to be about 0.66%. Although stability of such cells is relatively high (the ratio of total amount of gas evolved to catalyst present exceeded 5 after 400 hours of operation), the efficiency is low.

The most recent work on PEC cells involves development of double-sided CdS and CdSe quantum dot co-sensitized ZnO nanowire arrays, formatting a catalyst with incident-photon-to-current-conversion efficiency of up to 45%.<sup>[48]</sup> A current density of 12 mA/cm<sup>2</sup> was produced by the anode when illuminated by white light with energy density of 100 mW/cm<sup>2</sup> at 0.4 V vs Ag/AgCl. Similar to the metal sulfide photo-catalysts, these PEC cells are not stable during water splitting due to the low corrosion resistance.

The current highest water-splitting efficiency (12.4%) for a PEC device that operates under sunlight illumination incorporates a tandem configuration as shown in Figure 1.12.<sup>[20]</sup> This system consists of a p-GaInP<sub>2</sub> PEC electrode and a GaAs solar cell combined into a single monolithic device. Electrons are driven to the semiconductor electrolyte interface where they reduce water. Oxygen evolution occurs on the metal anode that is connected to the illuminated semiconductor by a wire. Even though the reported

system promotes the water oxidation process on an isolated metal anode, the configuration lasts only two to three days, while the use of the integrated photo-voltaic (PV) cell with a PEC electrode adds complexity and cost to the final system.

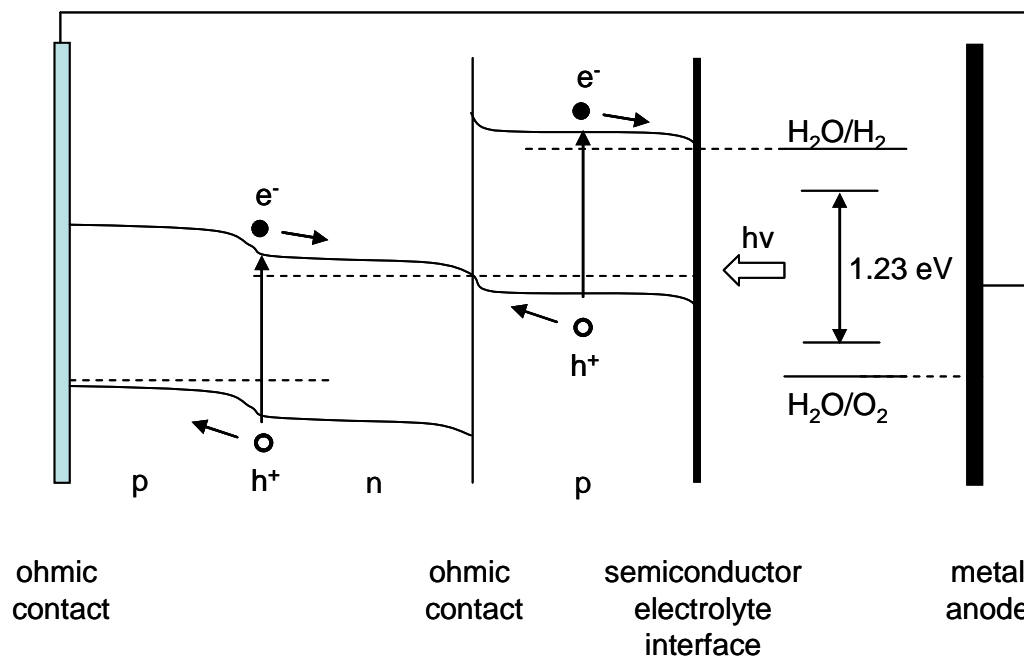


**Figure 1.12:** Energy diagram of the tandem water splitting system.<sup>[20]</sup>

In a monolithic device that combines PV and PEC cells, as shown in Figure 1.12, corrosion resistance of the semiconductor during water splitting was improved through water oxidation on the surface of the Pt catalyst. The light harvesting semiconductor in this structure, however, is still in contact with electrolyte (reduction of water on the surface of the p-type conductor) and deteriorates rapidly at high charge density. It can be concluded that separation of the light harvesting semiconductor from the aggressive environment of electrochemical water splitting is a promising technique to improve stability of PEC cells.

Overall, it can be seen from the above overview that materials capable of achieving high efficiencies towards the overall water splitting under solar illumination have very low corrosion resistance and rapidly decompose, while more stable materials have low values of efficiency.

### ***1.5. Aims of this project***

The general aims of this project are to develop a novel structure to create a stable PEC device based on metal sulfides for water splitting applications. Having high efficiencies for photo-electrochemical energy conversion, metal sulfides are promising candidates for use in commercial water splitting systems if their long-term stability can be improved. Cadmium sulfide was chosen for investigations as it is representative of the metal sulfide family due to its well known properties. The more detailed aims of the project can be stated as follows:

- To examine the influence of dopant and quantum size effects in nanoparticles on the energy structure of the material and their potential to improve light absorption.
- To develop novel methods for low cost, efficient deposition of high quality metal sulfide semiconductors and their alloys utilizing electrodeposition from ionic liquids at high temperatures.
- To develop and test novel PEC devices based on metal sulfides that provide high corrosion resistance of the cell during photo-electrochemical water splitting.

### ***1.6. Structure of thesis***

The thesis is divided into 5 chapters:

- General introduction
- Electrical and optical properties of CdS nanoparticles
- Light harvesting semiconductor thin films for photo-electrochemical energy conversion
- Photo-electrochemical water splitting
- General conclusions and future work

The main body of the work (Chapters 2 to 4) will generally contain six parts:

- Introduction
- Aims of this work
- Experimental
- Results and Discussion
- Conclusions
- References

Figures have been included within the body of the text. General conclusions (Chapter 5) draws together the specific conclusions from Chapters 2-4.

## References

- [1] M. S. Dresselhaus and I. L. Thomas, *Nature* **2001**, *414*, 332-337.
- [2] J. J. Conti in *Annual energy outlook 2010 with projections to 2035, Vol.* (Ed. Energy), Washington, DC, **2010**.
- [3] R. Bashyam and P. Zelenay, *Nature* **2006**, *443*, 63-66.
- [4] B. Sakintuna, F. Lamari-Darkrim and M. Hirscher, *Int. J. Hydrog. Energy* **2007**, *32*, 1121-1140.
- [5] M. Ni, M. K. H. Leung, D. Y. C. Leung and K. Sumathy, *Renew. Sust. Energ. Rev.* **2007**, *11*, 401-425.
- [6] S. Dunn, *Int. J. Hydrog. Energy* **2002**, *27*, 235-264.
- [7] L. Schlapbach and A. Züttel, *Nature* **2001**, *414*, 353-358.
- [8] S. A. Sherif, F. Barbir and T. N. Veziroglu, *Sol. Energy* **2005**, *78*, 647-660.
- [9] J. Turner, G. Sverdrup, M. K. Mann, P. C. Maness, B. Kroposki, M. Ghirardi, R. J. Evans and D. Blake, *Int. J. Energy Res.* **2008**, *32*, 379-407.
- [10] J. K. Hurst, *Science* **2010**, *328*, 315-316.
- [11] L. L. Duan, Y. H. Xu, P. Zhang, M. Wang and L. C. Sun, *Inorg. Chem.* **2010**, *49*, 209-215.
- [12] S. W. Kohl, L. Weiner, L. Schwartsburd, L. Konstantinovski, L. J. W. Shimon, Y. Ben-David, M. A. Iron and D. Milstein, *Science* **2009**, *324*, 74-77.
- [13] F. Jiao and H. Frei, *Angew. Chem.-Int. Edit.* **2009**, *48*, 1841-1844.
- [14] D. A. Lutterman, Y. Surendranath and D. G. Nocera, *J. Am. Chem. Soc.* **2009**, *131*, 3838.
- [15] M. W. Kanan and D. G. Nocera, *Science* **2008**, *321*, 1072-1075.
- [16] J. O. Bockris and T. Otagawa, *J. Electrochem. Soc.* **1984**, *131*, 290-302.
- [17] M. Yagi, A. Syouji, S. Yamada, M. Komi, H. Yamazaki and S. Tajima, *Photochem. Photobiol. Sci.* **2009**, *8*, 139-147.
- [18] T. Nakagawa, C. A. Beasley and R. W. Murray, *J. Phys. Chem. C* **2009**, *113*, 12958-12961.
- [19] M. Yagi, E. Tomita, S. Sakita, T. Kuwabara and K. Nagai, *J. Phys. Chem. B* **2005**, *109*, 21489-21491.

- [20] J. Kiwi and M. Gratzel, *Angew. Chem.-Int. Edit. Engl.* **1978**, *17*, 860-861.
- [21] P. Lessing in *Materials for Water Electrolysis Cells*, Vol. CRC Press, **2009**, 37-59.
- [22] T. A. Betley, Q. Wu, T. Van Voorhis and D. G. Nocera, *Inorg. Chem.* **2008**, *47*, 1849-1861.
- [23] Q. S. Yin, J. M. Tan, C. Besson, Y. V. Geletii, D. G. Musaev, A. E. Kuznetsov, Z. Luo, K. I. Hardcastle and C. L. Hill, *Science* **2010**, *328*, 342-345.
- [24] Y. V. Geletii, B. Botar, P. Koegerler, D. A. Hillesheim, D. G. Musaev and C. L. Hill, *Angew. Chem.-Int. Edit.* **2008**, *47*, 3896-3899.
- [25] M. Elam and B. E. Conway, *J. Appl. Electrochem.* **1987**, *17*, 1002-1020.
- [26] B. Winther-Jensen, K. Fraser, C. Ong, M. Forsyth and D. R. MacFarlane, *Adv. Mater.* **2010**, *22*, 1727-1730.
- [27] M. Arenz, V. Stamenkovic, T. J. Schmidt, K. Wandelt, P. N. Ross and N. M. Markovic, *Surf. Sci.* **2002**, *506*, 287-296.
- [28] F. Raimondi, G. G. Scherer, R. Kotz and A. Wokaun, *Angew. Chem.-Int. Edit.* **2005**, *44*, 2190-2209.
- [29] B. Winther-Jensen, O. Winther-Jensen, M. Forsyth and D. R. MacFarlane, *Science* **2008**, *321*, 671-674.
- [30] C. A. Novak and S. V. Mantgem in *What's So Cool About Cool Roofs?* **2009**.
- [31] R. M. N. Yerga, M. C. A. Galvan, F. del Valle, J. A. V. de la Mano and J. L. G. Fierro, *ChemSusChem* **2009**, *2*, 471-485.
- [32] A. Kudo and Y. Miseki, *Chem. Soc. Rev.* **2009**, *38*, 253-278.
- [33] A. J. Nozik, *Annu. Rev. Phys. Chem.* **1978**, *29*, 189-222.
- [34] A. L. Fahrenbruch and R. H. Bube, *Fundamentals of solar cells: photovoltaic solar energy conversion*, Academic Press, New York, **1983**, pp. 559.
- [35] K. D. Dobson, I. Visoly-Fisher, G. Hodes and D. Cahen, *Sol. Energy Mater. Sol. Cells* **2000**, *62*, 295-325.
- [36] X. H. Gao, W. C. W. Chan and S. M. Nie, *J. Biomed. Opt.* **2002**, *7*, 532-537.
- [37] A. Merkoci, M. Aldavert, S. Marin and S. Alegret, *Trac-Trends Anal. Chem.* **2005**, *24*, 341-349.
- [38] H. E. Katz, J. G. Laquindanum and A. J. Lovinger, *Chem. Mat.* **1998**, *10*, 633-638.
- [39] D. A. Fraser, *The physics of semiconductor devices*, Clarendon Press, Oxford, **1983**, pp. 190.
- [40] D. Lide, *CRC Handbook of Chemistry and Physics*, CRC, **2007**, pp. 2640.

- [41] S. M. Sze, *Physics of semiconductor devices*, Wiley-Interscience, Hoboken, NJ, **2007**, pp. 880.
- [42] O. Khaselev and J. A. Turner, *Science* **1998**, *280*, 425-427.
- [43] Y. Xu and M. A. A. Schoonen, *Am. Miner.* **2000**, *85*, 543-556.
- [44] J. P. Lowe, *Quantum chemistry*, Academic Press, Boston, **1993**, pp. 728.
- [45] S. Munnix and M. Schmeits, *Phys. Rev. B* **1983**, *28*, 7342-7345.
- [46] J. O. McCaldin, T. C. McGill and C. A. Mead, *J. Vac. Sci. Tech.* **1976**, *13*, 802-806.
- [47] H. Tributsch, *Ber. Bunsen-Ges. Phys. Chem. Chem. Phys.* **1977**, *81*, 361-369.
- [48] H. O. Finklea, *Semiconductor electrodes*, Elsevier, Amsterdam, **1988**, p. 542.
- [49] L. P. Colletti, B. H. Flowers and J. L. Stickney, *J. Electrochem. Soc.* **1998**, *145*, 1442-1449.
- [50] D. B. Fraser and H. Melchior, *J. Appl. Phys.* **1972**, *43*, 3120-3127.
- [51] M. C. Baykul and A. Balcioglu, *Microelectron. Eng.* **2000**, *51-2*, 703-713.
- [52] M. Ichimura, F. Goto and E. Arai, *J. Appl. Phys.* **1999**, *85*, 7411-7417.
- [53] K. Senthil, D. Mangalaraj and S. K. Narayandass, *Appl. Surf. Sci.* **2001**, *169*, 476-479.
- [54] U. Pal, R. SilvaGonzalez, G. MartinezMontes, M. GraciaJimenez, M. A. Vidal and S. Torres, *Thin Solid Films* **1997**, *305*, 345-350.
- [55] D. Barreca, A. Gasparotto, C. Maragno and E. Tondello, *J. Electrochem. Soc.* **2004**, *151*, G428-G435.
- [56] M. Tsuji, T. Aramoto, H. Ohyama, T. Hibino and K. Omura, *J. Cryst. Growth* **2000**, *214*, 1142-1147.
- [57] M. Innocenti, S. Cattarin, F. Loglio, T. Cecconi, G. Seravalli and M. L. Foresti, *Electrochim. Acta* **2004**, *49*, 1327-1337.
- [58] A. Cortes, H. Gomez, R. E. Marotti, G. Riveros and E. A. Dalchiele, *Sol. Energ. Mat. Sol. C.* **2004**, *82*, 21-34.
- [59] M. B. Ortuno-Lopez, M. Sotelo-Lerma, A. Mendoza-Galvan and R. Ramirez-Bon, *Thin Solid Films* **2004**, *457*, 278-284.
- [60] H. Metin and R. Esen, *Semicond. Sci. Tech.* **2003**, *18*, 647-654.
- [61] W. Lu, A. G. Fadeev, B. H. Qi, E. Smela, B. R. Mattes, J. Ding, G. M. Spinks, J. Mazurkiewicz, D. Z. Zhou, G. G. Wallace, D. R. MacFarlane, S. A. Forsyth and M. Forsyth, *Science* **2002**, *297*, 983-987.
- [62] S. Z. El Abedin and F. Endres, *Chemphyschem* **2006**, *7*, 58-61.

- [63] F. Endres, D. MacFarlane and A. Abbott, *Electrodeposition from ionic liquids*, Wiley-VCH, Weinheim, **2008**, pp. 387.
- [64] M. Forsyth, J. Pringle and D. R. MacFarlane, *Aust. J. Chem.* **2004**, *57*, 113-119.
- [65] J. H. Davis, *Chem. Lett.* **2004**, *33*, 1072-1077.
- [66] R. D. Rogers and K. R. Seddon, *Science* **2003**, *302*, 792-793.
- [67] D. Behar, C. Gonzalez and P. Neta, *J. Phys. Chem. A* **2001**, *105*, 7607-7614.
- [68] P. T. Kissinger and W. R. Heineman, *Laboratory Techniques in Electroanalytical Chemistry*, CRC Press, New York, **1996**, pp. 1008.
- [69] F. E. Osterloh, *Chem. Mat.* **2008**, *20*, 35-54.
- [70] K. Maeda, K. Teramura, D. L. Lu, T. Takata, N. Saito, Y. Inoue and K. Domen, *Nature* **2006**, *440*, 295-295.
- [71] R. Asahi, T. Morikawa, T. Ohwaki, K. Aoki and Y. Taga, *Science* **2001**, *293*, 269-271.
- [72] Z. G. Zou, J. H. Ye, K. Sayama and H. Arakawa, *Nature* **2001**, *414*, 625-627.
- [73] G. M. Wang, X. Y. Yang, F. Qian, J. Z. Zhang and Y. Li, *Nano Lett.* **2010**, *10*, 1088-1092.

## Chapter 2

# Electrical and optical properties of CdS nanoparticles

### Chapter overview

Thin film and nanoparticle forms of a semiconductor are often beneficial due to the short diffusion length for electrical charges produced during excitation before the subsequent processes can occur. However, the quantum confinement effect observed for semiconducting nanoparticles significantly alters electrical properties of these materials and therefore, it is of importance to fully characterize the electrical and optical properties of nanoparticles. This chapter focuses on synthesis and characterization of electroactive nanoparticles and nanostructures based on CdS, which is a well known material having potential use in photo-electrochemical water splitting. CdS is also of interest in photoluminescence applications and these characteristics of the prepared materials are also investigated here.

### 2.1. Introduction

Group II-VI semiconductor nanocrystals have been the subject of intensive research in recent years due to potential applications in optoelectronic devices (*e.g.* lasers and LEDs), photo-catalysis for solar energy conversion and fluorescent biological labels.<sup>[1-5]</sup> The chemical and electronic properties of the nanoparticles are determined by particle size, size distribution and chemical composition, as well as by defect sites that form inside the crystal lattice and on the surface. For example, in CdS the band gap can be tuned from around 2.42 eV (~500nm) for the bulk material to 4.5 eV (~276nm) for a molecular scale material.<sup>[6]</sup>

Use of competitive reaction chemistry has been reported for the synthesis of II-VI semiconductor nanocrystals doped with different activators.<sup>[3, 7-11]</sup> During synthesis,

reaction growth of the nanocrystals competes with surface passivation.<sup>[3]</sup> The size of the nanocrystals then depends on the rates of the competing reactions and can be controlled in the nanometer range.<sup>[3]</sup> Organically passivated nanocrystals, however, have a large number of unpassivated surface sites that in general can act as nonradiative recombination and photo-degradation sites. This, in turn, decreases the quantum yield and diminishes the material's photo-luminescent (PL) properties.<sup>[6, 12]</sup>

An alternate method, which is used to synthesize nanocrystals, is based on controlled growth of nanocrystals in colloidal solutions containing stabilizers, which allows the particles to grow and at the same time prevent them from forming aggregates.<sup>[6]</sup> One of the ways of carrying out this type of synthesis is the organometallic approach that involves a size selective growth of nanocrystals in stabilizers at high temperature.<sup>[13, 14]</sup> This method allows for control of size, size distribution and shape of the nanoparticles.<sup>[6]</sup>

### 2.1.1. Reverse micelle method

This method allows synthesis of a range of compound materials in an aqueous environment and at room temperature. The method is based on the ability of small amounts of water to form nanosized droplets (micelles) when introduced to the non-polar solvents such as heptane in the presence of surfactant as can be seen in Figure 2.1. The nanocrystals grow inside the aqueous core of the micelle, whose dimension limits the size of the nanocrystals.<sup>[6, 8, 15-19]</sup> Thus, nanoparticles of specific size and spherical shape can be created. The size of the micelles, as well as the nanoparticles, in this case is determined by the water to surfactant mole ratio and varies in the range of several nanometers.<sup>[20]</sup>

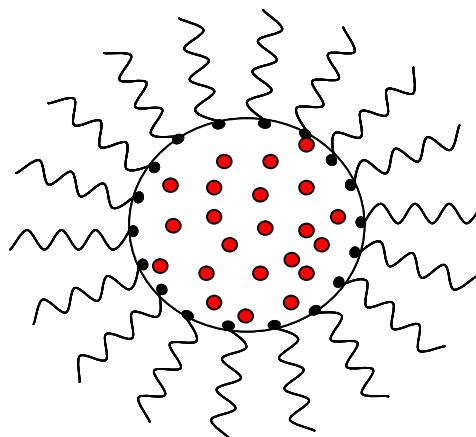


**Figure 2.1:** Formation of water droplets in reverse micelle solution.

Assuming that the microemulsion is strictly monodisperse, the radius of the micelle can be calculated using Equation 2.1.<sup>[20]</sup>

$$\frac{r^3}{(r-L)^3} = 1 + \frac{V_2}{WV_1} \quad (2.1)$$

Here  $W$  is the water to surfactant mole ratio ( $\frac{[water]}{[AOT]}$ ),  $V_1$  is the volume of a single water molecule ( $30 \text{ \AA}^3$ ),  $V_2$  is the volume of the surfactant,  $r$  is the radius of the droplet,  $L$  is the length of the surfactant molecule. For the molecular anion of sodium dioctyl sulfosuccinate (AOT) the anion length and its volume are  $30 \text{ \AA}$  and  $285 \text{ \AA}^3$  respectively, so that Equation 2.1 can be written as:<sup>[20]</sup>

$$\left(\frac{r+15}{r}\right)^3 - 1 = \frac{27.5}{W} \quad (2.2)$$

The ions dissolved in water are not confined to specific micelles and can be transferred between solutions when several micelles collide. Thus, by combining micelle solutions with different ions it becomes possible to grow a number of compound semiconductors inside the aqueous core of the micelles as shown in Figure 2.2.

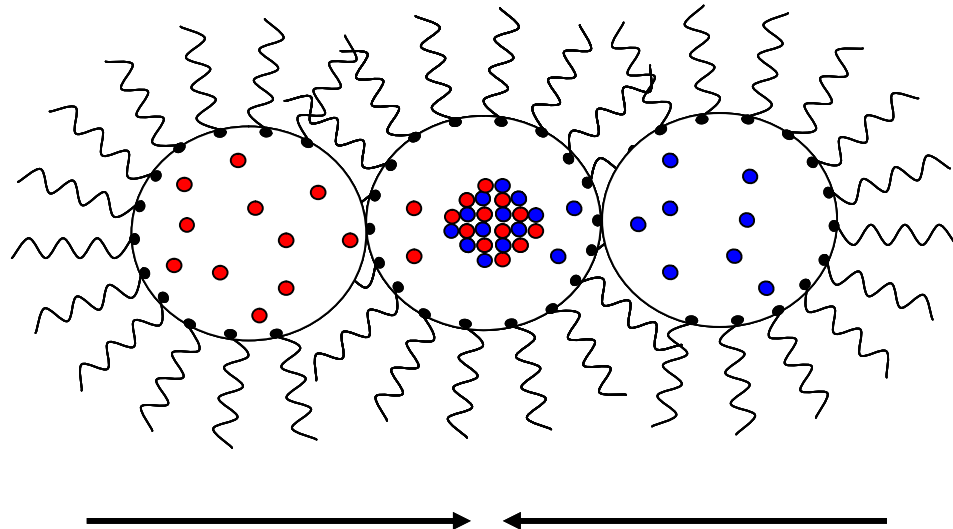


**Figure 2.2:** Synthesis of materials inside reverse micelles.

The ultimate presence of the surfactant on the surface of the nanoparticles prevents them from forming aggregates and hence, increases their lifetime.<sup>[12]</sup> Careful control of the synthesis procedure is crucial to obtain crystalline nanoparticles with narrow size

distribution in this reverse micelle method, because the microemulsion behavior is determined by the surface free energy of the surfactant film and is extremely sensitive to external parameters such as temperature and pressure.<sup>[20]</sup>

### 2.1.2. Optical properties of semiconductors

The optical properties of semiconductors are crucial for their successful implementation in energy conversion devices. Under light irradiation, photons with energy exceeding the band gap energy of a semiconductor can induce electron transfer from the valence to the conduction band.

When the thermal equilibrium between the charge carriers in a semiconductor is distorted, either by illumination or current injection, the concentrations of electrons and holes return to their equilibrium values through recombination. During recombination an electron is transferred from conduction to the valence band, thus removing the electron-hole pair. There are several ways, in which recombination in solids can occur as shown in Figure 2.3. Among them: recombination through traps (defect sites), radiative recombination and Auger recombination.

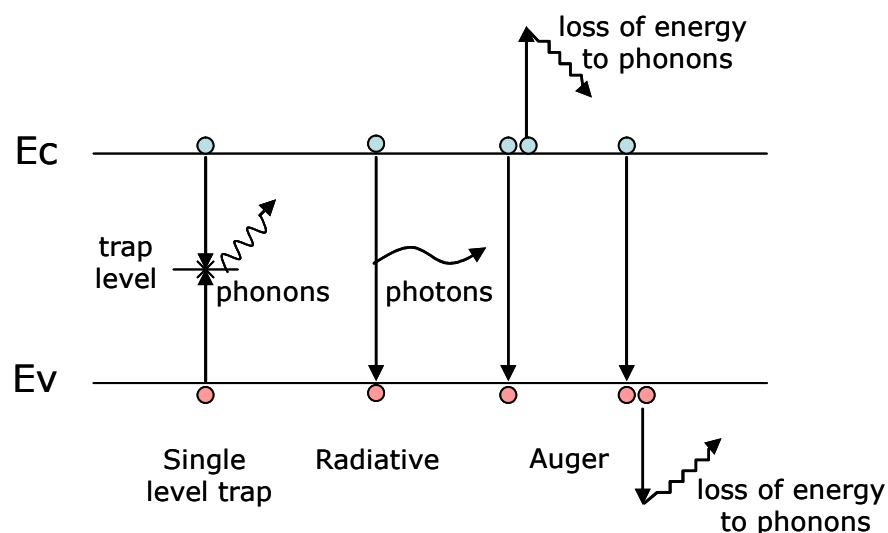


**Figure 2.3:** Recombination processes in the semiconductor.

Radiative recombination can be envisioned as the inverse process to optical excitation. The rate of such recombination is much higher in direct band gap semiconductors (*e.g.* CdS) compared to indirect band gap materials. During recombination the energy of the electron is transferred to the emitted photon. In Auger recombination, the energy of the electron is transferred to the phonon. It is the inverse process to impact

ionization, where the electron collides with a crystal atom, thus forming an electron-hole pair.

### 2.1.3. Applications

CdS nanoparticles that have been synthesized by reverse micelle methods at room temperature contain a high density of defect sites and generally exhibit low fluorescence quantum efficiencies (*i.e.*, of the order of 1-2% or less).<sup>[21]</sup> Highly luminescent CdS nanoparticles have been obtained through chemical passivation, which decreases the number of surface defect sites and enhances the yield of the excitonic emission.<sup>[22-24]</sup> For example, the fluorescence quantum efficiency of a ZnS\CdS\ZnS heterostructure synthesized *via* the reverse micelle approach was 4.52%.<sup>[22]</sup> In the previous report,<sup>[21]</sup> a broad emission from CdS nanocrystals has been enhanced from 2.8% to 12% by using photo-irradiation of the particles, after preparation, to remove surface attached groups.

As was mentioned earlier, the organometallic approach leads to synthesis of semiconducting nanocrystals with high quantum efficiency, but a narrow emission region. Blue emitting (around 400 nm)  $Zn_xCd_{1-x}S$  nanocrystals obtained by this method exhibit narrow and size dependent band edge photo-luminescence with quantum yield of 25-50%<sup>[4]</sup>. Heterostructures involving a ZnS capped CdSe nanoparticles with a green emission band centred at 550 nm have quantum efficiency of 50%. Such a strong luminescence is related to band edge emission of CdSe; the ZnS capping layer here is used to passivate the core crystallite, removing the surface traps.<sup>[23]</sup> Strong red emission with quantum efficiency up to 60-80% has been produced from ZnSe nanoparticles shelled with CdSe. This type of structure promotes spatial separation of electrons and holes that occupy different parts of the heteronanoparticles.<sup>[5]</sup>

Although these particles exhibit high quantum efficiency there are some concerns for their implementation in white light emitting optoelectronic devices due to differential aging of nanoparticles that correspond to different colors.<sup>[6, 24]</sup>

The broad emission in the yellow-green region has been previously reported from CdS nanoparticles synthesized *via* aqueous<sup>[25-27]</sup> and nonaqueous<sup>[2, 28]</sup> routes. In the thorough investigation of CdS particles in zeolites<sup>[26]</sup> it was shown that the yellow-green emission can be generated from CdS particles, which were heated in air at 350 °C. This

emission was attributed to the defects created by Cd atoms, which caused a broad absorption band in the 450-550 nm region.<sup>[26]</sup> It was also shown that the defects responsible for the yellow-green emission may come as the result of photo-chemistry. However, the exact mechanism for emission is not yet certain.

### **2.2. *Aims of this work***

The ability to tune electric properties of nanocrystals for photo-voltaic applications allows a wider range of materials to be used with subsequent improvement in the process efficiency. This work aims to prepare CdS nanoparticles of a variety of structures and to characterize their electrical and optical properties, which are of interest in water splitting and photo-luminescence applications. In the latter field, despite the success of the nanostructures in producing high efficiency and narrow band emission, the challenge of generating a broad (preferably white) emission with a high quantum yield still remains.

Specific aims of this work were:

- Synthesis of CdS nanoparticles using the reverse micelle method
- Characterization of prepared nanoparticles of various sizes using
- Dynamic light scattering to measure size of particles synthesized at different conditions and their relation to theoretically expected sizes.
- EDX to determine chemical composition
- Selected area electron diffraction to determine crystal structure
- High resolution TEM images to determine specific shape and structural integrity
- UV-vis and fluorescence spectroscopy to determine electronic structure

To alter electrical and optical properties for water splitting applications of CdS nanoparticles, prepare CdS particles of various sizes using carbonate as dopant during synthesis and characterize their electronic structure and size using UV-vis and fluorescence spectroscopy and DLS techniques.

In order to improve quantum efficiency, which is of interest in photo-luminescence applications, prepare “core shell” structures based on the particles developed earlier in this work and characterize their electronic structure and size using UV-vis and fluorescence spectroscopy and DLS techniques.

### **2.3. Experimental**

For synthesis of CdS nanoparticles  $\text{Cd}(\text{CH}_3\text{COO})_2$ ,  $\text{Na}_2\text{S}\cdot 9\text{H}_2\text{O}$ ,  $\text{Na}_2\text{CO}_3$  and dioctyl sulfosuccinate sodium salt (AOT) were purchased from Aldrich and used as received. Distilled water (resistivity  $18.2 \text{ M } \Omega$ ) and *n*-heptane were carefully deaerated by nitrogen bubbling prior to use in order to prevent additional reactions caused by the presence of carbon dioxide, carbonate and bicarbonate ions and/or oxygen in water.

#### **2.3.1. Synthesis of nanoparticles**

CdS nanoparticles were prepared using the reverse micelle-method as described in the literature.<sup>[21, 22]</sup> Nitrogen atmosphere was maintained at all stages. In a typical preparation 0.1 M aqueous solutions of sodium sulfide and cadmium acetate were admixed to 0.1 M solution of AOT in *n*-heptane. After thorough mixing, each micelle solution was kept for a half an hour prior to usage. The micelle solutions were combined at a very slow rate (around 0.5 ml/min) with continued agitation.

In order to introduce defects in the nanoparticles (labeled here as cmCdS), a small amount of sodium carbonate (5 mol %) was added to the sulfide micelle solution prior to synthesis.

In order to synthesize “core-shell” nanoparticles, four micelle solutions containing different ions for the core and shell growth were used. Synthesis of core particles was conducted through the procedure reported above. Afterwards the prepared particles were transferred to the solution for the shell growth. In all cases, equilibrium in micelle solutions was allowed to establish before the growth stage. The “core” particles with *W* of 1.39 and 2.78 were synthesized following the method reported above. For the “shell” growth, the overall value of *W* in the micelle solution was readjusted to 7.4 through the addition of the cadmium containing micelle solution. For example, 0.5 ml of solution containing “core” particles with *W* of 1.39 required addition of 2.2 ml of AOT heptane solution that contains 35  $\mu\text{l}$  of aqueous cadmium acetate (0.1M) in order to readjust overall *W* to 7.4.

### 2.3.2. Characterization techniques

The samples were examined in a 200keV JEOL 2011 TEM fitted with a LaB<sub>6</sub> filament and an analytical pole-piece with a nominal point resolution of 2.3Å. The TEM samples were prepared by deposition on an amorphous carbon film supported by 400 mesh copper grids. The samples were dried under a lamp to allow heptane to evaporate and then heated to 50°C for 1 hour, following 1 hour heating under vacuum. The samples were then left at room temperature under vacuum overnight.

The UV-vis measurements were carried out on a Varian, Cary 100 Bio, UV-visible spectrophotometer. UV-vis spectra were measured from 800 nm to 200 nm at a scan rate of 300 nm per min. Two quartz cells with path lengths of 1 and 0.5 cm were used to study absorption in the ultra violet region.

Dynamic light scattering (DLS) determined with zeta potential analyser (model BI-ZETAPLUS) was used to record a correlation function of the nanoparticles in heptane. In a typical experiment monochromatic light beam is passed through a solution containing the nanoparticles. Assuming that particles have spherical shape with the known viscosity and refractive index of the solvent, it becomes possible to calculate diffusion coefficients and the effective hydrodynamic diameter of particles in solution. The strength of the signal is proportional to diameter to the power of 6, which makes DLS extremely sensitive to any impurities that may be present.<sup>[29]</sup>

### 2.3.3. Quantum yield measurements

The fluorescence quantum yield is the ratio of photons absorbed by material to photons emitted through fluorescence. A comparative method reported by Williams *et al.*<sup>[30]</sup> was used to determine quantum yield. In this method standard samples used for calibration should absorb light at the excitation wavelength chosen for the test sample and if possible emit light in a similar region.

The procedure used to determine quantum yield is as follows: UV-vis absorption spectra are recorded for solvent and sample solution in order to determine absorption value at excitation wavelength. The fluorescence spectrum is recorded and integrated fluorescence intensity is calculated (area of the fluorescence spectrum). The procedure is repeated for a range of different concentrations. In order to minimize re-absorption effects,

absorbance at excitation wavelength was in all cases kept below 0.1. A graph of integrated fluorescence intensity *versus* absorbance can be plotted, with the gradient being proportional to the quantum yield of the sample. Absolute values of quantum yield are calculated using results obtained for standard solutions from Equation 2.3:

$$\Phi_x = \Phi_{st} \left( \frac{Grad_x}{Grad_{st}} \right) \left( \frac{\eta_x^2}{\eta_{st}^2} \right) \quad (2.3)$$

where the subscripts “st” and “x” denote standard and test samples, respectively,  $\Phi$  is the fluorescence quantum yield, Grad is the gradient from the plot of integrated fluorescence intensity *versus* absorbance, and  $\eta$  is the refractive index of the solvent.

Fluorescence quantum yields of the prepared samples were determined by comparison with the emission from standard samples: rhodamine 6G dissolved in ethanol (quantum yield of 0.95)<sup>[31]</sup> and coumarine 30 dissolved in acetonitrile (quantum yield of 0.67).<sup>[32]</sup> Cross calibration of quantum yield measurements between two standard samples led to an estimated absolute uncertainty of less than 1 %.

## **2.4. Results and Discussion**

The reverse micelle method was used to synthesize nanoparticles at W=7.4. The detailed TEM and EDX analysis of such particles dispersed on the carbon grid is presented below.

### **2.4.1. TEM and EDX results**

Detailed HRTEM was carried out in conjunction with Associate Professor Joanne Etheridge and Ms Hadas Katz; Ms Katz carried out the diffraction analysis described below. Individual nanoparticles were observed distributed across the carbon film. EDX spectra taken from clusters consisting of a few hundred nanoparticles identified by the presence of Cd, S and O elements only (as well as Cu from the specimen support grid).

Selected area electron diffraction (SAD) patterns of a large field of view, which included many nanoparticles spread across the carbon film, are shown in Figure 2.4. The radii of the resulting diffraction rings were carefully measured. A subset of rings was found to be consistent with the presence of cubic CdS with the zinc-blende structure, while another subset indicated presence of hexagonal CdS with the wurtzite structure.

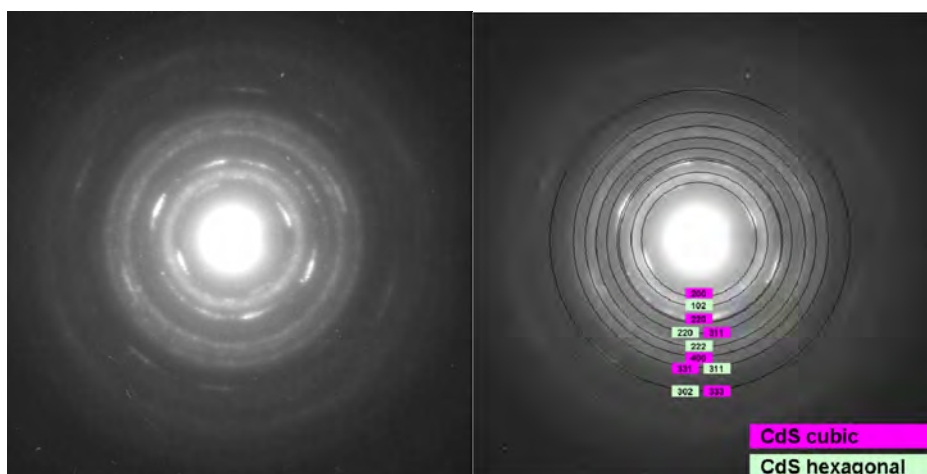


**Figure 2.4:** SAD pattern of a large field of view (left); the diffraction rings are indexed (right) and found to be consistent with the presence of hexagonal and cubic CdS.

High resolution electron microscopy images taken for individual nanoparticles indicate that the particles are clearly crystalline. The analyses of these images (typical examples are shown in Figure 2.5 and Figure 2.6) confirm presence of a cubic CdS structure.

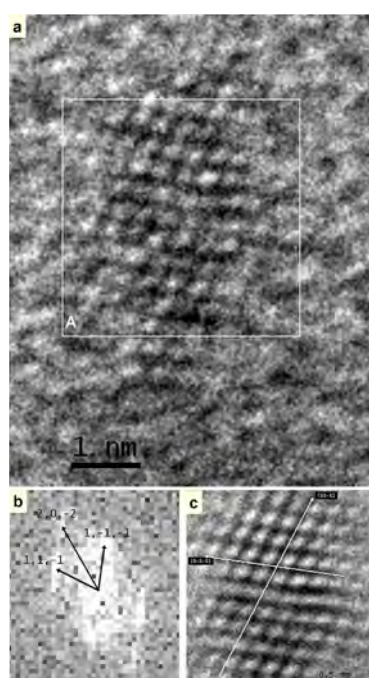


**Figure 2.5:** (a) HRTEM image of CdS nanoparticle supported on a carbon film. (b) Fourier transform taken from area A. The geometry is consistent with the CdS cubic zinc-blende crystal structure orientated down the  $\langle 101 \rangle$  zone axis. (c) Inverse of the Fourier transform with diffuse background masked to enhance atomic contrast. The orientations of the  $\{1\bar{1}\bar{1}\}$  and  $\{11\bar{1}\}$  atomic planes are marked.

Figure 2.5a shows a single nanoparticle  $\sim 3$  nm in diameter. By taking a Fourier transform of area A (as seen in Figure 2.5b), a ‘diffraction pattern’ of the image is generated and the relative spacing and orientation of the atomic planes can be measured. Analysis of this ‘diffraction pattern’ shows that it is consistent with a cubic nanocrystal oriented down the  $\langle 101 \rangle$  zone axis. This conclusion was also checked against a Fourier transform from a much larger region of the image incorporating nearby nanocrystals. The indices ascribed to the diffraction spots in the Fourier transform of the individual nanocrystal were found to be consistent with the relative spacing and indices of the ‘diffraction’ rings from the larger field of view.

By taking an inverse Fourier transform of the pattern in Figure 2.5b whilst masking everything but the diffraction spots, the atomic contrast is enhanced over the contrast from the supporting carbon film (as seen in Figure 2.5c). It can be seen more clearly from this figure that the nanoparticle is about 11 atoms wide at its widest point in projection.

Figure 2.6a shows a few nanoparticles supported on a carbon film, which appear to have spherical shape. The analysis of the Fourier Transform of the image (in Figure 2.6b,c) shows that the particles in area A are consistent with a cubic nanocrystals oriented down the  $\langle 001 \rangle$  zone axis (see Figure 2.6b) and down the  $\langle 101 \rangle$  zone axis (see Figure 2.6c).

By taking an inverse Fourier transform of the pattern in Figure 2.6b and Figure 2.6c, whilst masking everything but the diffraction spots, the atomic contrast is enhanced over the contrast from the supporting carbon film (see Figure 2.6d).

It can be concluded that on the basis of EDX measurements, synthesized nanoparticles are composed of Cd and S. Diffraction patterns indicate presence of both hexagonal and cubic CdS crystals, while HRTEM images indicate that nanocrystals assume a spherical shape. These observations are consistent with the hypothesis of nanocrystals growth inside micelles.

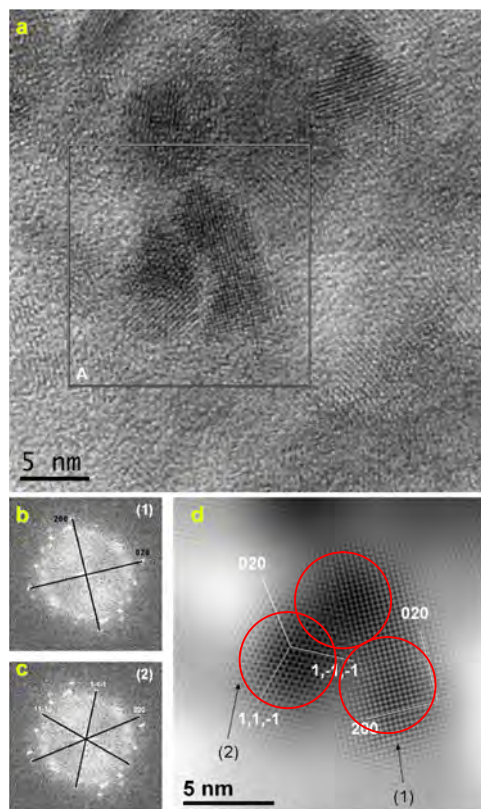


**Figure 2.6:** (a) HRTEM Image of CdS nanoparticles supported on a carbon film. Two nanoparticles shown in area A are analysed using a Fourier transform of the whole image shown in figure (b) and (c). Indexing of this Fourier transform reveals the presence of a particle (1) with cubic zinc-blende crystal structure orientated down the  $\langle 001 \rangle$  zone axis (see figure b) and another particle (2) with the cubic zinc-blende crystal structure orientated down the  $\langle 101 \rangle$  zone axis (see figure c). (d) Inverse of the Fourier transform with diffuse background masked to enhance atomic contrast. The crystal plane geometry of the two cubic nanocrystals orientated down the  $\langle 001 \rangle$  (particle 1)) and  $\langle 101 \rangle$  zone axis (particle 2) are marked.

#### 2.4.2. Size characterisation

Dynamic light scattering (DLS) determined with a zeta potential analyser (model BI-ZETAPLUS) was used to obtain a correlation function of the nanoparticles in heptane. From the known viscosity, refractive index and temperature, the effective hydrodynamic diameter of particles in solution was calculated.

On the assumption that the surfactant forms a continuous shell (with a thickness equal to the molecular chain length) on the spherical water droplet, it is possible to equate the water to surfactant volume ratio in the micelles with that in the stock solution. The radius of the micelles in this case can be calculated from Equation 2.2.<sup>[20]</sup> The data of DLS analysis and theoretical micelle sizes are summarized in Table 2.1.

**Table 2.1:** Effective hydrodynamic diameter of particles at different W based on the data of DLS measurements.

W	Count	Base	Effective	Average	Theoretical
	Rate, kcps	diff., %	diameter, nm	diameter, nm	diameter, nm
1.4	32.8	1.14	1	$0.94 \pm 0.16$	1.72
	32.9	0.83	0.9		
	31.8	0.59	0.8		
	34	0.11	1.2		
	31	0.8	0.8		
2.8	38.8	2.1	2.2	$1.52 \pm 0.59$	2.47
	38	0.3	1.9		
	39	0.6	0.9		
	38.7	0	1.7		
	39	0.3	0.9		
	39.2	0.5	0.9		
5.6	47.6	1.6	1.9	$2.28 \pm 0.74$	3.71
	48.6	0.15	2.1		
	49.5	0.25	3.6		
	49.2	1.3	1.9		
	50.2	0.95	1.9		
7.4	68.4	0.46	2.7	$2.976 \pm 0.57$	4.58
	66.1	0.06	3.2		
	64	0.07	3.48		
	71	0.4	2.1		
	69.8	1	3.4		
11.1	85	2.2	4.1	$4.08 \pm 0.27$	5.78
	85	3	4.2		
	86	2.7	4.3		
	86	3	4.2		
	85.8	0.93	3.6		

The effective diameter of the particles, based on DLS measurements, is plotted as a function of water to surfactant mole ratio (W) in Figure 2.7 and is seen to be a rising function of W.

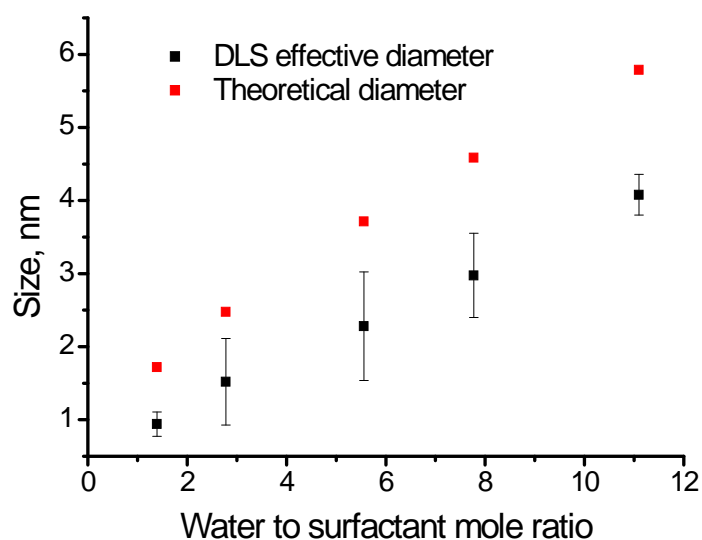


**Figure 2.7:** Dependence of calculated micelle size and measured effective diameter on the water to surfactant mole ratio.

It is suggested<sup>[22]</sup> that the ultimate particle size is similar to the size of the original micelles and this was borne out by the experimental data. Figure 2.7 also shows the dependence of the calculated micelle size on the water to surfactant mole ratio. Although the data obtained from DLS measurements should be treated with caution in the absolute sense, it can be seen that the general trend is clearly as expected from Equation 2.2 and that there is a good correspondence between the expected and measured sizes.

### 2.4.3. Optical and electrical properties of CdS nanoparticles

#### CdS nanoparticles

Typical UV-vis absorption spectrum obtained from CdS nanoparticles at  $W=11.1$  is shown in Figure 2.8. The spectrum was recorded in transmission mode for a sample dissolved in heptane and generally shows similar features compared to data reported in the literature.<sup>[10, 20, 24]</sup> Several absorption regions can be observed on the plot. The first one has an absorption edge around 400 nm and shows tendency to level at 340nm, while the second one appears at wavelengths less than 320 nm with a tendency to form a plateau at 280 nm.

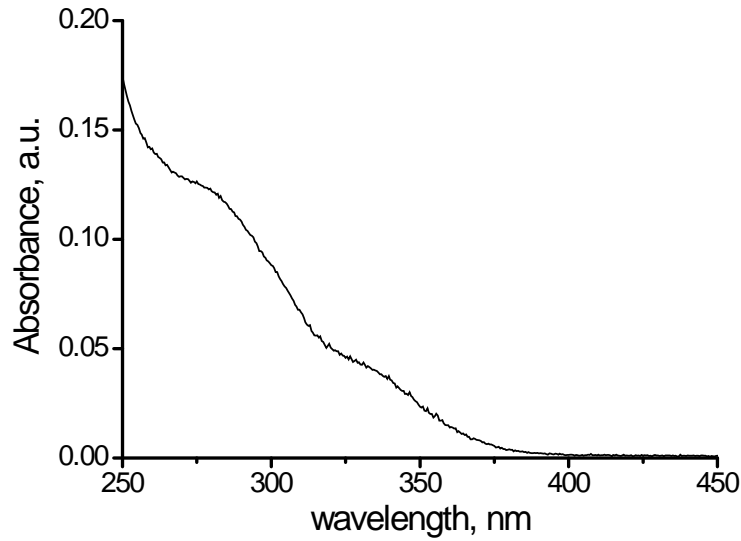


**Figure 2.8:** UV-vis absorption spectra of CdS nanoparticles in heptane synthesized at W=11.1

UV-vis spectra were used to calculate the electron transition energies from Equation 2.4 in the usual way as described elsewhere.<sup>[33, 34]</sup>

$$\alpha = k \frac{(h\nu - E)^m}{h\nu} \quad (2.4)$$

where  $k$  is a constant,  $h\nu$  is photon energy,  $E$  is the electron transition energy and  $m$  is a constant equal to 1/2 of a direct band gap material. For a semiconductor, the plot of  $(\alpha h\nu)^2$  versus  $h\nu$  yields the electron transition energy, which can be calculated as interpolation of linear parts of the curves to the point where  $(\alpha h\nu)^2 = 0$ . Figure 2.9 shows such a dependence for the CdS nanoparticles synthesized at W=11.1. As can be seen, two energies can be derived from the plot; their values for CdS nanoparticles synthesized at W= 11.1 are  $3.88 \pm 0.01$  eV and  $3.46 \pm 0.01$  eV.

The absorption corresponding to high energies around 3.9 eV may be attributed to band gap absorption. Its value is much higher than 2.42 eV reported for bulk CdS crystals, but lower than 4.5 eV, which corresponds to CdS on a molecular scale. This fact can be attributed to the quantum confinement effect commonly observed in CdS semiconductor nanocrystals.

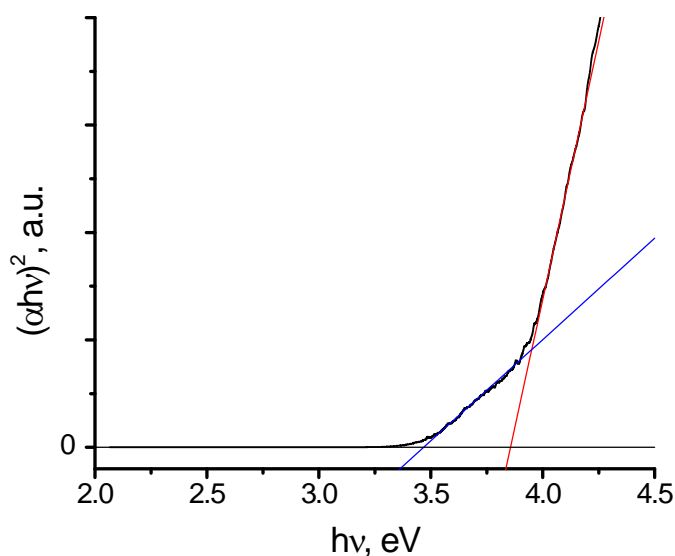


**Figure 2.9:** Typical  $(\alpha h\nu)^2$  versus  $h\nu$  plot derived from UV-vis spectra. Construction shown in the figure CdS at W=11.1 indicates the method used to determine electron transition energy.

The photo-luminescence spectrum as seen in Figure 2.10 shows several distinctive regions. The first is a rather narrow emission in the near UV with a maximum at ~345 nm and broad emission in the red region (600-750 nm).

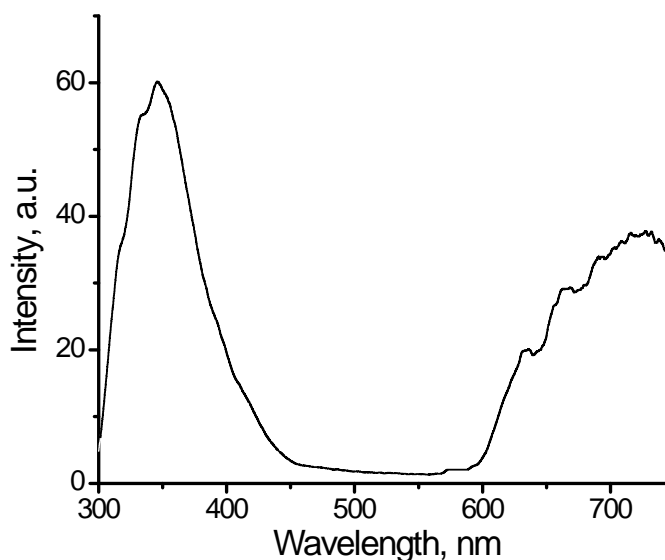


**Figure 2.10:** Emission spectrum of CdS nanoparticles (W=11.1) excited at 290 nm.

Photo-luminescence with a peak wavelength below 400 nm has rarely been observed from CdS nanocrystals (although in some previous reports the samples were not excited at energies high enough to stimulate this emission even if possible). In some cases

an emission band centred around 400 nm was detected<sup>[2, 35]</sup>. CdS is a direct band gap semiconductor, hence the emission observed in the present work around 345 nm may be related to band gap photoluminescence in the CdS and has a blue shift compared to the bulk crystal due to the quantum confinement effect commonly observed in nanoparticles. The emission in the red is also commonly observed from CdS nanoparticles.<sup>[8, 35]</sup>

An optical image of the particles excited with UV-LED (peak emission wavelength at 400 nm) is shown in Figure 2.11, confirming the predominantly blue emission from the sample.

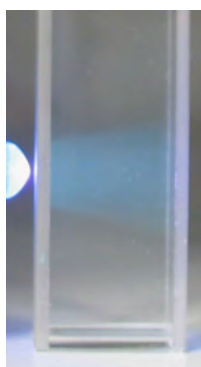


**Figure 2.11:** Optical image of CdS nanoparticles in heptane excited by UV-LED (peak emission at 400 nm).

The photo-luminescence spectra of CdS nanoparticles show no emission in the yellow-green region; hence they cannot be used to generate white light emission. In order to achieve emission in this region, small amount of sodium carbonate was added to the sodium sulfide solution prior to synthesis to create defects in the structure of CdS nanoparticles, thus producing chemically modified nanocrystals (cmCdS).

### **Chemically modified CdS nanoparticles**

UV-vis absorption spectra for a series of cmCdS particles synthesized at different values of  $W$  are shown in Figure 2.12. Similar to absorbance by CdS particles, two regions can be defined in the UV-vis spectra. The first region of absorbance, which is characterized by the presence of a plateau, for particles synthesized at different values of  $W$  lies within 320 and 450 nm. For absorbance in the second region (260 – 320 nm) formation of a well defined maximum at 280 nm can be observed for particles synthesized at  $W=5.6$ . As the value of  $W$  increases, there is a red shift of the absorption edge (*i.e.* from 380 to 425 nm), which can be related to quantum size effects commonly seen in nanoparticles.

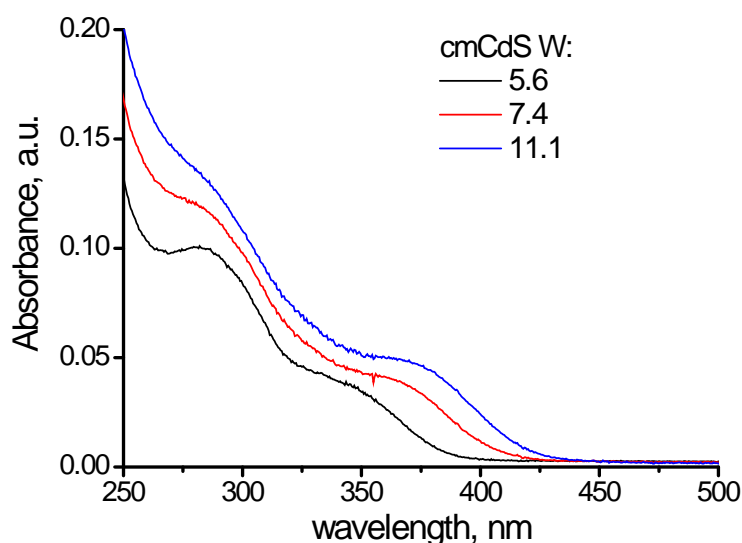


**Figure 2.12:** UV-vis absorption spectra of cmCdS nanoparticles in heptane synthesized at different values of  $W$ .

In the case of cmCdS the corresponding electron transition energies vary from 3.31 eV to 3.05 eV. It should be noted that in “pure” CdS nanoparticles synthesized at  $W=11.1$  the energy corresponding to the absorption edge is equal to 3.46 eV compared to 3.05 eV for the cmCdS particles of the similar size. It appears that the addition of the carbonate dopant significantly reduces the energy of band edge absorption for CdS particles, which can be seen in Table 2.2. No major differences were observed in the values of high energy transition between different particle types.

**Table 2.2:** Electron transition energies in different types of nanoparticles derived from the UV-vis spectra.

Type of nanoparticles	$W$	Theoretical size, nm	High energy transition, eV $\pm$ 0.01	Low energy transition, eV $\pm$ 0.01
CdS	11.1	5.78	3.88	3.46
cmCdS	5.6	3.71	3.83	3.31
	7.4	4.58	3.77	3.13
	11.1	5.78	3.77	3.05

Based on the data obtained from UV-vis spectra, two excitation energies were chosen in order to study electron transition processes in the semiconductor. One is sufficiently high at 290nm (4.28 eV) to induce both types of electron transition (as seen in Table 2.2), while the other at 350nm (3.54 eV) is sufficient only for electron transition corresponding to low energy absorption.

Photo-luminescence spectra shown in Figure 2.13 indicate formation of a broad emission band in the visible part of the spectra (400-700 nm). At excitation energies less than the high energy transition of the nanocrystals (energies corresponding to the lower energy absorption in the UV-vis spectra), emission from the yellow-green region is still observable. It can be speculated that the carbonate anions result in the formation of energy levels in the CdS energy structure, from which emission occurs.

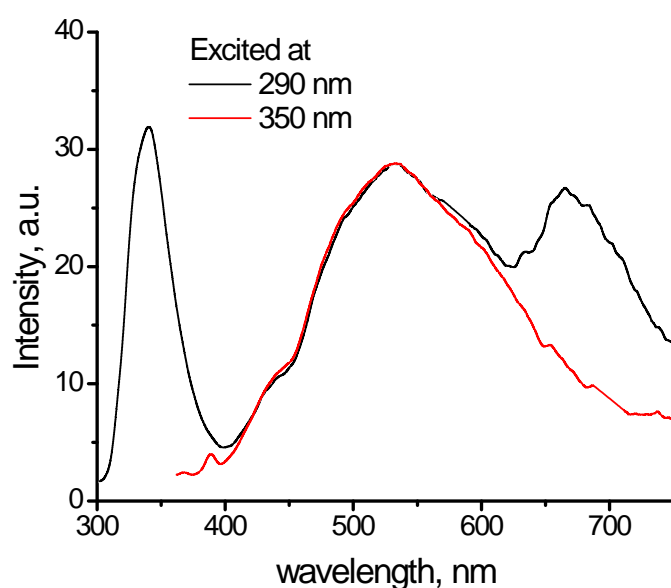


**Figure 2.13:** Typical emission spectra of chemically modified CdS excited at 290 and 350 nm.

Although the decomposition temperature of cadmium carbonate is 580 K,<sup>[36]</sup> it is also possible that cadmium carbonate decomposes under light irradiation to form cadmium oxide. In this case a heterojunction between CdO and CdS is formed.

The fluorescent spectra of cmCdS synthesized at various values of  $W$  are shown in Figure 2.14. With an increase in  $W$ , emission from the yellow-green region shifts to longer wavelengths (490 nm, 530 nm and 590 nm). However, the emission from near UV and red regions remain constant with respect to the size of nanoparticles. It can be seen from the Figure 2.14 that with a decrease in the particle size, the emission intensity from the yellow-green region becomes smaller. This observation is consistent with the data reported earlier,<sup>[15]</sup> where very small ZnS particles (1.5 nm in diameter) exhibited very little emission from dopant species.

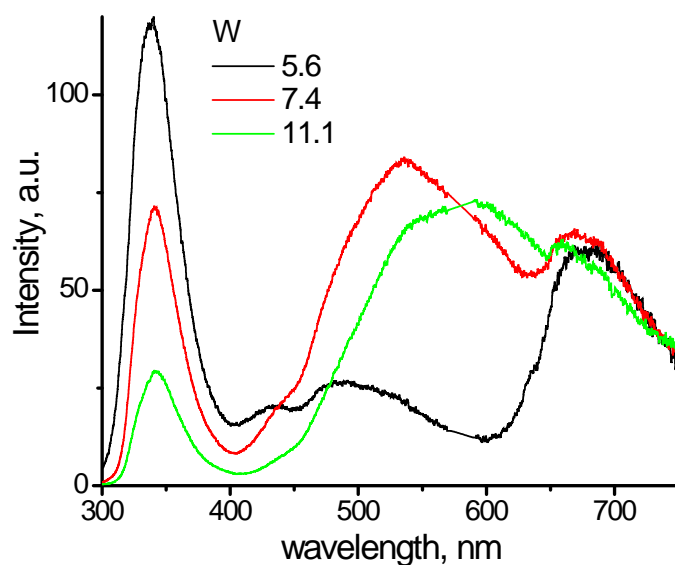


**Figure 2.14:** Emission spectra of cmCdS nanoparticles excited at 290 nm for different values of  $W$ .

The optical images of the particles excited with UV-LED (peak emission wavelength at 400 nm) are shown in Figure 2.15. The emission in this case of course will not contain the band in the near UV region and therefore, the visually observed emission is only due to the yellow-green region. The overall emission is observed to be tuneable from the blue through green to yellow as a function of particle size.

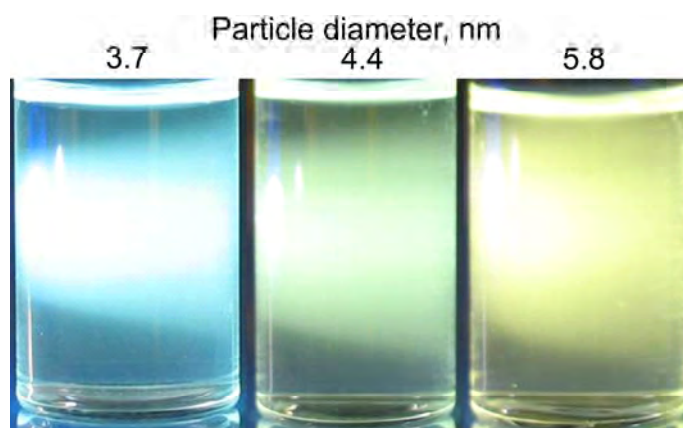


**Figure 2.15:** Optical images of cmCdS nanoparticles of different sizes in heptane excited by UV-LED (peak emission at 400 nm). The diameter of the glass tube containing the particle suspension is 16 mm.

Quantum efficiencies of cmCdS nanoparticles were calculated using Equation 2.3 and are presented in Table 2.3.

**Table 2.3:** Quantum efficiency of cmCdS nanoparticles

Size of the particles, W	Quantum efficiency, % $\pm 1$
5.6	10
7.4	9.3
11.1	9.1

Overall, with the use of carbonate dopant it was possible to increase light absorption of CdS particles in the visible part of the solar spectra, which is of importance in water splitting applications. The broad emission in the visible part of the spectra from these particles is size dependable and can be red shifted with an increase in particle size and allows them to be successfully used in photo-luminescence applications.

#### 2.4.4. “Core shell” structures based on cmCdS

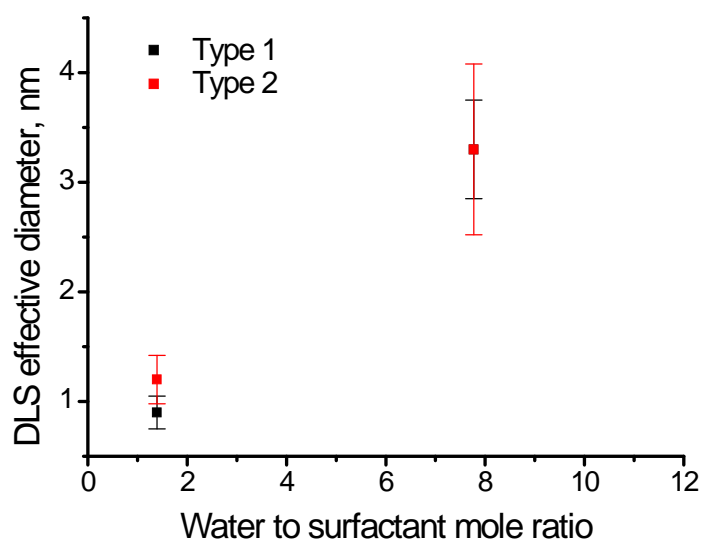
Although cmCdS particles show high values of quantum efficiency, the “core shell” structures can be used to significantly improve quantum efficiency and stability of nanocrystals for photoluminescence applications.

In this work “core shell” structures were based on cmCdS nanoparticles coated with a CdS shell. The effective hydrodynamic diameters of cmCdS nanoparticles with various W are given in Table 2.4. Cadmium sulfide nanoparticles containing carbonate (cmCdS) were synthesized separately at two different W (W=1.39 and 2.78) which correspond to the theoretical sizes 1.7 (denoted here as Type 1) and 2.46 nm (denoted here as Type 2) or experimental data from DLS 0.96 and 1.34 nm respectively. Then CdS was grown on these particles in a second step at W=7.4, increasing overall particle size to 4.6 nm (compared to the range 3.5 - 4 nm obtained by DLS).

The effective diameters of the particles, based on DLS measurements, are plotted as a function of the water to surfactant mole ratio (W) in Figure 2.16 and are seen to be a rising function of W.

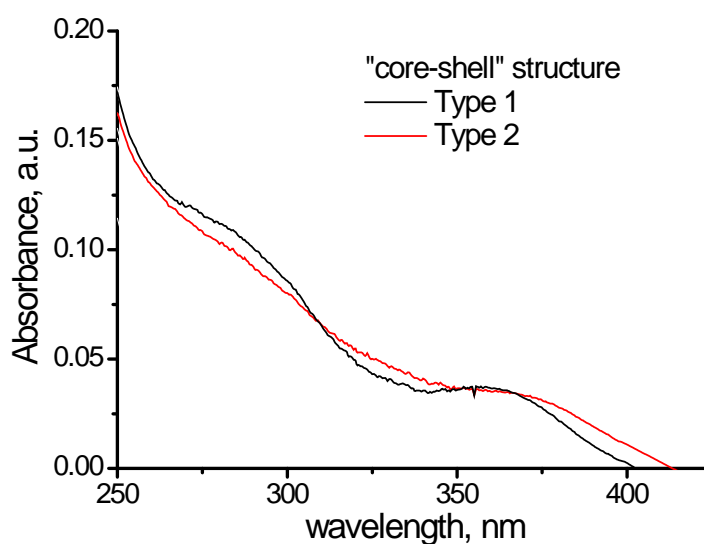
**Table 2.4:** Effective hydrodynamic diameter of particles at different W based on the data of DLS measurements.

material/W	Count Rate, kcps	Base diff., %	Effective diameter, nm	Average diameter, nm	Theoretical diameter, nm
cmCdS type 1 1.4	60.9	0.6	1.2	0.90 ± 0.15	1.72
	60.3	0.7	0.9		
	61.2	1.1	0.9		
	60.9	1.8	0.9		
cmCdS/CdS type 1 7.4	102.5	0.5	2.8	3.30 ± 0.45	4.58
	110.1	4.3	3.2		
	107.9	2.7	3.9		
	111.3	2.3	3.3		
cmCdS type 2 2.8	28	0.8	0.9	1.20 ± 0.22	2.47
	27.3	0.5	1		
	27	0.4	1.4		
	27.4	-0.33	1.2		
cmCdS/CdS type 2 7.4	117.9	0.23	4.6	3.30 ± 0.78	4.58
	119.4	0.4	4.8		
	118.9	0.85	3.4		
	118.4	0.2	3.3		



**Figure 2.16:** Dependence of measured effective diameter on the water to surfactant mole ratio.

UV-vis absorption spectra of the “core shell” particles are shown in Figure 2.17. Similarly to CdS and cmCdS, two absorption regions can be observed on the graphs. The energies corresponding to the absorption edges in these structures are also shifted from 3.46 eV for CdS to lower energies of cmCdS of 3.19 and 3.11 eV, which can be seen in Table 2.5.

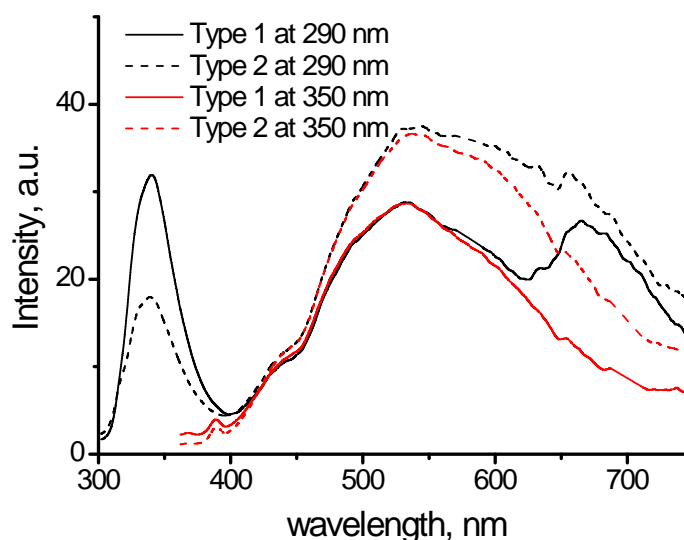


**Figure 2.17:** UV-vis absorption spectra of “core shell” nanoparticles of different types.

**Table 2.5:** Electron transition energies in different types of nanoparticles derived from UV-vis spectra.

Type of nanoparticles		High energy transition, eV $\pm$ 0.01	Low energy transition, eV $\pm$ 0.01
CdS	W=11.1	3.88	3.46
“core shell” CdS	Type1	3.83	3.19
	Type2	3.76	3.11

The fluorescent spectra of “core-shell” CdS (aged for six months) excited with light at 290 nm (4.28 eV) and 350 nm (3.54 eV) are shown in Figure 2.18. It can be seen from the graph that an increase in size of the core particle (Type 2) results in formation of a broader photoluminescence peak in the yellow-green region compared to the particles with the smaller core (Type 1). A slight red shift in the position of maximum fluorescence can also be observed for Type 2 particles. The values of quantum efficiency calculated from Equation 2.3 for “core shell” particles were around 20%, which almost doubles these obtained for cmCdS (around 10%). Over the six months period there was very little change in the shape of spectra and values of quantum efficiency.

**Figure 2.18:** Emission spectra of “core shell” CdS nanoparticles which have been aged for six months; excited at 290 nm (black) and 350 nm (red).

From the emission spectra of the nanoparticles excited at 350 nm the CIE coordinates were calculated. The values for Type1: (x, y)=(0.35, 0.41) and Type 2: (x, y)=(0.38, 0.36) correspond to almost white light emission as can be seen in Figure 2.19.

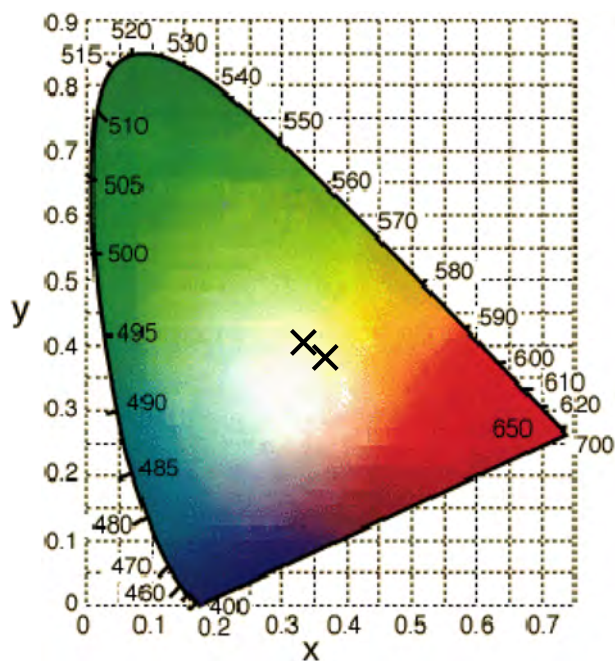


**Figure 2.19:** The CIE 1931 colour space chromaticity diagram.<sup>[37]</sup>

The optical image of the particles excited with UV-LED (peak emission wavelength at 400 nm) is shown in Figure 2.20.



**Figure 2.20:** Optical image of “core-shell” CdS nanoparticles in heptane excited by UV-LED with a peak emission at 400 nm. The diameter of the glass tube containing the particle suspension is 16 mm.

## 2.5. Conclusions

A novel method for creating defect states in CdS nanoparticles by using carbonate modification was developed in this work. With the use of carbonate dopant it became possible to increase light absorption of CdS particles in the visible part of the solar spectra, which is of importance in water splitting applications.

Highly luminescent CdS nanocrystals were synthesised *via* the reverse micelle method at room temperature in the aqueous solution. The average particle size of the crystallites was estimated by dynamic light scattering, which shows similar trend in particles sizes as expected from theoretical calculations.

From the data of the EDX measurements, the synthesized nanoparticles are composed of Cd and S, with diffraction patterns indicating presence of both hexagonal and cubic CdS crystals. HRTEM images show that nanocrystals assume spherical shape, which is consistent with the hypothesis of nanocrystals growing inside micelles.

The electronic structure of CdS was analysed with UV-vis spectra. Excitation of samples results in photoluminescence in near UV and red region. The addition of the carbonate dopant significantly reduces the energy of the absorption edge for CdS particles. In addition to emission in UV and red regions, the broad emission in the visible part of the spectra was observed for CdS nanoparticles synthesized in the presence of carbonate ions. The colour of photo-luminescence from cmCdS is size dependent and can be red shifted with an increase in particle size.

The use of “core shell” structures based on cmCdS significantly improved quantum efficiency of the nanocrystals, which remains around 20% even after six months of storage as a suspension in heptane. High values of quantum efficiency and long-term stability and almost white light emission allows “core shell” structures to be successfully used in photo-luminescent applications.

## References

- [1] E. Caponetti, *Mater. Sci. Eng. C* **2003**, *23*, 531-539.
- [2] Georgi G. Yordanova, E. Adachib and C. D. Dushkin, *Mater. Charact.* **2007**, *58*, 267-274.
- [3] H. Yang and P. Holloway, *J. Appl. Phys.* **2003**, *93*, 586-592.
- [4] X. Zhong, Y. Feng, W. Knoll and M. Han, *J. Am. Chem. Soc.* **2003**, *125*, 13559-13563.
- [5] S. A. Ivanov, J. Nanda, A. Piryatinski, M. Achermann, L. P. Balet, I. V. Bezel, P. O. Anikeeva, S. Tretiak and V. I. Klimov, *J. Phys. Chem. B* **2004**, *108*, 10625-10630.
- [6] D. R. Vij, *Handbook of Electroluminescent Materials*, Taylor & Francis, **2004**, p. 159.
- [7] C. Barglik-Chory, Remenyi C, Dem C, Schmitt M, Kiefer W, Gould C, Ruster C, Schmidt G, Hofmann DM, Pfisterer D and M. G, *Phys. Chem. Chem. Phys.* **2003**, *5*, 1639-1643.
- [8] H. Yang and P. H. Holloway, *Appl. Phys. Lett.* **2003**, *82*, 1695-1697.
- [9] A. Cruz, Q. Shen and T. Toyoda, *Thin solid films* **2005**, *499*, 104-108.
- [10] W. Peng, Qu, S, Cong, G, Zhang, X, Wang, Z, *J. Cryst. Growth* **2005**, *282*, 179-183.
- [11] J. Nanda, S. Sapra and D. Sarma, *Chem. Mater.* **2000**, *12*, 1018-1024.
- [12] Heesun Yang, Swadeshmukul Santra and P. Holloway, *J. Nanosci. Nanotechno.* **2005**, *5*, 1364-1375.
- [13] M. Malik, P. O'Brien and N. Revaprasadu, *J. Mater. Chem.* **2001**, *11*, 2382-2386.
- [14] K. Song and S. Lee, *Curr. Appl. Phys.* **2001**, *1*, 169-173.
- [15] H. Yang, Paul H. Holloway, G. Cunningham and K. S. Schanze, *J. Chem. Phys.* **2004**, *121*, 10233-10240.
- [16] H. Sfihi, Takahashi, H, Sato, W, Isobe, T *J. Alloy. Compd.* **2005**, *424*, 187-192.
- [17] T. Hirai and Y. Nomura, *J. Chem. Eng. Jpn.* **2004**, *37*, 675-678.
- [18] L. Cao, J. Zhang, S. Ren and S. Huang, *Appl. Phys. Lett.* **2002**, *80*, 4300-4302.
- [19] Alexandre R. Loukanov, Ceco D. Dushkin, Karolina I. Papazova, Andrey V. Kirov, M. V. Abrashev and E. Adachi, *Colloid. Surface. A.* **2004**, *245*, 9-14.
- [20] M. Zulauf and H. F. Eicke, *J. Phys. Chem.* **1979**, *83*, 480-486.
- [21] B. A. Harruff and C. E. Bunker, *Langmuir* **2003**, *19*, 893-897.

- [22] L. Cao, S. Huang and E. Shulin, *J. Colloid. Interf. Sci.* **2004**, 273, 478-482.
- [23] M. A. Hines and P. Guyot-Sionnest, *J. Phys. Chem.* **1996**, 100, 468-471.
- [24] P. O. Anikeeva, J. E. Halpert, M. G. Bawendi and V. Bulovic, *Nano Lett.* **2007**, 7, 2196-2200.
- [25] D. Kim, M. Miyamoto and M. Nakayama, *J. Appl. Phys.* **2006**, 100, 094313 (6 pp.).
- [26] Wang Y and H. N, *J. Phys. Chem.* **1988**, 92.
- [27] P Q Zhao, X L Wu, J.Y. Fan, P. K. Chuc and G. G. Siuc, *Scripta. Mater.* **2006**, 55, 1123-1126.
- [28] Paramita Saha Chowdhurya, P. Ghosha and A. Patra, *J. Lumin.* **2007**, 124, 6.
- [29] B. J. Berne and R. Pecora, *Dynamic Light Scattering: With Applications to Chemistry, Biology, and Physics*, Dover Publications, **2000**, pp. 384.
- [30] A. T. R. Williams, S. A. Winfield and J. N. Miller, *Analyst* **1983**, 108, 1067-1071.
- [31] R. F. Kubin and A. N. Fletcher, *J. Lumin.* **1982**, 27, 455-462.
- [32] G. Jones, W. R. Jackson, C. Choi and W. R. Bergmark, *J. Phys. Chem.* **1985**, 89, 294-300.
- [33] M. C. Baykul and A. Balcioglu, *Microelectron. Eng.* **2000**, 51-2, 703-713.
- [34] N. B. Chaure, S. Chaure and R. K. Pandey, *Sol. Energ. Mat. Sol.* **2004**, 81, 39-60.
- [35] Huijuan Zhou, Detlev M. Hofmann, Helder R. Alves and B. K. Meyer, *J. Appl. Phys.* **2006**, 99.
- [36] L. Biernacki and S. Pokrzywnicki, *J. Therm. Anal.* **1996**, 47, 1759-1762.
- [37] G. Waldman, *Introduction to Light: The Physics of Light, Vision, and Color*, Dover Publications, **2002**, pp. 240.

## Chapter 3

# Light harvesting semiconductor thin films for photo-electrochemical energy conversion

### Chapter overview

Semiconductors based on the group II-VI elements are promising materials that can be used in solar cells as “window” materials and light harvesters. This chapter focuses on the development of novel, low cost methods to deposit high quality metal sulfide films to be used as light harvesting semiconductors (LHSs) in photo-electrochemical cells.

#### **3.1. Introduction**

In the past several decades group II-VI semiconductors have attracted significant interest from the scientific community due to their promising electronic properties.<sup>[1]</sup> Having direct band gap transitions, they are commonly used materials for photovoltaic,<sup>[2]</sup> optoelectronic and electroluminescent applications.<sup>[3]</sup> CdS, in particular, is being widely used as a “window” layer material for hetero-junction solar cells (such as CdS/CdTe and CdS/CuInSe<sub>2</sub>) that show overall efficiency of more than 15%.<sup>[4]</sup> The vast majority of applications for these materials require high quality semiconducting films to be created at low cost. High quality is a significant performance parameter, since defect sites present in the lattice act as centers of recombination, decreasing charge carrier mobility and carrier separation efficiency. Thus, the overall efficiency of the thin film device is significantly affected.<sup>[5]</sup> Various methods for deposition of semiconductor thin films are summarized below.

##### **3.1.1. Deposition techniques**

In order to support high efficiency in solar cells, in particular CdS layers, should have compact structure and specific orientation.<sup>[4]</sup> Sputter deposition,<sup>[6]</sup> spray pyrolysis,<sup>[7]</sup>

and photo-chemical deposition<sup>[8]</sup> can be used to create CdS films, but high roughness and poor crystal structure are disadvantages of these techniques. Although films deposited *via* vacuum evaporation,<sup>[9, 10]</sup> chemical vapor deposition (CVD),<sup>[11]</sup> metal organic chemical vapor deposition (MOCVD),<sup>[4]</sup> and electrochemical atomic layer epitaxy (ECALE)<sup>[5, 12]</sup> are of better quality, the costs involved limit their wide application. Chemical bath deposition and electrochemical deposition techniques are the most promising in producing high quality semiconductors at low cost.

### **Chemical bath deposition**

One of the most widely used methods to deposit CdS films is chemical bath deposition (CBD), in which films are grown through the homogeneous precipitation of water-insoluble compounds and their solid solutions.<sup>[13]</sup> The synthesis of metal sulfides *via* CBD, is based on the slow release of the sulfur anion in an aqueous electrolyte that contains the metal cations and the complexing agent. Some examples of complexing agents include NH<sub>3</sub>, CN<sup>-</sup>, EDTA, triethanolamine (TEA) and trisodium citrate.<sup>[14]</sup> Most of the deposition processes are carried out in alkaline solutions; in this case the formation of complexes with the metal cations is one of the most important factors that allow for the reaction control. It prevents the formation of insoluble metal hydroxides as well as the immediate precipitation of the metal ions in the solution when the precipitating anions are released.

The anions in the solution are generated from the hydrolysis of the precipitating agent. The sulphur ions for deposition of metal sulfides can be generated from thiourea (following the reaction bellow) or thioacetamide.<sup>[15]</sup>



Generally, for metal sulfide deposition, ion by ion growth on a surface is accompanied by precipitation of colloidal metal sulfide formed in the solution.<sup>[16]</sup>

Although significant improvement of film quality was achieved using trisodium citrate as the complexing agent in the CBD process, the method produces very low yield (~2%), resulting in copious amounts of toxic waste.<sup>[17]</sup>

## Electrodeposition

Electrodeposition of compound materials can be effectively used, when there is the possibility for electrochemical generation of at least one reactant through oxidation or reduction of corresponding precursors. In principle, both anodic and cathodic deposition may be used for deposition of II—VI compound semiconductors.

As an example, CdS can be prepared by the anodic deposition of sulfur from a solution containing  $S^{2-}$  ions on a cadmium anode. Cathodic deposition can occur either by deposition of the individual components in the required ratio, or by deposition resulting from discharge and decomposition of a complex containing the two components. Atomic sulfur (S) and thiosulphate ions ( $S_2O_3^{2-}$ ) were used as sulfide precursors for cathodic deposition of CdS.<sup>[18, 19]</sup>

Thus far, electrodeposition of CdS films from aqueous solutions,<sup>[18, 19]</sup> ethylene glycol<sup>[20]</sup> and ionic liquids (ILs)<sup>[21]</sup> have been reported. The main disadvantages of water based methods are the inability to deposit at high temperatures and the presence of oxygen that drastically decreases the quality of the films. Even though electrodeposition from ethylene glycol and IL allow the growth to be carried out at higher temperatures, CdS films reported so far are of low quality.<sup>[20, 21]</sup>

The high temperature at which the deposition in an IL can, in principle, be conducted allows for atom diffusion on the surface during growth, which has a major positive influence on the quality of the films.<sup>[22]</sup> Ionic liquids have been successfully used for the electrodeposition of a number of metals such as Se, In, Cu, Au, Pt and some semiconductors including Ge, Si,  $TiO_2$ , AlSb, ZnSb, InSb, GaAs, CdTe, CuInSe, Cu(In,Ga)Se and ZnTe.<sup>[23-28]</sup> One of the key advantages of ionic liquids in this context is their combination, in some cases, of thermal and electrochemical stability that allows the electrodeposition process to be carried even at elevated temperatures with minimal interference from solvent chemical or electrochemical breakdown.<sup>[24, 25, 29]</sup>

Elemental sulfur is one of the most common precursors for electrochemical deposition of CdS.<sup>[20, 21]</sup> It was shown that the chemical composition of the films is significantly affected by the potential of the working electrode in this process. At a lower potential (*e.g.* from -0.6 to -0.8 V vs Pt) the appearance of the films shifts from pale yellow to brown, indicating presence of an excess amount of cadmium.<sup>[21]</sup> In order to minimize the

rate of cadmium reduction, sodium thiosulfate was proposed as a sulfide precursor in the aqueous electrodeposition studies of Rami *et al.*<sup>[30]</sup> Thus, an ionic liquid based method of electroreduction of thiosulfate to produce CdS would use the advantages of the ionic liquid as an electro-winning medium.

### 3.1.2. Substrates for CdS electrodeposition

For the electrodeposition of semiconductors, the applicability of the method relates to the stability of the substrate towards oxidative or reductive decomposition (or dissolution) in the electrolyte and the effectiveness of charge transfer through the electrical junction formed between the substrate and the semiconductor.<sup>[31]</sup>

Several theories exist to describe the contacts between metals and semiconductors. The ideal theory considers formation of a macroscopic interfacial dipole across the barrier while non-ideal theory additionally takes into account the influence of the charge neutrality levels on the formation of the microscopic interfacial dipole.<sup>[31, 32]</sup>

In ideal theory the formation of the macroscopic dipole depends on the relative position of the Fermi levels across the metal-semiconductor interface. Two distinct cases can be considered: the electron work function in the metal is higher than in the semiconductor ( $\Phi_M > \Phi_S$ ) as can be seen in Figure 3.1 and when it is lower than the semiconductor ( $\Phi_M < \Phi_S$ ). When two materials are brought into contact, the difference in the positions of the Fermi levels leads to a charge transfer across the interface, creating a macroscopic dipole and an electrical barrier ( $\Phi_B$ ).

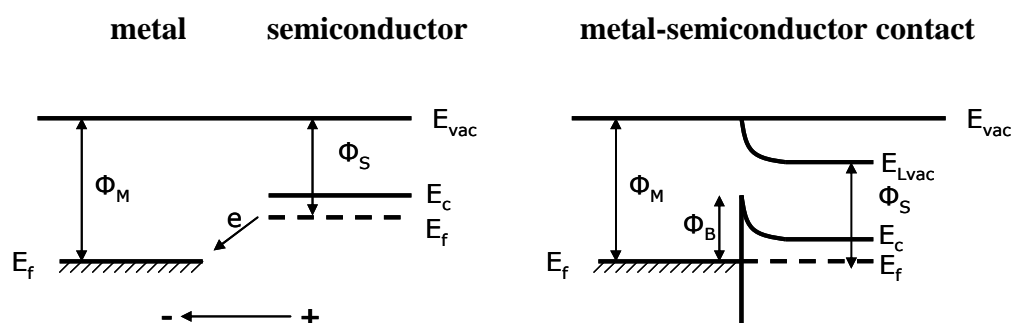


**Figure 3.1:** Formation of the ideal metal semiconductor Schottky barrier. The energy level positions are expressed in relation to the vacuum energy  $E_{vac}$  and local vacuum energy  $E_{Lvac}$  (Figure adapted from reference [31]).

In the non-ideal Schottky model, charge neutrality must be taken into consideration ( $E_{CNL}$ ). From an interface formation perspective this energy is established through the

relative alignment of the semiconductor band structure at the interface and affects charge transfer during interface formation.<sup>[31]</sup> When the electron work function of the charge neutrality level is higher than that of the metal, the induced charge transfer leads to the formation of a micro-dipole as shown in Figure 3.2. The created micro dipole significantly influences the value of barrier energy for electron transfer into the semiconductor. The height of the electric barrier  $\Phi_B$  represents the energy that an electron in the metal needs to overcome in order to transit into the semiconductor. In the case when  $\Phi_{CNL} > \Phi_M$  (top of the graph) the electrons are accumulated at the charge neutrality level, thus increasing the height of the potential barrier. On the other hand, when  $\Phi_{CNL} < \Phi_M$  (bottom of the graph) the micro dipole promotes electron transfer from the metal and the barrier height is reduced compared to the ideal model.

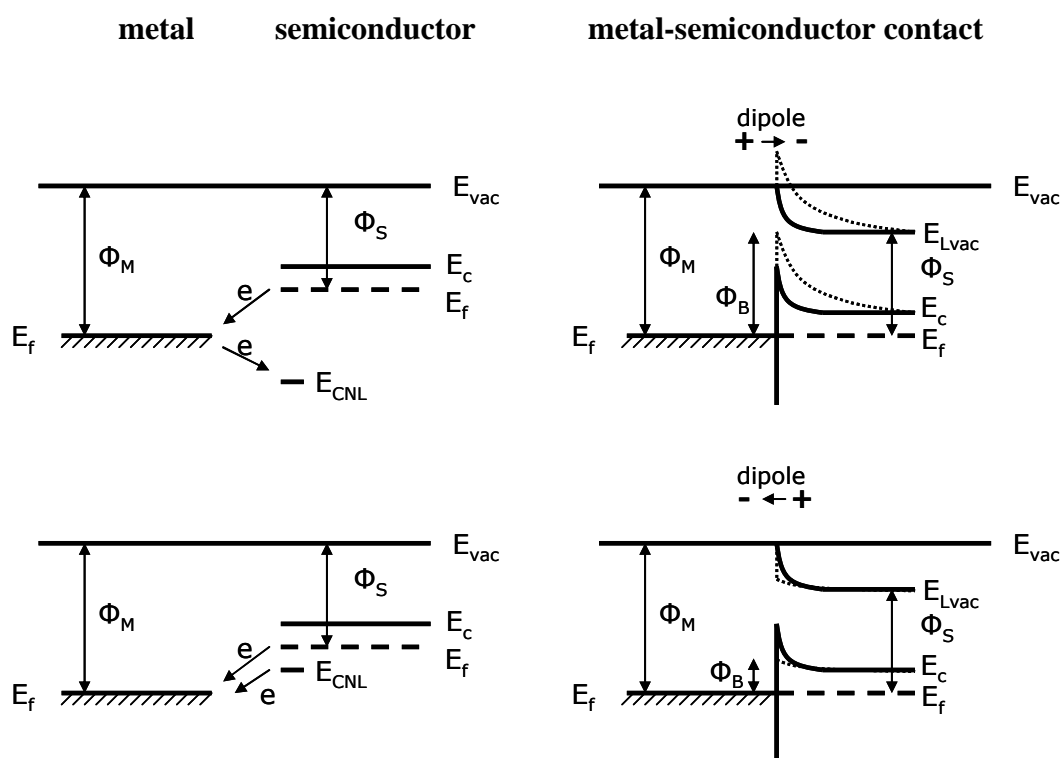


**Figure 3.2:** Formation of non-ideal metal semiconductor interface, where  $\Phi_{CNL} > \Phi_M$  (top) and  $\Phi_{CNL} < \Phi_M$  (bottom). Position of the band edges in the non-ideal system is shown as dotted lines (Figure adapted from reference [31]).

The electron work function of various semiconductors, metals and conducting polymer, poly(3,4-ethylenedioxythiophene) (PEDOT), used as a substrate for electrodeposition in this work and that of CdS are shown in Table 3.1. When the carrier concentration in one of the semiconductors is very high, such highly doped semiconductors can be considered as metals and the situation becomes similar to that in a Schottky

barrier.<sup>[31]</sup> This is the case for fluorine-doped tin-oxide (FTO) and TiO<sub>2</sub>, which are common semiconducting materials in solar technology.

From Table 3.1 it can be seen that electrical junction between CdS and substrate in these cases creates a rectifying contact (a “Schottky barrier”), where electrons are prevented from transfer into the semiconductor. This inhibits electrodeposition through reduction of a chemical precursor.

**Table 3.1:** Electron work function of materials (taken from reference <sup>[33-35]</sup>).

Material	Electron work function (Fermi energy), eV
CdS	~3.88
FTO	~4.55
n-TiO <sub>2</sub>	~4.16
Ti	~4.33
Au	5.1 - 5.47
Al	4.06 - 4.26
PEDOT	4.7 - 5.3

There are several ways, in which electron transfer can still occur, as shown in Figure 3.3. Through thermionic emission of electrons above the barrier (a), thermal field emission through the barrier top (b) and tunneling through the barrier (c).<sup>[33]</sup>

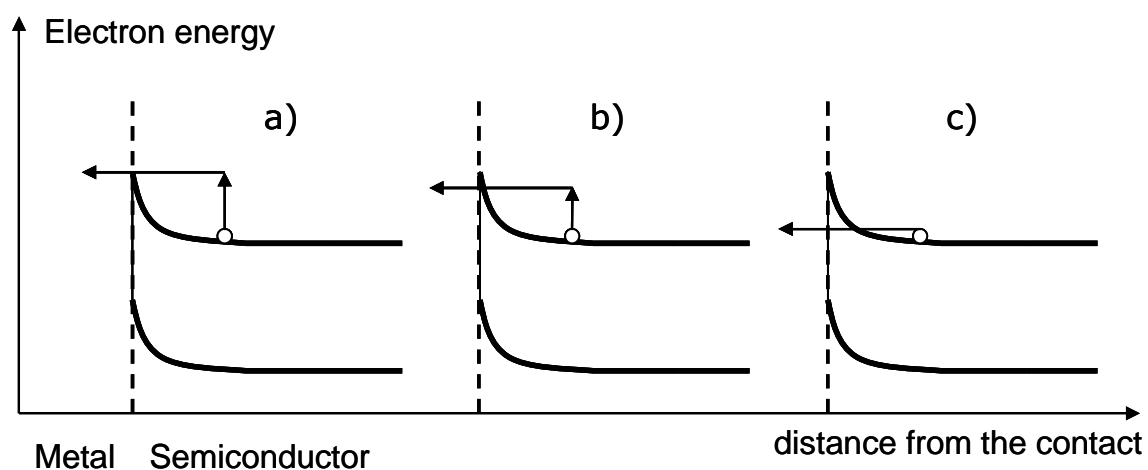


**Figure 3.3:** Mechanisms of current flow in metal semiconductor contacts.

One of the ways to make the Schottky barrier conductive is to use a heavily doped surface of the semiconductor. High concentration of majority carriers in the interface creates a high value of the barrier energy and a narrow barrier thickness. The junction in this case

becomes tunneling transparent and electrons are able to efficiently move through the entire length of the electrical barrier. The influence of temperature, potential barrier height and doping level on contact resistance due to the three types of emission in the Schottky junction is summarized in Table 3.2.

**Table 3.2:** Contact resistance in Schottky junction.

Increase in	Type of emission	Thermionic	Field emission	Thermal field emission
potential barrier height		exponentially increases	exponentially increases	exponentially increases
<b>temperature</b>		<b>decreases</b>	independent	<b>decreases</b>
doping (smaller barrier width)		light dependence ( $\Delta\Phi_B \propto N_D^{1/4}$ )	<b>decreases</b> <b>exponentially</b>	light dependence

From Table 3.2 we can establish then that the high levels of natural doping known for CdS<sup>[34]</sup> will decrease contact resistance between the semiconductor and the substrate due to the electron field emission, while elevated temperatures at which electrodeposition in ILs occurs allow for reduced contact resistance *via* thermionic and thermal field electron emissions. Thus, the use of ILs for electrodeposition of CdS at high temperatures is essential to achieve electrodeposition of CdS on various substrates.

### Adhesion of films to the substrate

It can be seen from the literature that thin films of CdS (<50 nm) generally show good adhesion to the substrates.<sup>[4, 21]</sup> Adhesion properties of thicker films, however, vary depending on the deposition method. As a common trend, adhesion seems to be better for films with higher fraction of amorphous phase present and, in this case, thick films of CdS can be created.<sup>[7, 8, 17]</sup> Due to the low stacking-fault energy of CdS, it becomes harder to dissipate the lattice mismatch between well ordered crystal structures of the grown film and those of the substrate.<sup>[10]</sup> The difference in thermal expansion coefficient between these can result in crack formation and loss of adhesion.<sup>[10, 17]</sup>

It is well known that the Ar-H<sub>2</sub> plasma can be effectively used to remove any organic residues. Moreover, it was shown that plasma polymerization of specific monomers significantly affects physical and chemical properties of the substrate.<sup>[35]</sup> For

instance, adhesion of deposited films to the substrate can be improved through the use of polymers with specific functional groups.

### 3.1.3. Tuning electric properties of LHS

The energy structure of semiconductors is of paramount importance and affects electric and physicochemical properties. Several approaches can be utilized to modify the band gap energy. As discussed in the previous chapter, one of the ways is to reduce the size of the crystal structure, which leads to reduction in electron density and affects delocalization of the energy levels.<sup>[36]</sup> The effect thus produced is broadly referred in the literature as the quantum-size effect. This method has been successfully used for elemental and compound semiconductors. The ability to tune properties of the nanoparticles by changing their size leads to a vast range of potential applications.<sup>[37]</sup> We can also dissolve one compound in another and control the desired properties by simply varying concentration of the former in the formed solid solution. The materials synthesized by this method form a broad area of compound semiconductors, which have fundamental importance in microelectronics.<sup>[38-40]</sup>

## 3.2. *Aims of this work*

The aim of this chapter is to develop novel methods for electrochemical deposition of metal sulfide semiconductors utilizing the advantages of the use of elevated temperatures and the unique attributes of ionic liquids. It is possible then to formulate specific aims:

1. The use of molecular sulfur as sulfide precursor for CdS electrodeposition from dry [P<sub>66614</sub>][DCA], [P<sub>4444</sub>][Cl], [P<sub>1444</sub>][Tosylate], [P<sub>66614</sub>][NTf<sub>2</sub>] ILs and investigate:
  - Stability of ILs at high temperature
  - Improvements in solubility of Cd(II) in ILs using organic solvents
  - Reduction potential of Cd(II) in ILs
  - Reduction potential of elemental sulfur and its stability during high temperature synthesis

2. The use of sodium thiosulfate as sulfide precursor for CdS electrodeposition from [P<sub>66614</sub>][NTf<sub>2</sub>], [P<sub>66614</sub>][DCA], [P<sub>1444</sub>][Tosylate] ILs and investigate
  - Reduction potential of thiosulfate and its stability at high temperature synthesis
3. Based on results of steps 1 and 2 characterization of CdS films successfully deposited from IL including:
  - Surface morphology characterized by using SEM microscopy.
  - Chemical analysis obtained through the use of EDX measurements.
  - Crystal structure of deposits determined from the data of XRD measurements.
  - The influence of experimental conditions on film thickness assessed by using profilometry.
  - Electronic structure and attenuation coefficient of material calculated from the data of Mott-Schottky impedance spectroscopy and UV-vis spectroscopy.
4. Using the developed method to investigate the deposition of CdS on various substrates such as plasma treated FTO, metals (Ti, Al, Au), conducting polymers (poly(3,4-ethylenedioxythiophene) (PEDOT)), and semiconductors (porous TiO<sub>2</sub>).
5. Using the developed method to investigate the deposition of FeS, In<sub>2</sub>S<sub>3</sub>, ZnS, and NiS as well as mixed metal sulfide materials.

The chapter will show that while sulfur is not a useful precursor for electrochemical deposition of the sulfides of interest, thiosulfate does produce high quality CdS films, but only from certain ionic liquids. The method is further extended to mixed metal sulfides for band gap control.

### 3.3. Experimental

#### Materials

Cadmium chloride ( $\text{CdCl}_2$ ) and sodium thiosulfate pentahydrate ( $\text{Na}_2\text{S}_2\text{O}_3 \cdot 5\text{H}_2\text{O}$ ) were purchased from Merck Pty. Limited. Iron (II) chloride ( $\text{FeCl}_2$ ), cadmium acetate, thiourea, sodium citrate, sodium thiosulfate from Sigma-Aldrich. Indium (III) chloride ( $\text{InCl}_3$ ) from Strem Chemicals Inc. Zinc chloride ( $\text{ZnCl}_2$ ) from BDH Industries Ltd.  $[\text{P}_{66614}][\text{NTf}_2]$ ,  $[\text{P}_{66614}][\text{DCA}]$ ,  $[\text{P}_{4444}]\text{Cl}$ ,  $[\text{P}_{1444}][\text{Tosylate}]$  from CYTEC Canada Inc.

#### Thin film deposition

Electrochemistry with dry ILs was carried out on a PAR VMP2Z potentiostat under an argon atmosphere (in an Ar drybox) to maintain a dry and oxygen free environment, or in the presence of air. Unless stated otherwise, FTO was used as a working electrode and platinum foil as a counter electrode. Typical setup is shown in Figure 3.4. FTO (sheet resistance 15 ohm/ ) glass slides were used as a substrate. Before the deposition the surface of the FTO was masked, leaving an area equal to  $0.25\text{cm}^2$ . Prior to use, the glass slides were sonicated in water solution of DOBATEC detergent, washed several times with deionized water, and sonicated in ethanol to remove traces of detergent. Several types of reference electrodes were used in this work. A saturated calomel electrode was employed as a reference electrode for measurements in aqueous electrolytes. A 66-EE009 ("No-Leak") Ag/AgCl (Cypress Systems) electrode was used as reference to study electrochemical processes in ILs, as well as the platinum pseudo reference electrode.

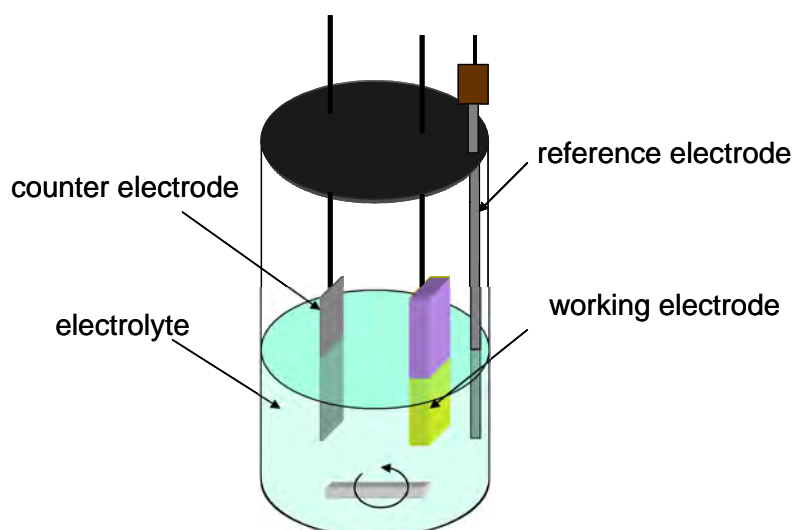


**Figure 3.4:** Electrochemical deposition cell.

CdS was also deposited from a chemical bath, following methods reported elsewhere in a setup shown in Figure 3.5.<sup>[17]</sup>

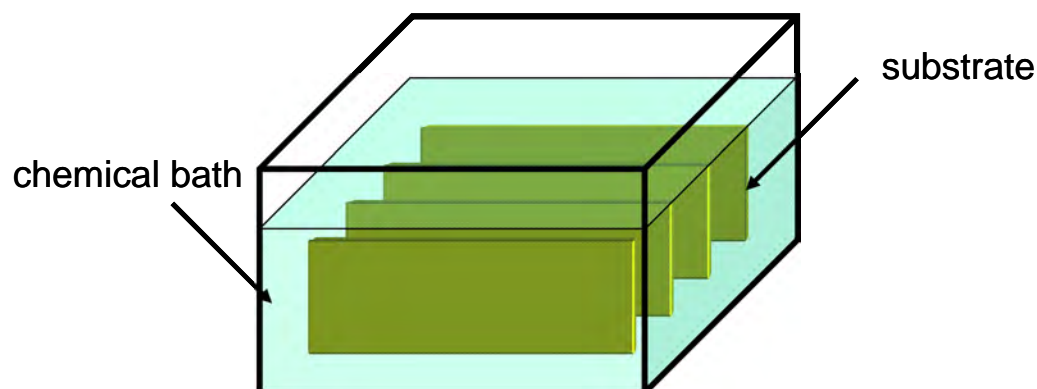


**Figure 3.5:** Chemical bath deposition setup.

In a typical experiment for CdS deposition using the CBD method, the solution was prepared by the sequential addition of 20 ml of 0.05 M cadmium chloride ( $\text{CdCl}_2$ ), 20 ml of 0.5 M sodium citrate ( $\text{C}_6\text{H}_5\text{O}_7\text{Na}_3\text{O}_7 \cdot 2\text{H}_2\text{O}$ ), 5 ml of 0.5 M potassium hydroxide (KOH), 5 ml of a pH of 10 borate buffer and 10 ml of a 0.5 M thiourea ( $\text{CS}(\text{NH}_2)_2$ ). Deionized water was added to the solution to make a total volume of 100 ml. The films were deposited on FTO glass slide substrates at a temperature of 70 °C. The solution was not stirred during the deposition process.

For the preparation of metal substrates vacuum evaporation was used to deposit thin metal films on the surface of glass and FTO electrodes. In this work electric current was passed through tungsten boats and wires to reach desired temperatures, using an Edward 308 vacuum evaporator. The distance between the source and the target was 10 cm and vacuum kept better than  $10^{-5}$  Torr. Electric glow discharge in argon was used in some cases to remove organic impurities from the films before deposition. Glass, FTO and variety of compound semiconductors and metals were used as a substrate during evaporation. Sheet resistance of these films was measured by the Jandel General Purpose Four Point Probe System (RM3-AR Test Unit).

For the preparation of polymer substrates, Poly(3,4-ethylenedioxythiophene) (PEDOT) films (0.5–1  $\mu\text{m}$ ) were prepared using vapor phase polymerization (VPP) of ethylenedioxythiophene (EDOT). In a typical procedure<sup>[41]</sup> Fe(III)PTS oxidant was coated onto the substrate (capton tape) from a 40% 1-butanol solution inhibited with 0.5 M pyridine. After drying in an oven for 1 min at 70 °C the sample was transferred to a glass

container containing 0.5ml EDOT to maintain EDOT vapor and left in a pre-heated to 70 °C oven for 30 min. When polymerization was complete, the sample was washed twice in ethanol to remove Fe(II) and excess PTS.

For the preparation of thin maleic anhydride films, some FTO samples were also treated with an AC plasma discharge in an Ar-H<sub>2</sub> mixture to remove organic residues from the substrates and then subjected to a plasma polymerization treatment using maleic anhydride following the procedure reported elsewhere.<sup>[35]</sup>

For electrodeposition of cadmium sulfide using thiosulfate as sulfide precursor, small amounts of water were used to assist with dissolution of sodium thiosulfate in IL. For example, aqueous solutions of 0.2 M CdCl<sub>2</sub> and 0.6 M Na<sub>2</sub>S<sub>2</sub>O<sub>3</sub> were added to the [P<sub>1444</sub>][Tosylate], forming respectively 0.01 M and 0.03 M solutions of these salts in IL, with 10% of water in electrolyte.

For the electrodeposition of FeS, In<sub>2</sub>S<sub>3</sub>, and ZnS, 0.01 M electrolytes were prepared from FeCl<sub>2</sub>, InCl<sub>3</sub> and ZnCl<sub>2</sub> respectively with 0.03 M Na<sub>2</sub>S<sub>2</sub>O<sub>3</sub> in IL with 10% water content.

For the deposition of NiS, the electrolyte was composed of 0.01 M NiCl<sub>2</sub> and 0.03 M Na<sub>2</sub>S<sub>2</sub>O<sub>3</sub> in IL with 10% water content, while for the deposition of mixed metal sulfide (CdNiS<sub>2</sub>), the concentrations of CdCl<sub>2</sub> and NiCl<sub>2</sub> were 0.005 M in IL solution.

The ratio of surface area to the amount of electrolyte for deposition of CdS on the metal substrates was considerably improved using the setup shown in Figure 3.6. The deposition chamber was made of teflon and inserted in the brass thermostat. The electrodes were prepared through vacuum evaporation on the surface of a microscope glass slide under high vacuum. To increase stability and durability of the titanium counter electrode, the Ti surface was additionally covered with a thin film (10-50 nm) of titanium dioxide using spray pyrolysis. Platinum wire was used as a reference electrode.

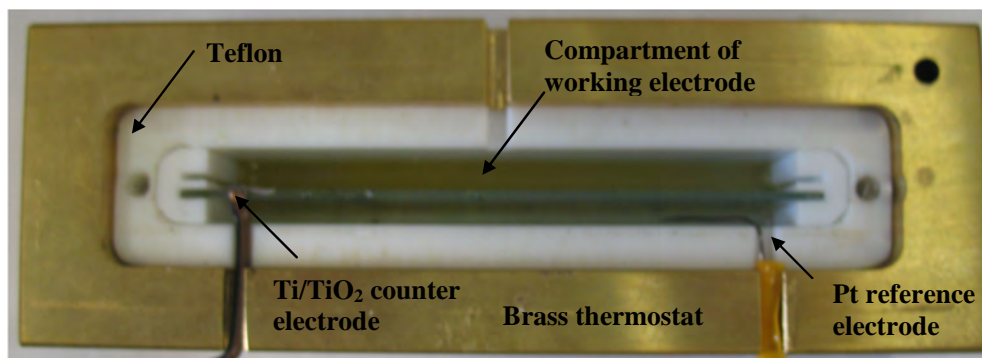


**Figure 3.6:** Electrochemical setup for electrodeposition of metal sulfides on metal electrodes.

### Characterization techniques

SEM measurements were performed on films coated with gold or graphite unless stated otherwise. SEM images were obtained on a JEOL 6300F Field Emission Gun Scanning Electron Microscope.

Dektak 150 surface profiler was used for characterization of the surface roughness as well as thickness of the film. Step height resolution of the instrument ranges from 1000 angstroms to approximately 65 microns.

XRD measurements were performed on Philips powder diffractometer with Cu radiation. Scans were performed at 2 °/min by varying  $2\theta$  angles from 20° to 60°.

The UV-vis measurements were carried out on a Varian, Cary 100 Bio, UV-visible spectrophotometer. UV-vis spectra were measured from 800 nm to 200 nm at a scan rate of 300 nm per min.

For the Mott-Shottky plot analysis the capacitance of the metal sulfide semiconductor thin films was measured in 0.1 M Na<sub>2</sub>S and 0.1 M NaOH aqueous solutions at 1 kHz with 20 mV peak to peak amplitude and standard calomel reference electrode.

### 3.4. Results and discussion

Elemental sulfur is commonly used as a precursor for electrochemical deposition of CdS.<sup>[20, 21]</sup> The potential of sulfur reduction is lower (-0.48 V vs NHE) than that of Cd(II) (-0.4 V vs NHE), which results in Cd reduction occurring during CdS deposition. The task becomes even more daunting for the deposition of various other metal sulfides as can be seen from Table 3.3,<sup>[42]</sup> for example reduction potential of Fe(III) is -0.04 V vs NHE.

**Table 3.3:** Standard electrochemical potentials for various metal cations

Electro-chemical reaction	Potential, V (NHE)
$Zn^{2+} + 2e^- \rightarrow Zn$	-0.76
$Cd^{2+} + 2e^- \rightarrow Cd$	-0.4
$In^{3+} + e^- \rightarrow In^{2+}$	-0.49
$In^{3+} + 3e^- \rightarrow In$	-0.345
$Pb^{2+} + 2e^- \rightarrow Pb$	-0.29
$Ni^{2+} + 2e^- \rightarrow Ni$	-0.25
$Fe^{3+} + 3e^- \rightarrow Fe$	-0.04

Also, FTO glass is a commonly used substrate in solar cell technology.<sup>[4]</sup> At low potentials the electrode surface may be reduced leading to loss of conductivity. Therefore, the reduction potential of the sulfide precursor should be higher compared to the reduction potential of the metal cation and FTO electrode.

As a way to tune the potentials involved, it is well known that a strong coordination between metal cations and ions in an IL can significantly shift electrodeposition potential of metals.<sup>[43, 44]</sup> Thus, several ILs were used as electrolytes for electrodeposition of CdS using elemental sulfur and thiosulfate as sulfide precursors.

### 3.4.1. Elemental sulfur as sulfide precursor and choice of IL

The use of [P<sub>4444</sub>]Cl, [P<sub>66614</sub>][DCA], [P<sub>66614</sub>][NTf<sub>2</sub>] and [P<sub>1444</sub>][Tosylate] was investigated for electrodeposition of CdS at elevated temperatures. The measurements were conducted in dry ILs under an Ar atmosphere. FTO coated glass was used as a working electrode, while Pt was used as pseudo reference and counter electrodes.

#### [P<sub>4444</sub>]Cl

The range of electrochemical potentials at which the IL remains stable towards reduction was determined from cyclic voltammograms. As can be seen in Figure 3.7, there is no electrochemical processes in the region of interest for [P<sub>4444</sub>]Cl.

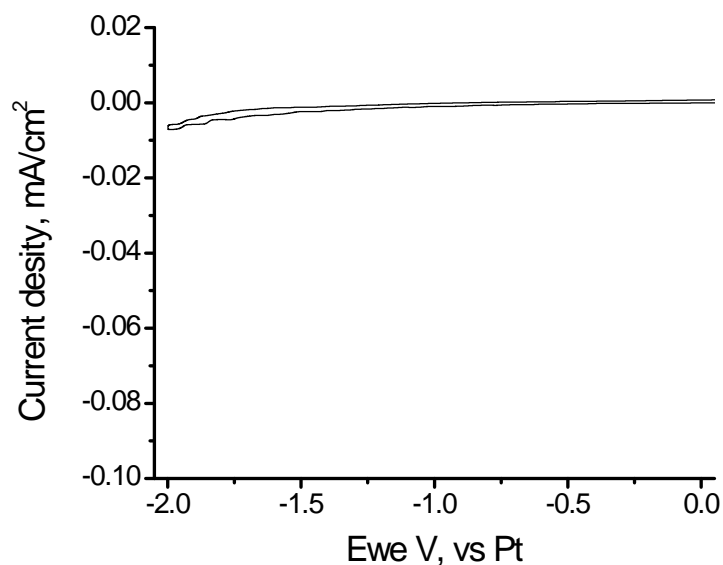


**Figure 3.7:** Cyclic voltammogram (scan rate 50 mV/s) at 100 °C of [P<sub>4444</sub>]Cl

Cyclic voltammograms of the IL with small amount of Cd(II) for two different potential regions are shown in Figure 3.8. Two reduction processes at around -1.0 V and at around -1.5 V vs Pt can be observed during cycling from 0 to -2.0 V vs Pt. A strong reduction wave below -1.0 V produces the oxidation peak at around -0.62 V. When the reduction potential during cycling was limited to -1.25 V the position of the oxidation peak was shifted to -0.5 V.

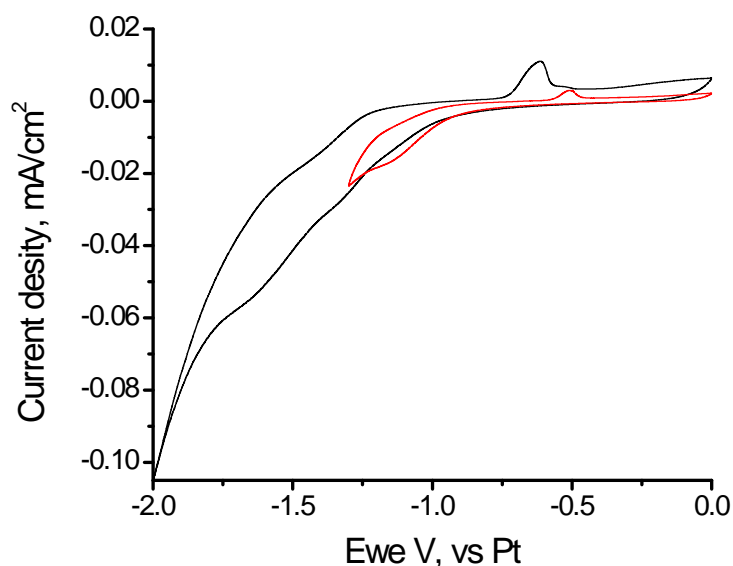


**Figure 3.8:** Cyclic voltammograms (scan rate 50 mV/s) at 100 °C of [P<sub>4444</sub>]Cl (left) and [P<sub>4444</sub>]Cl with 0.1 M CdCl<sub>2</sub> (right).

In order to enhance current densities related to both reduction processes, the temperature of the IL electrolyte containing Cd(II) was increased to 125 °C and the

corresponding cyclic voltammogram is shown in Figure 3.9. Similar to data obtained at a lower temperature, two regions can be seen during reduction scan. The onset potential of the first one is around -0.75 V with the current density reaching a plateau at -1.0 V. This is a characteristic trend commonly observed, when there is a diffusion limitation during a reduction process and hence, can be attributed to the reduction of Cd(II) in IL. The second reduction wave, at around -1.2 V, may be attributed to the reduction of the FTO substrate. Two peaks on the oxidation scan at -0.63 V and -0.43 V in this case may be due to the oxidation of reduced FTO and Cd<sup>0</sup> deposited on the electrode surface.

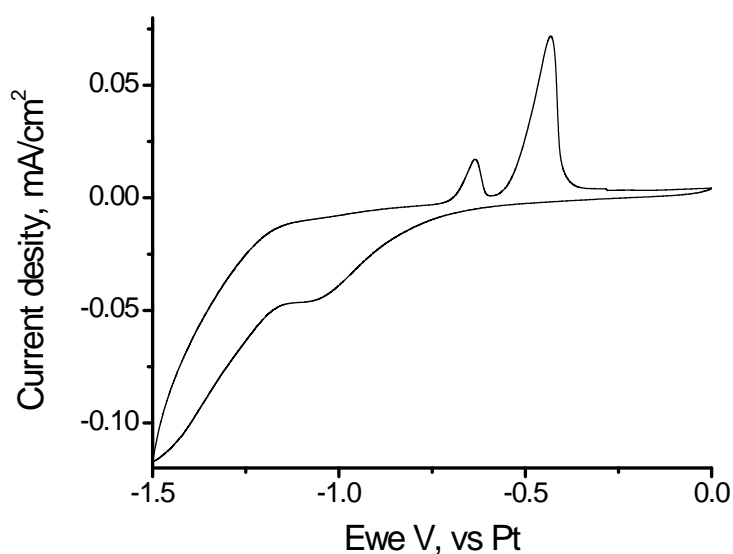


**Figure 3.9:** Cyclic voltammogram (scan rate 50 mV/s) at 125 °C of [P<sub>444</sub>]Cl with 0.1 M CdCl<sub>2</sub>.

Upon addition of sulfur to the IL containing Cd(II) the color of the electrolyte changes from deep blue to deep purple over time. In order to prove that Cd(II) does not form insoluble compounds and remains available for electrochemical synthesis, a small amount of hydrochloric acid was added to the solution. No color change was observed in this case. On the other hand, addition of a small amount of sodium sulfide solution resulted in formation of a yellow precipitate, which is characteristic for CdS and change in color of the electrolyte from deep purple to colorless. Thus, the change in color of the electrolyte upon addition of sulfur was attributed to the formation of a coordination complex between Cd(II), S and ions of the IL.

The cyclic voltammogram of the IL electrolyte containing Cd(II) and sulfur is shown in Figure 3.10. Two reduction peaks, which can be observed at -0.4 V and -0.9 V vs Pt, may be related to the reduction of Cd(II) to Cd(I) and Cd(I) to Cd(0). The absence of

oxidation peaks, which can be seen in Figure 3.8 and Figure 3.9, in the cyclic voltammogram suggest that the reduction process does not result in electrodeposition on the substrate. This was further confirmed using chronoamperometry at -1.0 V vs Pt, which does not result in the formation of films on the surface of FTO. It can be concluded then that [P<sub>4444</sub>]Cl with Cd(II) can not be used as an electrolyte for electrodeposition of CdS using atomic sulfur as sulfide precursor.

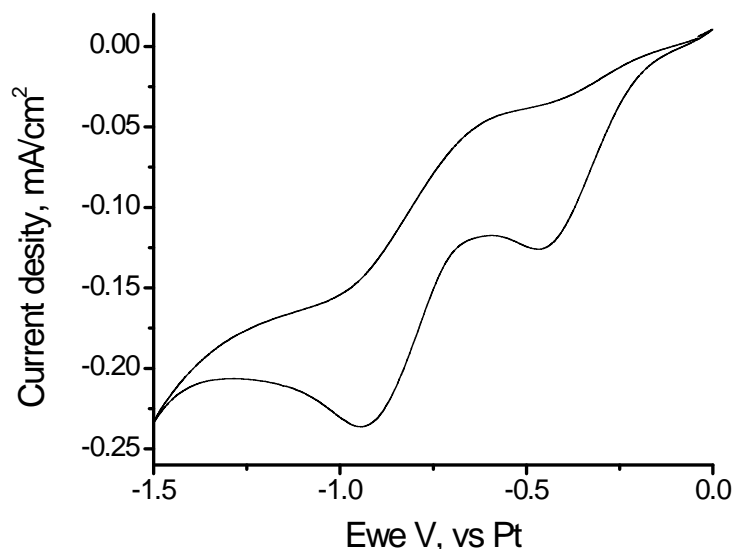


**Figure 3.10:** Cyclic voltammogram (scan rate 50 mV/s) at 125 °C of [P<sub>4444</sub>]Cl with 0.1 M CdCl<sub>2</sub> and 0.1 M Sulfur.

#### [P<sub>66614</sub>]DCA

The range of electrochemical potentials at which the IL remains stable towards reduction was determined from cyclic voltammogram shown in Figure 3.11. It can be seen that the onset potential for the reduction wave in the IL at 125 °C is around -0.7 V vs Pt. The peak may be attributed to reductive decomposition of the IL or reduction of IL contaminants (*e.g.* acid) that are common impurities in phosphonium ILs. At temperatures exceeding 125 °C the color of the IL electrolyte slowly changed towards yellow, which may indicate decomposition of the IL.

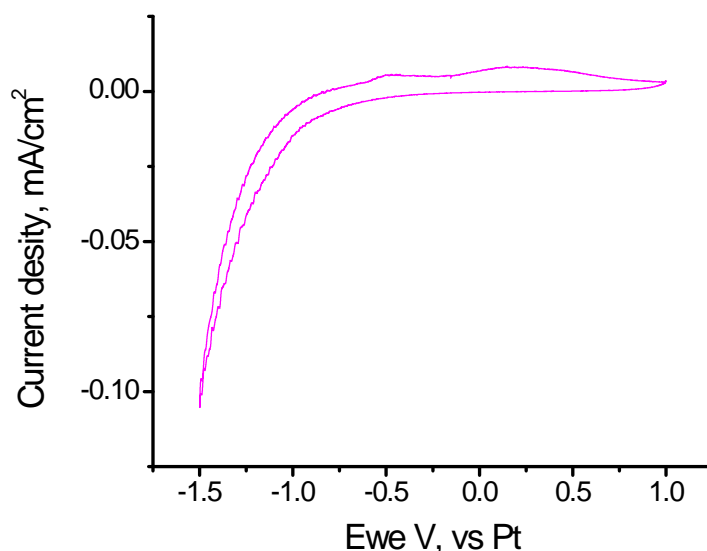


**Figure 3.11:** Cyclic voltammogram (scan rate 50 mV/s) of [P<sub>66614</sub>][DCA] at 125 °C

The current density at low potentials was significantly reduced during electrochemical cycling at temperatures below 100 °C as can be seen from Figure 3.12. This effect can be attributed to an increase in viscosity of the IL and hence, a decrease in ion mobility at low temperatures. Additionally, IL ions may become more stable towards reductive decomposition when the temperature is significantly reduced. Overall, it appears that [P<sub>66614</sub>][DCA] can be used as an electrolyte for electroreduction at potentials above -0.7 V vs Pt and temperatures not exceeding 125 °C.

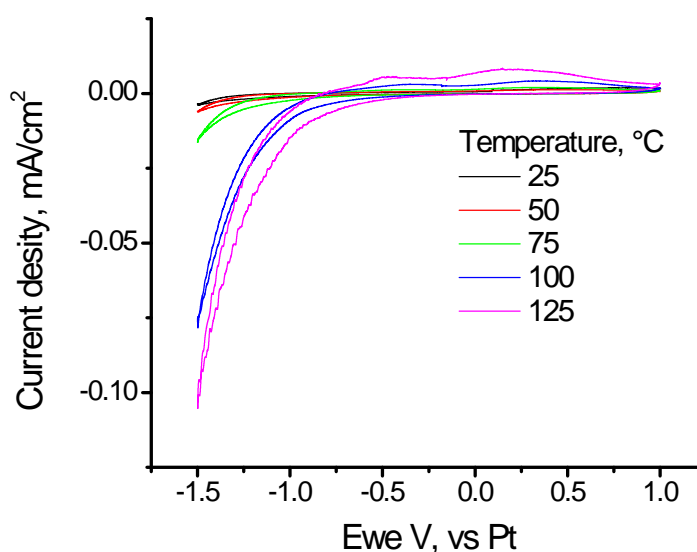


**Figure 3.12:** Cyclic voltammograms (scan rate 50 mV/s) of [P<sub>66614</sub>][DCA] at various temperatures.

For characterization of the Cd(II) reduction potential in [P<sub>66614</sub>][DCA] cyclic voltammograms of 0.01M CdCl<sub>2</sub> in the IL were measured at various temperatures as shown in Figure 3.13. As can be seen from the figure, presence of Cd(II) in the electrolyte has almost no impact on the shape and magnitude of the current density during the reduction scan. During the oxidation scan, on the other hand, a pair of reduction peaks around -0.7 V and oxidation peak around -0.5 V can be observed. The amplitude of the current density corresponding to these peaks shows strong temperature dependence and becomes significantly higher at temperatures above 100 °C. We may speculate then that strong coordination between DCA anions and Cd(II) cations prevents reduction of Cd(II) during the reduction scan. The activity of the electrode may be increased at low potentials and during the oxidation cycle reduction of Cd(II) occurs followed shortly thereafter by oxidation of Cd on the surface of the FTO electrode.

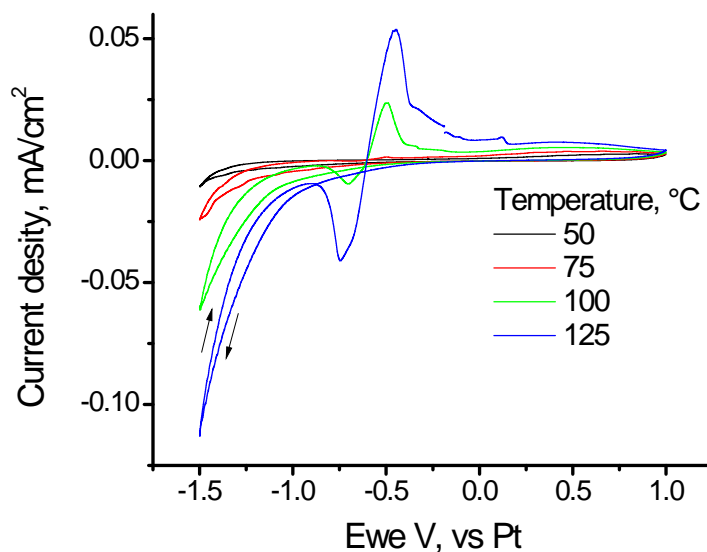


**Figure 3.13:** Cyclic voltammograms (scan rate 50 mV/s) [P<sub>66614</sub>][DCA] with 0.01 M CdCl<sub>2</sub> at various temperatures.

When a small amount of sulfur is added to the IL containing Cd(II), the color of the electrolyte gradually changes through deep blue to dark green over time. Similar to results obtained for [P<sub>4444</sub>][Cl], the change in color is due to the formation of a complex between Cd(II), sulfur and the electrolyte. Figure 3.14 shows cyclic voltammograms of [P<sub>66614</sub>][DCA] with 0.01 M CdCl<sub>2</sub> and 0.02 M S at various temperatures. The current density on the reduction wave, which may be attributed to the reduction of elemental sulfur, increases with an increase in electrolyte temperature. At high temperatures,

however ( $\geq 100\text{ }^{\circ}\text{C}$ ), there is a decrease in current density, which might be related to sulfur polymerization.<sup>[14]</sup> No films were formed on the substrate after prolonged reduction at  $-1.0\text{ V vs Pt}$ ,  $100\text{ }^{\circ}\text{C}$ . It can be concluded that  $[\text{P}_{66614}][\text{DCA}]$  cannot be used as an electrolyte when elemental sulfur is used as a sulfide precursor at temperatures exceeding  $75\text{ }^{\circ}\text{C}$ .

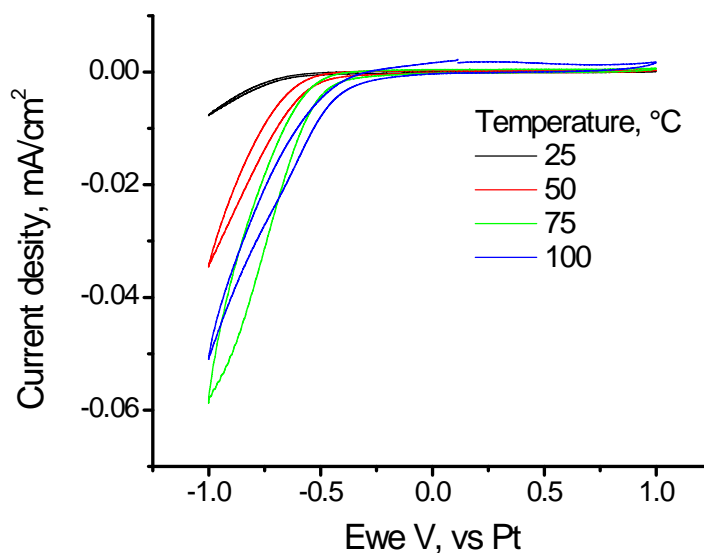


**Figure 3.14:** Cyclic voltammograms (scan rate 50 mV/s) at various temperatures of  $[\text{P}_{66614}][\text{DCA}]$  with 0.01 M  $\text{CdCl}_2$  and 0.02 M Sulfur.

#### $[\text{P}_{1444}][\text{Tosylate}]$

The cyclic voltammogram of  $[\text{P}_{1444}][\text{Tosylate}]$  shown in Figure 3.15 suggests that there are no electrochemical processes in the region of interest.

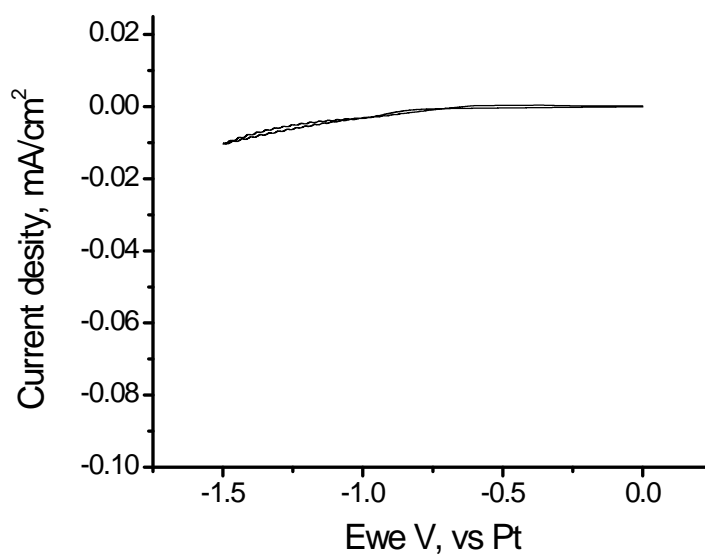


**Figure 3.15:** Cyclic voltammogram (scan rate 50 mV/s) of  $[\text{P}_{1444}][\text{Tosylate}]$  at  $110\text{ }^{\circ}\text{C}$ .

The cyclic voltammogram of the IL with small amount of Cd(II) is shown in Figure 3.16. The onset potential for the reduction wave occurs at about -0.75 V and can be attributed to the reduction of Cd(II); the oxidation peak at potential around -0.35 V is attributed to the oxidation of Cd(0).

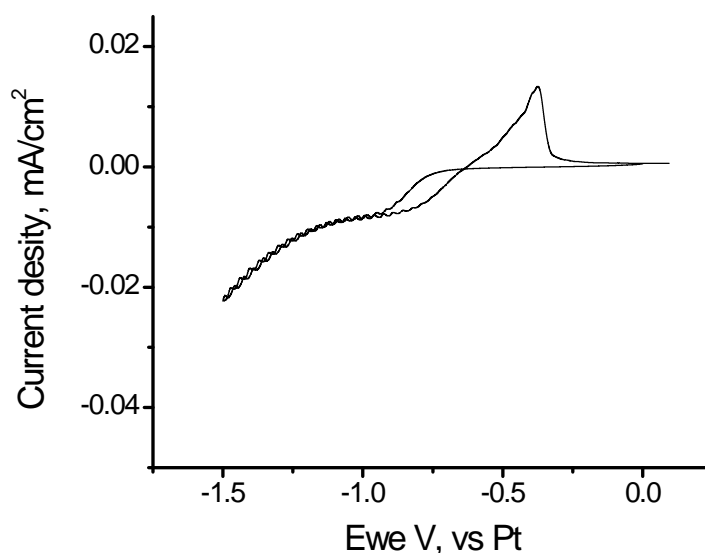


**Figure 3.16:** Cyclic voltammogram (scan rate 50 mV/s) of [P<sub>1444</sub>][Tosylate] with 0.01 M CdCl<sub>2</sub> at 110 °C.

Cyclic voltammograms of Cd(II) in [P<sub>1444</sub>][Tosylate] with various concentrations of sulfur at 110 °C are shown in Figure 3.17. The voltammograms show appearance of a strong reduction wave with onset potentials around -0.5 V and reduction peaks located at -1.0 V vs Pt, while oxidation peaks are observed at around -0.25 V. Formation of black deposits was observed on the surface of FTO at these conditions, which may be due to the deposition of elemental cadmium. The amplitude of the current density was found to increase upon addition of sulfur, reaching a maximum at equal concentrations of Cd(II) and S. Upon further increase in sulfur concentration, however, the amplitude of the reduction wave is significantly diminished while no peak was observed during oxidation scan. Although no oxidation process was observed, chronoamperometry in electrolyte containing 0.01 M CdCl<sub>2</sub> and 0.02 M S at -1.0 V vs Pt and 110 °C results in the formation of light brownish deposits on the surface of FTO which may be related to the reduction of Cd(II).

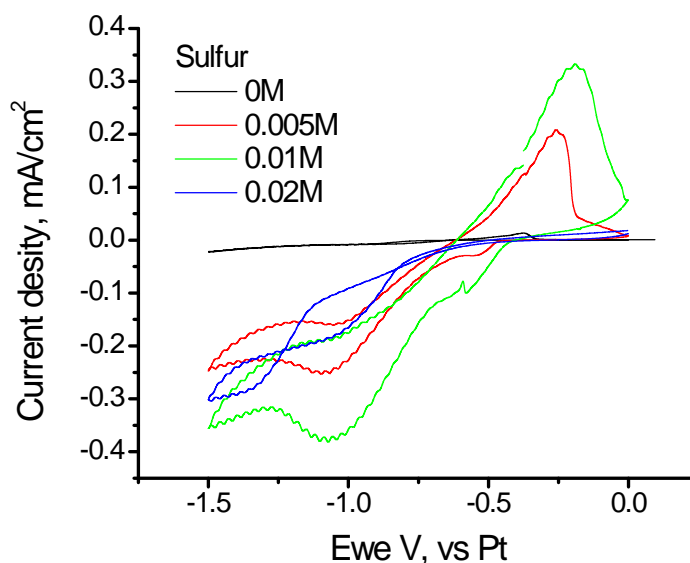


**Figure 3.17:** Cyclic voltammograms (scan rate 50 mV/s) of [P<sub>1444</sub>][Tosylate] with 0.01 M CdCl<sub>2</sub> and various sulfur content at 110 °C.

Figure 3.18 shows cyclic voltammograms of the IL with Cd(II) and S at various temperatures. It can be seen that current density increases with temperature up to 120 °C. At higher temperatures, however, there is a significant reduction in current density, which is almost totally diminished at 140 °C. This effect can be related to the sulfur polymerization at high temperatures that was similarly observed for [P<sub>4444</sub>]Cl and [P<sub>66614</sub>][DCA]. It can be concluded then that [P<sub>1444</sub>][Tosylate] cannot be used as an electrolyte when elemental sulfur is used as a sulfide precursor at temperatures exceeding 120 °C.

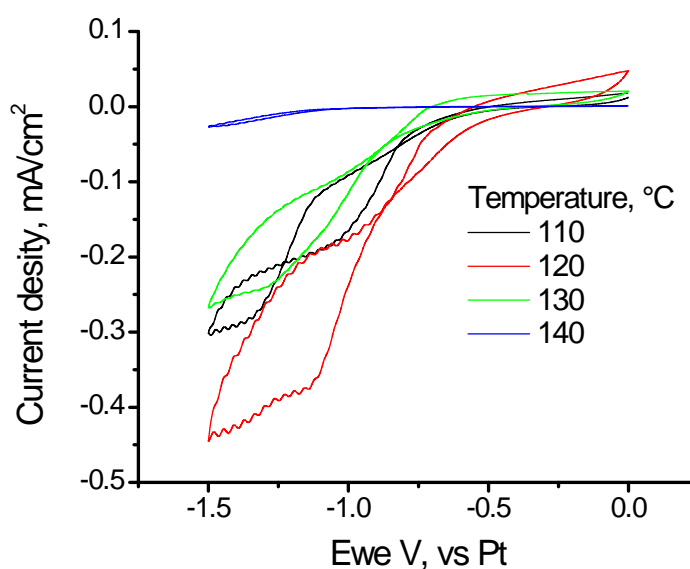


**Figure 3.18:** Cyclic voltammograms (scan rate 50 mV/s) of [P<sub>1444</sub>][Tosylate] with 0.01 M CdCl<sub>2</sub> and 0.02 M Sulfur at various temperatures (right).

**[P<sub>66614</sub>][NTf<sub>2</sub>]**

The range of electrochemical potentials at which the IL remains stable towards reduction was determined from the cyclic voltammogram, which is shown in Figure 3.19. The voltammogram shows no electrochemical processes in the region of interest for [P<sub>66614</sub>][NTf<sub>2</sub>].

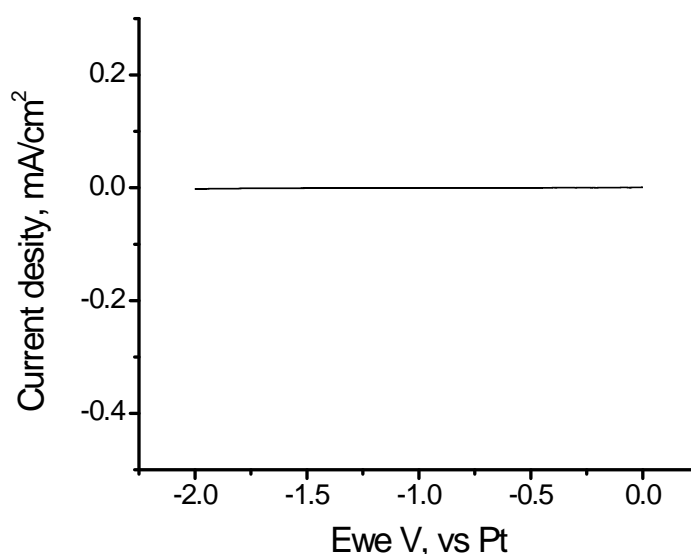


**Figure 3.19:** Cyclic voltammograms (scan rate 50 mV/s) of [P<sub>66614</sub>][NTf<sub>2</sub>] at 125 °C.

The cyclic voltammogram of the IL with small amount of Cd(II) is shown in Figure 3.20. The reduction wave occurs at about -0.5 V and can be attributed to the reduction of Cd(II), while no clear peak is observed during the oxidation scan. The solubility of cadmium chloride in dry [P<sub>66614</sub>][NTf<sub>2</sub>] is fairly low, leading to low current densities during the reduction cycle.

To improve the solubility of Cd(II), low molecular weight solvents (such as ethylene carbonate (EC) and methyl-ethyl carbonate (MEC)) were added to the electrolyte as can be seen in Figure 3.21. Although the addition of 5 volume % has almost no effect on the amplitude of current densities, the addition of more than 12.5 vol %, however, significantly enhances current density. The onset potential during reduction scan can be observed at around -0.5 V with the peak position at around -1.0 V vs Pt. No clear peak is observed during the oxidation scan. The positive effect from addition of low molecular

weight solvents may be due to an increase in Cd(II) solubility in the IL and an improvement in ion mobility, as a result of reduction in the electrolyte viscosity.

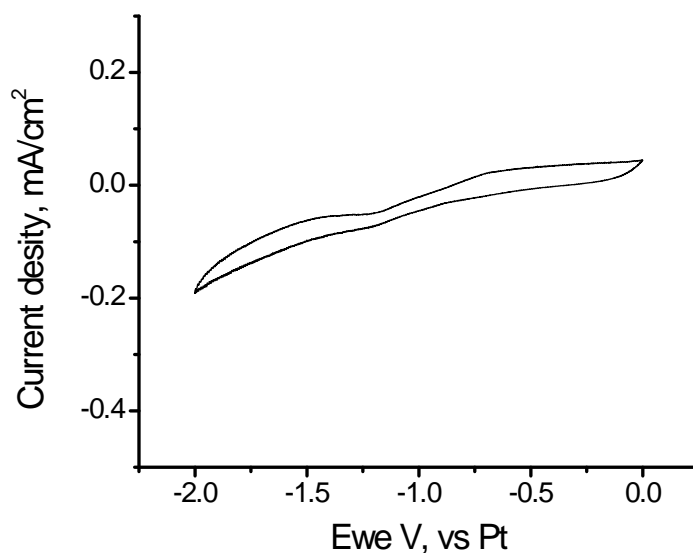


**Figure 3.20:** Cyclic voltammograms (scan rate 50 mV/s) of [P<sub>66614</sub>][NTf<sub>2</sub>] (black) and this with 0.01 M CdCl<sub>2</sub> (red) at 125 °C.

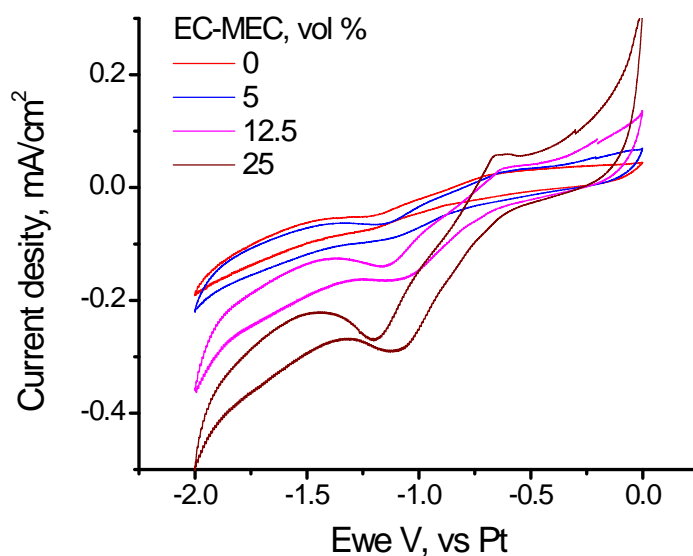


**Figure 3.21:** Cyclic voltammograms (scan rate 50 mV/s) of [P<sub>66614</sub>][NTf<sub>2</sub>] with 0.01 M CdCl<sub>2</sub> at 125 °C and various amount of EC-MEC.

Cyclic voltammograms of sulfur in the IL are shown in Figure 3.22. The strong reduction wave at potential around -0.5 V vs Pt can be attributed to sulfur reduction. Although elemental sulfur is readily soluble in [P<sub>66614</sub>][NTf<sub>2</sub>], an increase in current density was observed during reduction in the IL containing low molecular weight solvents

as can be seen from Figure 3.22. This positive effect may be related to the increase in ion mobility due to the reduction in electrolyte viscosity.

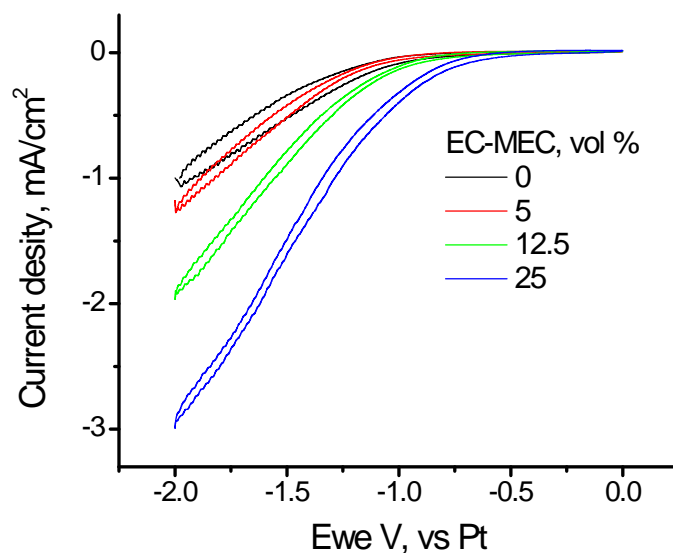


**Figure 3.22:** Cyclic voltammograms (scan rate 50 mV/s) of  $[P_{66614}][NTf_2]$  with 0.01 M Sulfur (black) and these with various volume amounts of EC-MEC mixture at 125 °C.

The cyclic voltammogram of the electrolyte containing Cd(II) and S is shown in Figure 3.23. A strong reduction wave is located at around -0.5 V vs Pt, while no oxidation wave can be observed in the cyclic voltammogram.

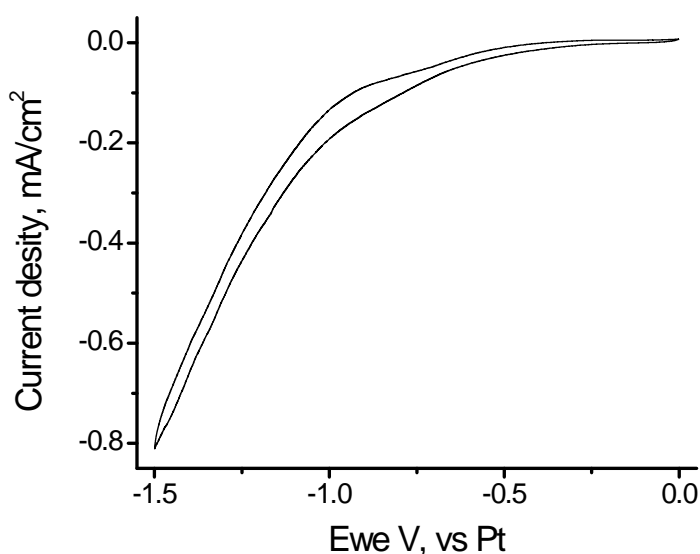
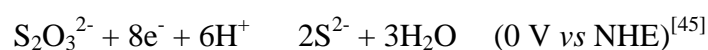


**Figure 3.23:** Cyclic voltammogram (scan rate 50 mV/s) of  $[P_{66614}][NTf_2]$  with 0.01 M  $CdCl_2$  and 0.01 M Sulfur with 25 vol% of the EC-MEC mixture at 125 °C.

Electrodeposition from this electrolyte results in the formation of poor quality films that optically resemble CdS. As was mentioned above, the potentials for Cd(II) and sulfur reduction are located around -0.5 V *vs* Pt. Even though the absolute current density for the sulfur reduction is higher compared to the reduction of Cd(II), it becomes possible for Cd(II) to be co-deposited during electrodeposition, which has a negative influence on the quality of the prepared films.

### 3.4.2. Sodium thiosulfate as sulfide precursor and choice of IL

During the deposition described here sulfide ions are required to be electrochemically generated at the substrate surface; in the presence of Cd(II) ions, the sulfide precipitates onto the substrate as CdS. Sodium thiosulfate was chosen as an alternative source of sulfide anion *via* reduction according to the reaction:<sup>[30]</sup>



Reduction of thiosulfate is reported to have a potential more suitable than that of the elemental sulfur:



Several ILs including [P<sub>66614</sub>][NTf<sub>2</sub>], [P<sub>66614</sub>][DCA] and [P<sub>1444</sub>][Tosylate] were chosen to investigate deposition of CdS using thiosulfate as sulfide precursor. The measurements were conducted in the presence of air. FTO coated glass was used as a working electrode, while Pt was used as pseudo reference and counter electrodes.

Sodium thiosulfate has very limited solubility in dry ILs. When introduced into [P<sub>66614</sub>][NTf<sub>2</sub>], a solution containing 0.01 M Na<sub>2</sub>S<sub>2</sub>O<sub>3</sub> became turbid and precipitation of a yellow solid was observed upon heating as seen in Figure 3.24. Formation of the precipitate intensified when the temperature was increased. This may be the result of further reduced solubility at elevated temperatures. It is important to note, however, that no precipitate was observed in an electrolyte containing equal amount of CdCl<sub>2</sub>. We can speculate then that the presence of Cd(II) significantly improves stability of thiosulfate in the IL. It is important to note that no precipitate was formed under the same conditions for [P<sub>66614</sub>][DCA] and [P<sub>1444</sub>][Tosylate].

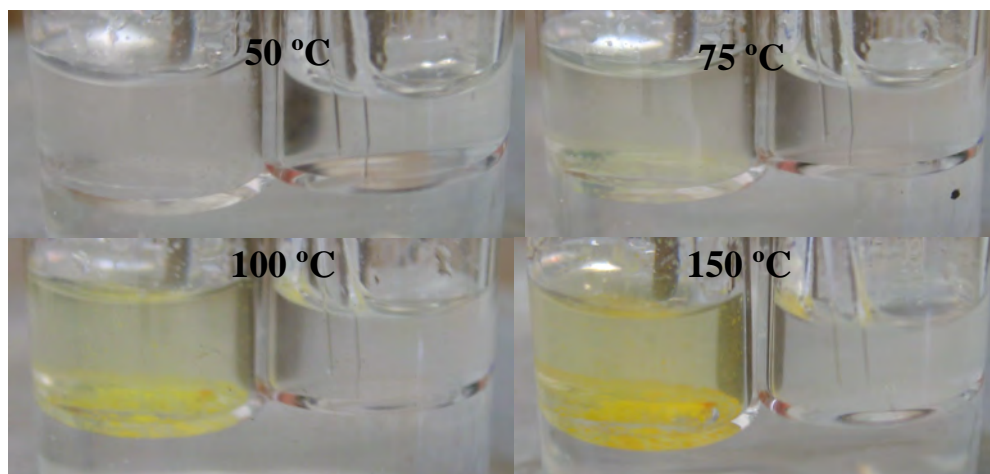


**Figure 3.24:**  $[P_{66614}][NTf_2]$  (1%  $H_2O$ ) at different temperatures with 0.01 M  $Na_2S_2O_3$  (left vial), 0.01 M  $Na_2S_2O_3$  and 0.01 M  $CdCl_2$  (right vial)

### Electrodeposition of CdS from $[P_{1444}][Tosylate]$

A typical cyclic voltammogram of  $[P_{1444}][Tosylate]$  at 100°C is shown in Figure 3.25a. This CV confirms that there are no electrochemical reactions related to the IL in the region of interest. From Figure 3.25b it can be seen that reduction of cadmium only takes place at potentials lower than -0.6V (*vs* Ag/AgCl) in  $[P_{1444}][Tosylate]$  at 100°C, which is consistent with -0.4V (*vs* NHE), the reduction potential of cadmium in aqueous electrolytes.<sup>[46]</sup>

The reduction of thiosulfate has a less negative potential than elemental sulfur, as can be seen in Figure 3.25c; this allows the choice of electrochemical conditions for the deposition under which the Cd(II) reduction will not be an interfering process.

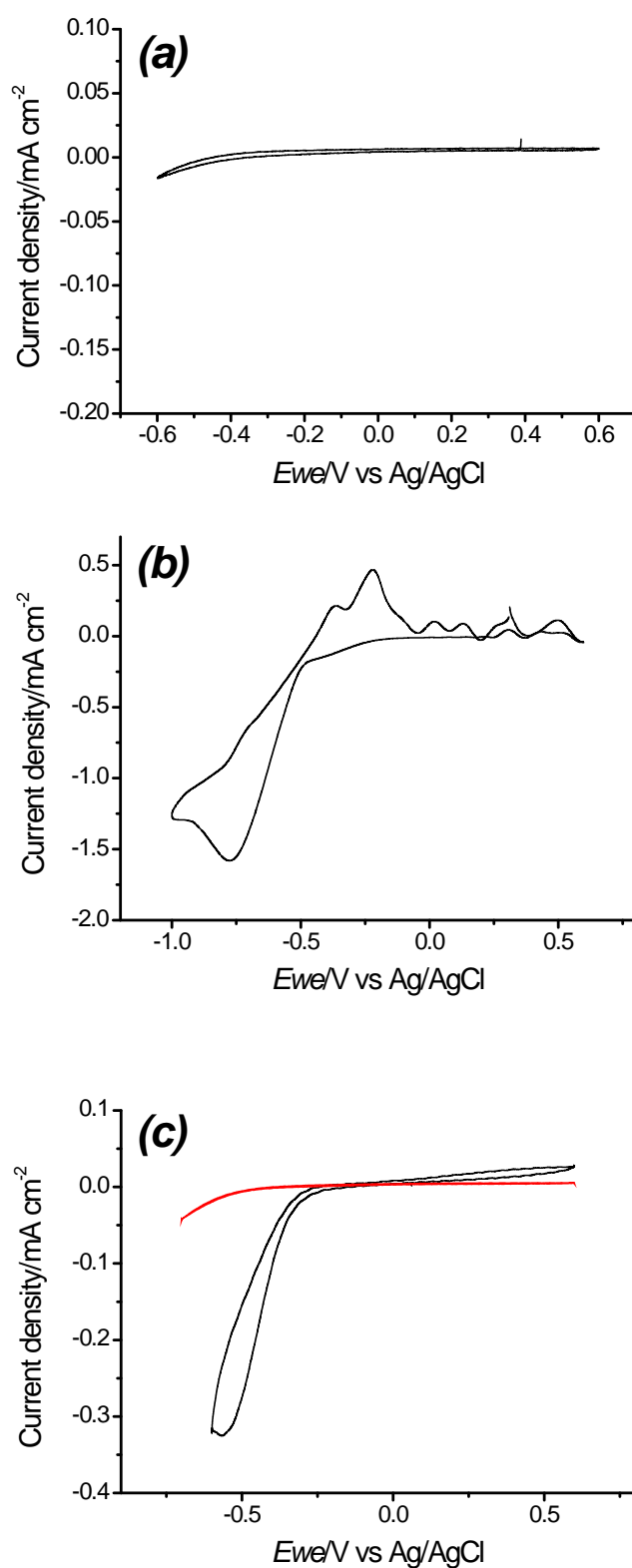


**Figure 3.25:** Cyclic voltammograms (scan rate 50 mV/s) at 100 °C of: a) [P<sub>1444</sub>][Tosylate]; b) 0.01 M CdCl<sub>2</sub> in [P<sub>1444</sub>][Tosylate]; c) 0.04 M Na<sub>2</sub>S<sub>2</sub>O<sub>3</sub> · 5H<sub>2</sub>O (black line) and 0.04 M Sulfur (red line) in [P<sub>1444</sub>][Tosylate]

The growth of thin CdS films was attempted using a staircase chronopotentiometry technique to find the optimum conditions. Figure 3.26 shows a typical plot of current density and electrode potential during deposition at 150 °C. At the beginning of the growth, current density was increased by 20  $\mu\text{A}/\text{cm}^2$  every minute up to 100  $\mu\text{A}/\text{cm}^2$ , at which electrodeposition took place. A slight further increase in the electrode potential with time can be attributed to additional resistivity due to the formation of the semiconductor. Since current density is kept constant, temperature will also affect the deposition potential. It should be stressed, though, that in all experiments the potential was not allowed to become more negative than -0.4 V *versus* Ag/AgCl.

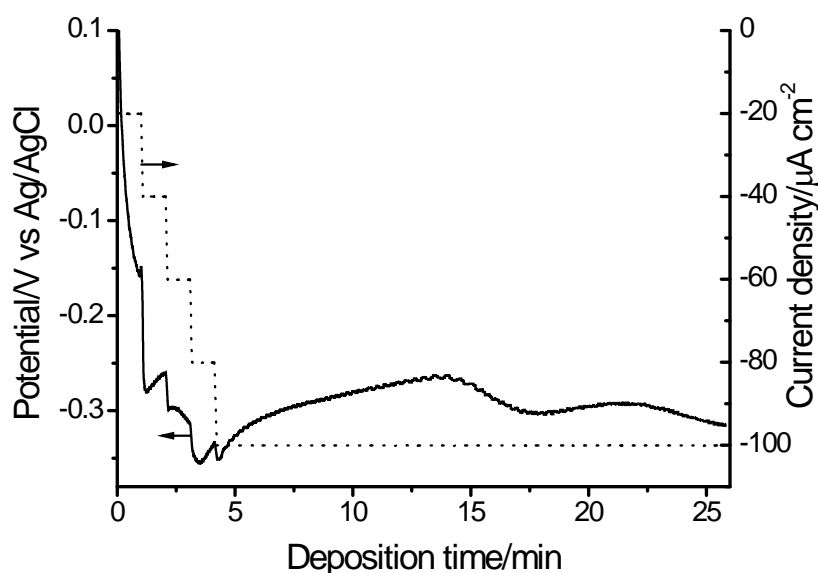


**Figure 3.26:** Typical chronopotentiometry plot during CdS electrodeposition.

From these studies we identified several main parameters that influence the CdS electrodeposition: the concentrations of Cd(II) and thiosulfate in the [P<sub>1444</sub>][Tosylate] and the deposition temperature. The relative influence of these parameters on the film quality (assessed using optical microscopy) is summarized in Table 3.4. It can be seen that deposition at high temperatures from electrolytes that contain higher concentration of thiosulfate compared to Cd(II) result in formation of better quality films.

**Table 3.4:** The influence of Cd(II) and thiosulfate concentration in the [P<sub>1444</sub>][Tosylate] and deposition temperature on relative quality of films prepared at 200  $\mu\text{A}/\text{cm}^2$  for 10  $\mu\text{Ah}$ .

Concentration (x = 0.01 M)		Temperature, °C			
Cd <sup>2+</sup>	S <sub>2</sub> O <sub>3</sub> <sup>2-</sup>	80	110	130	150
0.01 M	1x	-	-	-	+
	2x	-	-	+	++
	3x	-	+	++	+++
	4x	-/+	+	++	+++

An SEM image of a film (~80 nm) electrodeposited on the FTO surface is shown in Figure 3.27. The film shows a relatively uniform surface of crystallites of about 200nm in diameter. Importantly it shows no larger (>1  $\mu\text{m}$ ) precipitates, that are a known issue in thick film CBD deposits as can be seen in Figure 3.28.<sup>[16, 17]</sup>

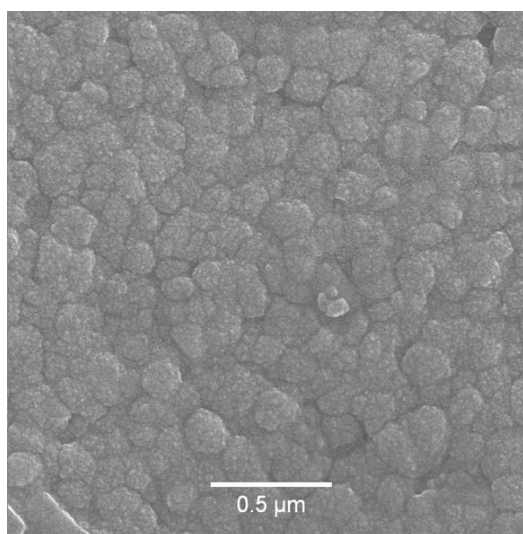


**Figure 3.27:** SEM image of CdS film (~80 nm) electrodeposited on the FTO substrate.

After thermal treatment of the CdS film it was possible to lift the film off the substrate. EDX spectra of a film on an FTO surface and a film that was lifted off the substrate are shown in the Figure 3.29a and Figure 3.29b, respectively. The atomic ratios obtained in the latter case were  $54\pm 3\%$  S and  $46\pm 3\%$  Cd indicating 1:1 stoichiometry. Chloride was previously observed in the CdS films electrodeposited from aqueous solutions of Na<sub>2</sub>S<sub>2</sub>O<sub>3</sub> and CdCl<sub>2</sub>.<sup>[30]</sup> The fact that no Cl signal could be detected in the present work suggests that the technique can be used to prepare Cl<sup>-</sup> free films, which in turn may enhance electrical properties. The EDX spectra are almost identical to the films

prepared by the spray pyrolysis as reported by Baykul *et al.*<sup>[7]</sup>, where the atomic ratio of cadmium to sulfur was also found to be practically stoichiometric.

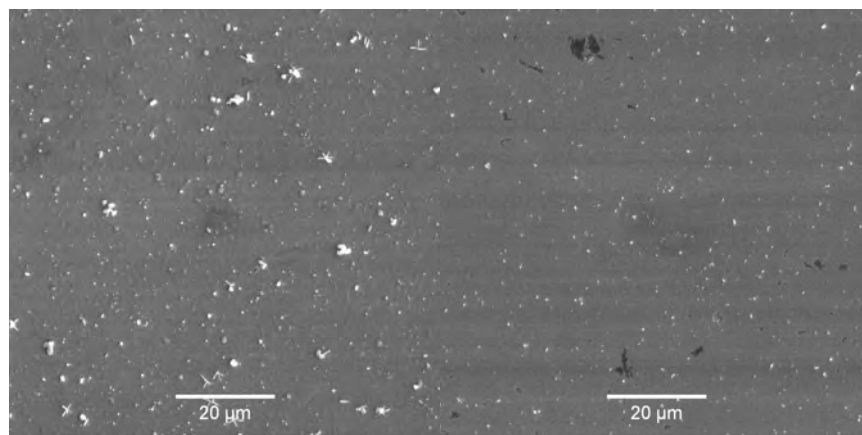


**Figure 3.28:** SEM image of CdS film deposited by conventional CBD (left) and electrochemical method (right) on the FTO substrate.

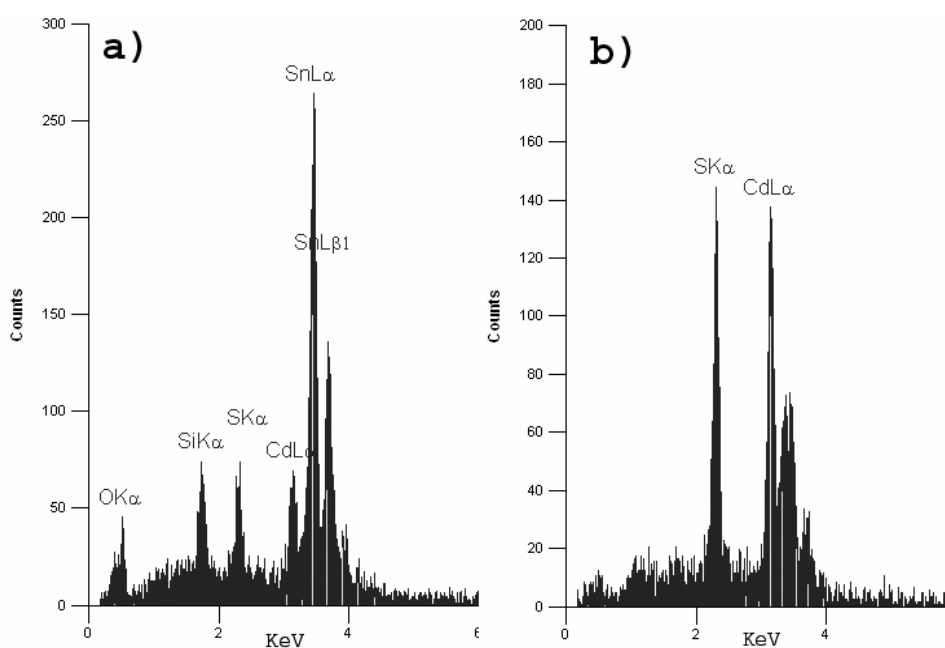


**Figure 3.29:** EDX spectra of CdS film (~80 nm): a) on the FTO substrate; b) lifted off from the FTO.

Hence, it was possible to electrodeposit CdS films with close to stoichiometric ratio between Cd and S that does not contain the large precipitates common for the CBD method.

#### Electrodeposition of CdS films from [P<sub>66614</sub>][NTf<sub>2</sub>] and [P<sub>66614</sub>][DCA]

In order to investigate electrodeposition of CdS using thiosulphate as sulfide precursor from hydrophobic ILs, [P<sub>66614</sub>][NTf<sub>2</sub>] and [P<sub>66614</sub>][DCA] were used in this work.

The conditions of the synthesis were adapted from these developed for [P<sub>1444</sub>][Tosylate] while the concentration of water in [P<sub>66614</sub>][NTf<sub>2</sub>] and [P<sub>66614</sub>][DCA] was around 2% (w/w).

Figure 3.30 shows the cyclic voltammogram of the electrolyte containing thiosulfate and Cd(II) in [P<sub>66614</sub>][NTf<sub>2</sub>] at high temperature. A strong reduction wave at around -0.6 V vs Pt and a small oxidation peak around -0.5 V vs Pt can be observed during cycling. Chronoamperometry at potentials between -0.5 and -1 V vs Pt results in the formation of black deposits on the surface of FTO that can be attributed to elemental Cd.

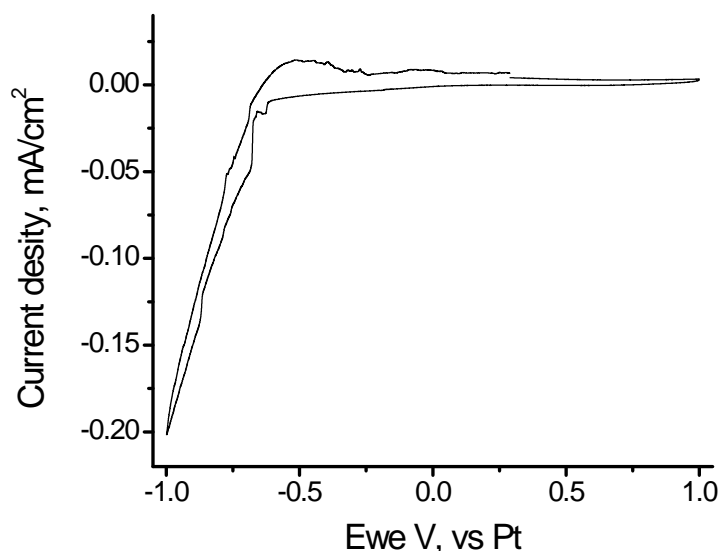


**Figure 3.30:** Cyclic voltammograms (scan rate 50 mV/s) of [P<sub>66614</sub>][NTf<sub>2</sub>] (2% H<sub>2</sub>O) (black) with 0.01 M CdCl<sub>2</sub>, 0.01 M Na<sub>2</sub>S<sub>2</sub>O<sub>3</sub> (red) at 150 °C.

Figure 3.31 shows the cyclic voltammogram of the electrolyte containing thiosulfate and Cd(II) in [P<sub>66614</sub>][DCA] at high temperature. A strong reduction wave around -0.5 V vs Pt and a broad oxidation peak around -0.4 V vs Pt can be observed during cycling. Chronoamperometry at potentials between -0.5 and -1.0 V vs Pt, results in formation of black deposits on the surface of FTO that can be attributed to elemental Cd.

It can be concluded then that [P<sub>66614</sub>][NTf<sub>2</sub>] and [P<sub>66614</sub>][DCA] cannot be used as electrolytes for electrodeposition of CdS using thiosulfate as a sulfide precursor. This fact maybe due to the influence of ILs on the electrochemical reduction of thiosulfate in the presence of Cd(II) and limited amount of water in the electrolyte.

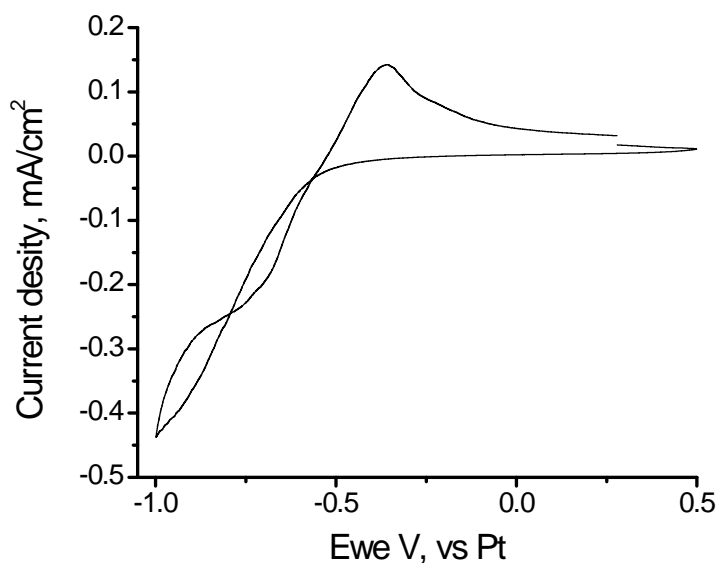


**Figure 3.31:** Cyclic voltammogram (scan rate 50 mV/s) of [P<sub>66614</sub>][DCA] (2% H<sub>2</sub>O) with 0.01 M CdCl<sub>2</sub>, 0.01 M Na<sub>2</sub>S<sub>2</sub>O<sub>3</sub> at 150 °C.

The properties of CdS films electrochemically deposited from [P<sub>1444</sub>][Tosylate] are further characterized below.

### 3.4.3. Crystal structure of the CdS films

The XRD pattern of the CdS thin film and FTO coated glass are shown in Figure 3.32. Several intense peaks can be seen in the patterns.

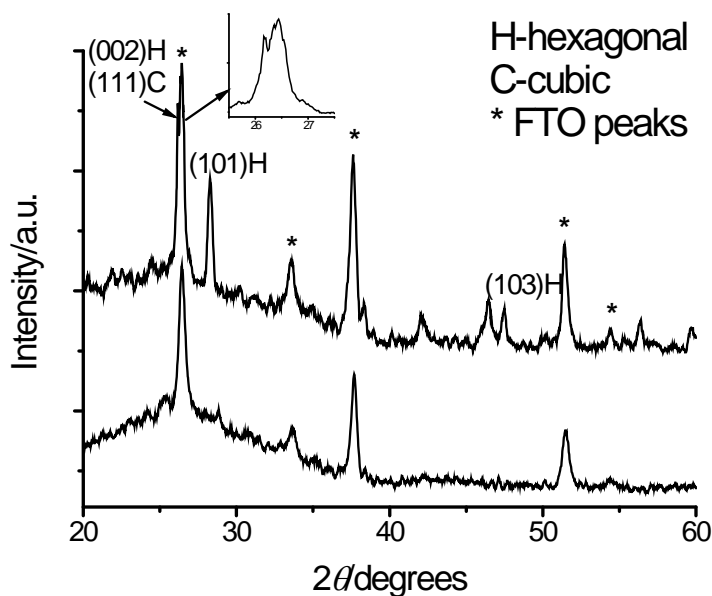


**Figure 3.32:** XRD pattern of CdS thin film on FTO (top) and bare FTO glass for comparison (bottom). The area for 2θ from 25.5° to 27.5° is shown in the inset.

The diffraction peaks at  $28.22^\circ$  and  $47.5^\circ$  coincide well with the (101) and (103) diffraction lines of hexagonal CdS.<sup>[17, 20, 47]</sup> A strong peak from the FTO at  $26.46^\circ$  shades the peak at  $26.16^\circ$  that could be assigned to the (002) and (111) planes of hexagonal and cubic phase respectively.<sup>[20, 47]</sup> Several small peaks at  $42^\circ$ ,  $46.5^\circ$  and  $56.4^\circ$  could not be assigned to any form of CdS, CdO or any other salt possibly present. The fact that several significant hexagonal CdS peaks are missing may indicate alignment of the crystals in the sample.

The average size of the crystals was calculated using the Scherrer equation (Equation 3.1),<sup>[48]</sup> where  $d$  is the average crystallite size,  $\lambda$  is the X-ray wavelength,  $\theta$  is the Bragg angle, and  $\beta$  is a FWHM of the diffraction peak in radians. The average crystallite sizes calculated for CdS(101) hexagonal and CdS(103) hexagonal diffraction peaks are  $\sim 25$  and  $\sim 27$  nm respectively. These values are higher than those reported for CdS prepared *via* CBD,<sup>[16]</sup> where the range of sizes between 9 and 20 nm was observed and similar to  $\sim 25$  nm observed for films prepared *via* the CVD route.<sup>[11]</sup>

$$d = \frac{0.94\lambda}{\beta \cos \theta} \quad (3.1)$$

The data presented here suggest that the reported method can be successfully used to electrodeposit materials with specific orientation. The polycrystalline films are composed of nanocrystals which are similar in size to those prepared *via* CVD.

#### 3.4.4. Thickness of films

Prior to deposition, a section of the FTO was electrically isolated by laser etching. A typical surface profile of the films is shown in Figure 3.33. This technique allows us to measure the height of the deposits on top of the FTO glass. The thickness of the films thus measured ranged between 10 nm and 200 nm. Table 3.5 lists the properties of a number of films prepared using various conditions in [P<sub>1444</sub>][Tosylate].

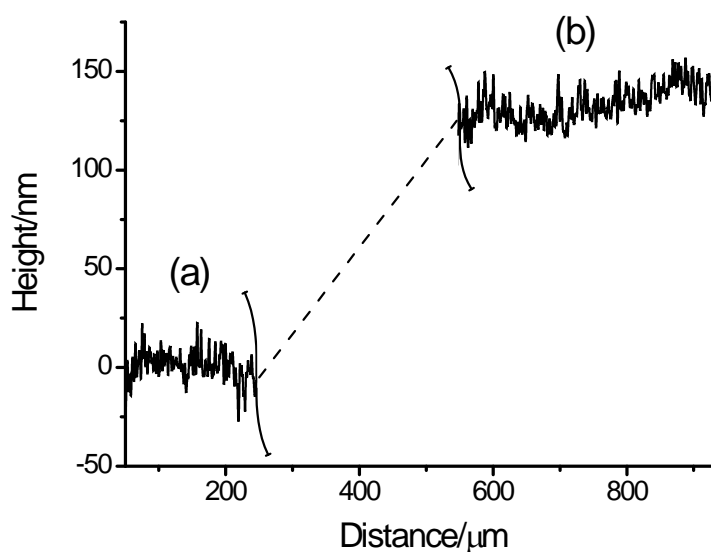


**Figure 3.33:** A typical profile of the films (s3 in Table 3.5): bare FTO surface (a) and CdS film (b). (Laser etched channel removed from the data).

**Table 3.5:** Properties of CdS films electrodeposited under different conditions

Name	Stair case current	T, °C	Current density, $\mu\text{A cm}^{-2}$	Charge, $\mu\text{Ah cm}^{-2}$	Thickness, nm +/- 10%
s1	no	130	200	72	~125
s2	no	130	200	56	~125
s3	no	130	200	76	~135
s4	no	130	200	21	~75
s5		130	200	88	~150
s6		130	200	49	~60
s7		130	200	25	~40
s8		130	200	12	~10
s9		130	200	106	-
s10		130	200	60	-
s11		130	200	50	-
s12		130	200	98	~190
s13		130	200	32	~55
s14		130	200	20	~50
s15		150	100	40	~120
s16		150	100	53	~145
s17		150	100	50	~180

The relationship between the film thickness and amount of charge passed for the growth at 130°C is shown in Figure 3.34. The linear trend suggests that the growth of the film is charge controlled. Hence, films of different thicknesses can easily be obtained simply by altering time or current.

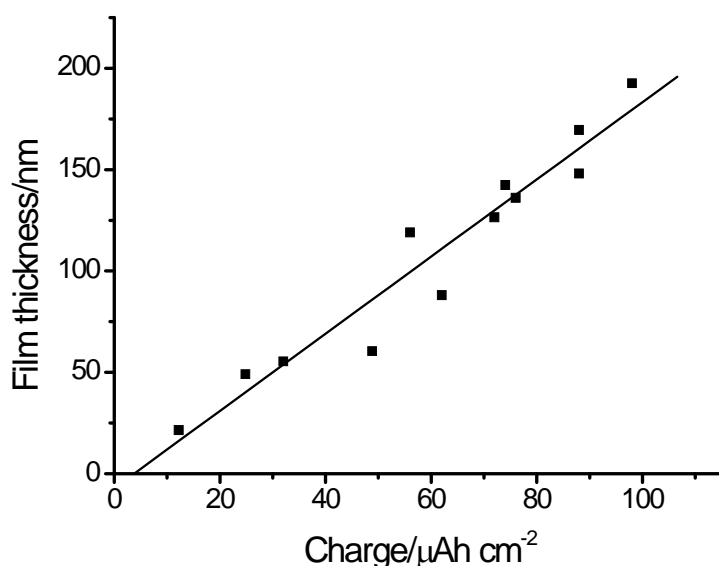


**Figure 3.34:** Dependence of film thickness on charge passed for growth at 130°C.

The UV-vis spectra of the CdS films of various thicknesses are shown in Figure 3.35. It can be seen that the absorption of the CdS is proportional to the film thickness. From these spectra the attenuation coefficient can be calculated. The slight discrepancies in the values of the attenuation coefficient may be related to variation in density of thicker films.

The value of the attenuation coefficient is of importance when the thicknesses of materials structures are to be analyzed. For the films deposited from ILs, the values of attenuation coefficient were calculated for the wavelength from 350 to 800 nm.

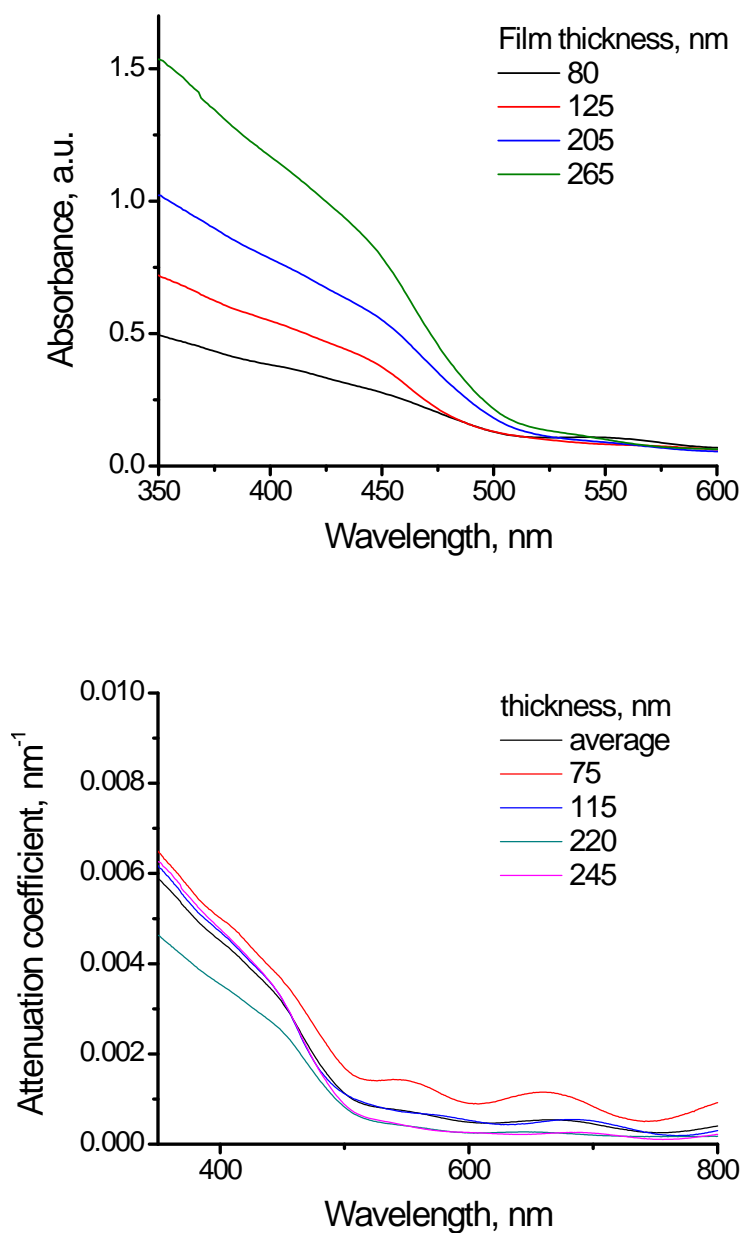


**Figure 3.35:** UV-vis absorption spectra (top) and attenuation coefficient (bottom) of electrodeposited CdS thin films.

### 3.4.5. Electric properties of CdS films

#### Mott-Shottky Impedance Spectroscopy

The flat band potential of the semiconductor was calculated from the Mott-Shottky plot recorded using impedance spectroscopy. In a typical measurement the semiconductor–electrolyte junction capacity was measured as a function of applied potential (*vs* SCE) at 1 kHz.<sup>[49]</sup> In order to prevent CdS film from deterioration 0.1 M Na<sub>2</sub>S and 0.1 M NaOH

were used in the electrolyte solution.<sup>[49]</sup> A typical Mott-Shottky plot of  $1/C_{SC}^2$  versus applied potential is shown in Figure 3.36, following Equation 3.2:

$$\frac{1}{C_{SC}^2} = \frac{2}{A^2 R^2 q N_d \epsilon \epsilon_0} \left( E - E_{fb} - \frac{kT}{q} \right) \quad (3.2)$$

where  $A$  is the surface area,  $R$  is the roughness,  $q$  is the electronic charge,  $N_D$  is the concentration of donors,  $\epsilon$  and  $\epsilon_0$  the relative and vacuum dielectric permittivities,  $k$  is the Boltzmann constant,  $T$  is the temperature, and  $E$  is the potential. By extrapolating the linear part of the plot, one can find the condition when  $1/C_{SC}^2 = 0$  at which the flat band potential is equal to electrode potential.

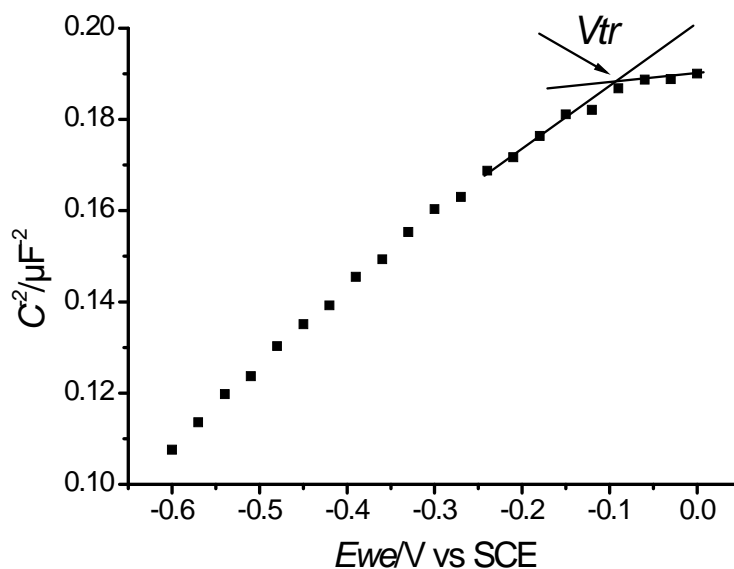


**Figure 3.36:** Typical Mott-Shottky plot of electrodeposited CdS films on bare FTO in 0.1 M Na<sub>2</sub>S and 0.1 M NaOH at 1 kHz, and determination of transition voltage,  $V_{tr}$ .

The flat band potentials of films deposited on the FTO substrates were found to be in the range of  $-0.88 \pm 0.08$  V (statistics of 5 films) (*vs* SCE). This value coincides very well with those reported in the literature for CdS thin films measured under the same conditions ( $-0.92$  V *vs* SCE).<sup>[49, 50]</sup> The flat band potential is known to be sensitive to preparation conditions ranging from  $-1.3$  to  $-0.8$  V (*vs* SCE). The more negative values in this range are close to those reported for single crystal CdS<sup>[49]</sup>.

With an increase in the applied voltage, the space charge region between the semiconductor and the electrolyte extends to the rear contact (FTO). This results in an

increase of the value of junction capacitance, which saturates at transition voltage potential. The determination of the transition voltage for CdS is shown in Figure 3.36. In our experiments the transition voltage was -0.09 V, which is also in agreement with literature values of -0.23 V.<sup>[49, 50]</sup>

### Band gap energy

UV-vis spectra (Figure 3.35) were used to calculate the band gap energies from Equation 3.3 in the usual way, as described elsewhere.<sup>[7, 51]</sup>

$$\alpha = k \frac{(h\nu - E_g)^m}{h\nu} \quad (3.3)$$

where  $k$  is a constant,  $h\nu$  is the photon energy,  $E_g$  is the band gap energy and  $m$  is equal to 1/2 for a direct band gap material. Here, the plot of  $(\alpha h\nu)^2$  versus  $h\nu$  yields the band gap energy at the point where the linear parts of the curve intersect.

The band gap of CdS films prepared in this work was thus found to be  $2.59 \pm 0.02$  eV (Figure 3.37a). A similar result of  $E_g = 2.61$  eV was measured for CdS films prepared by chemical bath deposition on the FTO substrate.

The reported values of the band gap for CdS thin films vary greatly from  $2.58^{[11, 52, 53]}$  to  $2.38$  eV.<sup>[54]</sup> There may be multiple reasons for such differences including quantum confinement effects, observed due to the polycrystalline nature of the film in some literature cases. It was shown that the value of the band gap for such films normally reduces with an increase in film thickness, because the probability of formation of bigger crystals increases at longer deposition times/film thickness<sup>[18]</sup>. In our work however, the band gap of samples appeared to be independent of film thickness as shown in Table 3.6 except at a very low film thickness (~10nm). A classical quantum confinement effect with an increase in value of  $E_g$  to 2.72 eV was observed for the ~10nm film (see Figure 3.37b). Although the crystal structure of the semiconductor has a major influence on the value of the band gap, the strain and imperfections that appear during the deposition may also have a tremendous effect on electric properties producing a wide range of data from different deposition techniques.<sup>[11]</sup>

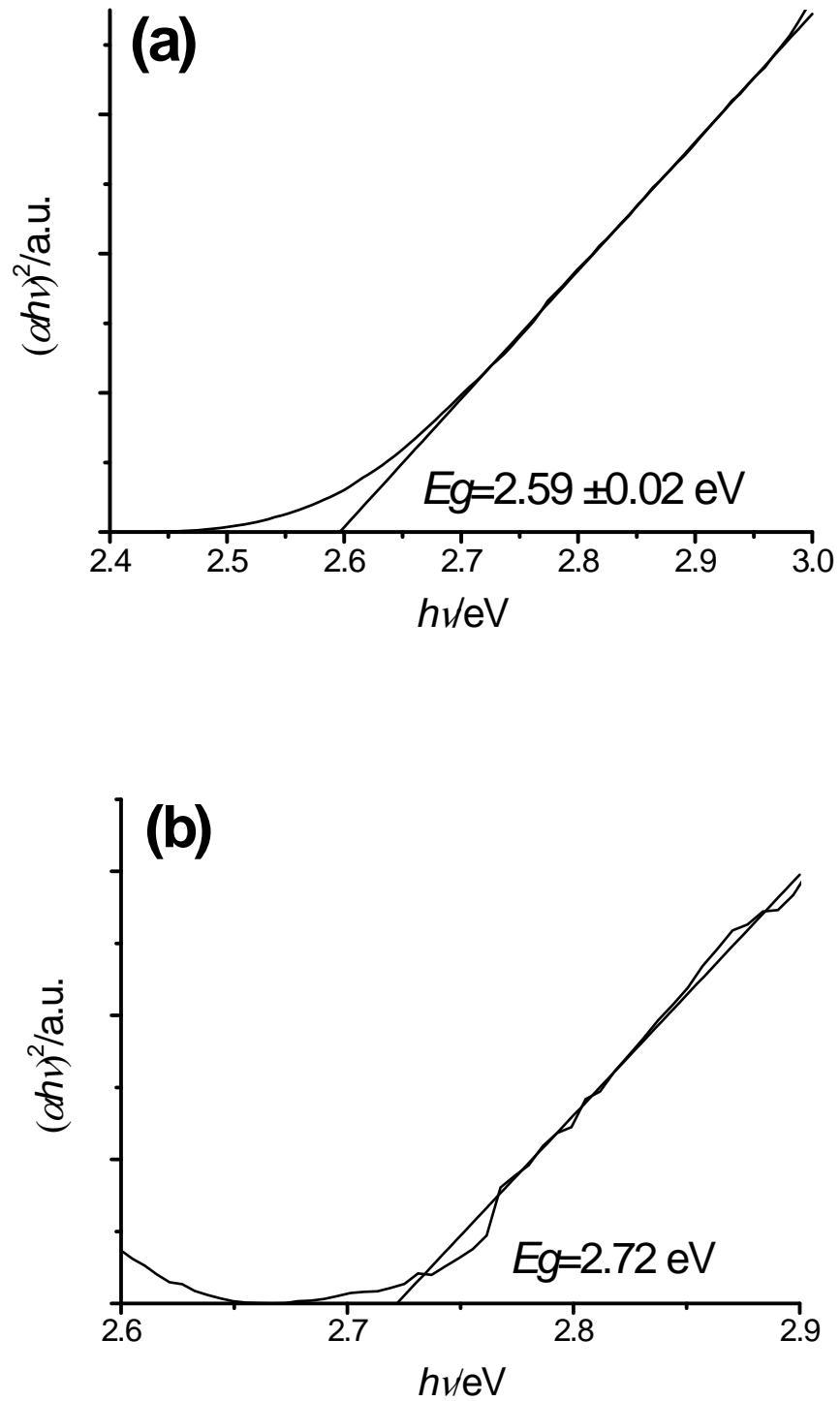


**Figure 3.37:**  $(\alpha h\nu)^2$  versus  $h\nu$  plot derived from UV-vis spectra: a) thickness  $> 10$  nm; b) thickness  $\sim 10$  nm.

**Table 3.6:** Properties of CdS films electrodeposited under different conditions

Name	Thickness, nm +/- 10%	Eg, eV +/- 0.02
s1	~125	2.59
s2	~125	2.59
s3	~135	2.57
s4	~75	2.57
s5	~150	2.58
s6	~60	2.59
s7	~40	2.57
s8	~10	2.72
s9	-	2.63
s10	-	2.58
s11	-	2.59
s12	~190	2.59
s13	~55	2.57
s14	~50	2.57
s15	~120	2.62
s16	~145	2.62
s17	~180	2.60

### Thermal annealing of CdS films

In order to study the influence of temperature on the optical and electrical properties of the deposits, some of the films were annealed in a nitrogen atmosphere for 1 hour at 350 °C. Such a low temperature compared to other reports was chosen to prevent sulfur evaporation from the surface (which occurs at  $T > 375^\circ\text{C}$ ).<sup>[22]</sup> The band gap was reduced from  $2.59 \pm 0.02$  eV to  $2.52 \pm 0.02$  eV during annealing. This decrease in the band gap value is well known in the literature<sup>[22, 49]</sup> and can be attributed to either annealing of defects including the size of the crystals increasing<sup>[16]</sup> or to changes in the crystal structure of the films (formation of the cubic phase).<sup>[22]</sup> Most importantly, no deterioration in optical and electrical properties of the films was observed. Such deterioration is common

for the films prepared *via* aqueous methods, where presence of incorporated Cd(OH)<sub>2</sub> and H<sub>2</sub>O leads to self oxidation of the sample.<sup>[22]</sup>

### 3.4.6. Mechanism of growth

It was shown previously that the reduction of thiosulfate in aqueous solutions may proceed in several ways. Disproportionation of thiosulfate can produce sulfur:



then reduction of S to H<sub>2</sub>S.<sup>[19]</sup> Alternatively, direct reduction of thiosulfate can take place:<sup>[30]</sup>



Negligible amounts of H<sup>+</sup> present in the electrolyte make formation of elemental sulfur unlikely. The comparison between the CVs of S<sup>0</sup> and S<sub>2</sub>O<sub>3</sub><sup>2-</sup> shown in Figure 3.25c reveals that a more negative potential is needed to reduce elemental sulfur. No film was grown when elemental sulfur was used instead of thiosulfate as the source of S<sup>2-</sup> in this work. Thus, the reaction (1) appears to not be operative in the ionic liquid medium used in this work. Once the S<sup>2-</sup> production is established at the interface (denoted here as “int” below) two subsequent processes can take place:



The second process may lead to precipitation of CdS in the bulk solution and therefore, be a source of inefficiency in the process. S<sup>2-</sup> may also migrate to the positive electrode in the present cell arrangement and be reoxidized. The growth of the film is therefore ultimately limited by the lower of the rates at which S<sup>2-</sup> is formed and Cd<sup>2+</sup> diffuses to the surface. The rate of the thiosulfate reduction is controlled by the current, while deposition temperature and cadmium concentration in the IL determine the rate of Cd<sup>2+</sup> diffusion to the surface. By controlling the rate of the sulfur reduction as well as the temperature of deposition we, therefore, have a means to control the deposition and hence, potentially achieve high efficiency atom by atom growth of the films.

### 3.4.7. Electrodeposition of CdS on metals, semiconductors and polymers

In the above section CdS films were successfully deposited on the surface of FTO from the IL electrolyte. Considering the wide range of applications for semiconducting materials (*e.g.* electroluminescent devices), the ability to deposit films on various other substrates such as metals, semiconductors and polymers is very important. This is investigated further in this section.

#### Maleic anhydride on FTO

In order to improve adhesion properties of the deposited films, plasma polymerized maleic anhydride on the surface of FTO coated glass was used as a substrate. The films deposited on plasma treated FTO surface were adherent to the substrate. Shock temperature treatment and peel tests show no tendency for the films to lift off in the plasma treated case, whereas in the bare FTO case shock temperature treatment resulted in films peeling very readily Figure 3.38.

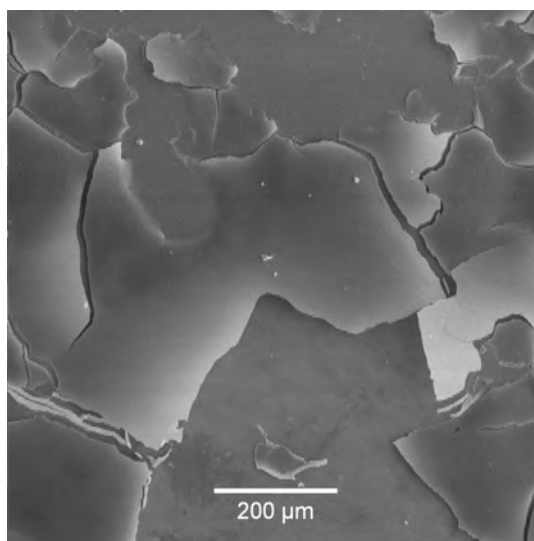


**Figure 3.38:** CdS films electrodeposited on bare FTO surface lifted off using shock temperature treatment.

The good adhesion observed in the case of the plasma treated FTO can be explained by the formation of chemical bonds between the CdS film and the substrate. It was shown before that the polymer film of maleic anhydride swells in the electrolyte forming a string like structure over the surface.<sup>[35]</sup> During the growth of the semiconductor the polymer chain may become trapped in the crystal structure of the CdS.

## Titanium

Titanium is well known for its superior corrosion resistance. Vacuum evaporation under high vacuum was used for deposition of thin films on the surface of a microscope glass slide. The optical images of Ti films thus produced, corresponding to thickness of 10 to 60 nm are shown in Figure 3.39.

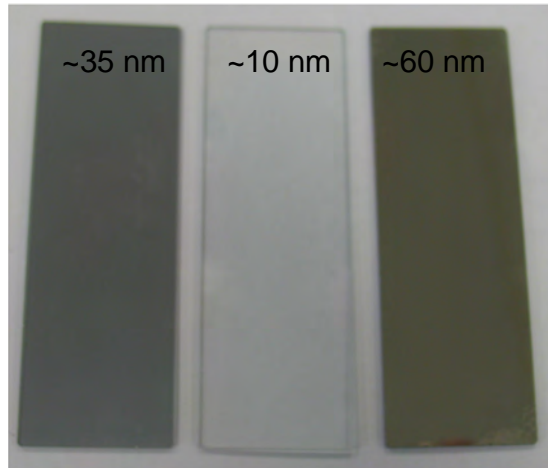


**Figure 3.39:** Thin Ti films evaporated on the surface of microscope glass slide.

It can be seen from Figure 3.40 that transparency of the film is significantly reduced for thicknesses exceeding 50 nm. As the metal thickness increases, conductivity is drastically increased, as shown in Table 3.7. For electrodeposition of CdS in this work, the thickness of Ti films was maintained around 60 to 100 nm, which provides good values of conductivity (for comparison, the sheet resistance of FTO electrode is 15 ohm/ ).

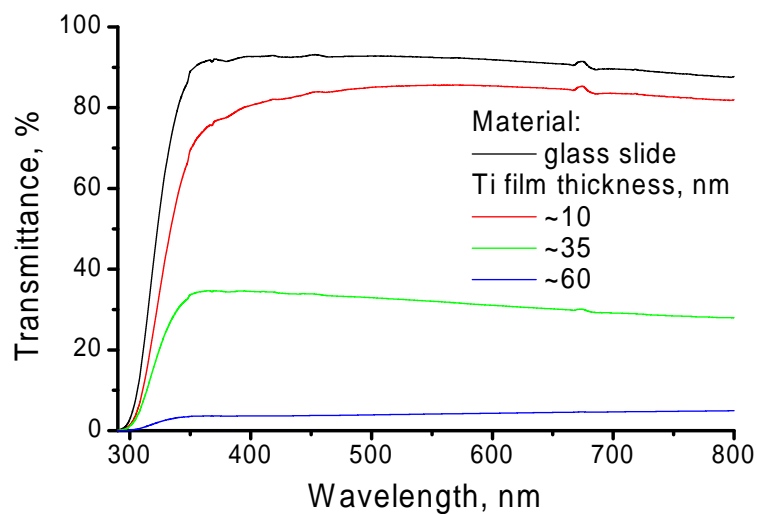


**Figure 3.40:** UV-vis transmittance spectra of the thin titanium films deposited on the glass slide.

**Table 3.7:** Sheet resistance and transmittance of thin Ti films.

Material	Sheet resistance ( $\Omega/$ )	Transmittance, %
Glass slide	non-conductive	91.9
10 nm Ti film	non-conductive	85.6
35 nm Ti film	550	31.6
60 nm Ti film	65	4.3

Deposition of CdS films on titanium was maintained using the chronopotentiometry technique. The typical dependence of electrode potential (*versus* the platinum reference electrode) during the deposition is shown in Figure 3.41.

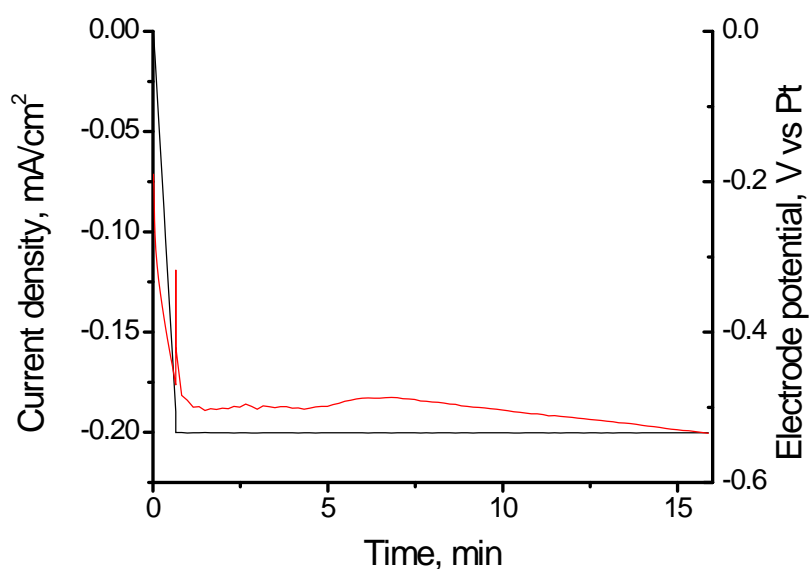


**Figure 3.41:** Electrochemical deposition of CdS on the surface of Ti electrodes. Current density corresponds to the black line, while the red line represents electrode potential.

Films deposited by this method were well adherent to the substrate, uniform and crack free as can be seen in Figure 3.42.

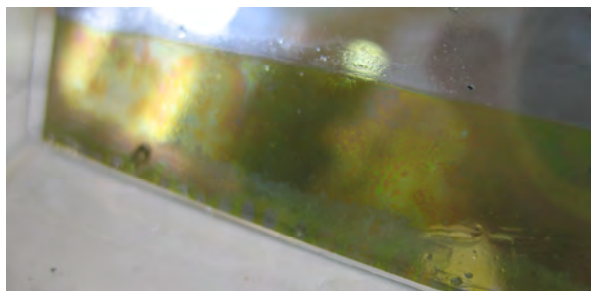


**Figure 3.42:** Optical image of films electrodeposited on Ti surface.

### Aluminum, gold

Due to the low corrosion resistance of some materials in the presence of thiosulfate ions at high temperatures (*e.g.* Al, Au) electrodeposition of CdS on such substrate is more difficult. Electrical conductivity of thin Al films (~100 nm) is comparable to that of the bulk material; when covered with a thin layer of Ti, such substrates can be effectively used for the electrodeposition as shown in Figure 3.43.

UV-vis spectroscopy of CdS films deposited on the FTO glass covered with a thin layer of Au (~50 nm) reveals presence of Au underneath the semiconducting layer. We might speculate then that the formation of CdS during deposition prevents further dissolution of Au films, making it possible to create an electric junction between these materials. High barrier height of such junction (shown in Table 3.1) allows the establishment of an ohmic contact between the CdS semiconductor and various substrates.

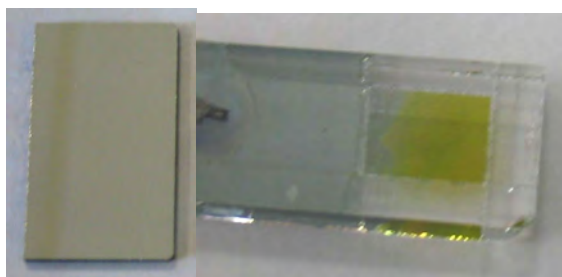


**Figure 3.43:** Optical images of thin Al films on glass (left) and electrodeposited CdS films on the FTO substrate covered with thin layer of Au.

### PEDOT

The method was equally successful for electrodeposition of CdS on the surface of conducting polymers at 130 °C in [P<sub>1444</sub>][Tosylate]. For the electrodeposition of CdS, thin films of PEDOT were deposited on plasma treated FTO substrates. The films appear to be uniform and featureless (see Figure 3.44).

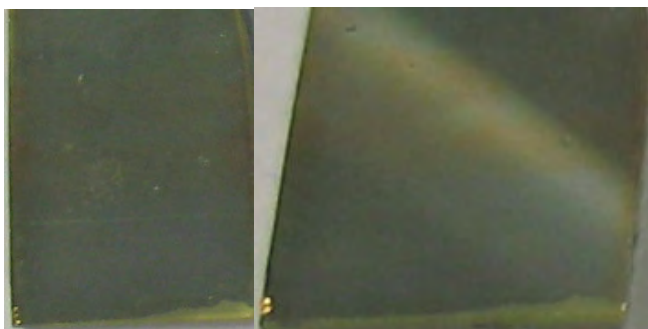


**Figure 3.44:** Optical images of thin CdS films electrodeposited on the FTO substrate covered with PEDOT film.

## TiO<sub>2</sub>

Among semiconductors, TiO<sub>2</sub> is one of the most interesting materials for electrodeposition of semiconductors, since its wide band gap energy and hence, low absorption of the visible part of the solar spectrum allows it to be effectively used in solar cell applications. Further, high surface area TiO<sub>2</sub> films can be prepared by screen printing of nanoparticles to significantly enhance light absorption of materials coated on its surface.<sup>[55]</sup> Hence, there is an interest in depositing CdS onto a porous TiO<sub>2</sub> film.

CdS was electrodeposited on the high surface area TiO<sub>2</sub> films prepared by screen printing of TiO<sub>2</sub> nanoparticles on the surface of the FTO electrode as can be seen from Figure 3.45 and Figure 3.46. The optical properties of CdS films deposited on TiO<sub>2</sub> are similar to those deposited on the surface of FTO.

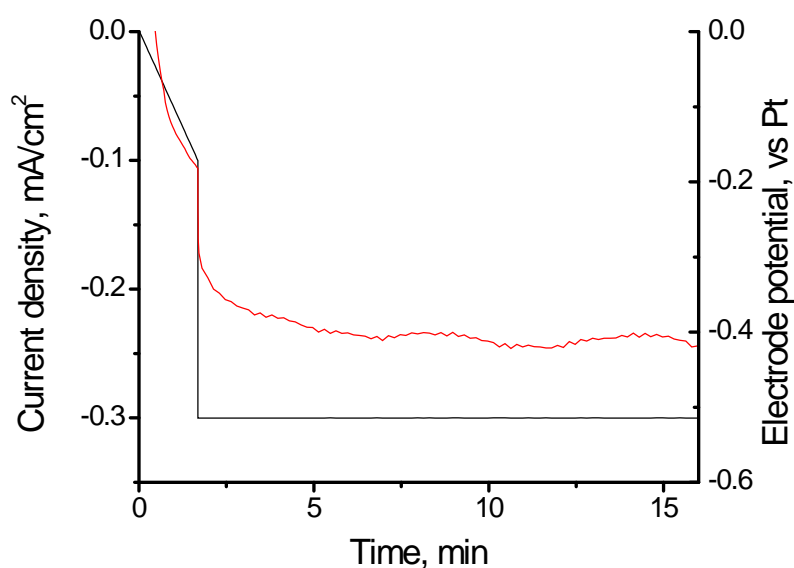


**Figure 3.45:** Electrochemical deposition of CdS on high surface area TiO<sub>2</sub> electrodes. Current density corresponds to the black line while the red line represents the electrode potential.

Even short deposition times produce films of exceptional absorbance as can be seen from Figure 3.47. Thus, we were able to combine the high absorption common for porous structures with the low recombination coefficients observed for thin films.

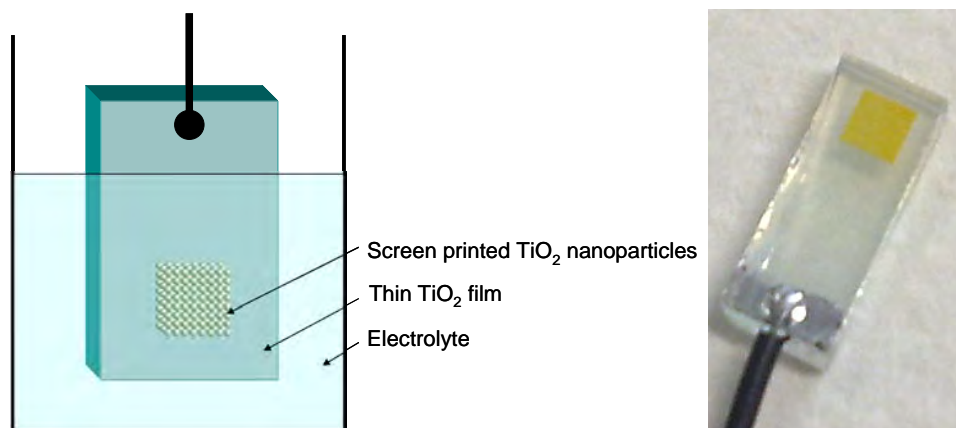


**Figure 3.46:** The schematic representation of electrodeposition on high surface area TiO<sub>2</sub> electrodes (left) and optical image of the deposited film (right).

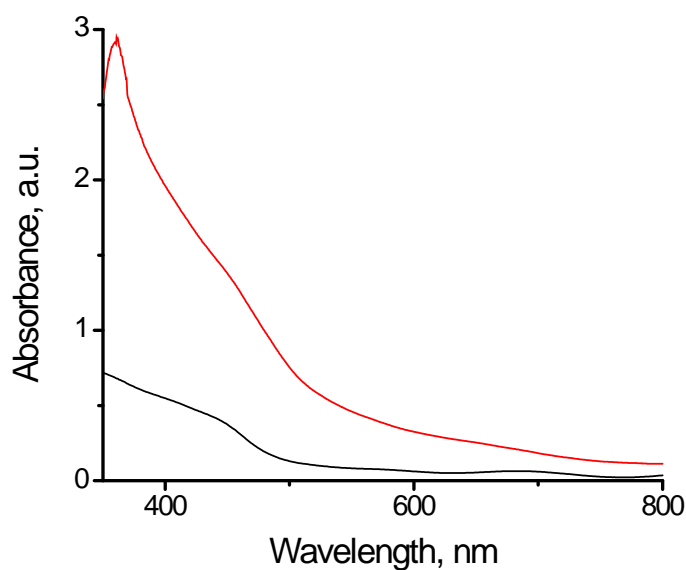


**Figure 3.47:** UV-vis absorption spectra of CdS film (125 nm) electrodeposited on FTO electrode (black line) and CdS film electrodeposited on porous TiO<sub>2</sub> surface using equivalent current density and deposition time (red line).

Overall, we have demonstrated the applicability of the developed method for electrodeposition of CdS on the surface of maleic anhydride, Ti, Al, Au, PEDOT and high surface area TiO<sub>2</sub>.

As was mentioned in the introduction, one of the ways to modify electric properties (*e.g.* the band gap energy) of materials is based on varying concentration of specific atoms

in the bulk of the “host” crystal. Thus, it is important to develop the means, by which solid solutions of different elemental composition can be effectively prepared. This is discussed in the next section.

### 3.4.8. Towards mixed metal sulfides

Chemical bath deposition is one of the most common methods for synthesis of metal sulfide semiconductors. The deposition is based on a slow release of anions in the solution as a product of hydrolysis of the precipitating agent in the alkaline solution (*e.g.* thiourea or thioacetamide for  $S^{2-}$  ions). Thus, for this method formation of complex ions between the metal and the ligand is the key factor in the reaction control. This prevents immediate precipitation of the metal ions in the solution when the precipitating anions are added to it and also avoids formation of insoluble metal hydroxides.<sup>[14]</sup> The task of establishing specific conditions (*e.g.* complex ions, temperature, pH *etc.*) at which good quality metal sulfide films can be chemically bath deposited is very challenging. It becomes even harder when mixed metal sulfides are to be deposited by this method.

The results presented in Section 3.4.2. show that films electrodeposited from ILs have superior properties to CBD films. The use of sodium thiosulfate as a sulfide precursor for electrochemical deposition of metal sulfides allows to lower the deposition potential compared to the use of molecular sulfur as a sulfide precursor. It becomes possible in principle then to synthesize mixed metal sulfides of elements, whose reduction potentials are lower than that of thiosulfate.

#### FeS and In<sub>2</sub>S<sub>3</sub>

Iron (II) and indium (III) sulfides are important materials in the solar cell technology.<sup>[55-57]</sup> For an attempt to electrodeposit these semiconductors from [P<sub>1444</sub>][Tosylate] at elevated temperatures 0.01 M FeCl<sub>2</sub> and InCl<sub>3</sub> were used as a source of metal cations. The chronopotentiometry plots of electrolytes containing Fe(II) and In(III) are shown in Figure 3.48. Absence of films on the surface of the FTO electrode suggest that the method developed for electrodeposition of CdS needs to be modified in order to allow for electrodeposition of FeS and In<sub>2</sub>S<sub>3</sub>. This will be further investigated in the future research.

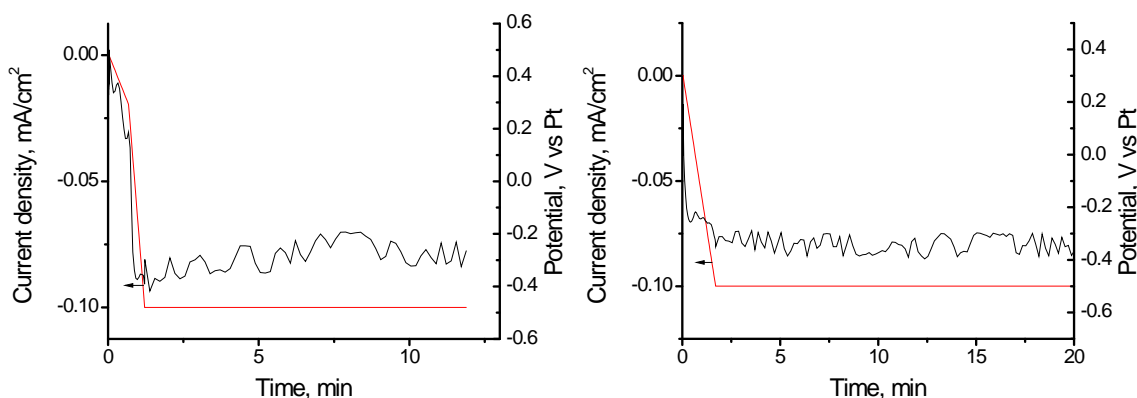


**Figure 3.48:** Typical chronopotentiometry plot during electrodeposition of FeS (left) and  $\text{In}_2\text{S}_3$  (right) at  $140\text{ }^\circ\text{C}$ .

### $\text{Cd}_x\text{Zn}_{1-x}\text{S}$

It is known that the band gap energy of CdS can be increased in the mixed  $\text{Cd}_x\text{Zn}_{1-x}\text{S}$  alloys.<sup>[56]</sup> Zn(II) has a reduction potential of  $-0.76\text{ V vs NHE}$ ,<sup>[42]</sup> which is low enough that the reduction of the thiosulfate ion can take place without deposition of Zn. Hence, it is clearly a good candidate for this technique. A set of films was electrodeposited using the method developed in Section 3.4.2. by varying a concentration of metal cations in the electrolyte as follows:  $x \cdot 0.01\text{ M}$  of  $\text{CdCl}_2$  and  $(1-x) \cdot 0.01\text{ M}$   $\text{ZnCl}_2$ , where  $x = 0, 20, 40, 60,$  and  $80\%$ . The chronopotentiometry plots of the electrolytes containing Cd(II) and Zn(II) are shown in Figure 3.49. It can be seen that the reduction in various concentration of Cd(II) leads to an increase in the deposition potential, reaching a maximum in the electrolyte containing only Zn(II).

UV-vis absorption spectra of the prepared films are shown in Figure 3.50. The band gap energy of ZnS is  $3.2\text{ eV}$ , compared to  $2.4\text{ eV}$  in CdS,<sup>[57]</sup> hence we can expect the band gap energy of the  $\text{Cd}_x\text{Zn}_{(1-x)}\text{S}$  films to gradually increase up to  $3.2\text{ eV}$  with an increase in the amount of Zn(II) present in the electrolyte. The values of the band gap energies calculated from UV-vis spectra (see the inset to Figure 3.50) increase steadily as expected, but only over a limited range. This suggests that the incorporation of Zn takes place at a rate which is only a fraction of its bulk solution value, perhaps because of the mass transport or electrochemical kinetic limitations. Nonetheless, the method successfully produces  $\text{Cd}_x\text{Zn}_{(1-x)}\text{S}$  films, demonstrating the potential of this process.

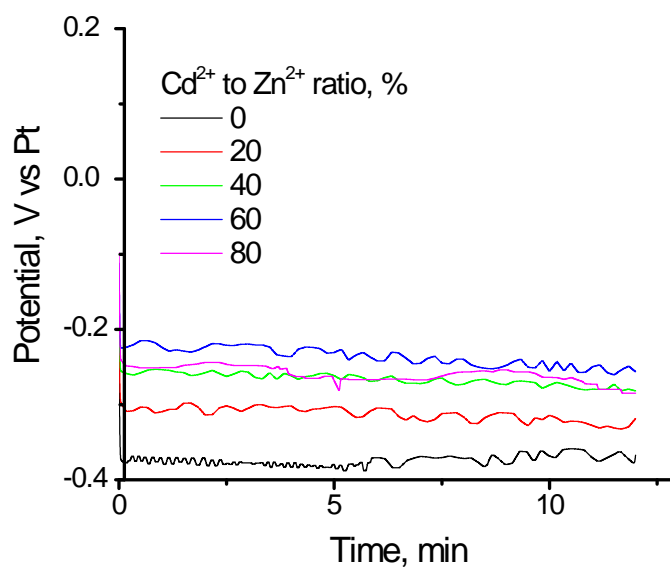


**Figure 3.49:** Typical chronopotentiometry plot during electrodeposition of  $\text{Cd}_x\text{Zn}_{(1-x)}\text{S}$  at  $140\text{ }^\circ\text{C}$ .

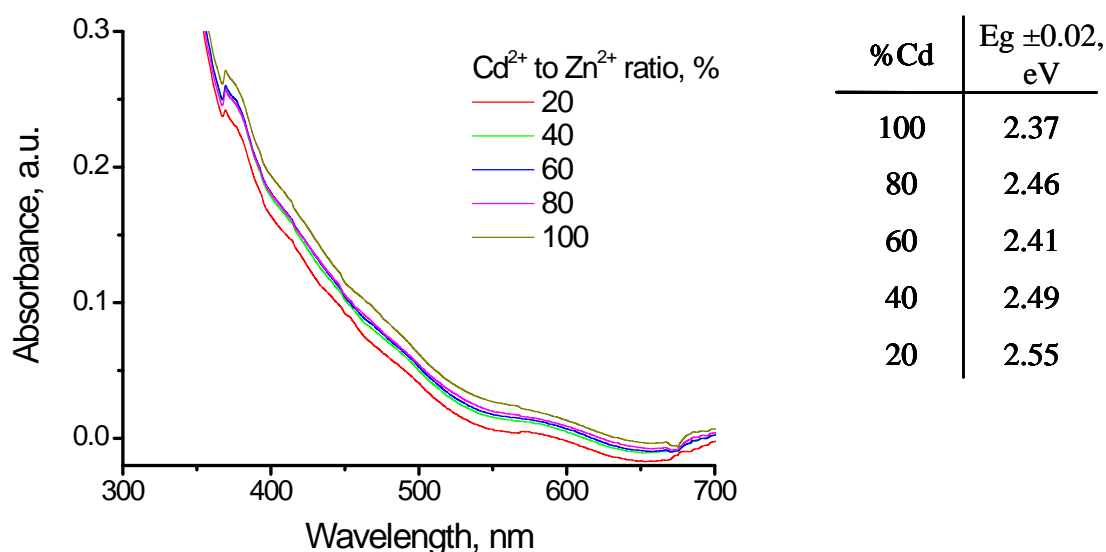


**Figure 3.50:** UV-vis absorption spectra of  $\text{Cd}_x\text{Zn}_{(1-x)}\text{S}$  films.

### $\text{Cd}_x\text{Ni}_{1-x}\text{S}$

$\text{Cd}_x\text{Ni}_{1-x}\text{S}$  is of interest as a light harvesting semiconductor as it has a reduced band gap energy compared to that of pure CdS as a result of the NiS incorporation. Ni(II) has the reduction potential of  $-0.25\text{ V vs NHE}$ ,<sup>[42]</sup> which is low enough that the reduction of the thiosulfate ion can take place without the deposition of metal Ni. Hence, in this section the potential for the electrodeposition of this material is investigated.

As a preliminary work, the electrodeposition of NiS was attempted by the method developed in section 3.4.2. with  $\text{NiCl}_2$  used as a source of metal cations. The chronopotentiometry plot of electrolyte containing Ni(II) is shown in Figure 3.51 results in the formation of black deposits on the FTO surface. Analysis of the films using SEM and EDX measurements of thick films confirms presence of Ni and S in the structure as can be seen in Figure 3.52.

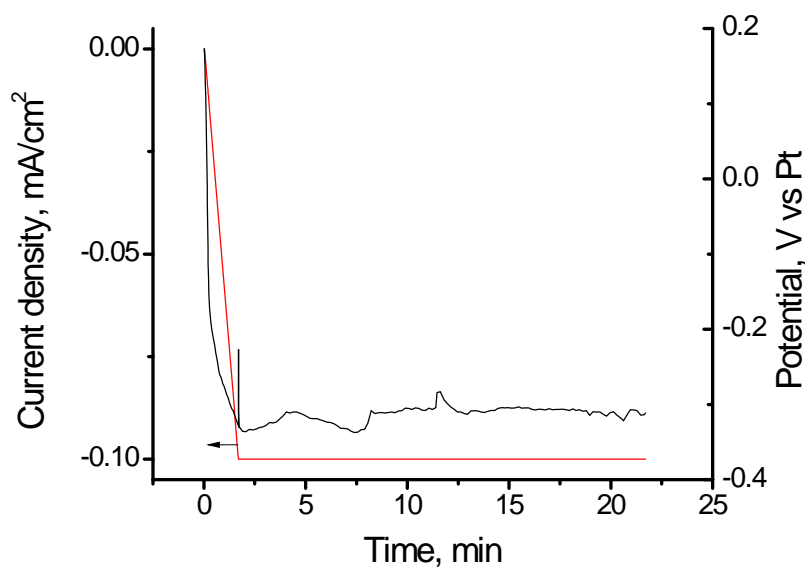


**Figure 3.51:** Typical chronopotentiometry plot during electrodeposition of NiS at 140 °C.

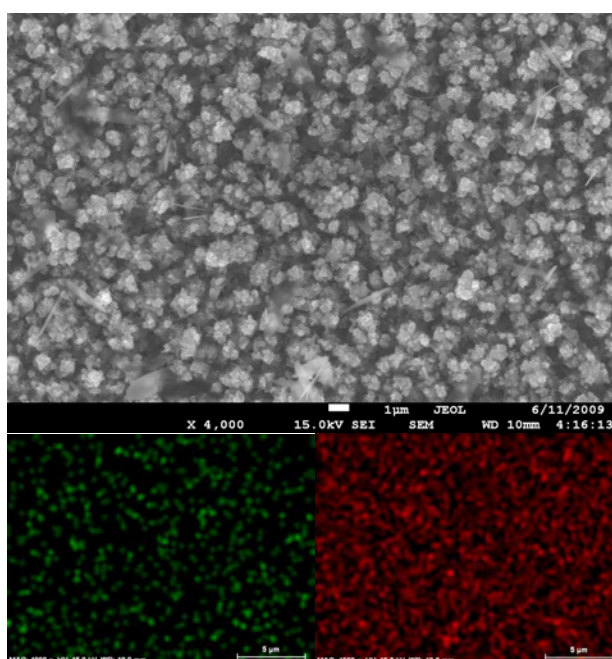


**Figure 3.52:** SEM image of NiS film (several  $\mu\text{m}$  thick) electrodeposited on plasma treated FTO (top); elemental mapping for Ni as green and S as red produced from EDX analysis (bottom).

In order to electrodeposit  $\text{CdNiS}_2$  equal amounts (0.005 M) of Cd(II) and Ni(II) were used in the electrolyte. The band gaps of NiS and  $\text{NiS}_2$  are 0.4 eV and 0.3 eV,<sup>[57]</sup> respectively, which makes electrodeposited NiS films appear as black deposits on a substrate. In combination with cadmium sulfide ( $\text{Cd}_x\text{Ni}_{1-x}\text{S}_y$ ), however, the color of the films is modified to reflect specific absorption from both materials as can be seen in Figure 3.53.

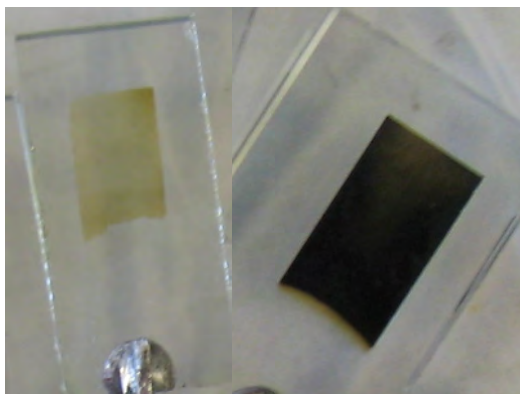


**Figure 3.53:** Optical images of <50 nm (left) and >200 nm (right)  $\text{Cd}_x\text{Ni}_{1-x}\text{S}_y$  films deposited on the plasma treated FTO.

A typical UV-vis spectrum of electrodeposited thin films of  $\text{Cd}_x\text{Ni}_{1-x}\text{S}_y$  is shown in Figure 3.54. The absorbance of  $\text{Cd}_x\text{Ni}_{1-x}\text{S}_y$  sample was recorded in the region between 350 and 800 nm due to the limitation of the UV-vis spectrometer. The absorption in the infrared region in this case is due to the presence of NiS, while characteristic absorption of CdS can be seen in the blue-green region.

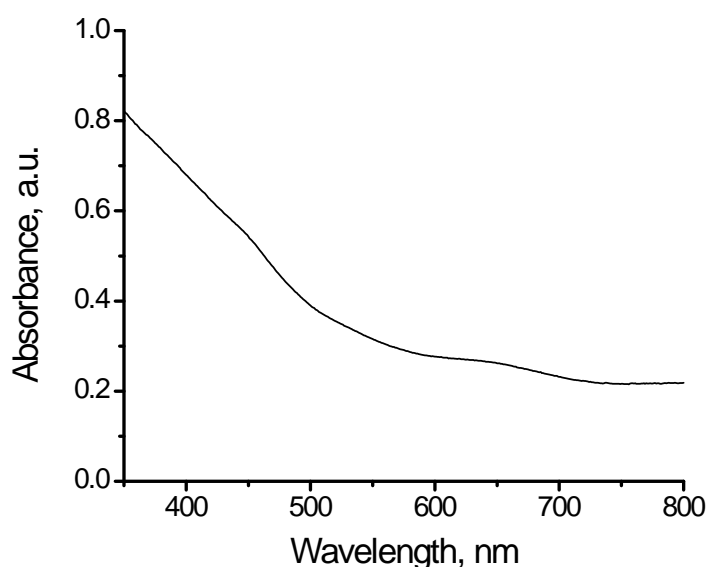


**Figure 3.54:** UV-vis absorption spectra of electrodeposited  $\text{Cd}_x\text{Ni}_{1-x}\text{S}_y$  thin films

The data from the UV-vis absorption spectrum presented in Figure 3.54 was used to construct the  $(\alpha h\nu)^2$  versus  $h\nu$  plot shown in Figure 3.55. It can be seen that the band gap energy calculated from the absorbance in the blue-green region, typical to CdS, is  $2.35 \pm 0.02$  eV. The value of band energy is reduced compared to the band gap energy of CdS of 2.42 eV, which may be due to the presence of nickel in the structure. The additional energy, which can be calculated from the graph corresponds to  $1.48 \pm 0.02$  eV and may be related to the  $\text{Cd}_x\text{Ni}_{1-x}\text{S}_y$  present in the sample. Further characterization of this material is needed to establish its electronic structure and photochemical properties in relation to its chemical composition.

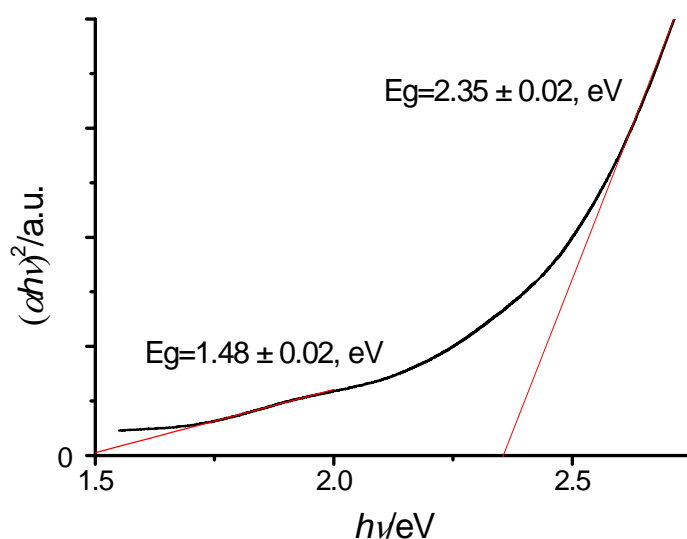


**Figure 3.55:**  $(\alpha h\nu)^2$  versus  $h\nu$  plot derived from UV-vis spectra.

Overall, it appears that this method can indeed successfully produce mixed metal sulfides of importance such as  $\text{Cd}_x\text{Ni}_{1-x}\text{S}_y$ .

### 3.5. Conclusions

Using the  $[\text{P}_{1444}][\text{Tosylate}]$  ionic liquid it was found that electrodeposition of CdS was possible from thiosulfate and Cd(II) containing electrolyte resulting in the formation of high quality films. By optimizing the condition of the synthesis, it was possible to electrodeposit CdS films with almost stoichiometric ratio between Cd and S that does not contain big precipitates common for the CBD method. The fact that no Cl signal can be detected in the present work suggests that the technique can be used to prepare Cl free films, which, in turn, may enhance electrical properties of CdS films. The XRD data suggest that this method can be successfully used to deposit materials with the specific

orientation. Analysis of XRD spectra leads to conclusion that polycrystalline films formed during the deposition are composed of nanocrystals similar in size compared to those prepared *via* CVD. The Mott-Schottky analysis of CdS films confirms typical trends seen in n-type semiconductors and the value of the flat band potential is as expected for CdS, while the band gap energy measured *via* UV-vis spectroscopy is in accord with the data reported in the literature. Typical quantum size effects were also observed in ultra thin films (<10nm) resulting in an increase in the band gap energy. It was observed that annealing of CdS films at high temperatures leads to reduction in the value of the band gap energy. No deterioration due to the presence of Cd(OH)<sub>2</sub> and water, which is otherwise seen in the literature, was observed in samples prepared in this work. For the films deposited from ILs, the values of attenuation coefficients, which are important when the thicknesses of materials structures are to be analyzed, were calculated for the wavelength from 350 to 800 nm.

In this work the applicability of the developed method was demonstrated for electrodeposition of CdS on substrates including maleic anhydride/FTO, Ti, Al, Au, high surface area TiO<sub>2</sub>, and PEDOT. Even short time of the deposition on porous TiO<sub>2</sub> produces CdS films of exceptional absorbance. Thus, it becomes possible to combine the high absorption of porous structures with the low recombination coefficients observed for thin films.

In this work the electrodeposition of NiS was also demonstrated under the conditions similar to the ones used for CdS deposition. Additionally we were also able to deposit mixed Ni and Cd sulfide by the technique developed in this work. Mixed metal sulfides of Cd with Zn and Cd with Ni were successfully deposited demonstrating the potential of the developed electrodeposition method to tune the band gap of the resulting material. Further work on optimizing properties of these materials is needed.

## References

- [1] O. Savadogo, *Sol. Energy Mater. Sol. Cells* **1998**, 52, 361-388.
- [2] P. J. Sebastian, R. Castaneda, L. Ixtlilco, R. Mejia, J. Pantoja and A. Olea, *P. Soc. Photo-Opt. Ins.* **2008**, 7044, 4405-4405.
- [3] P. O. Anikeeva, J. E. Halpert, M. G. Bawendi and V. Bulovic, *Nano Lett.* **2007**, 7, 2196-2200.
- [4] M. Tsuji, T. Aramoto, H. Ohyama, T. Hibino and K. Omura, *J. Cryst. Growth* **2000**, 214, 1142-1147.
- [5] L. P. Colletti, B. H. Flowers and J. L. Stickney, *J. Electrochem. Soc.* **1998**, 145, 1442-1449.
- [6] D. B. Fraser and H. Melchior, *J. Appl. Phys.* **1972**, 43, 3120-3127.
- [7] M. C. Baykul and A. Balcioglu, *Microelectron. Eng.* **2000**, 51-2, 703-713.
- [8] M. Ichimura, F. Goto and E. Arai, *J. Appl. Phys.* **1999**, 85, 7411-7417.
- [9] K. Senthil, D. Mangalaraj and S. K. Narayandass, *Appl. Surf. Sci.* **2001**, 169, 476-479.
- [10] U. Pal, R. SilvaGonzalez, G. MartinezMontes, M. GraciaJimenez, M. A. Vidal and S. Torres, *Thin Solid Films* **1997**, 305, 345-350.
- [11] D. Barreca, A. Gasparotto, C. Maragno and E. Tondello, *J. Electrochem. Soc.* **2004**, 151, G428-G435.
- [12] M. Innocenti, S. Cattarin, F. Loglio, T. Cecconi, G. Seravalli and M. L. Foresti, *Electrochim. Acta* **2004**, 49, 1327-1337.
- [13] R. Ortigaborges and D. Lincot, *J. Electrochem. Soc.* **1993**, 140, 3464-3473.
- [14] F. A. Cotton, G. Wilkinson, C. A. Murillo and M. Bochmann, *Advanced Inorganic Chemistry*, John Wiley & Sons, **1999**, pp. 1488.
- [15] W. H. R. Shaw and D. G. Walker, *J. Am. Chem. Soc.* **1956**, 78, 5769-5772.
- [16] A. Cortes, H. Gomez, R. E. Marotti, G. Riveros and E. A. Dalchiele, *Sol. Energy Mater. Sol. Cells* **2004**, 82, 21-34.
- [17] M. B. Ortuno-Lopez, M. Sotelo-Lerma, A. Mendoza-Galvan and R. Ramirez-Bon, *Thin Solid Films* **2004**, 457, 278-284.
- [18] I. Sisman, M. Alanyalioglu and U. Demir, *J. Phys. Chem. C* **2007**, 111, 2670-2674.
- [19] J. Nishino, S. Chatani, Y. Uotani and Y. Nosaka, *J. Electroanal. Chem.* **1999**, 473, 217-222.

- [20] K. Premaratne, S. N. Akuranthilaka, I. M. Dharmadasa and A. P. Samantilleka, *Renew. Energy* **2003**, 29, 549-557.
- [21] P. J. Dale, A. P. Samantilleke, D. D. Shivagan and L. M. Peter, *Thin Solid Films* **2007**, 515, 5751-5754.
- [22] H. Metin and R. Esen, *Semicond. Sci. Tech.* **2003**, 18, 647-654.
- [23] F. Endres and S. Z. El Abedin, *Phys. Chem. Chem. Phys.* **2006**, 8, 2101-2116.
- [24] F. Endres, D. MacFarlane and A. Abbott, *Electrodeposition from ionic liquids*, Wiley-VCH, Weinheim, **2008**, pp. 387.
- [25] W. Lu, A. G. Fadeev, B. H. Qi, E. Smela, B. R. Mattes, J. Ding, G. M. Spinks, J. Mazurkiewicz, D. Z. Zhou, G. G. Wallace, D. R. MacFarlane, S. A. Forsyth and M. Forsyth, *Science* **2002**, 297, 983-987.
- [26] O. Mann, G. B. Pan and W. Freyland, *Electrochim. Acta* **2009**, 54, 2487-2490.
- [27] S. Z. El Abedin, A. Y. Saad, H. K. Farag, N. Borisenko, Q. X. Liu and F. Endres, *Electrochim. Acta* **2007**, 52, 2746-2754.
- [28] D. D. Shivagan, P. J. Dale, A. P. Samantilleke and L. M. Peter, *Thin Solid Films* **2007**, 515, 5899-5903.
- [29] S. Z. El Abedin and F. Endres, *ChemPhysChem* **2006**, 7, 58-61.
- [30] M. Rami, E. Benamar, M. Fahoume and A. Ennaoui, *Phys. Status Solidi A-Appl. Res.* **1999**, 172, 137-147.
- [31] J. F. Wager, *Thin Solid Films* **2008**, 516, 1755-1764.
- [32] W. Mönch, *Semiconductor Surfaces and Interfaces*, Springer, **2001**, pp. 500.
- [33] T. V. Blank and Y. A. Gol'dberg, *Semiconductors* **2007**, 41, 1263-1292.
- [34] D. R. Vij, *Handbook of Electroluminescent Materials*, Taylor & Francis, **2004**, p. 159.
- [35] Z. Ademovic, J. Wei, B. Winther-Jensen, X. L. Hou and P. Kingshott, *Plasma Process. Polym.* **2005**, 2, 53-63.
- [36] T. Trindade, P. O'Brien and N. L. Pickett, *Chem. Mat.* **2001**, 13, 3843-3858.
- [37] Y. Wang and N. Herron, *J. Phys. Chem.* **1991**, 95, 525-532.
- [38] I. Vurgaftman, J. R. Meyer and L. R. Ram-Mohan, *J. Appl. Phys.* **2001**, 89, 5815-5875.
- [39] S. F. Fang, K. Adomi, S. Iyer, H. Morkoc, H. Zabel, C. Choi and N. Otsuka, *J. Appl. Phys.* **1990**, 68, R31-R58.
- [40] J. L. A. Alves, J. Hebenstreit and M. Scheffler, *Phys. Rev. B* **1991**, 44, 6188-6198.

- [41] B. Winther-Jensen, K. Fraser, C. Ong, M. Forsyth and D. R. MacFarlane, *Adv. Mater.* **2010**, *22*, 1727-1730.
- [42] D. Lide, *CRC Handbook of Chemistry and Physics*, CRC, **2007**, pp. 2640.
- [43] D. X. Zhuang, M. J. Deng, P. Y. Chen and I. W. Sun, *J. Electrochem. Soc.* **2008**, *155*, D575-D579.
- [44] M. J. Deng, P. Y. Chen, T. I. Leong, I. W. Sun, J. K. Chang and W. T. Tsai, *Electrochem. Commun.* **2008**, *10*, 213-216.
- [45] M. Pourbaix and J. Burbank, *J. Electrochem. Soc.* **1964**, *111*, 14C-15C.
- [46] *Encyclopedia of electrochemistry*, Weinheim; Cambridge: Wiley-VCH, **2001-2007**, pp. 7720.
- [47] P. K. Nair, O. G. Daza, A. A. C. Readigos, J. Campos and M. T. S. Nair, *Semicond. Sci. Tech.* **2001**, *16*, 651-656.
- [48] B. D. Cullity, *Elements of X-ray Diffraction*, Addison-Wesley, **1978**, pp. 664.
- [49] M. E. Ozsan, D. R. Johnson, M. Sadeghi, D. Sivapathasundaram, G. Goodlet, M. J. Furlong, L. M. Peter and A. A. Shingleton, *J. Mater. Sci.-Mater. Electron.* **1996**, *7*, 119-125.
- [50] T. Watanabe, Fujishim.A and K. I. Honda, *Chem. Lett.* **1974**, 897-900.
- [51] N. B. Chaure, S. Chaure and R. K. Pandey, *Sol. Energy Mater. Sol. Cells* **2004**, *81*, 39-60.
- [52] M. Z. Huang and W. Y. Ching, *Phys. Rev. B* **1993**, *47*, 9449-9463.
- [53] S. Adachi, *Handbook on physical properties of semiconductors*, Boston : Kluwer Academic Publishers, **2004**, pp. 1431.
- [54] D. J. Kim, Y. M. Yu, J. W. Lee and Y. D. Choi, *Appl. Surf. Sci.* **2008**, *254*, 7522-7526.
- [55] B. Oregan and M. Gratzel, *Nature* **1991**, *353*, 737-740.
- [56] X. Zhong, Y. Feng, W. Knoll and M. Han, *J. Am. Chem. Soc.* **2003**, *125*, 13559-13563.
- [57] Y. Xu and M. A. A. Schoonen, *Am. Miner.* **2000**, *85*, 543-556.

## Chapter 4

# Photo-electrochemical water splitting

### Chapter overview

A state-of-the-art PEC water splitting cell has 12.4% efficiency under the visible light irradiation and combines several semiconducting materials in a monolithic device.<sup>[1]</sup> Although efficient, this cell is able to split water only for a few days, making the possibility of commercial application daunting.

In this chapter we introduce a PEC cell structure, where the light harvester is separated from the electrooxidation and reduction processes that occur in the water splitting cell. The increase in stability of the light harvesting semiconductor in cells of this type is demonstrated for the example of a metal sulfide (*e.g.* CdS), which is one of the most efficient yet unstable semiconducting materials used in PEC cells. In principle, the structure should enhance the lifetime of any photo-sensitive semiconductor.

### **4.1. Introduction**

In photo-electrolysis, the energy of photons that can be gathered from the sun light is converted into the chemical energy. Some basic examples include decomposition of water into hydrogen and oxygen and reduction of carbon dioxide to form methanol.<sup>[2, 3]</sup> Photo-induced electrochemical reactions take place at the semiconductor-electrolyte interface, a characteristic that has great impact on the efficiency and stability of the PEC cell.

#### **4.1.1. Semiconductor electrolyte interface**

When a semiconductor is in contact with an electrolyte under equilibrium conditions the electrochemical potentials of electrons in both phases must be equal. For

liquid electrolytes the electrochemical potential is determined by the redox potential of the redox couple present in the electrolyte.<sup>[2]</sup>

When the Fermi energy in the semiconductor is higher than that in the electrolyte (e.g. in CdS vs water) excess electrons move from the conduction band of the semiconductor into the electrolyte and the uncompensated positive charge left behind creates a space charge layer inside the semiconductor. The conduction and valence band edges become bent, so that an electrical barrier is established against further charge transfer Figure 4.1.

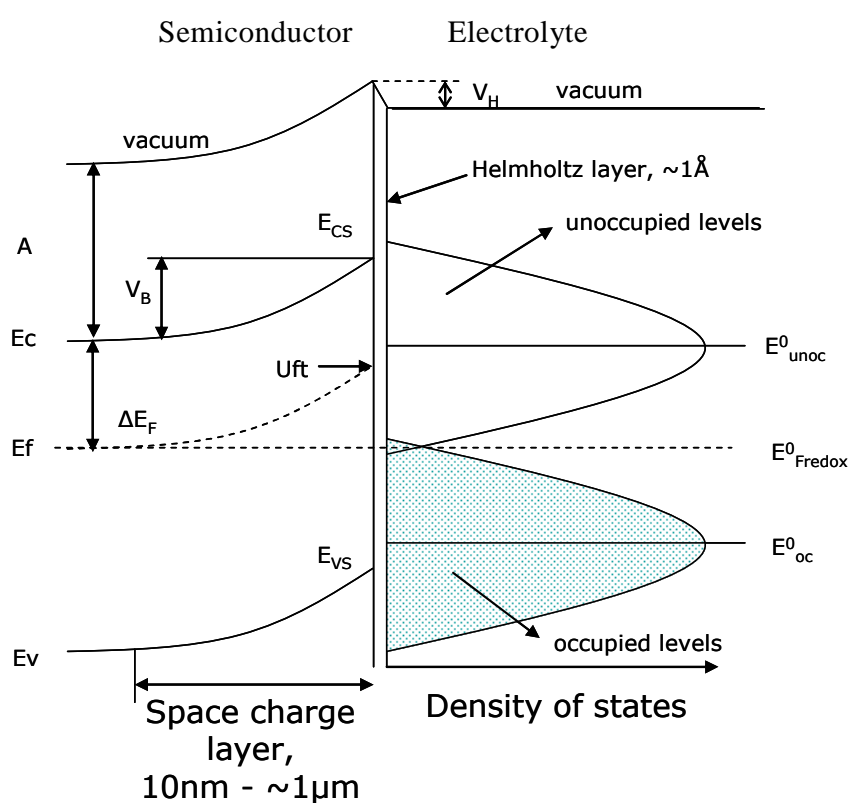


**Figure 4.1:** Energy level diagram of the semiconductor electrolyte interface, where  $V_H$  is the potential drop across the Helmholtz layer,  $E_C$  and  $E_V$  are conduction and valence band edges,  $E_F$  is the Fermi level,  $E_{CS}$  and  $E_{VS}$  are conduction and valence band edges at the surface,  $U_{ft}$  is flat band potential,  $V_B$  is band bending,  $A$  is electron affinity,  $E_{\text{Fredox}}^0$  is the standard Fermi level of the redox couple;  $E_{\text{unoc}}^0$  and  $E_{\text{oc}}^0$  are energies of unoccupied and occupied states of the redox couple.<sup>[2]</sup>

The charged layer is formed by absorption of the charged ions from the electrolyte and is called the Helmholtz layer. These ions are mostly of the opposite charge to the charge induced in the semiconductor electrode, while the width of the layer is in the order of angstroms. Presence of the Helmholtz layer significantly affects the band bending.

Without such an interference the band bending (following an ideal model) could be calculated as a difference between the Fermi levels in the electrolyte and semiconductor.<sup>[2]</sup>

One of the most important characteristics of the semiconductor electrolyte interface that determines the cell efficiency is the width of the depletion layer, which extends into the semiconductor. The width of the depletion layer determines the region of the semiconductor, in which the electron-hole pair can be effectively separated. For a specific semiconductor, the thickness of the depletion layer can be calculated from Equation 4.1.<sup>[2]</sup> An increase in light absorption of the semiconductor of thickness exceeding that of the depletion layer does not result in a proportional increase in cell efficiency. In contrast, it is expected that efficiency of such a cell will be reduced, due to the higher recombination rates in the bulk of semiconductor.

$$w = \left( \frac{2\epsilon\epsilon_0 V_B}{qN} \right)^{\frac{1}{2}} \quad (4.1)$$

Here  $w$  is the thickness of space charge layer,  $V_B$  is amount of band bending,  $N$  is charge carrier density and  $\epsilon$  is dielectric constant of the semiconductor.

Based on the data for CdS which has flat band potential of -0.658 V vs NHE measured at pH = 14, assuming values of  $\epsilon=8.5$  and  $N=9.87 \cdot 10^{16}$  1/cm<sup>3</sup> as previously reported for CdS, one can estimate that the depletion layer thickness is 64 nm. Thus, in this work thin films of CdS (about 100 nm maximum) are used in PEC cell.

In order to be stable in the PEC cell structure, the light harvesting semiconductor (LHS) should meet following requirements:

- The redox potential of the oxidative decomposition reaction of the semiconductor has a more positive value (the NHE scale) than the valence band edge.
- The redox potential of the reductive decomposition reaction has a more negative value (the NHE scale) than the conduction band edge.

Typically, one or both of the redox potentials of the semiconductor decomposition reactions lies within the band gap and hence, becomes thermodynamically possible. The

examples in Figure 4.2 demonstrate relative positions of oxidative decomposition for  $\text{TiO}_2$ , CdS and water. In summary, the potential of the oxidative decomposition of  $\text{TiO}_2$  is much higher than that of water, thus making the water oxidation more thermodynamically favorable. On the other hand for CdS, oxidative decomposition of the semiconductor is thermodynamically favorable, which leads to electrode instability and low lifetime unless a sacrificial electron donor is present in the electrolyte (*e.g.*  $\text{S}^{2-}/\text{S}^0$  for metal sulfides).<sup>[4]</sup>

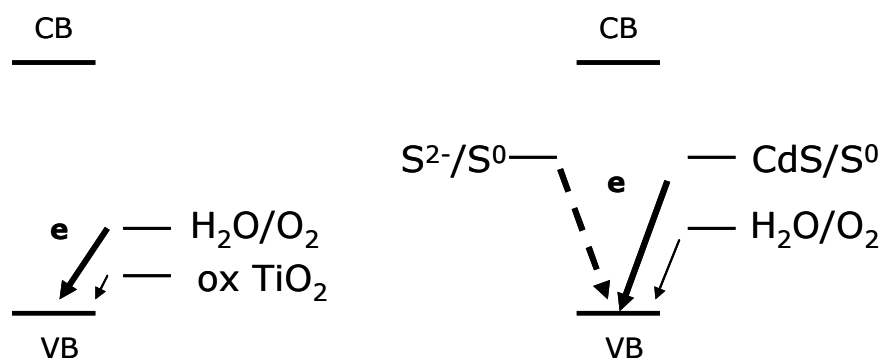


**Figure 4.2:** Energy diagram that represents energy levels of the semiconductor (CB, VB) and relative potentials for oxidative decomposition of  $\text{H}_2\text{O}$ ,  $\text{TiO}_2$  (left), and CdS,  $\text{S}^{2-}$  (right).<sup>[2, 4]</sup>

In order to prevent oxidative decomposition of the semiconductor, its surface has to be isolated from the electrolyte. In the structure proposed in this work, this role is placed upon a thin covering layer, which is catalytically active towards the water oxidation reaction.

#### 4.1.2. Hole conductors and catalysts for water oxidation

It was shown in the literature that combination of a semiconductor and a co-catalyst allows for significant improvement of efficiency of the semiconductor towards water splitting as well as of overall stability.<sup>[5-7]</sup> A co-catalyst (*e.g.* Pt,  $\text{RuO}_2$  *etc.*) being in direct contact with the semiconductor may assist with charge separation, and thus, result in higher efficiency. Moreover, due to the charge transfer, water redox reactions are less likely to occur on the semiconductor-electrolyte interface but rather on the surface of co-catalyst and thus, result in better stability. By separating the light harvester from the electrocatalyst it becomes possible to combine the advantages of high efficiency of the former with the good stability of the latter. It is important to note that in photo-synthesis photo-generated charges are also transferred from the light harvester to the oxygen evolving catalytic site. The catalytic centre that nature chose for water oxidation is composed of a  $\text{Mn}_3\text{CaO}_4$  cluster.<sup>[8]</sup>

It is important to highlight the specific requirements of the hole conducting material for water splitting. In order to provide effective charge separation, an electric barrier should be formed between the light harvesting semiconductor (LHS) and the hole conductor (HC) as shown in Figure 4.3. Thus, the value of the electron work function (Fermi energy) in the HC has to be higher than that in the LHS to create a double layer and hence, a depletion region in the LHS. Holes can be effectively injected into the HC only if the valence band edge of the LHS has a lower energy compared to this in HC. Additionally, the Fermi energy in the HC should be sufficient to drive the water oxidation reaction.

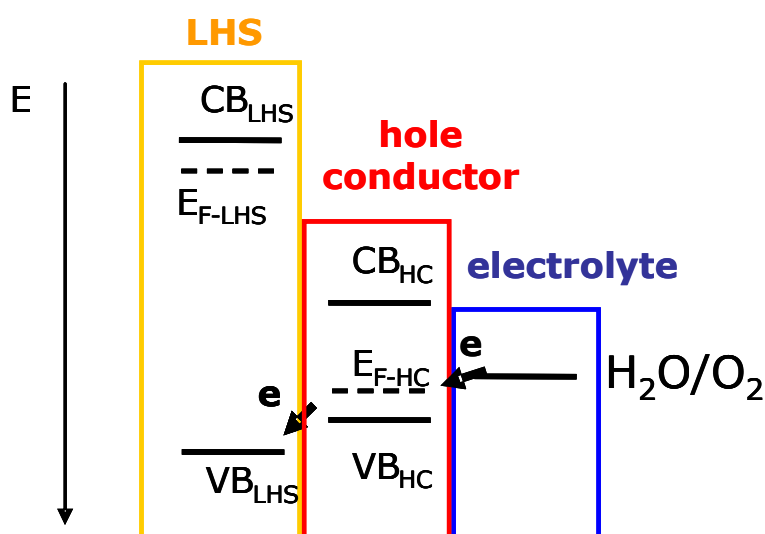


**Figure 4.3:** Relative positions of conduction and valence band edges between light harvesting semiconductor and hole conductor.

A number of materials can be applicable as a HC for the water oxidation reaction. The energy diagrams of MnO<sub>2</sub> and Fe<sub>3</sub>O<sub>4</sub> in relation to CdS and the water oxidation potential at pH = 0 are shown in Figure 4.4. Both materials have the required energy structure to be able to oxidize water, even at pH = 0. MnO<sub>2</sub> was chosen in this work as the hole conductor due to its known catalytic activity towards the water oxidation reaction.<sup>[9-11]</sup>

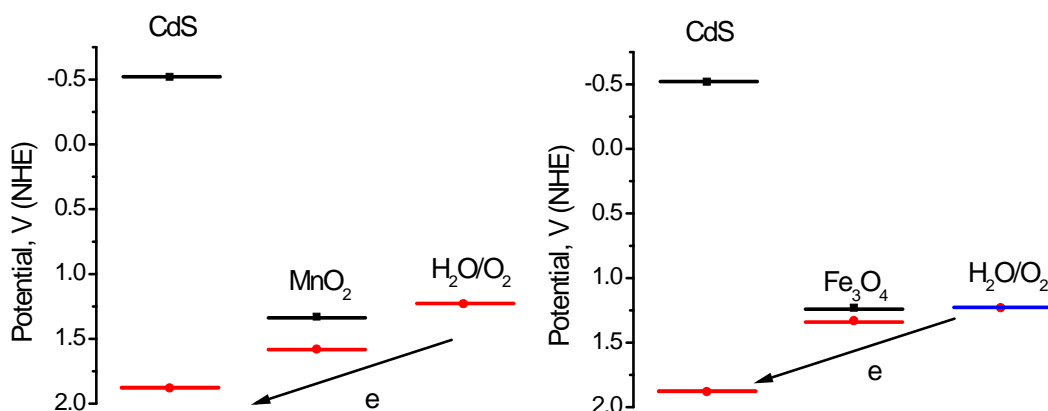


**Figure 4.4:** Energy levels in CdS, MnO<sub>2</sub>, Fe<sub>3</sub>O<sub>4</sub> and their relative position comparing with the water oxidation potential at pH=0. Conduction and valence band edges in semiconductors are shown as black and red lines respectively.

### MnO<sub>2</sub> deposition

Electrodeposition is a promising technique for the deposition of metal oxides. It is fairly simple, has low cost and a high yield of the process. So far, MnO<sub>2</sub> films have been successfully electrodeposited from aqueous electrolytes on different metal substrates such as Ni<sup>[12-14]</sup>, Pt<sup>[10]</sup>, Ti, Si<sup>[15]</sup>, Au<sup>[10]</sup>, FTO<sup>[16]</sup> and graphite<sup>[10, 17]</sup>. The main disadvantages of water based methods, however, are their inability to sustain high deposition temperatures and consequential presence of structural oxygen and water in the deposited films, which, in turn, significantly decreases their quality.<sup>[12]</sup> It was shown, however, that the water content decreases almost linearly with an increase in deposition temperature.<sup>[18]</sup>

The high temperature, at which the deposition in an IL in principle can be conducted, allows for atom diffusion on the surface during growth, which has a major positive influence on the quality of the films.<sup>[19]</sup> Ionic liquids have been successfully used for the electrodeposition of a number of metals such as Se, In, Cu, Mn, Au, Pt and some semiconductors including Ge, Si, TiO<sub>2</sub>, AlSb, ZnSb, InSb, GaAs, CdTe, CuInSe, Cu(In,Ga)Se and ZnTe.<sup>[20-27]</sup> One of the key advantages of ionic liquids in this context is their combination, in some cases, of thermal and electrochemical stability that allows the electrodeposition process to be carried even at elevated temperatures with minimal interference from solvent chemical, or electrochemical, breakdown.<sup>[20-22]</sup>

It has previously been shown that presence of surfactants<sup>[28, 29]</sup> and polyethylenamine<sup>[14]</sup> strongly affects the morphology and crystal growth of MnO<sub>2</sub>. Thus,

by varying the type of ions in an IL and conditions of synthesis, we can promote the growth of metal oxide films with specific morphology.

Various methods can be considered for deposition of multilayered structures. In this work low cost and readily adaptable electrochemical techniques were chosen for deposition of various elements of the proposed PEC cell structure. It is well known that electrodeposition occurs through reduction or oxidation of some chemical precursors which requires a continuous charge transfer between various elements of the cell. Thus, it is essential to consider the energy diagram of the proposed system in detail. When the LHS and HC are placed in contact, a heterojunction is formed between the two types of semiconductors. In order to create such a junction the type of major charge carriers can be the same in both materials. The general principles involved in the formation of such barriers are similar to these in metal semiconductor junctions.

In the ideal model, the difference in Fermi levels between two materials causes formation of a macroscopic dipole across the interface<sup>[30]</sup> as shown in Figure 4.5. Similar to Schottky barriers, the macroscopic dipole is formed during electron transfer from the material with a lower electron work function (*e.g.* from LHS to HC). However, the negative charge in the HC is located in the interfacial region rather than the interfacial sheet, consequently causing a band bending.<sup>[30]</sup> Positive conduction band discontinuity in this case is the analog of a positive n-type semiconductor barrier.

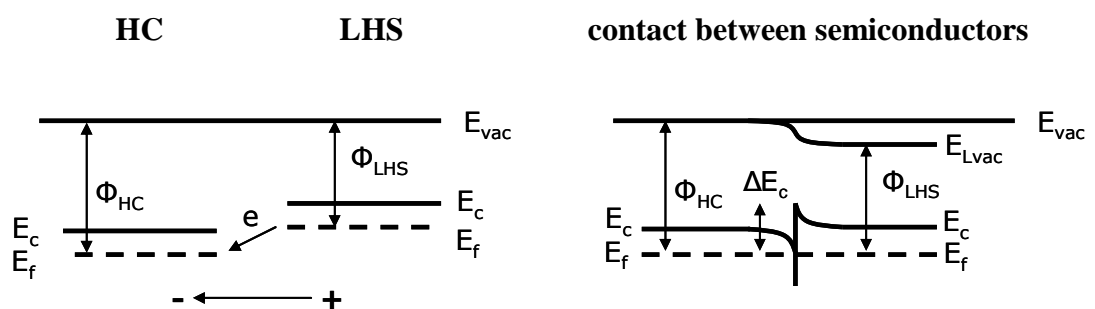


**Figure 4.5:** Energy band diagram of two n-type semiconductors and the heterojunction forming across the interface.

In the non-ideal model of the heterojunction formation however, the direction of charge transfer and the height of the barrier due to the microscopic dipole are determined by the relative positions of the charge neutrality levels in both materials as shown in Figure 4.6. The relative position of these levels can either increase or diminish the height of the formed electric barrier.

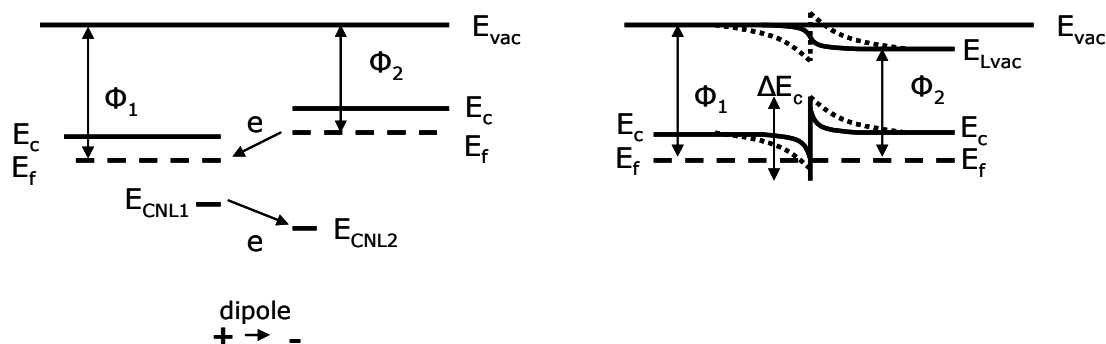


**Figure 4.6:** Energy band diagrams of the heterojunction formation according to non-ideal theory.<sup>[30]</sup>

As can be seen from the energy structure described above, by applying an external potential it becomes possible to move the electron from the LHS to HC but not the other way around. Hence, for an electrochemical deposition technique to be viable, the HC should be formed on the surface of LHS through a reduction process and is therefore not obviously applicable for the proposed PEC configuration. On the other hand, the situation is completely reversed when photo-generated electrons and holes are considered. The electrical junction formed between the LHS and the HC promotes deposition of the HC through the electrochemical oxidation. Thus, photo-driven electrochemical deposition was investigated for the deposition of HC on the surface of LHS.

During water splitting the LHS, fully covered by the layer of water oxidation catalyst, is isolated from the electrolyte and hence, is protected from oxidative decomposition. During operation, however, the difference in thermal expansion coefficients and lattice mismatch between crystal structures of LHS and HC may result in the formation of cracks, which expose the areas of the unprotected semiconductor, leading to oxidative decomposition of LHS. In order to increase stability of the PEC cell, the areas of the unprotected semiconductor should be isolated from the electrolyte with the use of a self-repair agent as discussed further below.

### 4.1.3. Self-repair agents

Several groups of materials were chosen for development of an effective self-repair agent. One of the groups consists of conducting polymers, while another group is based on the oxidative decomposition of various anions. It should be noted, however, that conductivity of the deposits in this case is not essential; the main objective is to deposit dense films with high resistance towards oxidation.

A target structure of our PEC cell is shown in the schematic structure in Figure 4.7. Due to the difference in energy available at the surface of the light absorber and the water oxidation catalyst, it is possible to deposit the self-repair agent on the surface of the LHS rather than the HC. For this selectivity the oxidation potential for deposition of the self-repair agent should exceed the potential available at the surface of the HC and be lower than the potential available at the interface of the LHS.

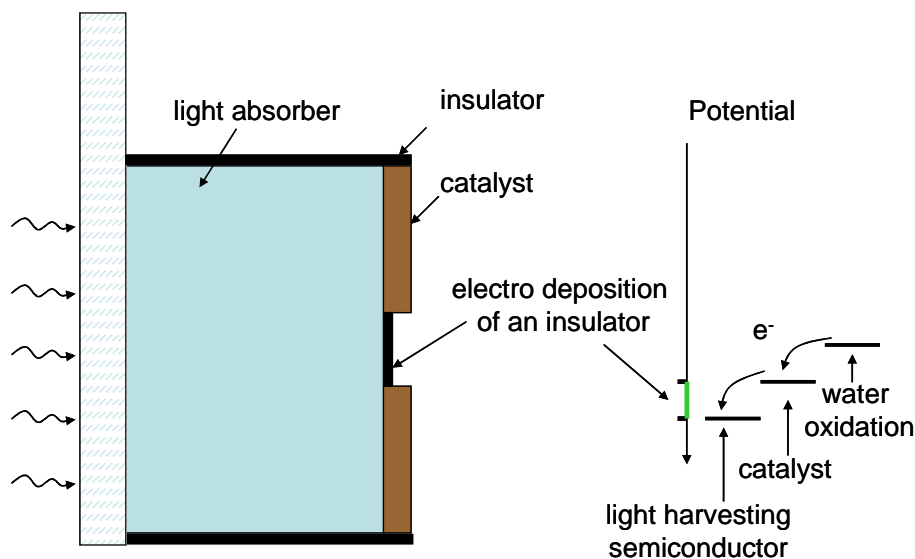


**Figure 4.7:** Electrodeposition of an insulator as a self-repair agent in the water splitting cell.

To determine the required potential for electrodeposition of the self-repair agent, the energy levels in CdS are compared to the valence band edges in  $\text{MnO}_2$  and  $\text{Fe}_3\text{O}_4$ , as well as the water oxidation potential at  $\text{pH} = 0$  in Figure 4.8.

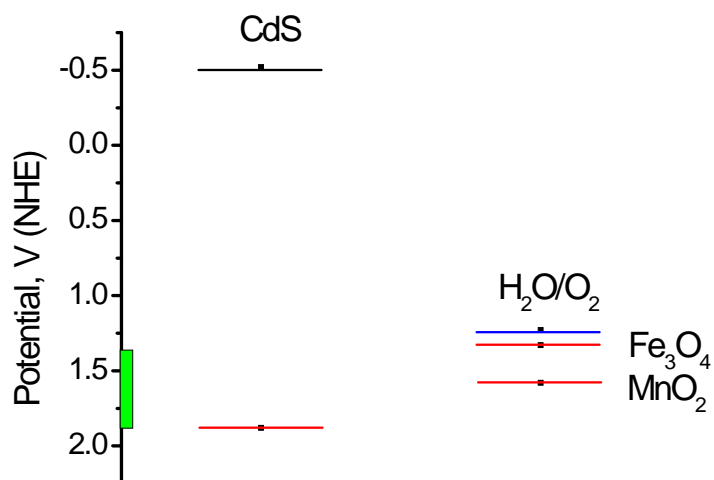


**Figure 4.8:** Energy levels in CdS,  $\text{MnO}_2$ ,  $\text{Fe}_3\text{O}_4$  and their relative position compared with the water oxidation potential at  $\text{pH}=0$ .

The differences in energy between the valence band edges in CdS and those in MnO<sub>2</sub> and Fe<sub>3</sub>O<sub>4</sub> are 0.3 and 0.55 V, respectively. Thus, for CdS the potential of deposition for the insulator should not exceed 1.88 V *vs* NHE and be higher than 1.58 V (for MnO<sub>2</sub>) and 1.33 V (for Fe<sub>3</sub>O<sub>4</sub>) *vs* NHE.

Electrodeposition of conducting polymers from various precursors is well known in the literature.<sup>[31, 32]</sup> For example, the use of electrodeposited PPy films on a metal surface was able to provide a corrosion protection.<sup>[33]</sup> In this work we have examined the electrochemical properties of PPy and PolyBiThiophene (PBTh) in relation to required properties of self-repair agent in PEC cell structure.

Significant interest, in recent years, was given to development of ILs for corrosion protection.<sup>[4-7]</sup> When ILs were originally used as electrolytes for lithium metal electrodes a unique surface film, termed the Solid Electrolyte Interphase (SEI), was formed on the surface of the electrode. This film prevented corrosion of the metal electrode and at the same time allowed for transport of lithium ions.<sup>[34]</sup> Deposition of a surface film with the use of applied potential, in the presence of [P<sub>66614</sub>][DPP], resulted in better protection of magnesium alloys in aggressive chloride solutions.<sup>[35]</sup> Thus, this was also investigated as a self-repair agent in the PEC cell structure.

### **4.2. Aims of this work**

This chapter focuses on development of a novel PEC cell structure, in which the light harvesting semiconductor is separated from the electrooxidation and the reduction processes. The functions of the HC are the chemical protection of the LHS, at the same time as catalysing water oxidation. The former function can be fulfilled with the use of uniform dense films, while the later requires a high surface area electrode. To achieve these properties a multilayer structure is needed. Hence, the specific aims were:

- To develop a technique that is able to produce various structural morphologies of the target HC (MnO<sub>2</sub>) and to produce both the high surface area and compact structures. For this purpose a number of ILs were considered as electrolytes in this work.
- To characterize the physical, chemical and electric properties of the films using cyclic voltammetry, profilometry, impedance spectroscopy, Mott-Schottky

impedance spectroscopy, EDX, SEM, Raman spectroscopy, and UV-vis spectroscopy.

- To ascertain the attenuation coefficient of the formed films using UV-vis spectroscopy.
- To assess catalytic activity and long-term stability towards the water oxidation reaction of the prepared films in neutral and basic electrolytes.
- To deposit HC on the surface of LHS using photo-induced electrochemical deposition from electrolytes and under conditions developed earlier in this section.
- To characterize morphology and chemical composition of the HC films using EDX and SEM techniques, while estimating their thickness using UV-vis absorption spectroscopy.
- To investigate the use of PPy, PBTh, [P<sub>66614</sub>][DCA] and [P<sub>66614</sub>][DPP] as potential self-repair agents in the PEC cell
- To investigate electrochemical oxidation of PPy, PBTh, [P<sub>66614</sub>][DCA] and [P<sub>66614</sub>][DPP] on the surface of FTO.
- To deposit the self-repair agent on the surface of LHS using photo-induced electrochemical deposition from electrolytes and under conditions developed above.
- To characterize the morphology and chemical composition of the films using EDX and SEM techniques.
- To assess overall stability of the PEC cell structure
- To characterize, using UV-vis spectroscopy, corrosion resistance of the PEC cell structure using accelerated conditions.
- To characterize stability of the PEC cell structure during prolonged light irradiation.

### 4.3. Experimental

#### Materials preparation

Ethyl ammonium nitrate for this work was prepared by neutralizing ethyl ammonium hydroxide with a diluted solution of nitric acid and subsequent drying under vacuum to remove water.

FTO (sheet resistance 15 ohm/ ) glass slides were used as a substrate. Before the deposition the surface of the FTO was masked, leaving an active area equal to 0.25cm<sup>2</sup>. Prior to use, the glass slides were sonicated in water solution of the DOBATEC detergent, washed several times with deionized water, and sonicated in ethanol to remove traces of the detergent.

In order to improve the catalytic performance of the FTO electrodes, nanoislands of platinum were deposited through thermal decomposition of hexachloroplatinic acid hexahydrate at 400 °C. In a typical procedure the 10 mM solution in ethanol was doctor bladed on the surface of the FTO with a subsequent heat treatment for 15 minutes using a Leister HOTWINDS hot air blower.

For the deposition of semiconductors used in water splitting experiments, FTO coated glass electrodes with defined surface area were prepared as shown in Figure 4.9. Laser etching was used to electrically isolate the electrode working area with a VersaLaser.

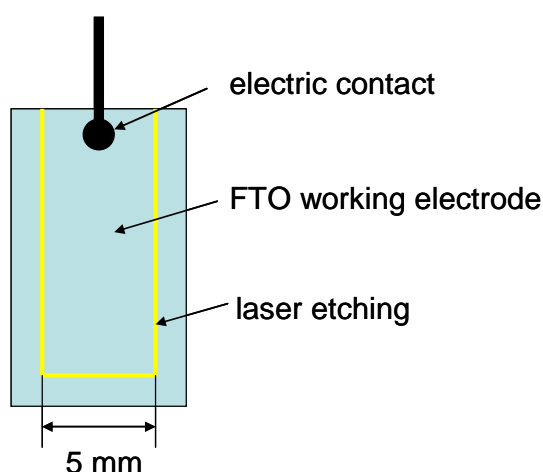


**Figure 4.9:** FTO working electrode for the electrochemical deposition of semiconductors.

For comparison, spray pyrolysis was used to prepare MnO<sub>2</sub> films on the surface of CdS. In a typical experiment formation of the film is based on decomposition of ethanol

based precursor at 450-600 °C. Manganese acetate was chosen as a precursor for the deposition of  $\text{MnO}_2$ .<sup>[36]</sup>

### Electrochemical deposition

Electrochemical deposition was carried out using a VMP-2 multichannel potentiostat with a standard three-electrode configuration using chronoamperometry and chronopotentiometry techniques. The deposition was studied on FTO and Pt electrodes with saturated calomel, 66-EE009 ("No-Leak") Ag/AgCl (Cypress Systems) and Pt wire (pseudo-electrode) used as reference electrodes. The typical setup is shown in Figure 4.10.

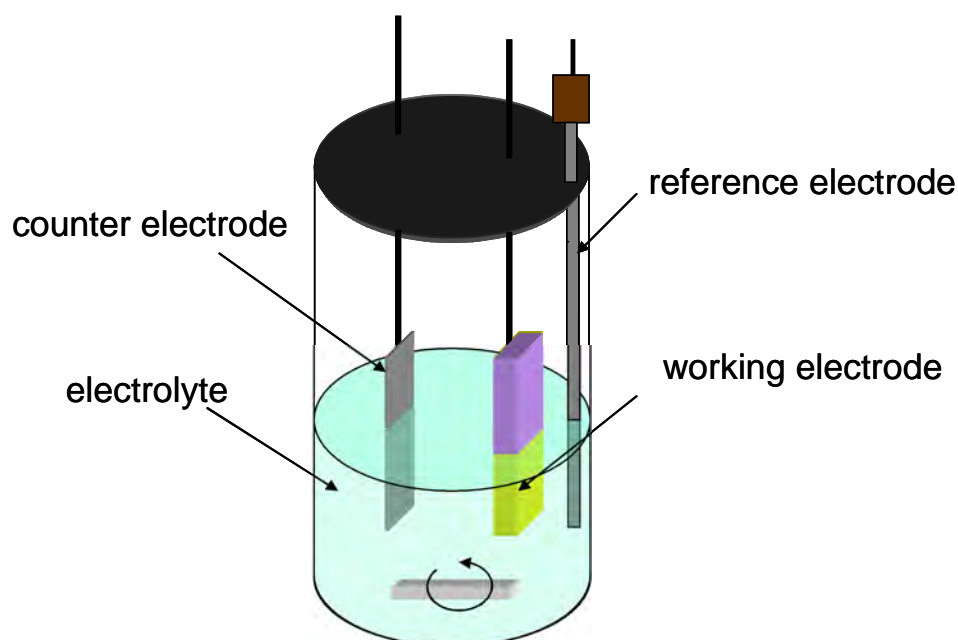


**Figure 4.10:** Electrochemical deposition cell.

For electrodeposition of manganese dioxide, a small amount of water was used to assist with the dissolution of manganese acetate in the ILs. In a typical procedure, an aqueous solution of 0.1 M  $\text{Mn}(\text{Ac})_2$  was added to the EAN and  $\text{P}_{4444}\text{Cl}$ , forming a 0.01 M solution in IL, with 10% (w/w) water in electrolyte.

### Photo-driven electrochemical deposition (PdED)

Thin films of  $\text{MnO}_2$ , polymers and insulators were deposited on the surface of CdS using the setup shown in Figure 4.11. The growth of  $\text{MnO}_2$  was maintained for the period when the photo-current remained higher than 50% of the original value. The PPy films were grown, so that the drop in photo current did not exceed 10-20 %.

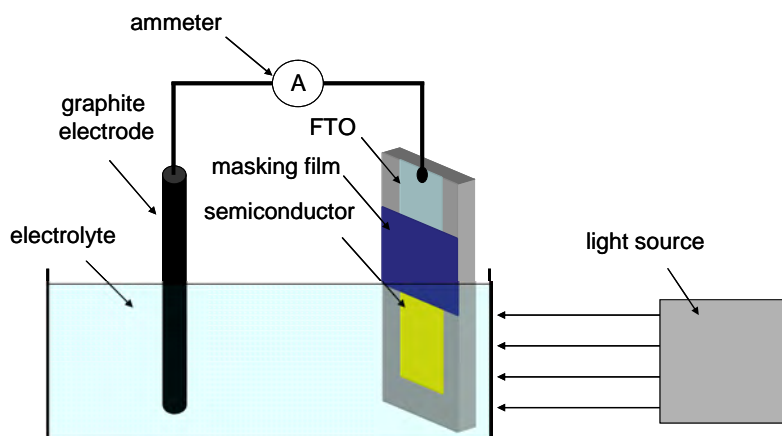


**Figure 4.11:** Schematic representation of the unit for photo-driven deposition of  $\text{MnO}_2$  and polymers and insulators on the surface of CdS.

### Materials characterization

A Dektak 150 surface profiler was used for characterization of the surface roughness as well as thickness of the film. Step height resolution of the instrument ranges from 1000 angstroms to approximately 65 microns.

Samples for SEM measurements were coated with gold or graphite unless stated otherwise. SEM images were obtained on a JEOL 6300F Field Emission Gun Scanning Electron Microscope.

Specific capacity,  $C_s$ , of the  $\text{MnO}_2$  films was calculated using Equation 4.2.<sup>[14]</sup> Where,  $Q$  is half the integrated area of the CV curves,  $m$  is the mass of the electrode and the  $\Delta V$  is width of the potential window:

$$C_s = \frac{Q}{m\Delta V} \quad (4.2)$$

The Raman spectra were recorded with a NT-MDT Integra AFM-RAMAN spectrometer in the triple subtractive mode with a CCD detector. The 532 nm line of a doubled diode-pumped Nd:YAG laser was used for excitation with a power of 200 mW measured at the laser head. All the data were collected in a  $180^\circ$  backscattering geometry.

The UV-vis measurements were carried out on a Varian, Cary 100 Bio, UV-visible spectrophotometer. UV-vis spectra were measured from 800 nm to 200 nm at a scan rate of 300 nm per min.

A typical Mott-Schottky plot of  $\text{MnO}_2$  thin films was measured in 0.1 M  $\text{NaNO}_3$  at 10kHz with 20 mV peak to peak amplitude and a standard calomel reference electrode.

### Stability during photo-driven electrochemical water splitting

Several techniques were employed to assess the stability of the water splitting cell toward oxidation. In the primary set-up shown in Figure 4.11 the semiconductor is irradiated by a xenon lamp (Intralux 6000) and its photocatalytic performance recorded over time using a Protek 506 digital multimeter. CdS semiconductors and hetero-structures based on this material were used as the photo-anode, while graphite was used as a cathode. The area of the electrode was defined with epoxy resin.

UV-vis spectroscopy was used to assess corrosion resistance of the cell. In a typical setup shown in Figure 4.12 absorption of light at a characteristic wavelength for the semiconductor was measured over time. A concentrated sodium perchlorate solution was used as a strong oxidizer to accelerate the process in order to provide rapid comparison of different structures.

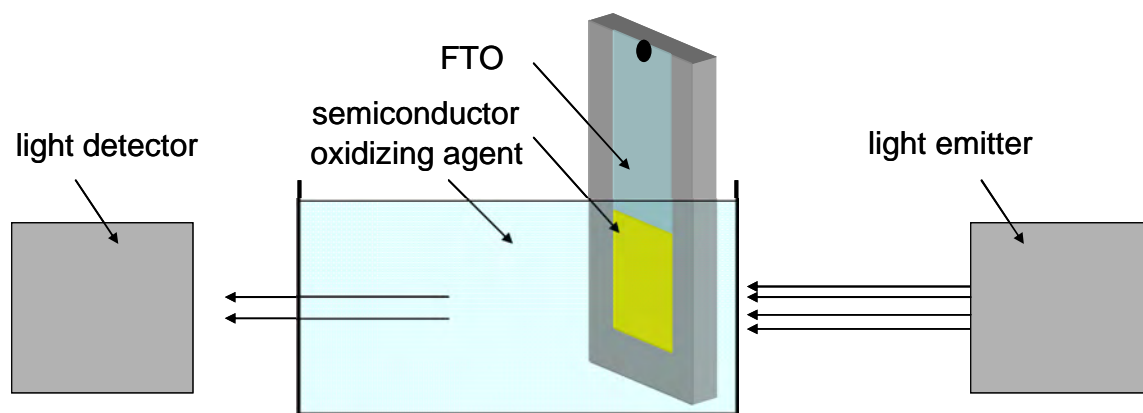


**Figure 4.12:** Assessment of corrosion resistance of the water splitting cell in aggressive environments.

Various types of water splitting cells were prepared as follows. Thin films of CdS (~100 nm) were electrodeposited on the FTO electrode following the procedures described in the previous chapter. Thin films of  $\text{MnO}_2$  were deposited from EAN (20% $\text{H}_2\text{O}$ ) containing 0.1 M  $\text{Mn}(\text{Ac})_2$  at 130 °C upon light irradiation for a time equal to 50% reduction in current density. Thin films of PPy were deposited from aqueous electrolyte containing 0.1 M  $\text{NaNO}_3$  and 0.01 M Pyrrole at room temperature upon light irradiation, so that the drop in current densities does not exceed 10-20%. During the photo-driven

electrochemical deposition (PdED), the CdS semiconductor was illuminated by the Xe light source with light intensity close to 1 sun.

Photo-driven water splitting was carried out in a setup shown in Figure 4.13. The surface area, equal to 0.25 cm<sup>2</sup>, was isolated with a masking film based on the epoxy resin.

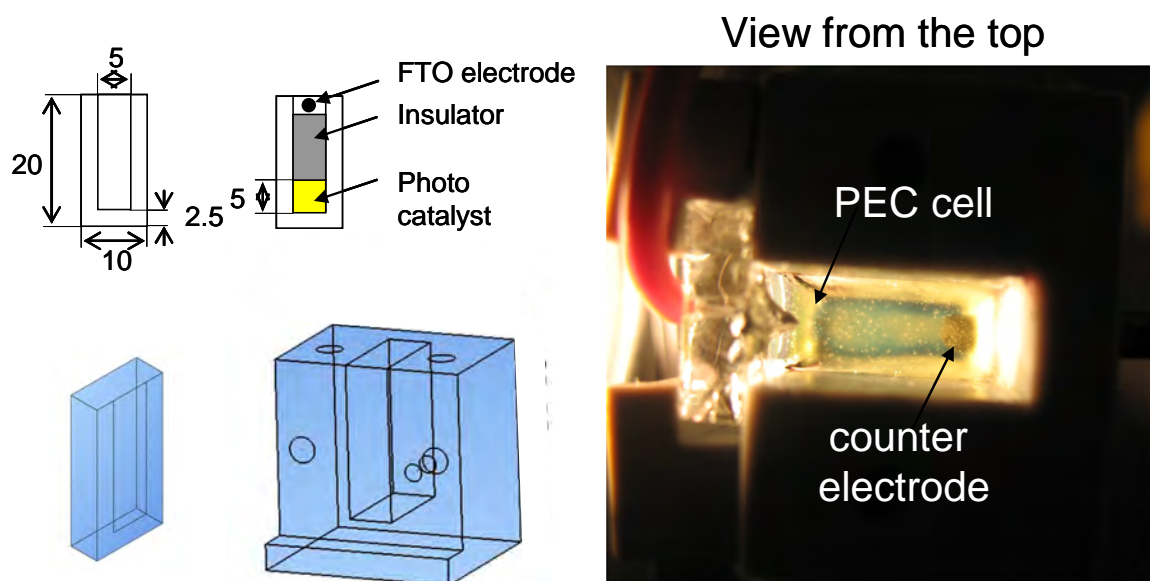


**Figure 4.13:** Schematic representation of the unit for photo-driven water splitting.

#### 4.4. MnO<sub>2</sub> hole conductor/catalyst deposition

Manganese dioxide was used as a hole conductor in this work due to its appropriate energy structure and known catalytic activity towards water oxidation.<sup>[10]</sup> A variety of ILs, including phosphonium based hydrophobic ILs: [P<sub>66614</sub>][NTf<sub>2</sub>], [P<sub>66614</sub>][DCA], and hydrophilic ILs: [P<sub>4444</sub>][Cl] and EAN were used as electrolytes for MnO<sub>2</sub> electrodeposition.

##### 4.4.1. Electrodeposition of MnO<sub>2</sub> from ILs

###### Hydrophobic ILs: [P<sub>66614</sub>][NTf<sub>2</sub>] and [P<sub>66614</sub>][DCA]

Although [P<sub>66614</sub>][NTf<sub>2</sub>] and [P<sub>66614</sub>][DCA] are immiscible with water, it was shown before that hydrophobic ILs tend to absorb a certain amount of water.<sup>[37]</sup> Presence of dissolved Mn(II) in these ILs however does not result in an oxidation wave typical for Mn(II). Neither was presence of MnO<sub>2</sub> deposits observed on the substrate after

chronoamperometry at 0.6 V *vs* Ag/AgCl for ten minutes, as can be seen from Figure 4.14. It appears that these ILs are not useful as media for this deposition process.

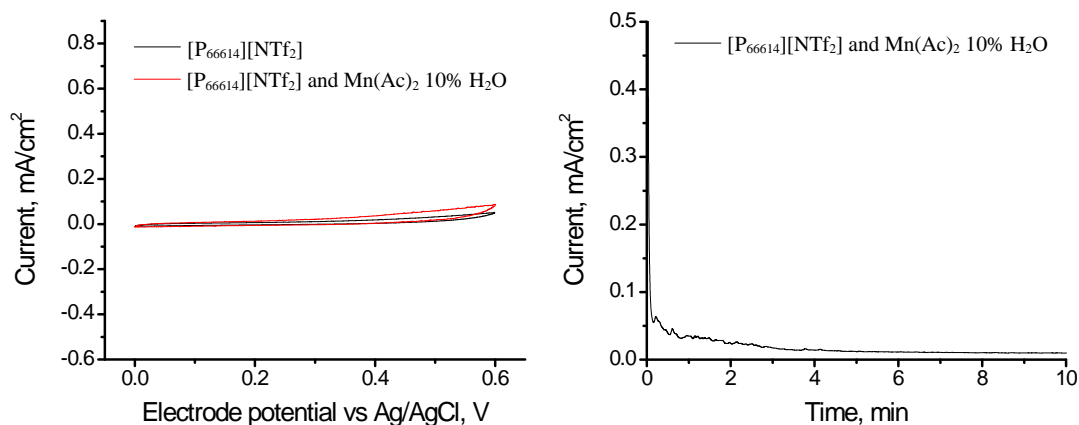
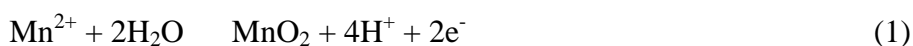


**Figure 4.14:** The cyclic voltammetry of 0.01 M Mn(Ac)<sub>2</sub> in [P<sub>66614</sub>][NTf<sub>2</sub>] at 100°C (left) and typical plot of MnO<sub>2</sub> electro deposition from [P<sub>66614</sub>][NTf<sub>2</sub>] at a constant potential of 0.6V *vs* Ag/AgCl (right).

#### Hydrophilic ILs: [P<sub>4444</sub>][Cl] and EAN

Hydrophilic [P<sub>4444</sub>][Cl] and EAN are, on the other hand, completely miscible with water. A typical cyclic voltammogram of the [P<sub>4444</sub>][Cl] and EAN at 100°C are shown in Figure 4.15a and Figure 4.15b. These CVs confirm that there are no electrochemical reactions related to the ILs in the region of interest. Upon the addition of Mn(II) the oxidation wave becomes distinct, following reaction (1).<sup>[38]</sup>



Cyclic voltammetry in [P<sub>4444</sub>][Cl] is shown in Figure 4.15a. The current density during oxidation wave rises to an ill-defined peak about 0.8 V *vs* Ag/AgCl. The equivalent cyclic voltammetry in EAN is shown in Figure 4.15b, the current density has a well defined maximum at 0.6 V *vs* Ag/AgCl. During the reduction wave the maximum in current density appears at 0.3 V *vs* Ag/AgCl.

Films were electrodeposited on the FTO substrates at a constant potential of 0.6 V *vs* Ag/AgCl being the potential of the maximum current for the EAN case. Figure 4.16 shows a typical plot of current density during deposition at 135°C. It could be seen that the current density does not change significantly during the film growth, confirming the low resistance of the films, which would otherwise add series resistance to the circuit.

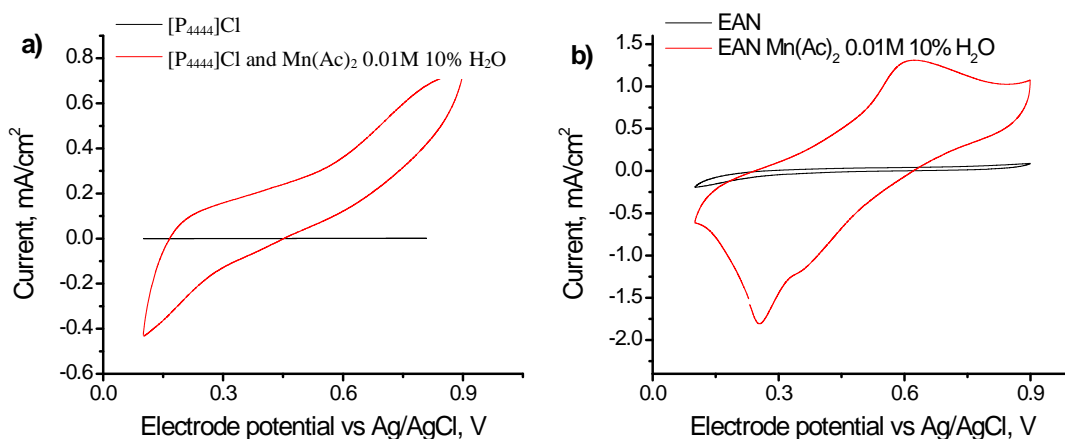


**Figure 4.15:** Cyclic voltammetry of 0.01 M Mn(Ac)<sub>2</sub> in: a) [P<sub>4444</sub>]Cl at 100°C; b) EAN at 100°C.

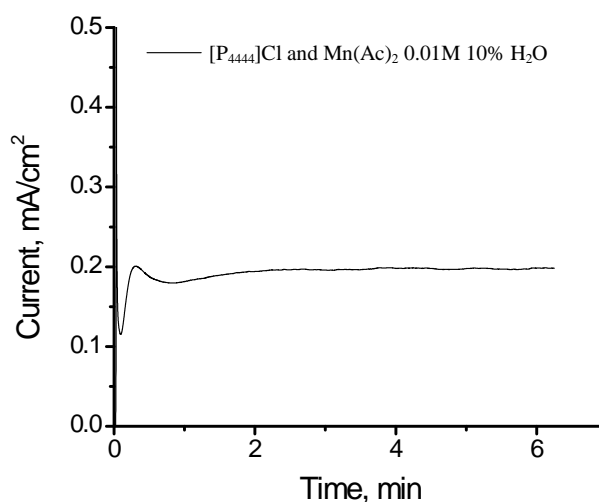


**Figure 4.16:** Typical plot of electro deposition from [P<sub>4444</sub>]Cl at a constant potential of 0.6V vs Ag/AgCl.

Films obtained for different deposition times were analyzed using the surface profilometry. The dependence of the film thickness on amount of charge passed during the growth in [P<sub>4444</sub>]Cl at 135°C is shown in Figure 4.17. The linear trend suggests that the growth of the film is charge controlled. Hence, films of different thicknesses can easily be obtained.

The Figure 4.17 additionally shows the predicted dependence of film thickness on charge passed calculated from Faraday's Law assuming formation of dense MnO<sub>2</sub> films. It can be seen from the graph that the thickness of electrodeposited film is higher comparing to theoretically expected values for dense MnO<sub>2</sub> films. This may be related to the high porosity of films deposited from [P<sub>4444</sub>]Cl and is thus investigated further below.

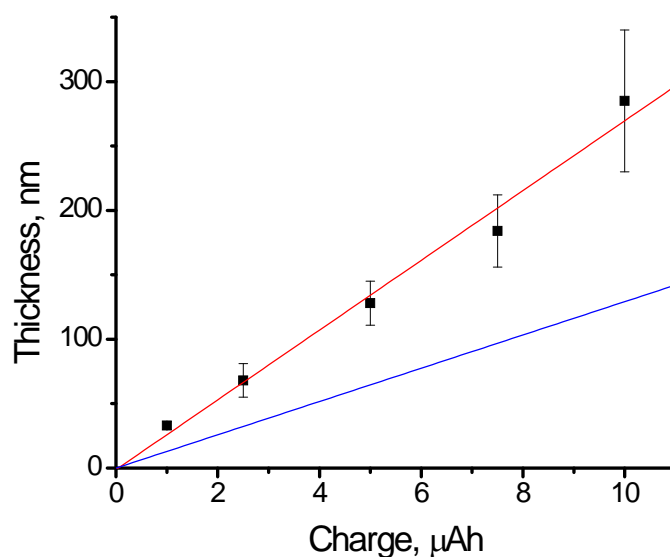


**Figure 4.17:** Dependence of film thickness on charge passed for the growth in  $[\text{P}_{444}]\text{Cl}$  at  $135^\circ\text{C}$ . Linear fit of the data is shown as a red line and theoretically expected thickness dependence as blue line.

#### 4.4.2. Chemical composition and surface morphology

The EDX spectra of the films prepared from  $[\text{P}_{444}]\text{Cl}$  given in Figure 4.18 show presence of manganese, as well as oxygen and tin, that correspond to the substrate (FTO). Similar spectra were obtained for the samples deposited from EAN.

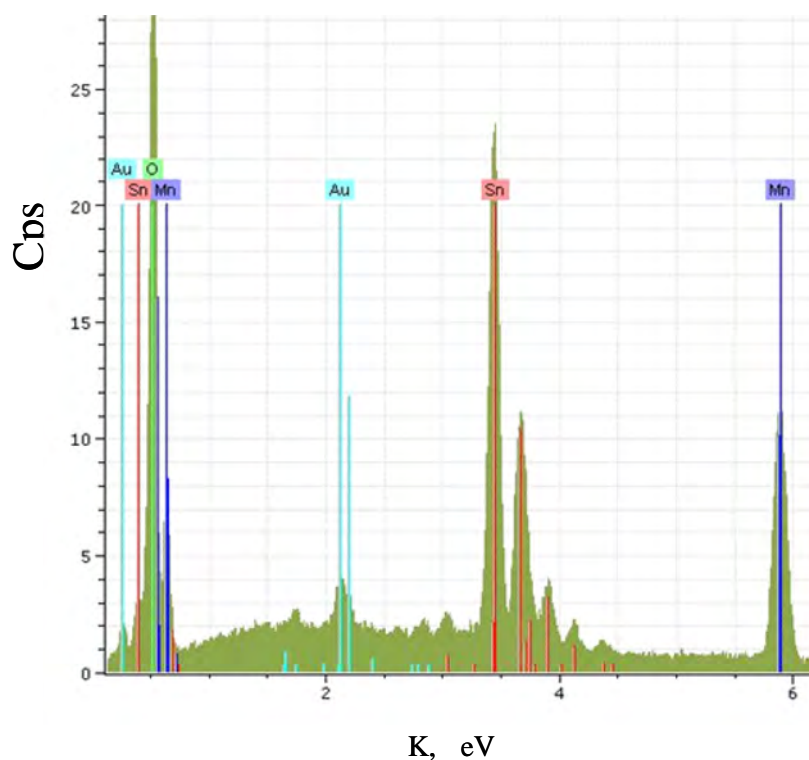


**Figure 4.18:** Typical EDX spectra of manganese oxide prepared from ILs at  $135^\circ\text{C}$ .

The typical Raman spectrum of the thin films deposited from [P<sub>4444</sub>]Cl and EAN given in Figure 4.19 consists of three main peaks at 635, 580, and 510 cm<sup>-1</sup>. Similar peak positions are reported in the literature for  $\gamma$ -MnO<sub>2</sub> (649, 570 and 509 cm<sup>-1</sup>).<sup>[16, 39]</sup> These results are similar to the literature reports, where preferential formation of  $\gamma$ -MnO<sub>2</sub> was observed during the electrochemical oxidation in acidic electrolytes.<sup>[29]</sup> The presence of a broad peak at 635 cm<sup>-1</sup> is likely to be a result of manganese dioxide being reduced in the laser beam.<sup>[39]</sup>

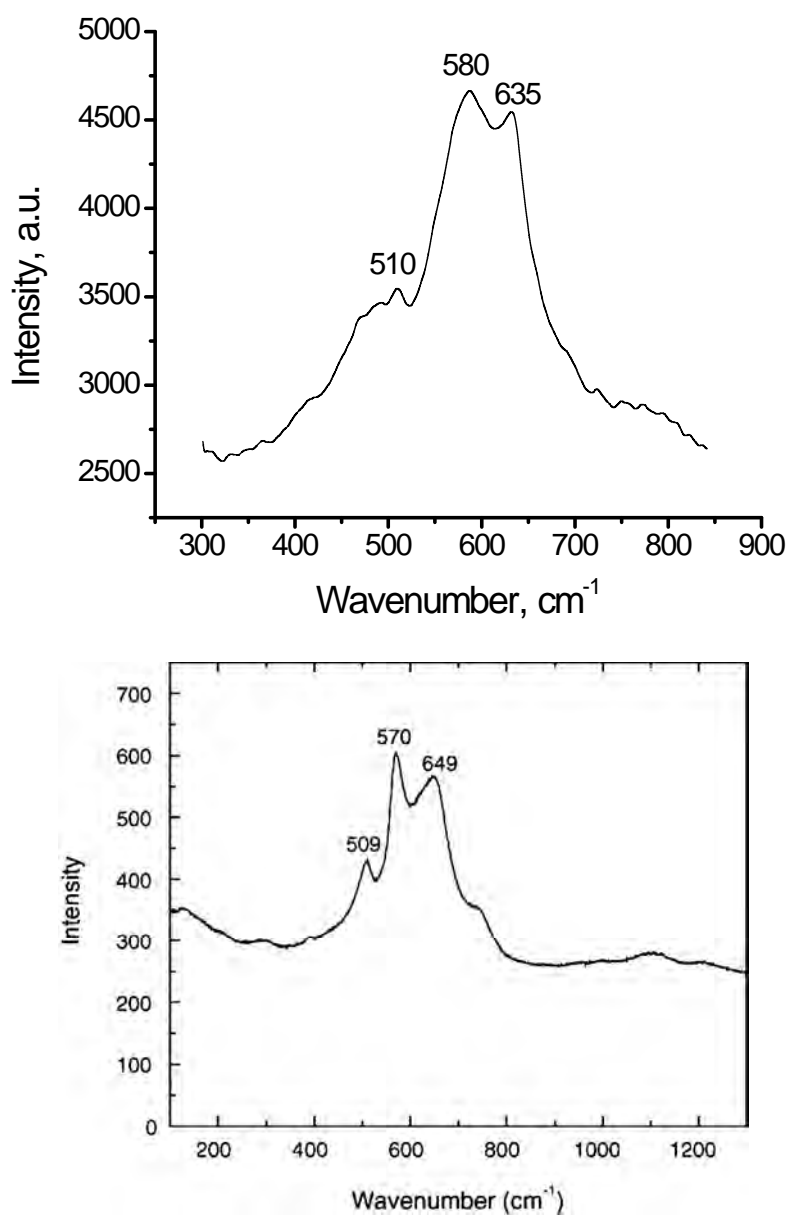


**Figure 4.19:** Typical Raman spectrum (top) of manganese oxide prepared in this work from ILs at 135°C; Raman spectra of the nanostructured  $\gamma$ -MnO<sub>2</sub> (bottom) prepared by Liu *et al.*<sup>[16]</sup>

The ideal water oxidation catalyst should be able to oxidize water at high current densities and form uniform, impenetrable films to protect the surface of the light harvesting semiconductor. Thus, it becomes important to control morphology of the films during deposition, so that a thin dense inner layer can be created for the chemical protection as well as a high surface area outer layer material for efficient water oxidation. It was shown before that presence of various additives such as metal ions<sup>[38]</sup> (e.g. Mo) or specific anions<sup>[17]</sup> (e.g. acetate salts) can alter the morphology of the films. The deposition *via* cyclic voltammetry generally results in the formation of one dimensional nanostructures, whereas the potentiostatic technique leads to the growth of two dimensional surface structures.<sup>[40]</sup> In this work we investigated the influence of various electrodeposition conditions on the morphology of the films.

Films deposited from [P<sub>4444</sub>]Cl at 135 °C are shown in Figure 4.20. The films have clear 3D morphology and consist of nano-flakes. During the deposition, according to reaction (1), hydrogen cations are generated on the surface creating a gradient in pH. The growth is then more favorable at a distance from the substrate, where the pH is higher, leading to formation of flake-like structures. From Figure 4.20 it can be seen that at low current densities, the morphology of the films changes to a more compact structure, while two dimensional growth prevails in acidic solutions.

SEM images of manganese dioxide films deposited from EAN at 135°C is shown in Figure 4.21 at the same magnification as in Figure 4.20. The film appears to be much more compact compared to the ones deposited from [P<sub>4444</sub>]Cl. MnO<sub>2</sub> films deposited from EAN show good adhesion to the substrate but tend to form cracks in the film structure. One of the reasons for crack formation in such films can be higher density of the material and hence, inability of the deposits to dissipate lattice mismatch and difference in the thermal expansion coefficient with the FTO substrate.

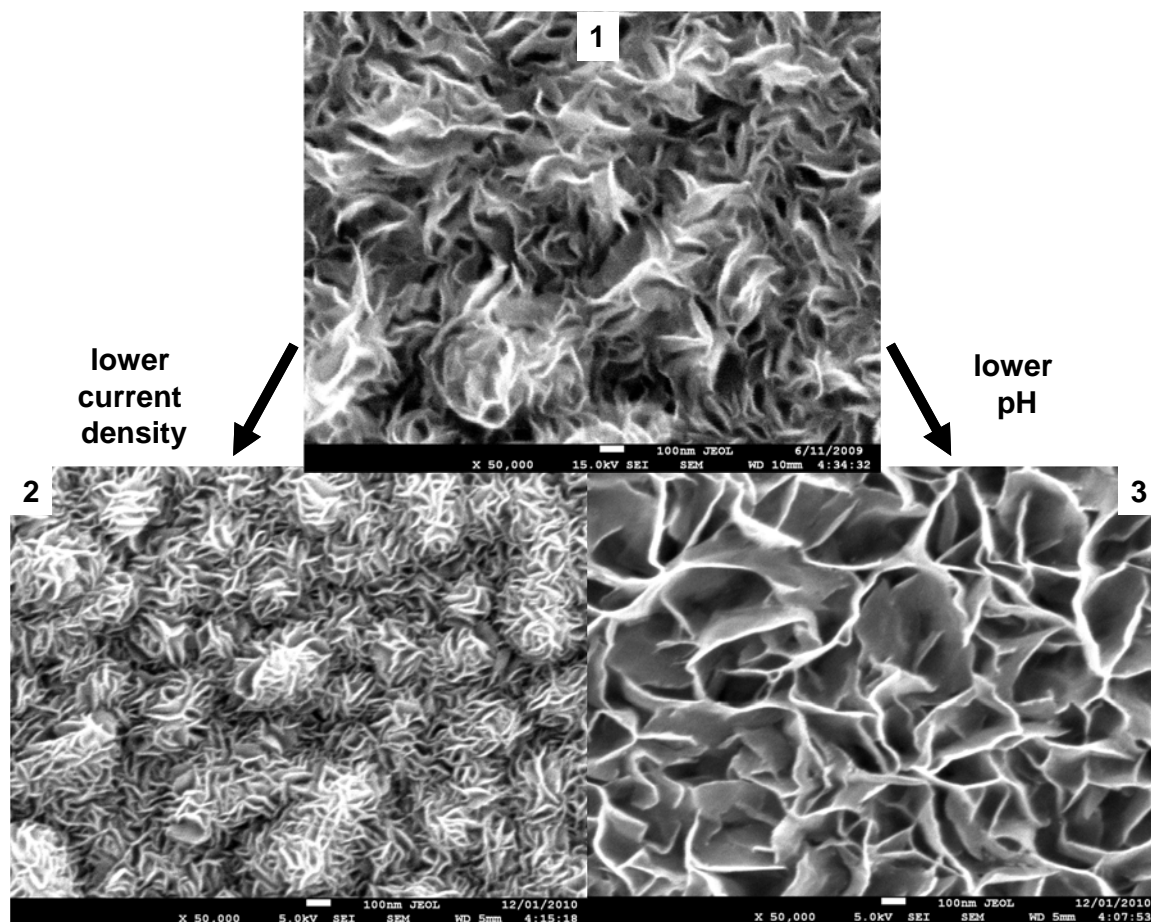


**Figure 4.20:** SEM image of manganese dioxide electrodeposited from [P<sub>4444</sub>]Cl at 135°C; 1 - deposition at 0.6 V vs Ag/AgCl pH = 7; 2 - deposition at 0.5 V vs Ag/AgCl pH = 7; 3 - deposition at 0.6 V vs Ag/AgCl pH = 4. Scale bar on the pictures is equivalent to 100 nm.

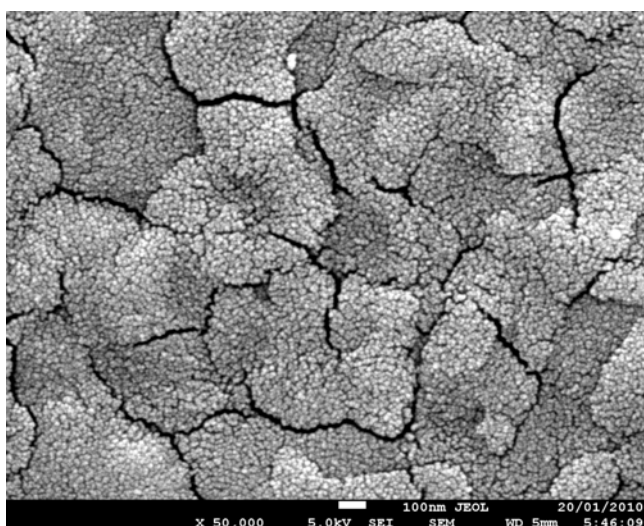


**Figure 4.21:** SEM image of manganese dioxide electrodeposited from EAN at 135°C. Scale bar on the picture is equivalent to 100 nm.

### 4.4.3. Electric properties of MnO<sub>2</sub> thin films

Capacitance of thin MnO<sub>2</sub> films is believed to be due to the redox processes associated with the reduction of MnO<sub>2</sub> to MnOOH. The process involves incorporation of protons and electrons into the MnO<sub>2</sub> lattice and eventual formation of an amorphous MnOOH.<sup>[12]</sup> The value of charge-storage capacity depends on the effectiveness of the proton diffusion in and out of the MnO<sub>2</sub> lattice.<sup>[29]</sup> We can expect that porous films with a high surface area would have higher values of specific capacity compared to films with a higher density.

The cyclic voltammetry of the 70 nm and 450 nm thick films deposited from [P<sub>4444</sub>]Cl and EAN respectively are shown in Figure 4.22. The specific capacities calculated from the data presented in Figure 4.22a are 57, 51, 49 F/g for 10, 50 and 100 mV/s, respectively, while specific capacities calculated based on the data in Figure 4.22b are 14, 12, 11 F/g, respectively. For the highly porous structure of manganese dioxide, the reported value of specific capacity is around 300 F/g,<sup>[12, 13, 29]</sup> thus suggesting the deposition of dense MnO<sub>2</sub>.

The data presented in Figure 4.23 show a linear dependence of the current on the value of the scan rate. This fact indicates that the film capacity is mainly determined by the surface reactions and not diffusion in the material. Much lower values of specific capacity measured for films deposited from EAN compared to [P<sub>4444</sub>]Cl further confirm formation of a more compact structure which is a highly desirable property of the HC layer.

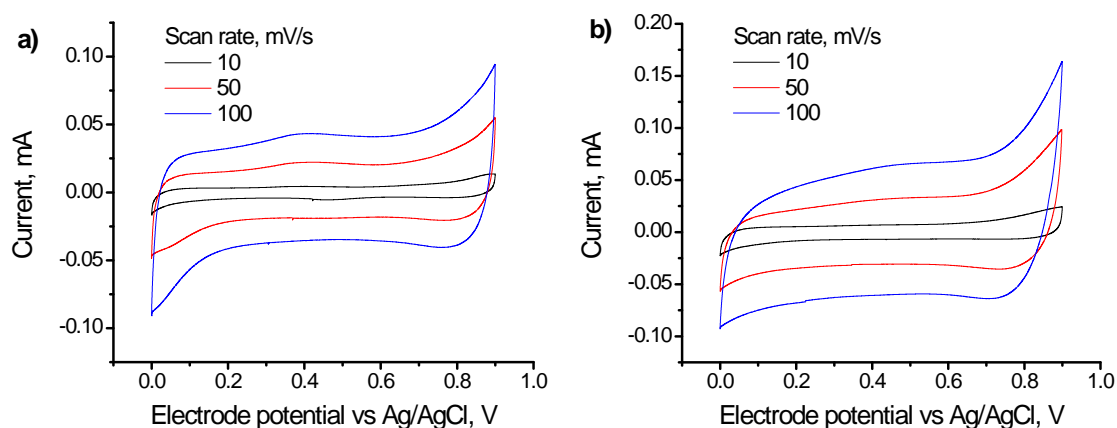


**Figure 4.22:** Typical cyclic voltammograms of MnO<sub>2</sub> films in 0.1 M Na<sub>2</sub>SO<sub>4</sub> electrodeposited from a) [P<sub>4444</sub>]Cl at 135 °C; b) EAN at 135 °C.

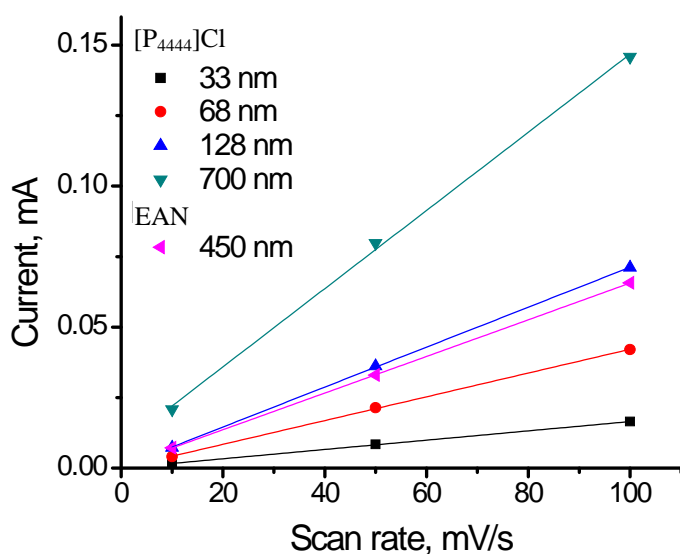


**Figure 4.23:** Dependence of the current at 0.5 V vs Ag/AgCl on the scan rate for films of different thicknesses.

The Nyquist impedance spectra are shown in Figure 4.24. At low frequencies, the intercept on the real axis is a combination of ionic resistance from the electrolyte, intrinsic resistance of the active material, and contact resistance between the active material and the current collector interface.<sup>[13]</sup> At the low frequencies a capacitance forms a straight line along the imaginary axis. This line usually has a finite slope due to the diffusive resistance of the electrolyte in electrode pores.<sup>[40]</sup>

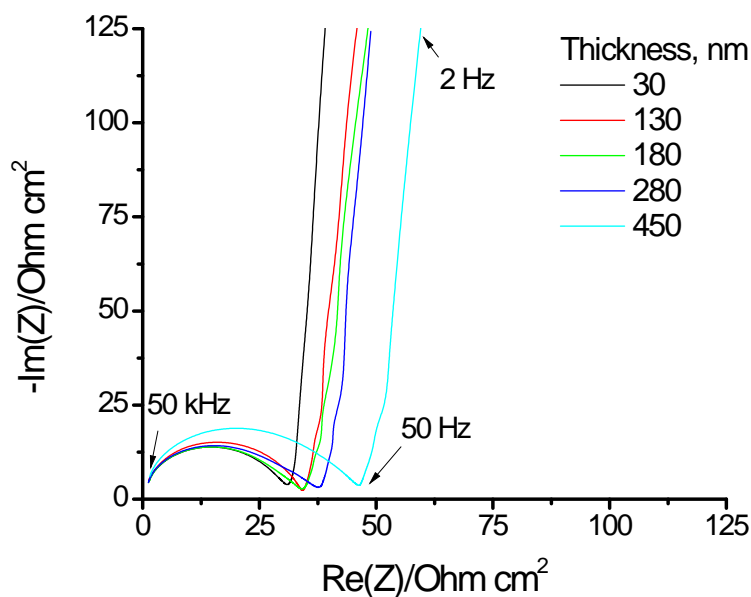


**Figure 4.24:** Nyquist plot for manganese oxide films of different thicknesses prepared from [P<sub>4444</sub>]Cl.

It is suggested that the contact resistance of the manganese dioxide electrode with FTO and the electrolyte resistance are constant for the films of different thicknesses.<sup>[14]</sup> Thus, the difference in resistance between films can be considered to be largely due to the resistance of the manganese dioxide films. The values of resistance obtained from Figure 4.24 are plotted in Figure 4.25 and appear to be a rising function of the film thickness. The linear fit of the data allows calculation of the resistivity of the MnO<sub>2</sub> films, which is equal to 370 kΩ cm.

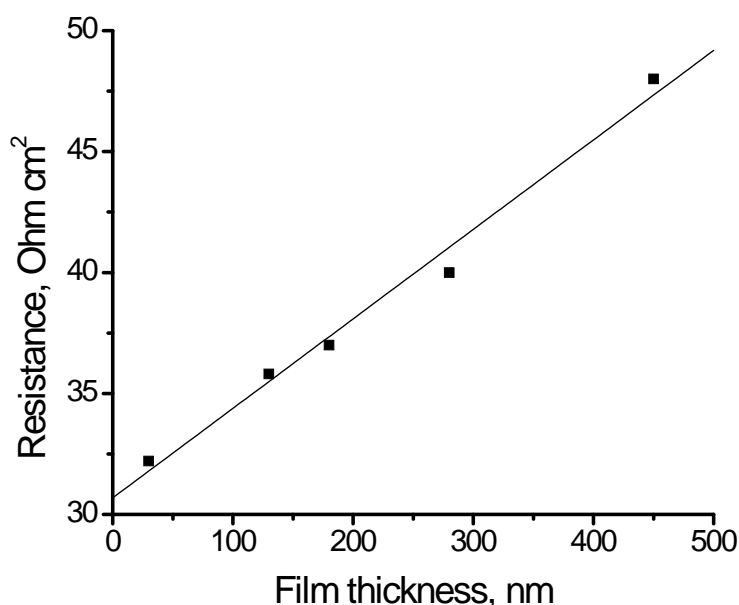


**Figure 4.25:** Resistance for films of different thickness derived from an intercept on the real axis of Nyquist plot.

This value of resistivity compares well with the resistivity of pure bulk MnO<sub>2</sub> (~100 kΩcm<sup>[31]</sup>). The water content in manganese dioxide is known to affect the electrochemical reactivity, thermodynamic stability and electrical conductivity of various MnO<sub>2</sub> phases as it causes a variation in the crystal lattice,<sup>[12]</sup> this may be responsible for the difference observed here. Thus, through the use of ILs and deposition at elevated temperatures we were able to prepare materials similar in properties to pure MnO<sub>2</sub>. Only thin layers are required to achieve high levels of chemical protection,<sup>[2]</sup> hence, they do not contribute high resistance to the electrical circuit of the PEC cell.

The Mott-Schottky plot of electrodeposited films shown in Figure 4.26 has the characteristic slope typical of a p-type semiconductor. The value of the flat band potential

calculated through the linear fit of the data shown on the graph is 1.59 V vs SCE, which is similar to the value expected for bulk MnO<sub>2</sub> (1.57 - 1.82 V vs SCE).<sup>[41]</sup>

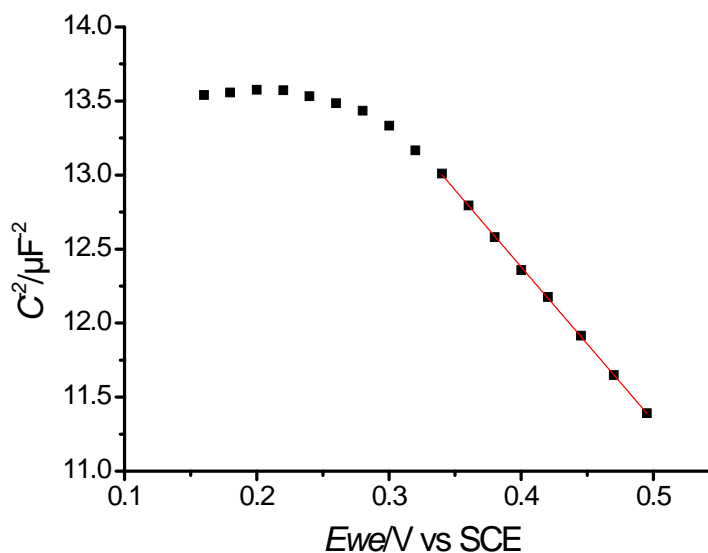


**Figure 4.26:** Mott-Schottky plot of electrodeposited MnO<sub>2</sub> films in 0.1 M NaNO<sub>3</sub> at 10kHz.

#### 4.4.4. UV-vis spectroscopy

The UV-vis spectra of the manganese dioxide films of various thicknesses are shown in Figure 4.27. It can be seen that the optical absorption of the MnO<sub>2</sub> is proportional to the film thickness. Thus, the attenuation coefficient given in Figure 4.27 can be calculated by dividing the absorbance at any wavelength by the film thickness. The slight discrepancies in the value of the attenuation coefficients from different film thicknesses are probably due to higher porosity of the thicker films, which leads to variable density of the material.

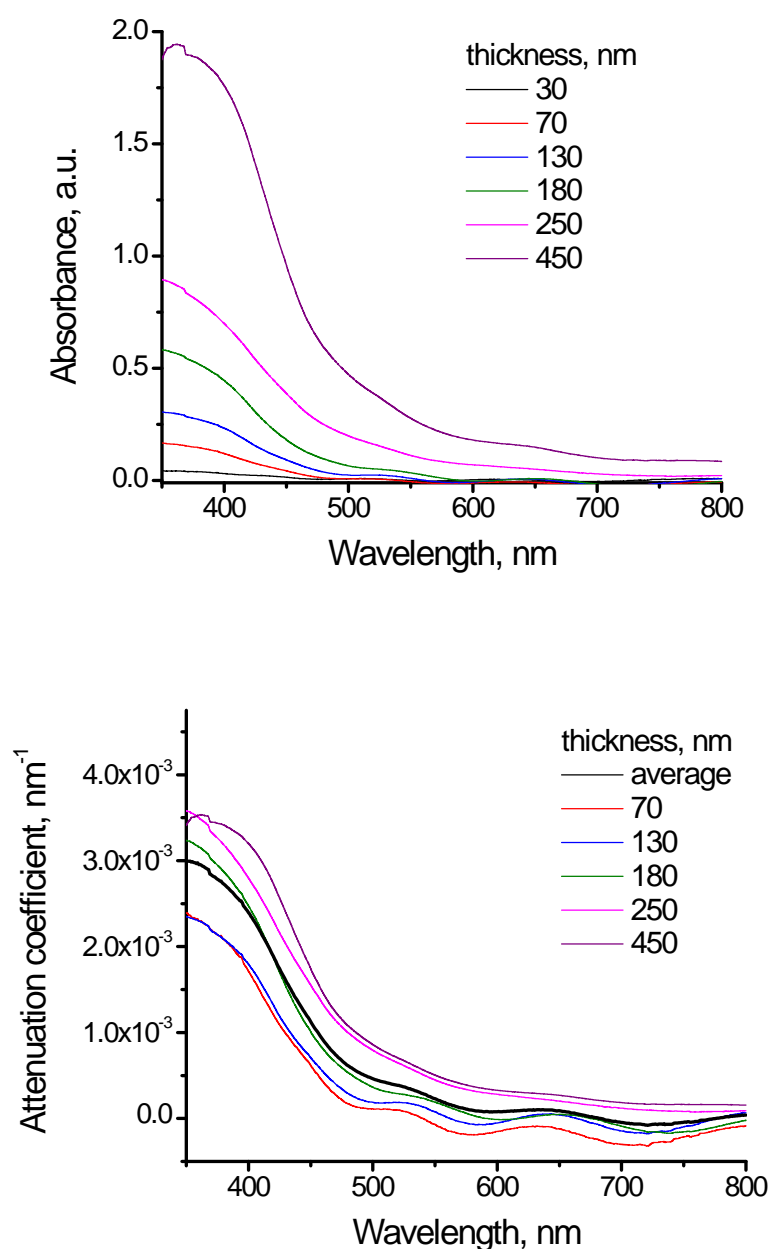


**Figure 4.27:** UV-vis spectra (top) and attenuation coefficient (bottom) of manganese oxide films electrodeposited from  $[P_{4444}]Cl$  at 135 °C.

#### 4.4.5. Catalytic activity and electrochemical stability

The oxygen evolution reaction was studied on platinized FTO electrodes and  $MnO_2$  films deposited on FTO electrodes in neutral and basic conditions. Linear scan voltammograms for the oxygen evolution reaction in a neutral solution are shown in Figure 4.28a. The onset potential for the water oxidation on the platinised FTO electrode in the neutral solution is around 1.1 V vs Ag/AgCl, while for  $MnO_2$  electrode is around 1.25 V vs Ag/AgCl. In basic electrolytes the potential for both electrodes is around 0.8 V vs

Ag/AgCl, as shown in Figure 4.28b. It can be seen that the catalytic activity of MnO<sub>2</sub> films is superior to Pt electrodes in the basic solution even after prolonged oxidation of water at 1.0 V vs SCE.

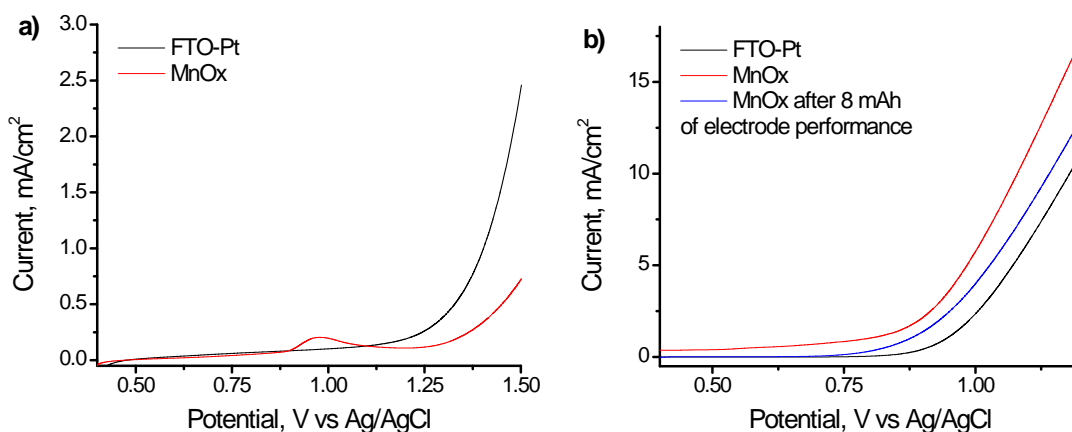


**Figure 4.28:** Linear scan voltammograms for the oxygen evolution reaction at platinised FTO electrode and electrodeposited manganese dioxide films (as prepared – red; after 2 mAh of performance - blue) in a) 0.1 M Na<sub>2</sub>SO<sub>4</sub> solution and b) 0.5 M KOH solution.

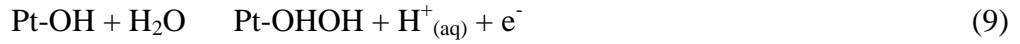
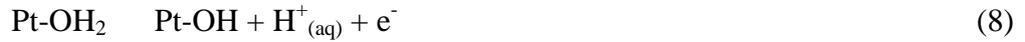
In alkaline media, the oxygen evolution reaction may be represented as a combination of several consecutive steps (2)-(5).<sup>[42]</sup>



The electrocatalytic activity of manganese dioxide nanoparticles electrodeposited on Pt, Au, and glassy carbon electrodes towards water oxidation in basic solutions was studied by Ohsaka *et al.*<sup>[10]</sup> Performance was enhanced significantly through the deposition of the manganese oxide. Similar to the work on nickel oxide catalysts,<sup>[43]</sup> a plausible explanation for the high catalytic activity was based on the role of a catalytic mediator  $\gamma$ -MnOOH on the charge transfer during water oxidation (6,7).



Catalytic oxidation of water on the surface of a Pt catalyst can be expressed as a series of reactions (8-11).<sup>[44]</sup>



Based on the mechanisms of water oxidation on the surface of Pt and MnO<sub>2</sub> described above, we can expect strong dependence of MnO<sub>2</sub> catalytic activity on the electrolyte pH. The data shown in Figure 4.28 indicates a relatively similar position of the potential for water oxidation between both types of the catalyst. The value of the overpotential observed for the MnO<sub>2</sub> electrode, however, increases with a decrease in the electrolyte pH. The latter fact can be clearly observed as a value of the slope on the current-potential curve at high potentials. For the MnO<sub>2</sub> electrode in neutral solution it is significantly reduced compared to Pt.

Electrochemical cycling of MnO<sub>2</sub> generally leads to the formation of cracks, an increase in porosity and formation of a fibrous microstructure as a result of partial dissolution of manganese dioxide during cycling (reaction 12).<sup>[14]</sup> Dissolution of MnO<sub>2</sub> can also take place by a disproportionation reaction if reactions (12) and (13) shown below are involved simultaneously.<sup>[45]</sup>



During cycling, the disproportionation in the films can also occur through the irreversible formation of complex oxides such as Mn(OH)<sub>2</sub>, Mn<sub>2</sub>O<sub>3</sub>, Mn<sub>3</sub>O<sub>4</sub>, Mn<sub>5</sub>O<sub>8</sub>, *etc.*<sup>[12]</sup>

In order to assess the long-term stability of the electrodeposited MnO<sub>2</sub> films, water oxidation at a constant potential equal to 1.0 V *vs* SCE was conducted for several consecutive days. As can be seen from Figure 4.29, the value of current density steadily declines.

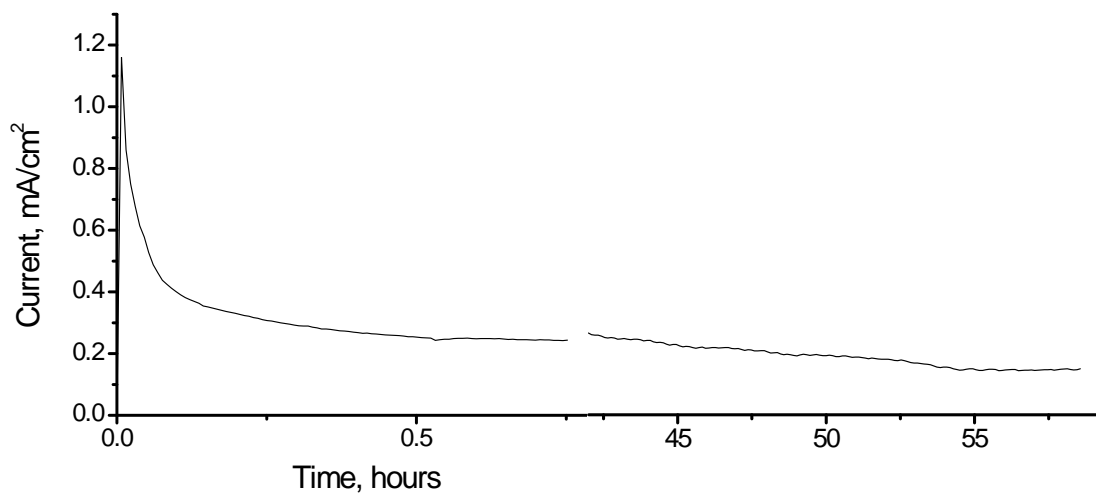


**Figure 4.29:** Oxygen evolution reaction at manganese oxide electrode with time in 0.5 M NaOH ( $E = 1$  V vs SCE).

After prolonged water oxidation no changes were observed in the optical appearance of the film. Although SEM images before and after the long-term water oxidation, shown in Figure 4.30, confirm maintenance of the structural integrity by MnO<sub>2</sub> films, we can observe various changes in film morphology.

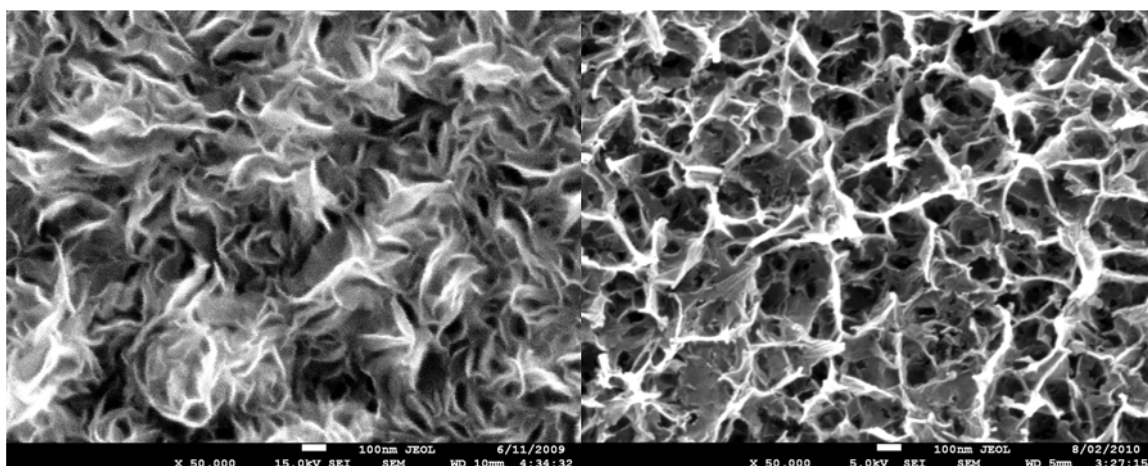


**Figure 4.30:** SEM image of MnO<sub>2</sub> film: as deposited (left) and after long term water oxidation (right). Scale bar on the picture is equivalent to 100 nm.

Thus electrodeposited MnO<sub>2</sub> films show good catalytic activity and long term stability towards water oxidation reaction. The catalytic performance is comparable to Pt electrodes in neutral electrolytes and exceeds that of Pt in basic solutions.

#### 4.4.6. Photo-driven electrodeposition of $\text{MnO}_2$

CdS films electrodeposited on the FTO coated glass were used as substrates for photo-driven electrochemical deposition (PdED). A typical electric current response from CdS in electrolyte containing  $\text{Mn}(\text{Ac})_2$  is shown in Figure 4.31. Over a period of time the current dies out due to the high resistance of the formed film.

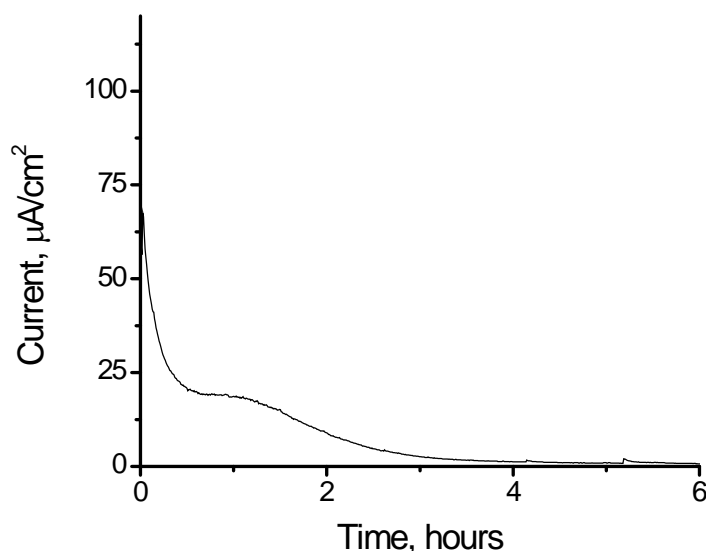


**Figure 4.31:** PdED of  $\text{MnO}_2$  on the surface of CdS in 0.05 M  $\text{Mn}(\text{Ac})_2$  in EAN (20%  $\text{H}_2\text{O}$ ) at 130 °C.

A photo-driven electrochemical deposition of  $\text{MnO}_2$  was carried out in EAN at room temperature and at 130 °C, with other conditions similar to the electrodeposition on FTO as described above. As can be seen from the SEM images in Figure 4.32, the surface morphology of the films deposited at elevated temperatures is more uniform compared to the films deposited at room temperature. Appearance of cracks in the structure may be related to post processing techniques applied to the films (*e.g.* washing and drying).

For comparison, thin films of  $\text{MnO}_2$  were deposited using spray pyrolysis at 400 °C. SEM images of the air annealed CdS films and these covered with  $\text{MnO}_2$  deposited *via* the spray pyrolysis are shown in Figure 4.33. It can be seen that the overall morphology of the thin  $\text{MnO}_2$  layer is far less uniform than films prepared through the photo-driven electrochemical deposition.

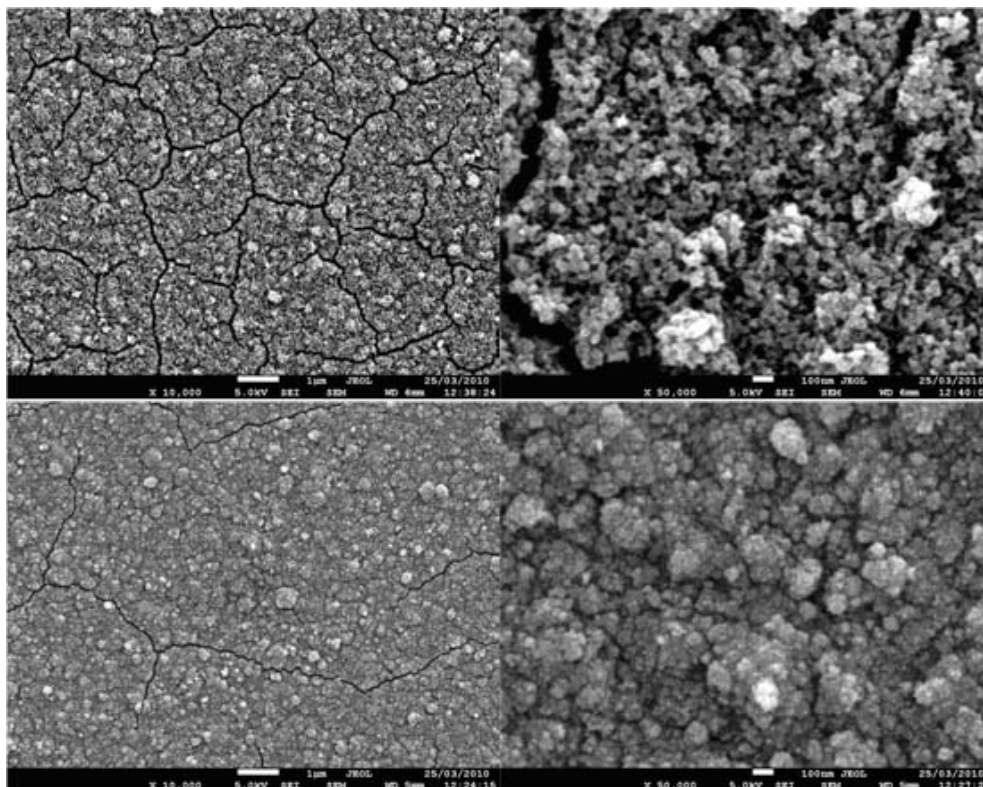


**Figure 4.32:** SEM images of MnO<sub>2</sub> deposited from 0.1 M Mn(Ac)<sub>2</sub> solution in EAN (20% H<sub>2</sub>O) at room temperature (top) and 130 °C (bottom). Scale bars on the pictures are equivalent to 1 μm (left) and 100 nm (right).

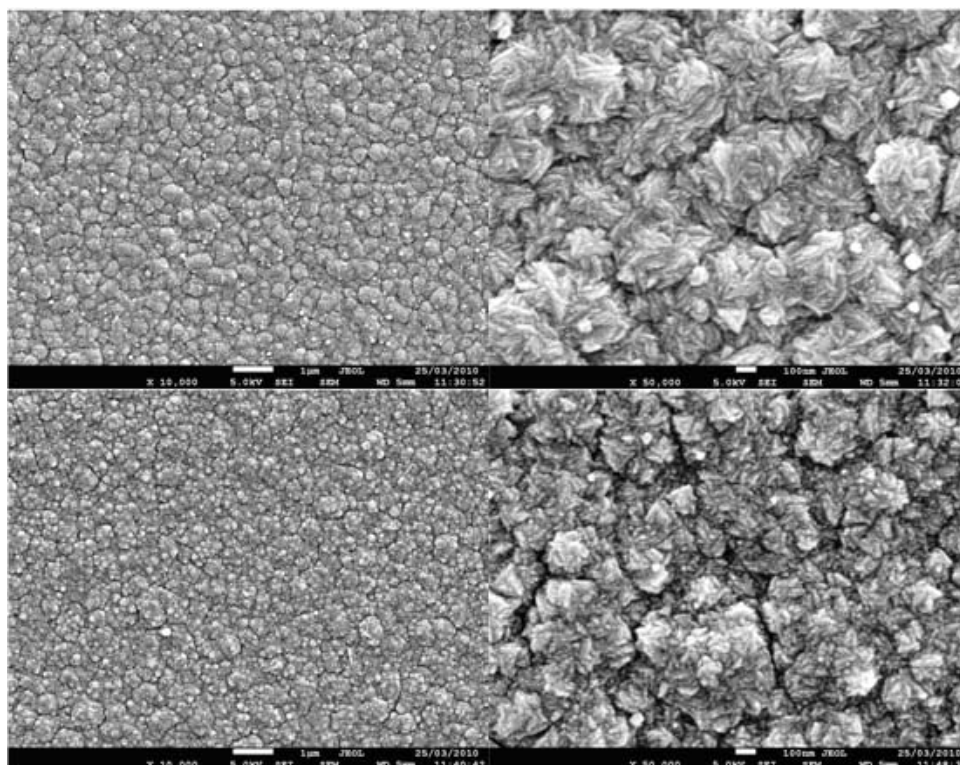


**Figure 4.33:** SEM images of CdS annealed at 400 °C in the air (top) and these coated with MnO<sub>2</sub> by spray pyrolysis at 400 °C (bottom). Scale bars on the pictures are equivalent to 1 μm (left) and 100 nm (right).

A typical EDX spectrum of  $\text{MnO}_2$  films deposited on CdS shown in Figure 4.34 confirms the presence of Mn in both PdED and spray pyrolysed films.

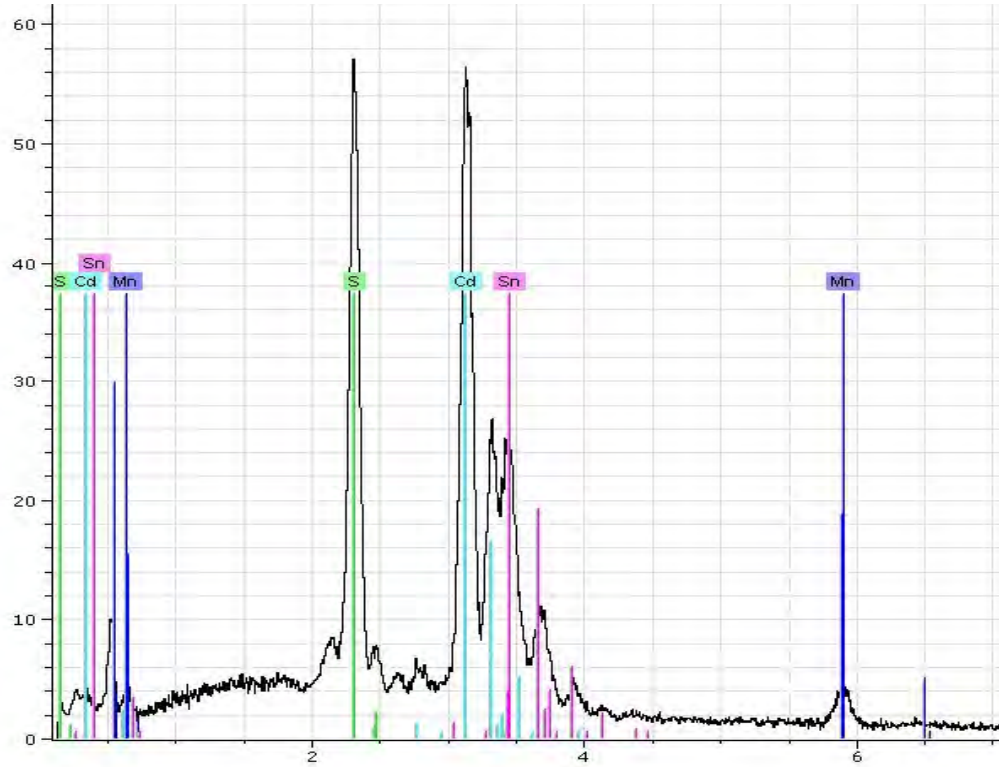


**Figure 4.34:** EDX spectrum of PdED manganese dioxide films on CdS substrate.

### UV-vis spectroscopy of $\text{MnO}_2$ deposited on CdS

Earlier in this work we calculated values of the attenuation coefficients for CdS and  $\text{MnO}_2$  films electrodeposited on the FTO substrate (see Figure 4.35). It is possible to define the linear region on these graphs with end points corresponding to 400 and 450 nm. In the multilayer structure, the total absorbance can be calculated as a sum of the attenuations from CdS and  $\text{MnO}_2$ . Based on the values of attenuation coefficients in the linear region of the plot (red line in Figure 4.35) and known overall absorption of the CdS- $\text{MnO}_2$  structure it becomes possible to calculate the thickness of the separate elements by solving Equations 4.3:

$$\begin{aligned} Abs^{400} &= \epsilon_{CdS}^{400} \cdot h_{CdS} + \epsilon_{MnO_2}^{400} \cdot h_{MnO_2} \\ Abs^{450} &= \epsilon_{CdS}^{450} \cdot h_{CdS} + \epsilon_{MnO_2}^{450} \cdot h_{MnO_2} \end{aligned} \quad (4.3)$$

Where  $Abs^{400}$  and  $Abs^{450}$  are absorbances at 400 and 450 nm, respectively,  $\epsilon_{CdS}^{400}$ ,  $\epsilon_{CdS}^{450}$  and  $\epsilon_{MnO_2}^{400}$ ,  $\epsilon_{MnO_2}^{450}$  are attenuation coefficients at 400 and 450 nm for CdS and

MnO<sub>2</sub>;  $h_{\text{CdS}}$  and  $h_{\text{MnO}_2}$  are thicknesses of CdS and MnO<sub>2</sub> respectively. The thickness of films calculated in this manner lead to the value of uncertainty around 10%.

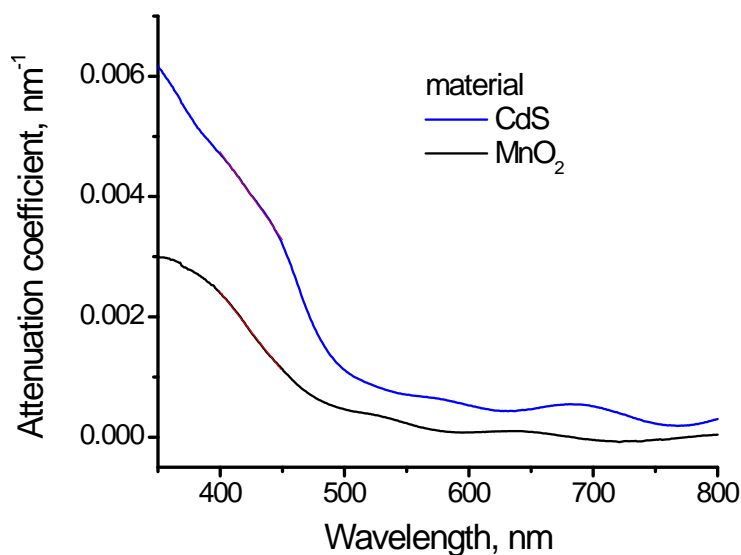


**Figure 4.35:** Attenuation coefficient of semiconductors electrodeposited on the FTO electrode.

A typical UV-vis absorption spectrum of the CdS-MnO<sub>2</sub> structure is shown in Figure 4.36. As an example, the data analysis based on calculations described above leads to thicknesses of CdS and MnO<sub>2</sub> films to be 100 and 115 nm, respectively.

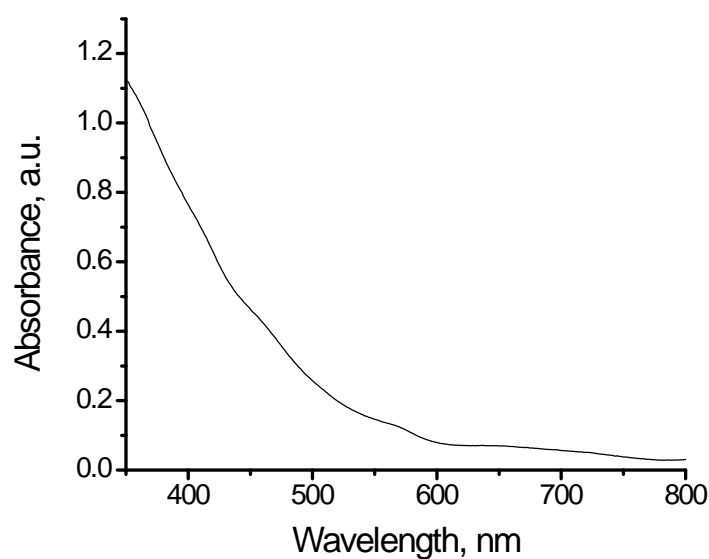


**Figure 4.36:** UV-vis absorption spectrum of PdED MnO<sub>2</sub> films on the CdS semiconductor.

## 4.5. *Self-repair agents*

For PEC cells in this work we chose MnO<sub>2</sub> electrodeposited from EAN as the HC material. As can be seen from Figure 4.21, along with the formation of a dense layer, the electrodeposited MnO<sub>2</sub> films have a number of cracks in the structure. The presence of such defects leads to slow deterioration of the LHS and subsequent total loss of the photocatalytic activity. Thus, it is important to develop a method, by which the negative influence of such defects in the structure of the HC can be effectively neutralized.

To achieve such protection a range of conducting polymers and inhibitors was investigated in this work. The essential electrochemical properties in relation to the HC material that any successful self-repair agent should satisfy are discussed in detail below.

### 4.5.1. **Electrodeposition of self-repair agent**

The electrochemical, structural and physical properties of electrodeposited PPy films are extremely sensitive to deposition conditions<sup>[46]</sup>. For example, conductivity of PPy films fall by two orders of magnitude with an increase in deposition temperature from 2 to 75 °C. Despite good conductivity however, low temperature synthesis generally leads to formation of more rugged films with lower levels of adhesion to substrates. Conducting PPy films can be electrodeposited at relatively low oxidation potentials, as can be seen from the first oxidation cycle in Figure 4.37. The variation in pH of the electrolyte does not affect the deposition potential of PPy films, hence neutral electrolyte was used for deposition in this work.<sup>[46]</sup>

One of the most important properties of PPy films for this work is their ability for irreversible over-oxidation. When over-oxidized, PPy films lose electroactivity, change color and increase film thickness.<sup>[46]</sup> It was shown before that over oxidation of films begins on the side next to the electrode and subsequently develops toward the side in contact with the electrolyte, during which carbon is oxidized into C=O and -NH<sup>+</sup> is mostly replaced by -NH-.<sup>[47]</sup>

The potential for electrochemical over-oxidation of PPy is around 0.9 V *vs* Ag/AgCl.<sup>[47]</sup> Thus, there is a significant drop in the current density upon further cycles during the electrodeposition of the polymer. The potential available at the surface of CdS during irradiation far exceeds this value, making photo-chemical deposition of a PPy-based insulator possible.

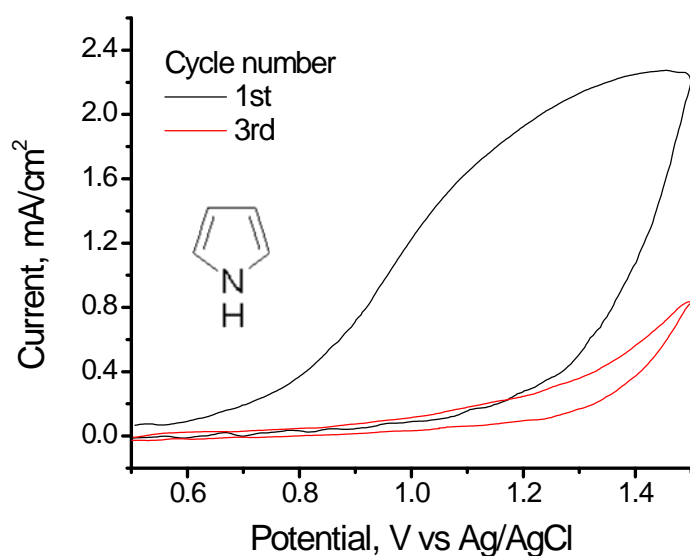


**Figure 4.37:** Cyclic voltammogram of the FTO electrode in aqueous electrolyte containing pyrrole and 0.1 M solution of NaNO<sub>3</sub>.

The potential of biThiophene electrooxidation is around 0.8 V vs Ag/AgCl, as seen in the first cycle Figure 4.38. In comparison, the potential for deposition of Thiophene and terThiophene are around 1.12 and 0.55 V vs Ag/AgCl, respectively.<sup>[48]</sup> Similarly to PPy, the PBTh films undergo irreversible over-oxidation at potentials exceeding 1.2 V vs Ag/AgCl. This process significantly reduces the value of the current density during further cycling (see Figure 4.38).<sup>[48]</sup>

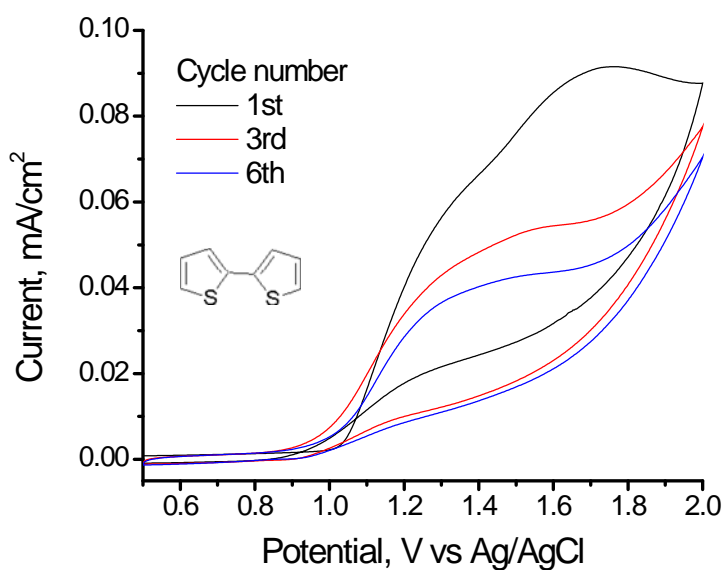


**Figure 4.38:** Cyclic voltammogram of FTO electrode in aqueous electrolyte containing 2,2'-Bithiophene.

In this work electrooxidation of  $[P_{66614}][DCA]$  and  $[P_{66614}][DPP]$  was also studied for the purpose of the chemical protection of LHS in PEC cells. Cyclic voltammograms for electrodeposition of insulators from acetonitrile solutions containing  $[P_{66614}][DCA]$  and  $[P_{66614}][DPP]$  on the FTO substrate are shown in Figure 4.39 and Figure 4.40, respectively. Similar to the data for PPy and PBTh films, there is a significant reduction in the current density upon cycling due to the oxidative decomposition of the DCA and DPP anions.

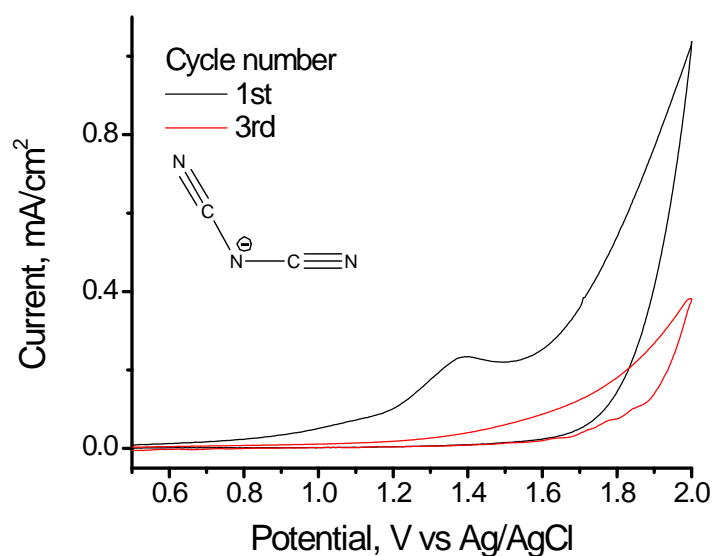


**Figure 4.39:** Cyclic voltammogram of the FTO electrode in acetonitrile containing  $[P_{66614}][DCA]$ .

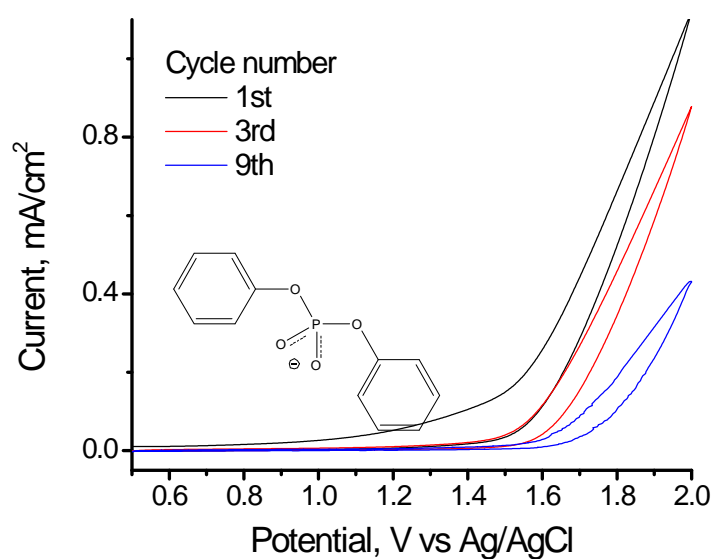


**Figure 4.40:** Cyclic voltammogram of the FTO electrode in acetonitrile containing  $[P_{66614}][DPP]$ .

In a related study, dicyanoimine, cyanourea, dicyandiamide and 1,2,3,5 tetrazine compounds were found as products of cyanamide oxidation.<sup>[49]</sup> The products of oxidative decomposition of [P<sub>66614</sub>][DPP] on the Mg surface studied by ToF-SIMS indicated the formation of a thin film composed of several phosphate species, including PO, PO<sub>2</sub> and PO<sub>3</sub>.<sup>[35]</sup>

Based on the electrochemical properties described above, all of the investigated compounds formed insulating films upon oxidation on the FTO electrode. The films based on oxidation of PPy, PBTh, and DCA were chosen for further investigation as potential self-repair agents in the PEC cell.

#### 4.5.2. Photo-driven electrochemical deposition of self-repair agents

As can be seen from Figure 4.32, a number of cracks appear at the surface of the HC. In order to enhance stability of the PEC cell, an efficient mechanism should be available for the deposition of the self-repair agent. Following the success of the photo-driven electrochemical deposition of HCs described above, it is possible to utilize the same technique for the deposition of the self-repair agent.

Among the materials investigated in this work, the highest potential for oxidative deposition was recorded for 2,2'-bithiophene (over 1.2 V *vs* NHE). Although the potential at the MnO<sub>2</sub> surface (1.58 V *vs* NHE) is theoretically sufficient to oxidize these materials, the rate of deposition (hence, film density) is expected to be smaller compared to the oxidation on the surface of CdS (1.88 V *vs* NHE) as desired if the MnO<sub>2</sub> surface itself is not to be coated with the repair agent.

A typical electric current response from the PEC cell based on CdS with MnO<sub>2</sub> as a HC layer in an electrolyte containing pyrrole is shown in Figure 4.41. Over a period of time the current dies out due to the high resistance of the polymer layer formed on the surface. Insulating films based on PBTh and oxidative decomposition of [P<sub>66614</sub>][DCA] were similarly prepared.

SEM images of the various protective films thus formed on the surface of the PEC cell are shown in Figure 4.42. PBTh and products of [P<sub>66614</sub>][DCA] oxidation form thin films on the surface of CdS and MnO<sub>2</sub>, which effectively inhibit electrochemical reactions. In contrast, it is possible to deposit comparatively thicker films in the case of PPy.

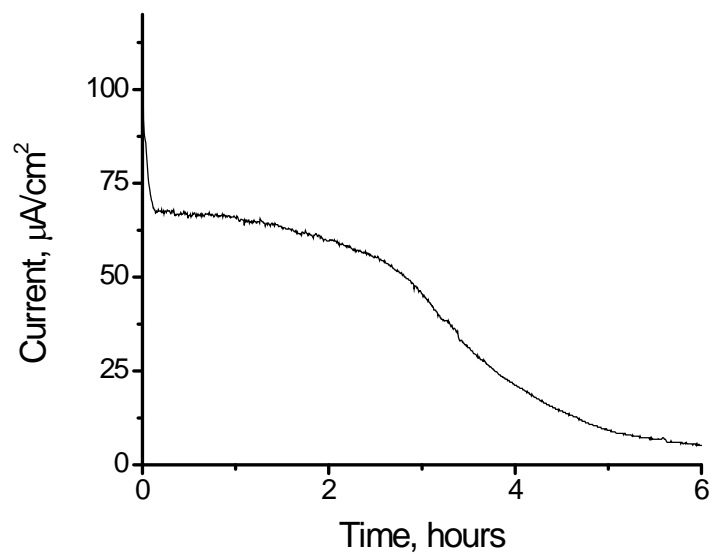


**Figure 4.41:** PdED of PPy on the surface of the PEC cell in 0.1 M NaCl aqueous electrolyte containing 0.01 M Pyrrole.

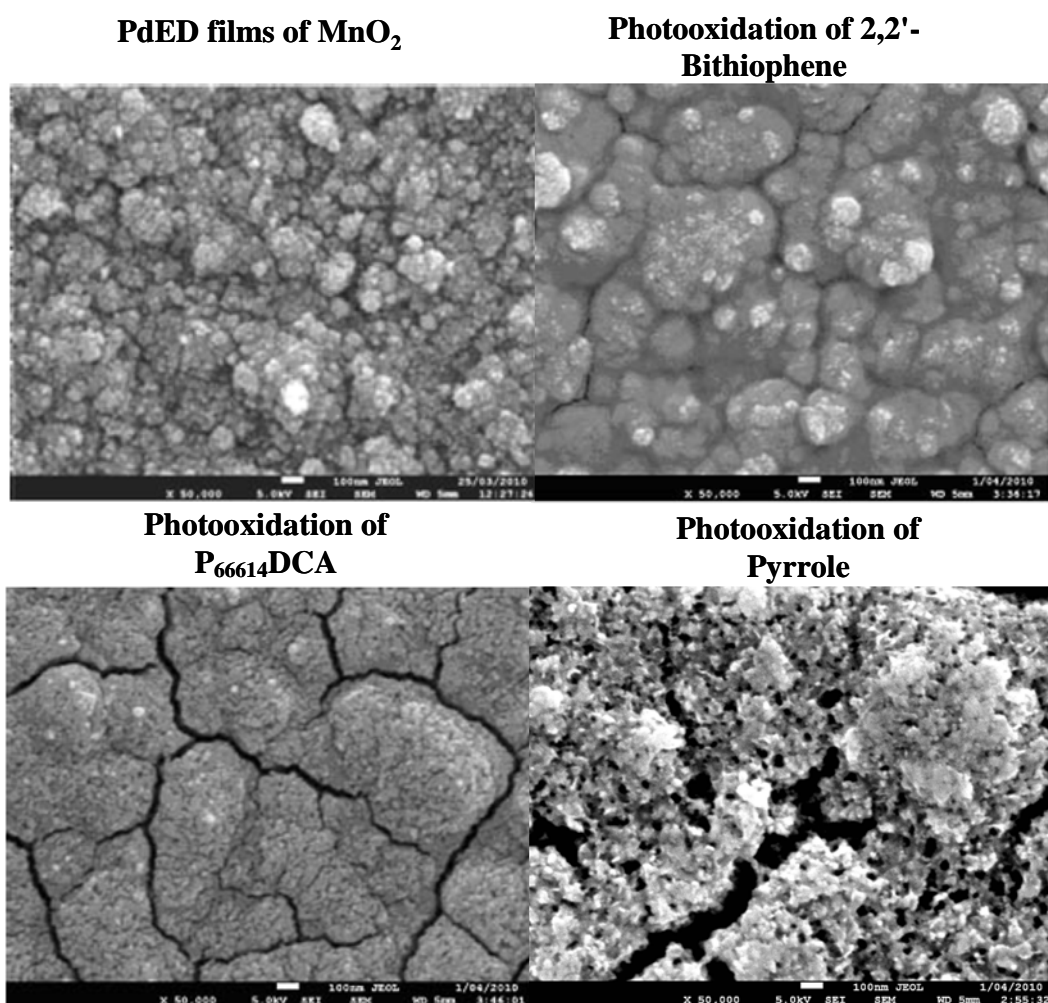


**Figure 4.42:** SEM images of several structures formed during PdED of 2,2'-Bithiophene, [P<sub>66614</sub>][DCA] and Pyrrole on the surface of CdS/MnO<sub>2</sub>.

EDX spectra of PPy films PdED on the surface of the CdS/MnO<sub>2</sub> structure are shown in Figure 4.43. Although such PEC cell becomes electrochemically inactive due to the insulation from the PPy film (see Figure 4.41), presence of Cd, S, Mn and carbon can be clearly seen in the EDX spectrum. These facts confirm the ability of PPy to effectively passivate the electrode surface, which is the key property of the self-repair agent in the water splitting cell.

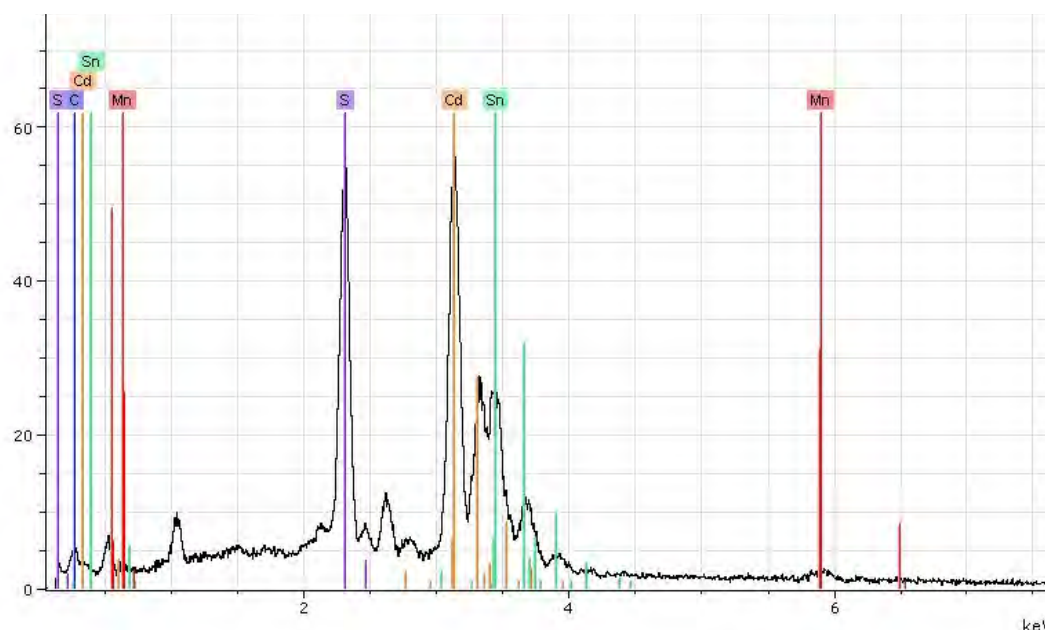


**Figure 4.43:** EDX spectrum of PdED PPy films on the surface of CdS/MnO<sub>2</sub> electrode.

As can be seen from the data presented above, insulating films based on PBTh and [P<sub>66614</sub>][DCA] are very effective and are able to insulate not only LHS but also the surface of HC, hence making the water oxidation impossible. On the contrary, it was possible to grow thicker films based on PPy without deterioration in the photo-driven electrochemical activity (see Figure 4.41). With a higher potential available at the surface of the LHS compared to the HC, it becomes possible to establish deposition conditions when the LHS is protected, while the HC remains active towards the water oxidation reaction.

#### **4.6. Performance of the water splitting cell**

As was discussed above, stability of the water splitting cell strongly depends on isolation of the LHS from the aggressive environment generated by the water oxidation process. The results shown above allow us to effectively deposit the HC and self-repair agents on the surface of the LHS.

Several ways can be utilized for assessment of the PEC cell stability towards oxidation. One is based on the use of an external oxidation agent, which may be dissolved in the electrolyte, while the other is determined by the photo-generated charges produced during cell operation as shown in Figure 4.44.

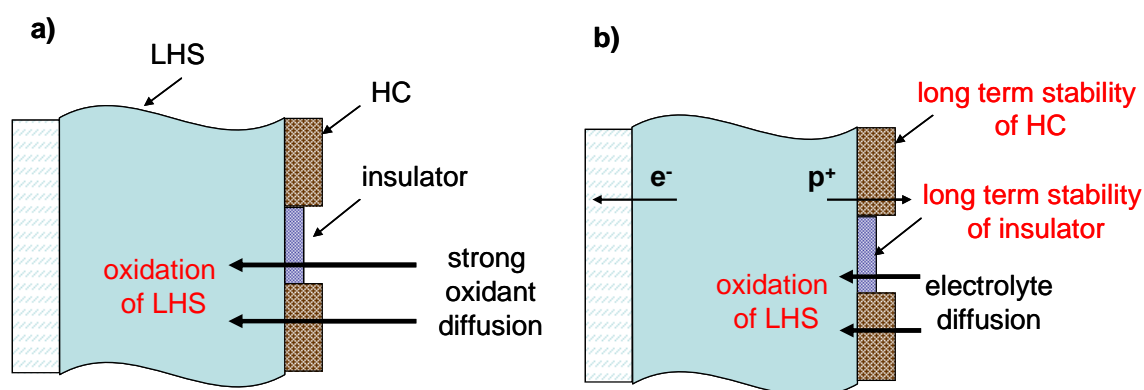


**Figure 4.44:** Stability assessment of the water splitting cell using a) strong oxidizing agent; b) water electrolysis under light illumination.

The former method is advantageous for it can relatively quickly provide assessment of the PEC cell performance by answering the question: How effectively is the LHS isolated from the electrolyte? Although more time consuming, the second method is the ultimate in assessment of the PEC cell performance. Stability measured by this method also includes the influence of the HC and self-repair agent on the overall performance of the water splitting cell.

#### 4.6.1. Stability of water splitting cells in the presence of a strong oxidizing agent

The main advantages of this method lie in its simplicity and the speed, at which general assessment of the films quality can be made. The film thickness of the LHS is measured with the use of UV-vis absorption spectroscopy at 400 nm. Reduction in absorbance at this wavelength and loss of the photo-chemical current during the water splitting process indicate dissolution of the light harvesting material. In multilayered structures of the PEC cell, additional absorption at 400 nm is due to the presence of  $\text{MnO}_2$  and over-oxidized PPy films. These materials were found to be stable in a concentrated sodium perchlorate solution and do not change the absolute value of absorption at 400 nm over time.

In order to compare data obtained for multilayered structures with those for uncoated CdS, relative absorption ( $A_{rel}$ ) was calculated from Equation 4.4, where  $A_{fin}$  and  $A_{max}$  are final and maximum values of absorption, respectively. The final value of absorption, when all of the CdS is dissolved corresponds to the absorption by PPy and  $MnO_2$ .

$$A_{rel} = \frac{A - A_{fin}}{A_{max} - A_{fin}} \cdot 100\% \quad (4.4)$$

During oxidation in a concentrated solution of sodium perchlorate, CdS, CdS/ $MnO_2$ , and CdS/PPy, became photo-chemically inactive, indicating total dissolution of CdS. As can be seen from Figure 4.45 the oxidative dissolution of CdS is rapid. Although presence of  $MnO_2$  and PPy films significantly enhances corrosion resistance of CdS, even such films completely deteriorate after a few minutes.

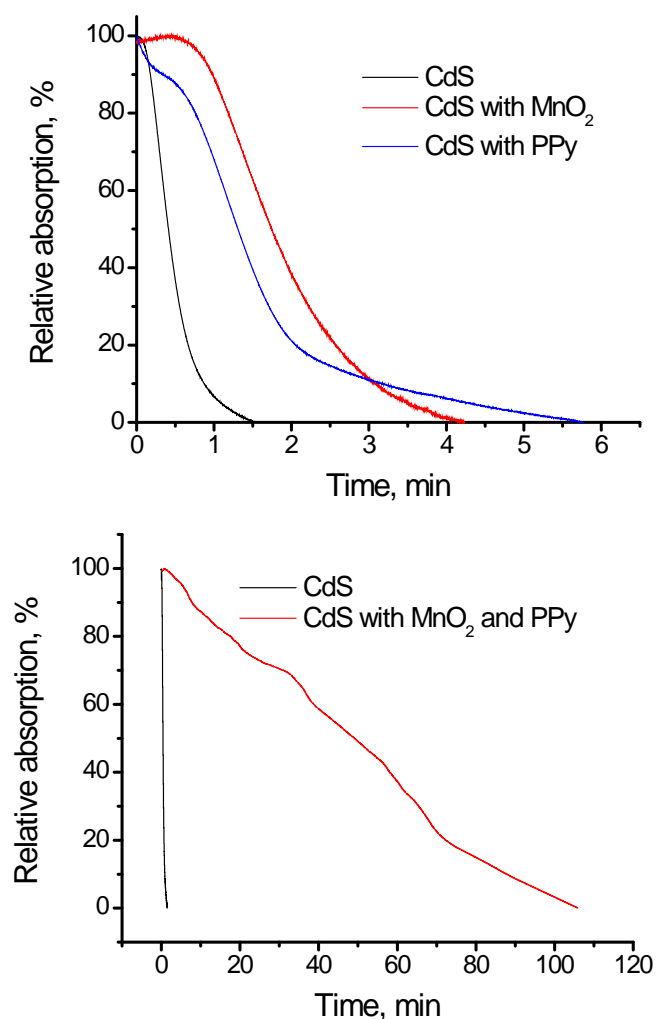


**Figure 4.45:** Relative absorbance of films at 400 nm in a concentrated solution of sodium perchlorate.

When over-oxidized PPy films were used as a self-repair agent in the PEC cell, stability of the LHS was greatly enhanced as shown in Figure 4.45. Even after prolonged exposure to the aggressive environment of concentrated sodium perchlorate, the PEC cell thus prepared was able to generate current upon photo-irradiation, indicating presence of intact CdS. Thus, we confirmed that presence of the HC and self-repair agent can help isolate the LHS from a contact with the electrolyte.

#### 4.6.2. Photo-electrochemical test of the water splitting cell

In this type of experiment, the PEC cell was illuminated by a Xe light source (light intensity close to 1 sun) in an aqueous electrolyte. The electron current from the collector (FTO) to the counter electrode (graphite) was measured over time.

Similar to the stability results obtained for the experiments with the strong oxidizing agent, PdED of HC significantly improved the stability of the PEC cell compared to unprotected CdS films as shown in Figure 4.46. It should be noted, however, that although the improved electrocatalytic activity of such cells reduces significantly after 10-15 hours following a typical trend shown in the inset Figure 4.46.

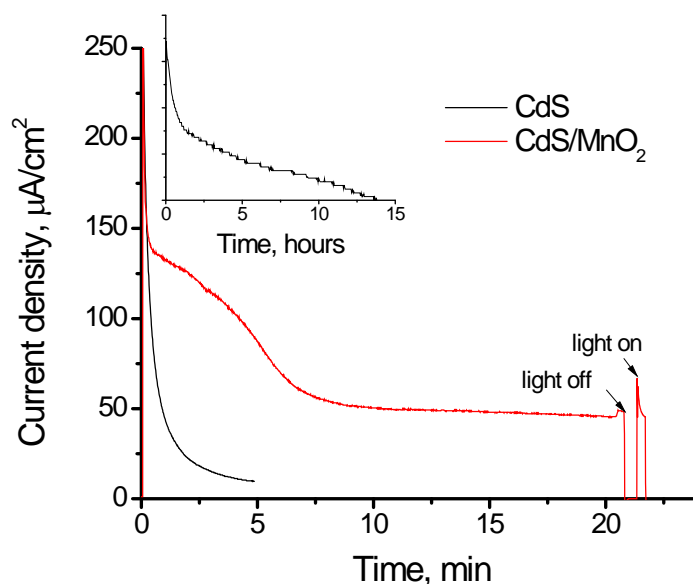


**Figure 4.46:** Dependence of photocurrent over time for a CdS/MnO<sub>2</sub> electrochemical cell in an aqueous solution of 0.1 M Na<sub>2</sub>SO<sub>4</sub> under 1 sun light irradiation. A typical dependence of current density over a long period of time is shown in the inset.

The photo-electrochemical response of the PEC cell based on CdS films and CdS films protected with MnO<sub>2</sub> and PPy is shown in Figure 4.47.

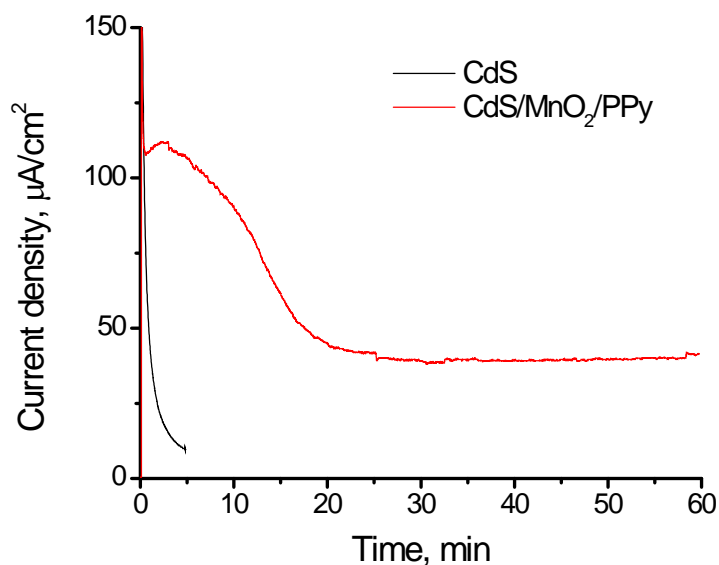


**Figure 4.47:** Dependence of photocurrent on time for the CdS/MnO<sub>2</sub>/PPy electrochemical cell in aqueous solution of 0.1 M Na<sub>2</sub>SO<sub>4</sub> under 1 sun light irradiation.

Films protected by a combination of MnO<sub>2</sub> and PPy show exceptional performance compared to untreated CdS films, maintaining their catalytic activity for more than 76 hours as seen in Figure 4.48.

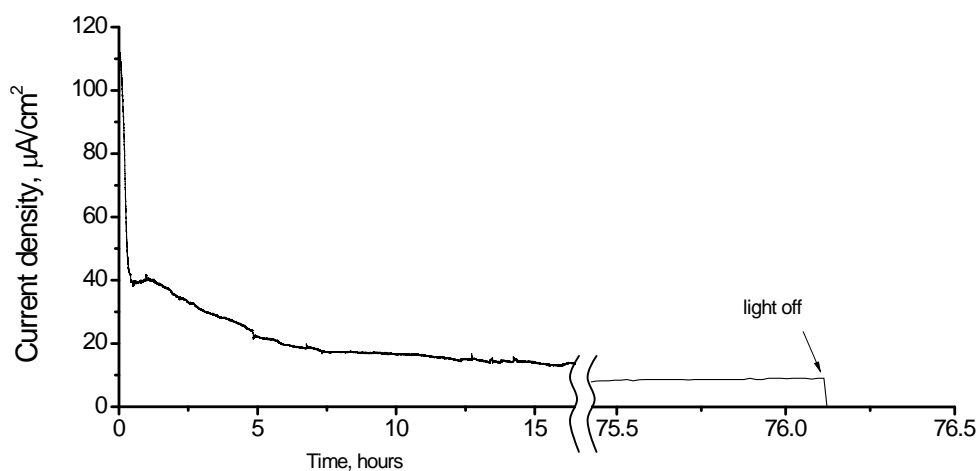


**Figure 4.48:** Dependence of photocurrent over prolong period of time for the CdS/MnO<sub>2</sub>/PPy electrochemical cell in an aqueous solution of 0.1 M Na<sub>2</sub>SO<sub>4</sub> under 1 sun light irradiation.

The data obtained from the water splitting experiments under the visible light irradiation are consistent with those obtained from experiments involving a strong oxidizing agent. These experiments confirm the validity of the hypothesis that

improvement in stability of PEC cells can be achieved through the separation of the LHS layer from the electrochemical catalyst.

#### 4.7. Conclusions

A novel method of  $\text{MnO}_2$  electrochemical deposition utilizing various types of ILs was developed in this work. The data obtained from EDX confirm the presence of manganese in the films, while Raman spectra suggest the formation of  $\gamma\text{-MnO}_2$ . During the electrodeposition from EAN and  $[\text{P}_{4444}]\text{Cl}$ , film thickness can be easily controlled through the deposition time (*i.e.* charge), while variation in the electrolyte pH and current density allows for the tailoring of the structural morphology of the HC layer and production of both high surface area and compact  $\text{MnO}_2$  structures.

Electrodeposited  $\text{MnO}_2$  films show a good capacitive behavior. The calculated specific capacity further proves the ability to deposit more compact structures from EAN compared to  $[\text{P}_{4444}]\text{Cl}$ . The value of the film resistance changes linearly with the film thickness and is similar to that of pure  $\text{MnO}_2$  crystals. The later became possible through the electrodeposition from ILs at high temperatures. The Mott-Schottky analysis confirms typical trends seen in p-type semiconductors and the value of the flat band potential similar to that expected from  $\text{MnO}_2$ . The value of the attenuation coefficient calculated for  $\text{MnO}_2$ , for wavelengths from 350 to 800 nm, allows analysis of the film thickness in multilayered structures.

The electrodeposited  $\text{MnO}_2$  films show good catalytic activity and long-term stability towards the water oxidation reaction. The catalytic performance is comparable to the Pt electrode in neutral electrolytes and exceeds that of Pt in basic solutions.

In this work PdED was used for the deposition of the HC layer in the PEC cell. By utilizing the natural advantages of LHS with the chemical properties and thermal stability of ILs, it became possible to deposit compact and uniform  $\text{MnO}_2$  films. Presence of manganese is confirmed by the data obtained from EDX measurements, while UV-vis absorption spectroscopy can be effectively used to estimate the thickness of the film deposited on the CdS surface.

All compounds investigated as potential self-repair agents formed insulating films upon oxidation on the FTO electrode. Films based on oxidation of PPy, PBTh, and DCA,

were used as self-repair agents in the PEC cell. PdED was also successfully used for the deposition of the self-repair agent in the PEC cell. EDX spectra confirm presence of LHS and HC (Cd, S, and Mn) in the structure after deposition. Thin films are sufficient to isolate the CdS layer when PBTh or DCA oxidation products were used as self-repair agents. It was also possible to deposit thicker films for PPy, which can be seen in the SEM images.

When over-oxidized PPy films were used as self-repair agent in the PEC cell, stability of the LHS in the presence of the strong oxidizing agent was greatly enhanced. The data obtained from the water splitting experiments under the visible light irradiation are consistent with those obtained from experiments involving a strong oxidizing agent. The PEC cell prepared in such a manner was able to maintain its catalytic activity for more than 76 hours under continuous light irradiation (light intensity equivalent to about 1 sun).

The concept developed in this work is based on the separation of the LHS from the electrooxidation site in the PEC cell to enhance the overall stability of the water splitting cell. Such concept can potentially be applied to a variety of efficient, yet unstable systems to achieve efficient and long-lasting water splitting.

## References

- [1] O. Khaselev and J. A. Turner, *Science* **1998**, 280, 425-427.
- [2] A. J. Nozik, *Annu. Rev. Phys. Chem.* **1978**, 29, 189-222.
- [3] A. Kudo and Y. Miseki, *Chem. Soc. Rev.* **2009**, 38, 253-278.
- [4] F. E. Osterloh, *Chem. Mat.* **2008**, 20, 35-54.
- [5] N. Buhler, K. Meier and J. F. Reber, *J. Phys. Chem.* **1984**, 88, 3261-3268.
- [6] K. Kalyanasundaram, E. Borgarello, D. Duonghong and M. Gratzel, *Angew. Chem. Int. Ed.* **1981**, 20, 987-988.
- [7] J. F. Reber and M. Rusek, *J. Phys. Chem.* **1986**, 90, 824-834.
- [8] K. N. Ferreira, T. M. Iverson, K. Maghlaoui, J. Barber and S. Iwata, *Science* **2004**, 303, 1831-1838.
- [9] K. Fujimura, T. Matsui, K. Izumiya, N. Kumagai, H. Habazaki, A. Kawashima, K. Asami and K. Hashimoto, *Mater. Sci. Eng. A-Struct. Mater. Prop. Microstruct. Process.* **1999**, 267, 254-259.
- [10] M. S. El-Deab, M. I. Awad, A. M. Mohammad and T. Ohsaka, *Electrochem. Commun.* **2007**, 9, 2082-2087.
- [11] F. Jiao and H. Frei, *Chem. Commun.* 46, 2920-2922.
- [12] S. C. Pang, M. A. Anderson and T. W. Chapman, *J. Electrochem. Soc.* **2000**, 147, 444-450.
- [13] M. S. Wu, *Appl. Phys. Lett.* **2005**, 87, 153102 (3 pp.).
- [14] N. Nagarajan, H. Humadi and I. Zhitomirsky, *Electrochim. Acta* **2006**, 51, 3039-3045.
- [15] C. L. Xu, S. J. Bao, L. B. Kong, H. Li and H. L. Li, *J. Solid State Chem.* **2006**, 179, 1351-1355.
- [16] P. Liu, S. H. Lee, Y. F. Yan, C. E. Tracy and J. A. Turner, *J. Power Sources* **2006**, 158, 659-662.
- [17] J. N. Broughton and M. J. Brett, *Electrochim. Acta* **2005**, 50, 4814-4819.
- [18] P. Ruetschi, *J. Electrochem. Soc.* **1988**, 135, 2657-2663.
- [19] H. Metin and R. Esen, *Semicond. Sci. Tech.* **2003**, 18, 647-654.
- [20] S. Z. El Abedin and F. Endres, *ChemPhysChem* **2006**, 7, 58-61.

- [21] Frank Endres, Douglas MacFarlane and A. Abbott., *Electrodeposition from ionic liquids*, Chichester : Wiley-VCH, 2008, Weinheim, **2008**, pp. 387.
- [22] W. Lu, A. G. Fadeev, B. H. Qi, E. Smela, B. R. Mattes, J. Ding, G. M. Spinks, J. Mazurkiewicz, D. Z. Zhou, G. G. Wallace, D. R. MacFarlane, S. A. Forsyth and M. Forsyth, *Science* **2002**, 297, 983-987.
- [23] F. Endres and S. Z. El Abedin, *Phys. Chem. Chem. Phys.* **2006**, 8, 2101-2116.
- [24] O. Mann, G. B. Pan and W. Freyland, *Electrochim. Acta* **2009**, 54, 2487-2490.
- [25] S. Z. El Abedin, A. Y. Saad, H. K. Farag, N. Borisenko, Q. X. Liu and F. Endres, *Electrochim. Acta* **2007**, 52, 2746-2754.
- [26] D. D. Shivagan, P. J. Dale, A. P. Samantilleke and L. M. Peter, *Thin Solid Films* **2007**, 515, 5899-5903.
- [27] J. K. Chang, C. H. Huang, W. T. Tsai, M. J. Deng, I. W. Sun and P. Y. Chen, *Electrochim. Acta* **2008**, 53, 4447-4453.
- [28] M. Ghaemi, L. Khosravi-Fard and J. Neshati, *J. Power Sources* **2005**, 141, 340-350.
- [29] S. Devaraj and N. Munichandraiah, *Electrochem. Solid State Lett.* **2005**, 8, A373-A377.
- [30] J. F. Wager, *Thin Solid Films* **2008**, 516, 1755-1764.
- [31] S. A. Sherif, F. Barbir and T. N. Veziroglu, *Sol. Energy* **2005**, 78, 647-660.
- [32] H. J. Lee and S. M. Park, *J. Phys. Chem. B* **2005**, 109, 13247-13254.
- [33] A. Michalik and M. Rohwerder, *Z. Phys. Chemie-Int. J. Res. Phys. Chem. Chem. Phys.* **2005**, 219, 1547-1559.
- [34] D. R. MacFarlane, J. M. Pringle, P. C. Howlett and M. Forsyth, *Phys. Chem. Chem. Phys.* **12**, 1659-1669.
- [35] P. C. Howlett, T. Khoo, G. Mooketsi, J. Efthimiadis, D. R. MacFarlane and M. Forsyth, *Electrochim. Acta* **2010**, 55, 2377-2383.
- [36] N. Miyamoto, S. Kugino and T. Nakamoto, *Electrochemistry* **2000**, 68, 254-256.
- [37] L. Cammarata, S. G. Kazarian, P. A. Salter and T. Welton, *Phys. Chem. Chem. Phys.* **2001**, 3, 5192-5200.
- [38] M. Nakayama, A. Tanaka, Y. Sato, T. Tonosaki and K. Ogura, *Langmuir* **2005**, 21, 5907-5913.
- [39] M. C. Bernard, A. H. L. Goff, B. V. Thi and S. C. Detorresi, *J. Electrochem. Soc.* **1993**, 140, 3065-3070.
- [40] S. L. Chou, F. Y. Cheng and J. Chen, *J. Power Sources* **2006**, 162, 727-734.

- [41] Y. Xu and M. A. A. Schoonen, *Am. Miner.* **2000**, *85*, 543-556.
- [42] A. M. Fundo and L. M. Abrantes, *Russ. J. Electrochem.* **2006**, *42*, 1291-1297.
- [43] S. Deabate and F. Henn, *Electrochim. Acta* **2005**, *50*, 2823-2835.
- [44] F. Tian, R. Jinnouchi and A. B. Anderson, *J. Phys. Chem. C* **2009**, *113*, 17484-17492.
- [45] A. Era, Z. Takehara and Yoshizawa, S., *Electrochim. Acta* **1967**, *12*, 1199-1212.
- [46] J. Rodriguez, H. J. Grande and T. F. Otero, *Handbook of Organic Conductive Molecules and Polymers*, John Wiley & Sons, New York, **1997**, pp. 415.
- [47] H. L. Ge, G. J. Qi, E. T. Kang and K. G. Neoh, *Polymer* **1994**, *35*, 504-508.
- [48] B. Rasch and W. Vielstich, *J. Electroanal. Chem.* **1994**, *370*, 109-117.
- [49] K. Kubo, T. Nonaka and K. Odo, *Bull. Chem. Soc. Jpn.* **1976**, *49*, 1339-1341.

## Chapter 5

### General conclusions and future work

#### 5.1. General conclusions

The aims of this work were to:

- Examine the influence of dopant and quantum size effects in nanoparticles on the energy structure of the material and its potential to improve their light absorption.
- Develop novel methods for low cost, efficient deposition of high quality metal sulfide semiconductors and their alloys utilizing electrodeposition from ionic liquids at high temperatures.
- Develop and test novel PEC cell structures based on metal sulfides that provide high corrosion resistance of the cell during photo-electrochemical water splitting.

A novel method for creating defect states in CdS nanoparticles by using carbonate modification was developed that allowed for synthesis of highly luminescent CdS nanocrystals *via* a reverse micelle method at room temperature in aqueous solution. The data measured with HRTEM and DLS confirm presence of spherical particles, whose size can be controlled by variation of the water to surfactant mole ratio. The addition of the carbonate dopant significantly reduces the energy of the absorption edge for CdS particles. In addition to emission in the UV and red regions, a broad emission in the visible part of the spectra was observed for CdS nanoparticles synthesized in the presence of carbonate ions. The color of the photo-luminescence from chemically modified CdS (cmCdS) is size dependant and can be red shifted with an increase in particle size. The use of “core shell” structures based on cmCdS significantly improved quantum efficiency of the nanocrystals, which remains around 20% even after six months of storage as a suspension in heptane.

For electrodeposition of metal sulfides in this work, elemental sulfur was used as a sulfide precursor in ionic liquid electrolytes based on [P<sub>66614</sub>][DCA], [P<sub>4444</sub>][Cl], [P<sub>1444</sub>][Tosylate], and [P<sub>66614</sub>][NTf<sub>2</sub>]. It is possible to establish that all ILs are electrochemically stable at high temperatures in the region of interest for sulfur reduction. In the case of [P<sub>66614</sub>][NTf<sub>2</sub>] it was shown that solubility of CdCl<sub>2</sub> in the IL can be increased when small amount of organic solvents (EC-MEC) are added to IL electrolyte. Sulfur has by far the greater solubility in the ILs investigated, compared to CdCl<sub>2</sub> and tends to form colored complexes with Cd(II) in [P<sub>66614</sub>][DCA] and [P<sub>4444</sub>][Cl]. A concentration of sulfur in electrolytes higher than that of Cd(II) led to absence of Cd(II) reduction on the substrate, with sulfur reduction becoming unstable at high temperatures (*i.e.* [P<sub>66614</sub>][DCA] at T ≥ 100 °C and in [P<sub>1444</sub>][Tosylate] at T ≥ 130 °C). When sodium thiosulfate was used as the sulfide precursor in electrolytes containing [P<sub>66614</sub>][NTf<sub>2</sub>], [P<sub>66614</sub>][DCA], electrodeposition resulted in formation of black deposits on the electrode surface. With the use of [P<sub>1444</sub>][Tosylate], however, it was possible to produce uniform films that have the optical characteristics of CdS.

By optimizing the conditions using [P<sub>1444</sub>][Tosylate], it was possible to electrodeposit CdS films with almost 1:1 stoichiometric ratio between Cd and S that did not contain the large precipitates that are common in the CBD method. The fact that no Cl signal can be detected in the present work suggests that the technique can be used to prepare Cl free films, which in turn may enhance electrical properties. The XRD data suggest that the deposited polycrystalline films have specific orientation and are composed of nanocrystals similar in size to these prepared *via* CVD. The Mott-Schottky analysis of the CdS films confirms typical trends seen in n-type semiconductors and the value of the flat band potential was similar to that expected for CdS, while the band gap energy measured *via* UV-vis spectroscopy is in accord with data reported in the literature. Typical quantum size effects were also observed in ultra thin films (<10nm). During annealing of CdS films at a high temperature, the value of the band gap energy was reduced, while no deterioration due to the presence of Cd(OH)<sub>2</sub> and water, known in the literature, was observed.

The applicability of the method developed was demonstrated for electrodeposition of CdS on maleic anhydride, Ti, Al, Au, high surface area TiO<sub>2</sub>, and PEDOT substrates. Even short time of deposition on porous TiO<sub>2</sub> produces CdS films of exceptional absorbance. Thus, it becomes possible to combine the high absorption of porous structures

with the low recombination coefficients observed for thin films. Although the reported method would need to be modified to be applied to the deposition of FeS and In<sub>2</sub>S<sub>3</sub>, electrodeposition of NiS and ZnS was demonstrated under conditions similar to the ones used for CdS. Thus, we were also able to deposit mixed NiS and CdS as well as ZnS and CdS by the technique developed in this work.

The photo-electrochemical cell developed in this work consists of a light harvesting semiconductor (*i.e.* CdS), a hole conductor/electro catalyst (*i.e.* MnO<sub>2</sub>), and self-repair agent (*i.e.* polypyrrole). One of the functions that are placed upon the hole conductor (HC) is chemical protection of the light harvesting semiconductor (LHS). Electrochemical deposition from electrolytes based on EAN and [P<sub>4444</sub>]Cl resulted in formation of  $\gamma$ -MnO<sub>2</sub> with electrical properties similar to pure MnO<sub>2</sub>. The thickness can be easily controlled through the deposition time (charge), while a variation in electrolyte pH and current density allows for synthesis of both high surface area and compact MnO<sub>2</sub> structures, which was supported by the SEM images and specific capacity measurements. Electrodeposited MnO<sub>2</sub> films show a good catalytic activity and long term stability towards the water oxidation reaction. The catalytic performance is comparable to the Pt electrode in neutral electrolytes and exceeds that of Pt in basic solutions.

All investigated compounds tested as potential repairing agents formed insulating films upon oxidation on the FTO electrode. Films based on oxidation of PPy, PBTh, and DCA, were used as repairing agents in the PEC cell.

By utilizing the natural advantages of LHS films with the chemical properties and thermal stability of ILs it became possible to deposit compact and uniform MnO<sub>2</sub> films using a photo-driven electrochemical deposition technique. Presence of manganese was confirmed by the data obtained from EDX measurements, while UV-vis absorption spectroscopy can be effectively used to estimate thickness of films deposited on the CdS surface.

The photo-driven electrochemical deposition was also successfully used for the deposition of the repairing agent in the PEC cell. EDX spectra confirm presence of LHS and HC (Cd, S, and Mn) in the structure after the deposition.

When over-oxidized PPy films were used as self-repair agents in the PEC cell structure, stability of the LHS in the presence of a strong oxidizing agent was greatly

enhanced. The data obtained from water splitting experiments under visible light irradiation were also consistent with those obtained from experiments involving strong oxidizing agent. The PEC cell prepared in such a manner was able to maintain its catalytic activity for more than 76 hours under continuous light irradiation (equivalent to about 1 sun).

The concept developed in this work is based on separation of the LHS from the electrooxidation site in the PEC cell, so that it becomes possible to oxidize water on the surface of  $\text{MnO}_2$  and enhance the overall stability of the water splitting cell. Such a concept can potentially be applied to a variety of efficient, yet unstable systems to achieve efficient and long lasting water splitting.

## 5.2. *Future work*

Highly luminescent semiconducting nanocrystals developed in this work can be applied in electroluminescent devices to obtain high levels of efficiency and broad emission spectra.

In this work the novel method was developed for electrochemical deposition of high quality CdS thin films on various substrates using thiosulfate as sulfide precursor. The applicability of this technique for deposition of mixed metal sulfides was demonstrated with  $\text{Zn}_x\text{Cd}_{1-x}\text{S}_y$  and  $\text{Ni}_x\text{Cd}_{1-x}\text{S}_y$ . Further work should be done to establish the electric properties of these materials in relation to their chemical composition, which is essential to successfully tune the electric properties of compound semiconductors. The method can be additionally modified to allow for electrodeposition of a broader range of metal sulfides (*e.g.* FeS,  $\text{In}_2\text{S}_3$ ).

Further work on electrodeposition of metal sulfides should include optimization of the technique for electrodeposition of compound semiconductors with various chemical compositions (*e.g.*  $\text{Zn}_x\text{Cd}_{1-x}\text{S}_y$  and  $\text{Ni}_x\text{Cd}_{1-x}\text{S}_y$ ) and characterization of their electric properties for potential use in photo-electrochemical water splitting.

Future work on photo-electrochemical water splitting could include

- The use of a LHS with high photoelectrochemical conversion efficiency (*e.g.* GaAs) in the PEC cell structure.

- Electrochemical and photo-driven electrochemical deposition of various water oxidation catalysts (iron oxides and cobalt oxides) for the use in the PEC cell structure.
- Electrochemical polymerization and photo-driven electrochemical polymerization of self-repair agents for the use in the PEC cell structure (e.g. 3-thiophenecarbonitrile and 3,4-propylenedioxy-thiophene).

## Chapter 6

### Appendix

#### 6.1. Publications

1. R. Vijayaraghavan, A. Izgorodin, V. Ganesh, M. Surianarayanan and D. R. MacFarlane, *Angew. Chem. Int. Edit.* 49, 1631-1633.
2. A. Izgorodin, O. Winther-Jensen, B. Winther-Jensen, D. R. MacFarlane, *Phys. Chem. Chem. Phys.*, 2009, 11, 8532 – 8537.

#### Conference contributions

- 5<sup>th</sup> Annual International Electromaterials Science Symposium and 4<sup>th</sup> Australasian Symposium on Ionic Liquids (ASIL-4). February 17 - 19 2010, Monash University, Melbourne. Oral presentation entitled “Electrodeposition of compound semiconductors for water splitting applications”.
- 3<sup>rd</sup> International Congress on Ionic Liquids, May 31 - June 4 2009, Cairns Australia. Poster presentation entitled “Electrodeposition of thin film CdS”.
- Annual Australian Centre of Excellence for Electromaterials Science (ACES) Symposium, St. Vincent’s Institute of Medical Research, Melbourne, Australia, 3-4 October 2007. Oral presentation entitled “Highly luminescent CdS nanocrystals”

# Long-Term Structural and Chemical Stability of DNA in Hydrated Ionic Liquids\*\*

Ranganathan Vijayaraghavan, Aleksey Izgorodin, Venkatraman Ganesh, Mahadevan Surianarayanan, and Douglas R. MacFarlane\*

There is much interest in the use of DNA as an advanced material.<sup>[1]</sup> For example, DNA has been discussed as the “ultimate” material for molecular computing<sup>[2]</sup> and there is much effort directed towards investigating this application. Recently, DNA has also been employed in templated chemical synthesis, nanomachines, and biosensors.<sup>[3–5]</sup> The use of DNA as a biomaterial from a variety of readily available sources has gained importance in recent years, especially for the surface treatment of implanted materials.<sup>[6]</sup> Since it is rich in phosphate groups it has a strong affinity for bone, and DNA has been modified for use as a bone-guiding scaffold by intercalating antibiotics between the stacked base pairs.<sup>[7]</sup> The water-insoluble form of DNA also finds a range of other applications as a biomaterial.<sup>[8,9]</sup>

Although DNA is considered to be reasonably stable in aqueous solution, there are various conditions of temperature, pH, ionic strength, depurination, deamination, solvents, etc. that can disrupt the DNA helix and cause denaturation.<sup>[10,11]</sup> The solubility and stability of DNA has been studied in a variety of nonaqueous<sup>[12]</sup> and mixed solvents<sup>[13]</sup> and it was shown that DNA loses its double-helical structure when dissolved in dimethyl sulfoxide, formamide, or methanol, whereas the structure is retained in ethylene glycol and to some extent in glycerol. Conventionally DNA is stored under refrigeration for short- and long-term applications and the influence of storage temperature has been discussed in the literature;<sup>[14]</sup> however, DNA molecules are not stable in solution at ambient temperatures for long periods ( $\geq 1$  month). Therefore, finding a medium in which DNA is soluble without loss of its structure and in which it is stable for long periods of use at room temperature is an important bottleneck in this field.

In recent years, a number of biocompatible hydrated ionic liquids (ILs) have been identified, for example, choline

dihydrogenphosphate (CDP) with 20% dissolved water, and shown to be good solvents for proteins.<sup>[15,16]</sup> In the ionic solution, some proteins are tremendously stabilized as compared to aqueous solutions,<sup>[17,18]</sup> thus leading to a variety of applications in drug delivery and sensor development. The presence of a solute amount of water in these systems is an important aspect of these media. The effect of ILs as solvents on the stability of other biopolymers such as DNA is unknown; hence, this work focuses on the solubility, structure, and long-term stability of DNA in a number of these novel, choline-based solvent media.

Circular dichroism spectra (Figure 1) were recorded for DNA (from salmon testes) dissolved in choline lactate (CL) IL and in aqueous solution controls, stored at different

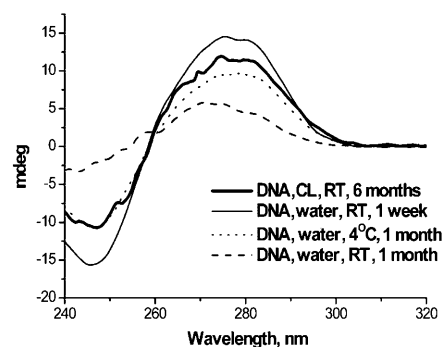


Figure 1. Circular dichroism spectra of DNA in water or IL stored for different time intervals at room temperature (RT) or 4 °C.

temperatures and time intervals. It can be seen from Figure 1 that the presence of the characteristic positive band at 275 nm (arising from base stacking) and a negative band at 245 nm resulting from the B conformation of DNA<sup>[19,20]</sup> (with a crossover at 258 nm) in the IL/DNA samples indicates that the native double-helical structure is indeed retained in these IL solutions. Such solubility with retention of structure is probably associated with the ability of the IL ions to engage in hydrogen bonding with the exterior of the DNA helix. Since DNA is anionic, the most likely H-bonding would be with the choline cation hydroxy group. Furthermore, these characteristic bands are still present even after 6 months of storage at room temperature. A similar storage stability was observed in CDP and choline nitrate (CN) solutions. On the other hand, the sample dissolved in water and stored at room temperature for 1 month had lost the double-helical structure.

Fluorescence experiments<sup>[21]</sup> were also carried out to assess the effect on stability of different levels of water in the hydrated IL. The results (Figure 2) show that the samples

[\*] Dr. R. Vijayaraghavan, A. Izgorodin, Prof. D. R. MacFarlane  
School of Chemistry, Monash University  
Clayton, Victoria 3800 (Australia)  
E-mail: d.macfarlane@sci.monash.edu.au

Dr. V. Ganesh  
Department of Human Genetics, Sri Ramachandra University  
Porur (India)

Dr. M. Surianarayanan  
Chemical Engineering Division, Central Leather Research Institute  
Chennai (India)

[\*\*] The authors gratefully acknowledge funding from the Australian Research Council for this work including the Federation Fellowship to D.R.M.

Supporting information for this article is available on the WWW under <http://dx.doi.org/10.1002/anie.200906610>.

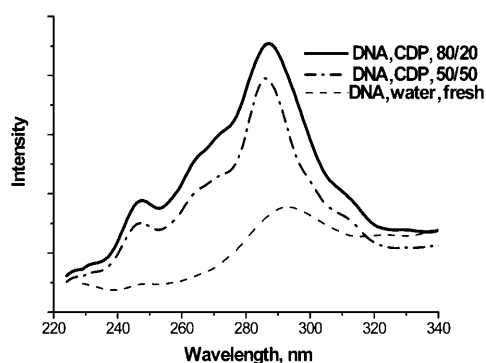


**Figure 2.** Fluorescence spectra of DNA samples in hydrated CDP stored at room temperature for 6 months.

produced the characteristic native DNA fluorescence emission at 287 nm in both the 50:50 and 80:20 aqueous CDP/water mixtures. It has been reported<sup>[22]</sup> that the fluorescence is a result of the presence of the hydrogen-bonded adenine base in native DNA and its intensity and band shape depend on the pH of the medium, being weak at neutral pH. CDP at 20% water content will be slightly more acidic than the 50% water and pure water samples, because of the residual acidity of the dihydrogenphosphate anion, and the intensity differences are therefore as expected.<sup>[22]</sup>

A separate set of experiments was carried out to demonstrate the effect of pH on the fluorescence emission intensity of the DNA samples; the results (Supporting Information, Figure ESI-1) clearly show that the intensity increases with acidity. This intensity increase is attributed to the increased protonation of the base involved (adenine) under these pH conditions. In a separate experiment, the fluorescence spectra of the neat ILs were obtained to confirm that there was no emission in the 240–320 nm region.

To evaluate the stability of DNA dissolved in hydrated CDP at elevated temperatures, fluorescence spectroscopy was carried out at different temperatures on DNA samples in the CDP/H<sub>2</sub>O 50:50 medium; these samples had already been stored for 1 year at room temperature. The fluorescence was recorded over a period of 2 hours at different temperatures (40 and 90 °C and then after returning to room temperature). The results (Figure 3) show that there was only a slight change

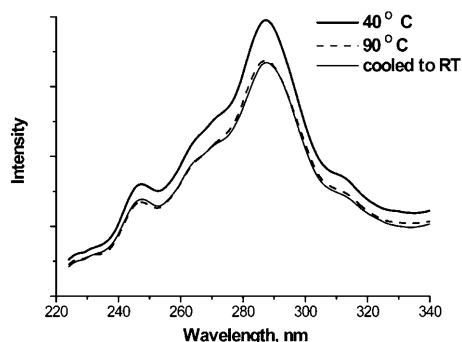


**Figure 3.** Fluorescence spectroscopy of DNA samples in aqueous CDP (50:50) at different temperatures.

in the intensity of fluorescence as a result of the excursion to 90 °C. Differential scanning calorimetry data (not shown) also indicate that no denaturation exotherm is observed below 100 °C. An aqueous sample would be substantially denatured by this excursion. This finding suggests that the DNA sample is stabilized at higher temperatures by the hydrated IL medium, as has been observed in the case of proteins.<sup>[15,16]</sup> This is understood to be the result of the solvent thermodynamics, which strongly favor the denatured state in an aqueous medium at elevated temperature.

CL, CN, and CDP appear to provide good stabilization, whereas it was observed that although DNA was soluble in choline formate (CF), it rapidly denatures in this IL since no fluorescence emission was observed from this sample. The detrimental effect of this IL is possibly connected with its radical activity.<sup>[23]</sup>

To determine if any degradation in molecular weight was taking place during storage, gel electrophoresis studies<sup>[24]</sup> were carried out. Figure 4 shows that the samples of DNA

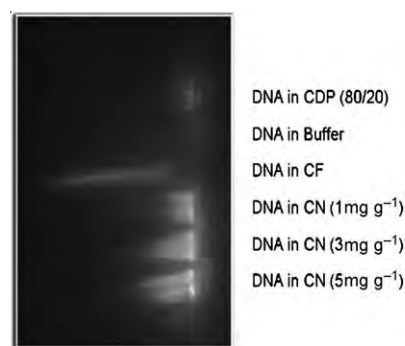


**Figure 4.** Gel electrophoresis of DNA samples stored at room temperature for 6 months.

in buffer and CF stored at room temperature for about 6 months underwent degradation, whereas the DNA samples in CDP (lane 1) and CN (lanes 4–6, with different DNA concentrations) remained intact.

In conclusion, DNA was found to be soluble and exhibit exceptional long-term stability in hydrated ILs based on CL, CN, or CDP. These ILs provide a mild H-bonding environment that is of relatively low water activity, hence slowing the rate of hydrolytic reactions that would otherwise slowly depolymerize or degrade the molecule.

### Experimental Section

Choline salts were prepared as per literature procedures,<sup>[23]</sup> including CDP, CL, CF, and CN. Choline hydroxide (45% in methanol), nitric acid (aqueous 70%), formic acid (99%), lactic acid (99%), phosphate buffer (pH 7.4), and DNA from salmon testes were all purchased from Sigma–Aldrich, while phosphoric acid (85%) was purchased from Merck. CDP and CN are solids with melting points of 185 and 34 °C, respectively, whereas CL and CF are liquid at room temperature. CDP and CN become liquid on addition of small amounts of water; in all cases 20% (w/w) is sufficient to produce a clear, fluid liquid at room temperature. Typically, DNA (1 mg g<sup>-1</sup>) was added to the hydrated ILs. The dissolution of DNA in the hydrated ILs was

slow (ca. 3–4 weeks was required for full dissolution) and depended on the water content: the higher the water content, the more rapidly soluble the DNA became. After dissolution the samples were stored in sealed vials at room temperature.

Received: November 24, 2009

Published online: January 27, 2010

**Keywords:** DNA · fluorescence · helical structures · ionic liquids · solubility

- 
- [1] T. H. LaBean, H. Li, *Nano Today* **2007**, *2*, 26–35.
- [2] D. Normile, *Science* **2002**, *295*, 951.
- [3] Z. J. Gartner, B. N. Tse, R. Grubina, J. B. Doyon, T. M. Snyder, D. R. Liu, *Science* **2004**, *305*, 1601–1605.
- [4] H. Liu, D. Liu, *Chem. Commun.* **2009**, 2625–2636.
- [5] M. Yamada, M. Yokota, M. Kaya, S. Satoh, B. Jonganurakkun, M. Nomizu, N. Nishi, *Polymer* **2005**, *46*, 10102–10112.
- [6] A. Goldman, T. Glumoff, *Nucleic Acids in Chemistry and Biology*, 2nd ed., Oxford University Press, Oxford, **1996**, pp. 375–441.
- [7] M. H. Werner, A. M. Gronenborn, G. M. Clore, *Science* **1996**, *271*, 778–784.
- [8] M. Yamada, K. Kato, M. Nomizu, N. Sakairi, K. Ohkawa, H. Yamamoto, N. Nishi, *Chem. Eur. J.* **2002**, *8*, 1407–1412.
- [9] L. Wang, J. Yoshida, N. Ogata, S. Sasaki, T. Kajiyama, *Chem. Mater.* **2001**, *13*, 1273–1281.
- [10] Y. K. Cheng, B. M. Pettitt, *Prog. Biophys. Mol. Biol.* **1992**, *58*, 225–257.
- [11] T. Lindahl, B. Nyberg, *Biochemistry* **1972**, *11*, 3610–3618.
- [12] G. Bonner, A. M. Klibanov, *Biotechnol. Bioeng.* **2000**, *68*, 339–344.
- [13] B. Hammouda, D. Worcester, *Biophys. J.* **2006**, *91*, 2237–2242.
- [14] J. Legoff, C. Tanton, M. Lecerf, G. Gresenguet, K. Nzambi, H. Bouhlal, H. Weiss, L. Belec, *J. Virol. Methods* **2006**, *138*, 196–200.
- [15] K. Fujita, D. R. MacFarlane, M. Forsyth, *Chem. Commun.* **2005**, 4804–4806.
- [16] a) K. Fujita, D. R. MacFarlane, M. Forsyth, M. Y. Fujita, K. Murata, N. Nakamura, H. Ohno, *Biomacromolecules* **2007**, *8*, 2080–2086; b) K. Fujita, M. Forsyth, D. R. MacFarlane, R. W. Reid, G. D. Elliott, *Biotechnol. Bioeng.* **2006**, *94*, 1209–1213; c) R. Vijayaraghavan, B. C. Thompson, D. R. MacFarlane, Ramadhar Kumar, M. Surianarayanan, S. Aishwarya, P. K. Sehgal, *Chem. Commun.* **2010**, *46*, 294–296.
- [17] N. Byrne, C. A. Angell, *J. Mol. Biol.* **2008**, *378*, 707–714.
- [18] N. Byrne, L. M. Wang, J. P. Belieres, C. A. Angell, *Chem. Commun.* **2007**, *26*, 2714–2716.
- [19] a) W. C. Johnson, *Determination of Conformation of Nucleic Acids by Electronic CD*, Plenum, New York, **1996**; b) C. H. Spink, J. B. Chaires, *J. Am. Chem. Soc.* **1997**, *119*, 10920–10928.
- [20] P. Uma Maheswari, M. Palaniandavar, *J. Inorg. Biochem.* **2004**, *98*, 219–230.
- [21] a) M. C. Murphy, I. Rasnik, W. Chang, T. M. Lohman, T. Ha, *Biophys. J.* **2004**, *86*, 2530–2537; b) J. R. Lakowicz, *Topics in Fluorescence Spectroscopy, Vol. 7: DNA Technology*, Kluwer, New York, **2003**.
- [22] A. N. Pisarevskii, S. N. Cherenkevich, V. T. Andrianov, *J. Appl. Spectrosc.* **1966**, *5*, 452–454.
- [23] O. Winther-Jensen, R. Vijayaraghavan, J. Sun, B. Winther-Jensen, D. R. MacFarlane, *Chem. Commun.* **2009**, 3041–3043.
- [24] J. Sambrook, D. W. Russell, *Molecular Cloning: A Laboratory Manual*, 3rd ed., Cold Spring Harbor Laboratory Press, Cold Spring Harbor, **2001**.
-

# CdS thin-film electrodeposition from a phosphonium ionic liquid†

Alexey Izgorodin, Orawan Winther-Jensen, Bjorn Winther-Jensen  
and Douglas R. MacFarlane\*

Received 6th April 2009, Accepted 12th June 2009

First published as an Advance Article on the web 14th July 2009

DOI: 10.1039/b906995j

Thin, adherent films of CdS were electrodeposited on FTO coated glass by reduction of a thiosulfate precursor in the presence of Cd(II) ions in methyltributylphosphonium (P<sub>1,4,4,4</sub>) tosylate ionic liquid at 130–150 °C. The structural properties of the deposits have been characterized by profilometry, scanning electron microscopy (SEM) and optical microscopy. Energy dispersive X-ray spectroscopy (EDX) was used to evaluate the chemical composition, which was found to be close to stoichiometric. Semiconductor properties including the band gap and flat band potential were calculated from UV-Vis and impedance spectroscopy measurements. The crystal structure was analyzed by X-ray diffraction (XRD). The data obtained from XRD and band gap measurements suggest the presence of hexagonal CdS crystals. The possible growth mechanism of the films is also addressed.

## Introduction

In the past several decades group II–VI semiconductors have attracted significant interest from the scientific community due to their promising electronic properties.<sup>1</sup> Having direct band gap transitions, they are commonly used materials for photovoltaic,<sup>2</sup> optoelectronic and electroluminescent applications.<sup>3</sup> CdS, in particular, is being widely used as a “window” layer material for hetero-junction solar cells (such as CdS/CdTe and CdS/CuInSe<sub>2</sub>) that show overall efficiency of more than 15%.<sup>4</sup> The vast majority of applications of these materials require high quality semiconductor films to be created at low cost. High quality is a significant performance parameter since defect sites present in the lattice act as centers of recombination, decreasing charge carrier mobility and carrier separation efficiency. Thus, the overall efficiency of the thin film device is significantly affected.<sup>5</sup> In order to support high efficiency in solar cells in particular, CdS layers should have compact structure and specific orientation.<sup>4</sup> Sputter deposition,<sup>6</sup> spray pyrolysis<sup>7</sup> and photochemical deposition<sup>8</sup> can be used to create CdS films, but high roughness and poor crystal structure are disadvantages of these techniques. Although films deposited *via* vacuum evaporation,<sup>9,10</sup> chemical vapor deposition<sup>11</sup> (CVD), metal–organic chemical vapor deposition<sup>4</sup> (MOCVD), and electrochemical atomic layer epitaxy<sup>5,12</sup> (ECALE) are of better quality, the costs involved limit their wider application.

One of the most widely used methods to deposit CdS is chemical bath deposition (CBD). The method is based on the slow release of the sulfide anion in an aqueous electrolyte of a cadmium complex (*e.g.* its complex with ammonia).<sup>13</sup> In a typical procedure, ion by ion growth on the surface is accompanied by precipitation of colloidal CdS that is formed in the solution.<sup>13</sup> Thus, although significant improvement of film quality was achieved in the ammonia-free CBD process, the method produces very low yield (~2%), resulting in copious amounts of toxic waste.<sup>14</sup>

Electrodeposition is also a promising technique for deposition of metal sulfides. It is fairly simple, has low cost and produces films at very high yield. Thus far, electrodeposition of CdS films from aqueous solutions,<sup>15,16</sup> ethylene glycol<sup>17</sup> and ionic liquids (ILs)<sup>18</sup> have been reported. The main disadvantages of water based methods are an inability to deposit at high temperatures and the presence of oxygen that drastically decreases the quality of the films. Even though electrodeposition from ethylene glycol and IL allow the growth to be carried out at higher temperatures, CdS films reported so far are of low quality.<sup>17,18</sup> The high temperature at which the deposition in an IL can in principle be conducted allows atom diffusion on the surface during growth, which has a major positive influence on the quality of the films.<sup>19</sup> Ionic liquids have been successfully used for the electrodeposition of a number of metals such as Se, In, Cu, Au, Pt and some semiconductors including Ge, Si, TiO<sub>2</sub>, AlSb, ZnSb, InSb, GaAs, CdTe, CuInSe, Cu(In,Ga)Se and ZnTe.<sup>20–26</sup> One of the key advantages of ionic liquids in this context is their combination, in some cases, of thermal and electrochemical stability that allows the electrodeposition process to be carried out even at elevated temperatures, with minimal interference from solvent chemical, or electrochemical, breakdown.<sup>20–22</sup>

Elemental sulfur is one of the most common precursors for electrochemical deposition of CdS.<sup>17,18</sup> It was shown that the chemical composition of the films is significantly affected by the potential of the working electrode in this process. At a lower potential (*e.g.* from –0.6 to –0.8 V vs. Pt) the appearance of the films shifts from pale yellow to brown, indicating an excess of cadmium.<sup>18</sup> In order to minimize the rate of cadmium reduction, sodium thiosulfate was proposed as a sulfide precursor in the aqueous electrodeposition studies of Rami *et al.*<sup>27</sup> Thus in this work we have developed an ionic liquid based method of electroreduction of thiosulfate to produce CdS, building on the advantages of the ionic liquid as an electro-winning medium. The optical and electrical properties of CdS films thus prepared in this work were of the same or better quality than those prepared *via* ammonia-free CBD, while significantly increasing the deposition yield.

Australian Centre for Electromaterials Science, Monash University,  
Clayton, VIC 3800, Australia.

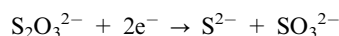
E-mail: d.macfarlane@sci.monash.edu.au

† Electronic supplementary information (ESI) available: SEM images and Mott–Schottky plots of CdS films. See DOI: 10.1039/b906995j

It can be seen from the literature that thin films of CdS (<50 nm) generally show good adhesion to the substrates.<sup>4,18</sup> Adhesion properties of thicker films, however, vary depending on the deposition method. As a common trend, adhesion seems to be better for films with higher fraction of amorphous phase present and, in this case, thick films of CdS can be created.<sup>7,8,14</sup> Due to the low stacking-fault energy of CdS, it becomes harder to dissipate the lattice mismatch between the well ordered crystal structures of the grown film and those of the substrate.<sup>10</sup> The difference in thermal expansion coefficient between them can result in crack formation and loss of adhesion.<sup>10,14</sup> In this work adhesion properties of the films deposited on bare and plasma treated fluorine doped tin oxide (FTO) glass surfaces are also compared; films on plasma treated FTO show very good adhesion to the surface of FTO, thus not limiting the film thickness.

## Results and discussion

During the deposition described here sulfide ions are electrochemically generated at the substrate surface; in the presence of Cd(II) ions, the sulfide precipitates onto the substrate as CdS. The basis for this process is as follows. A typical cyclic voltammogram (CV) of the P<sub>1,4,4,4</sub> tosylate at 100 °C is shown in Fig. 1a. This CV confirms that there are no electrochemical reactions related to the IL in the region of interest. From Fig. 1b it can be seen that reduction of cadmium only takes place at potentials lower than -0.6 V (vs. Ag/AgCl) in P<sub>1,4,4,4</sub> tosylate at 100 °C, which is consistent with the -0.4 V (vs. NHE) reduction potential of cadmium in aqueous electrolytes.<sup>28</sup> Sodium thiosulfate was chosen as the source of sulfide anion *via* reduction according to the reaction:<sup>27</sup>



This process has a less negative reduction potential than elemental sulfur, as can be seen in Fig. 1c; this allows the choice of electrochemical conditions for the deposition under which Cd(II) reduction will not be an interfering process.

Thin films of CdS were thus electrodeposited using the staircase chronopotentiometry technique to find the optimum conditions. Fig. 2 shows a typical plot of current density and electrode potential during deposition at 150 °C. At the beginning of the growth, current density was increased by 20  $\mu\text{A cm}^{-2}$  every minute up to 100  $\mu\text{A cm}^{-2}$ , at which electrodeposition took place. A slight further increase in the electrode potential with time can be attributed to additional resistivity due to the formation of the semiconductor. Since current density is kept constant, temperature will also affect the deposition potential. It should be stressed, though, that in all experiments the potential was not allowed to become more negative than -0.4 V *versus* Ag/AgCl.

A typical surface profile of the films is shown in Fig. 3. Prior to deposition, a section of the FTO was electrically isolated by laser etching. This technique allows us to measure the height of the deposit on top of the FTO glass. The thickness of the films thus measured ranged between 10 nm and 200 nm. The films were quite adherent to the substrate showing no tendency to wash off in water as has often been observed in the literature.<sup>18</sup> Peel tests show no tendency for the films to lift off in the plasma treated case, whereas in the bare FTO case the film

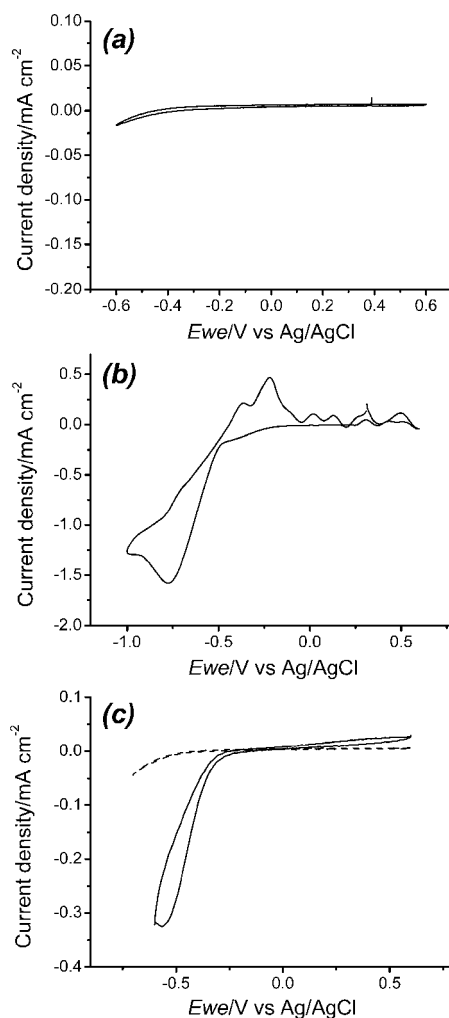


**Fig. 1** Cyclic voltammograms (scan rate 50 mV s<sup>-1</sup>) at 100 °C of: (a) P<sub>1,4,4,4</sub> tosylate; (b) 0.01 M CdCl<sub>2</sub> in P<sub>1,4,4,4</sub> tosylate; (c) 0.04 M Na<sub>2</sub>S<sub>2</sub>O<sub>3</sub>·5H<sub>2</sub>O (solid line) and 0.04 M S (dashed line) in P<sub>1,4,4,4</sub> tosylate.

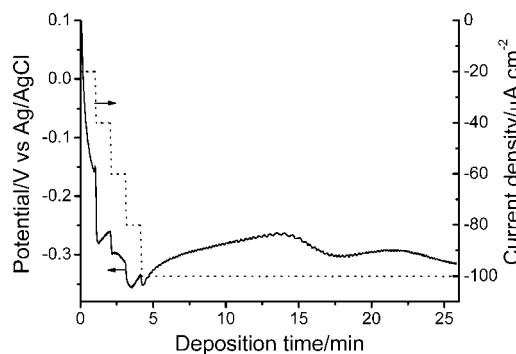


**Fig. 2** Typical chronopotentiometry plot during CdS electrodeposition.

peeled very readily. SEM pictures of the films (see ESI†) provide further evidence of good adhesion in the former case.

Table 1 lists the properties of a number of films prepared using various conditions. The relationship between the film thickness and amount of charge passed for the growth at 130 °C is shown in Fig. 4. The linear trend suggests that the growth of the film is charge controlled. Hence films of different thicknesses can easily be obtained simply by altering time or current.

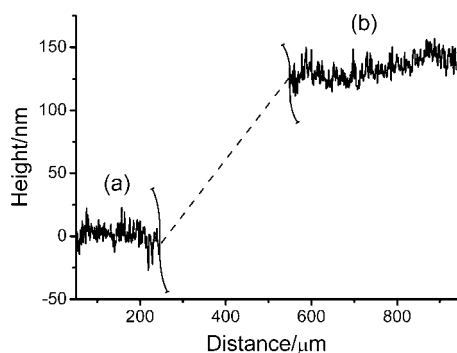


**Fig. 3** A typical profile of the films (s3 in Table 1): bare FTO surface (a) and CdS film (b). (Laser etched channel removed from the data.)

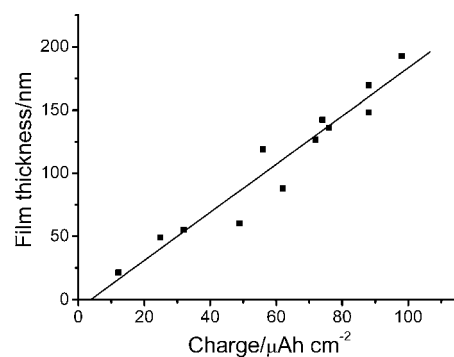


**Fig. 4** Dependence of film thickness on charge passed for growth at 130 °C.

An SEM image of the CdS film ( $\sim 80$  nm) electrodeposited on plasma treated FTO is shown in Fig. 5. The film shows a relatively uniform surface of crystallites of about 200 nm in diameter. Importantly it shows no larger ( $> 1 \mu\text{m}$ ) precipitates, which are a known issue in thick film CBD deposits.<sup>13,14</sup> By thermal treatment of the CdS on bare FTO it was possible to lift the CdS film off the substrate. Fig. 6 shows EDX spectra of a film on plasma treated FTO (Fig. 6a) and a film lifted off the FTO substrate (Fig. 6b). The atomic ratios obtained in the latter case were  $54 \pm 3\%$  S,  $46 \pm 3\%$  Cd. Although Cl was observed in the CdS films electrodeposited from aqueous solutions of  $\text{Na}_2\text{S}_2\text{O}_3$  and  $\text{CdCl}_2$ ,<sup>27</sup> no Cl signal could be detected in the present work. The EDX spectra are almost identical to those reported by Baykul and Balcioğlu,<sup>7</sup> where the atomic ratio of cadmium to sulfur was also found to be almost stoichiometric. Optical microscopy showed that the films were homogeneous (featureless) and crack free.

The XRD pattern of the CdS thin film and FTO coated glass are shown in Fig. 7. Several intense peaks can be seen in the patterns. The diffraction peaks at  $28.22^\circ$  and  $47.5^\circ$  coincide well with the (101) and (103) diffraction lines of hexagonal CdS.<sup>14,17,29</sup> A strong peak from the FTO at  $26.46^\circ$  shades the peak at  $26.16^\circ$  that could be assigned to the (002) and (111) planes of hexagonal and cubic phase, respectively.<sup>17,29</sup> Several small peaks at  $42^\circ$ ,  $46.5^\circ$ , and  $56.4^\circ$  could not be assigned to any form of CdS, CdO or any other salt possibly present. The

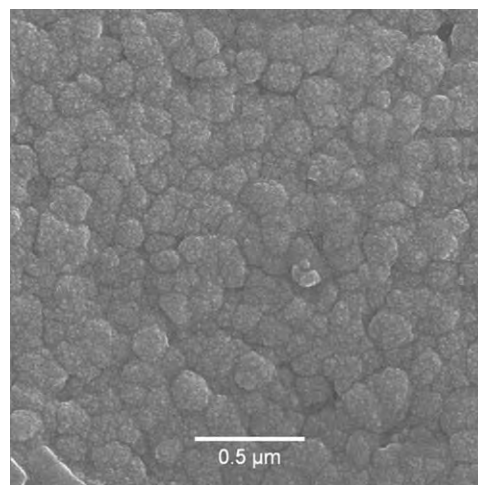


**Fig. 5** SEM image of CdS film ( $\sim 80$  nm) electrodeposited on plasma treated FTO.

fact that several significant hexagonal CdS peaks are missing may indicate alignment of the crystals in the sample.

The average size of the crystals was calculated using the Scherrer equation<sup>30</sup> (eqn (1)), where  $d$  is the average crystallite size,  $\lambda$  is the X-ray wavelength,  $\theta$  is the Bragg angle, and  $\beta$  is a FWHM of the diffraction peak in radians. The average crystallite sizes calculated for CdS(101) hexagonal and CdS(103) hexagonal diffraction peaks

**Table 1** Properties of CdS films electrodeposited under different conditions

Name	Stair case current	$T/^\circ\text{C}$	Current density/ $\mu\text{A cm}^{-2}$	Charge/ $\mu\text{Ah cm}^{-2}$	Thickness/nm $\pm 10\%$	Band gap/eV $\pm 0.1$
s1	No	130	200	72	$\sim 125$	2.59
s2	No	130	200	56	$\sim 125$	2.59
s3	No	130	200	76	$\sim 135$	2.57
s4	No	130	200	21	$\sim 75$	2.57
s5	Yes	130	200	88	$\sim 150$	2.58
s6	Yes	130	200	49	$\sim 60$	2.59
s7	Yes	130	200	25	$\sim 40$	2.57
s8	Yes	130	200	12	$\sim 10$	2.72
s9	Yes	130	200	106	—	2.63
s10	Yes	130	200	60	—	2.58
s11	Yes	130	200	50	—	2.59
s12	Yes	130	200	98	$\sim 190$	2.59
s13	Yes	130	200	32	$\sim 55$	2.57
s14	Yes	130	200	20	$\sim 50$	2.57
s15	Yes	150	100	40	$\sim 120$	2.62
s16	Yes	150	100	53	$\sim 145$	2.62
s17	Yes	150	100	50	$\sim 180$	2.60

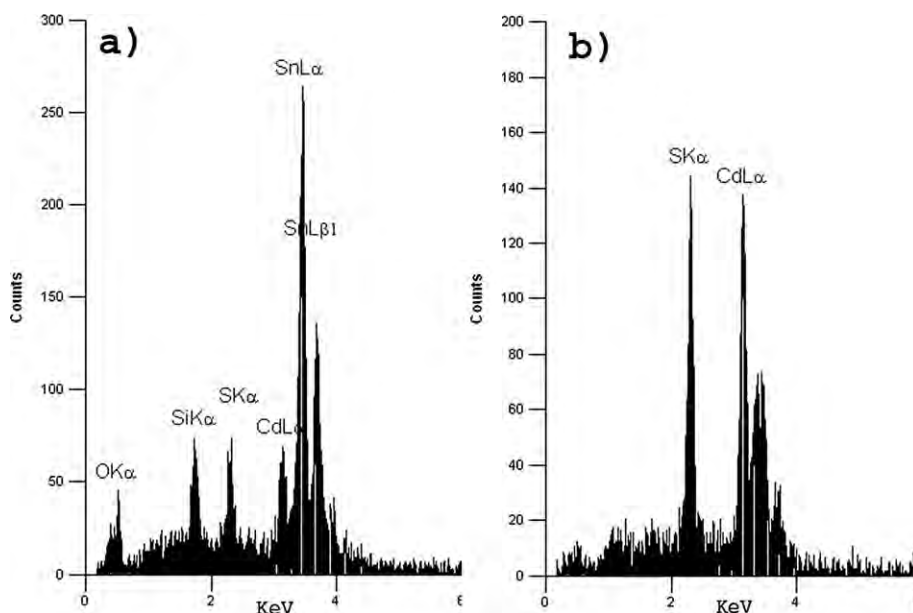


Fig. 6 EDX spectra of CdS film (~80 nm): (a) on the FTO substrate; (b) lifted off from the FTO.

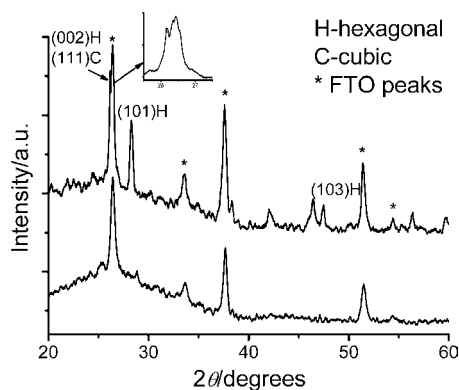


Fig. 7 XRD pattern of CdS thin film on FTO (top) and bare FTO glass for comparison (bottom). The area for  $2\theta$  from  $25.5^\circ$  to  $27.5^\circ$  is shown in the inset.

are ~25 and ~27 nm, respectively. These values are higher than those reported for CdS prepared *via* CBD where the range of sizes 9–20 nm was observed<sup>13</sup> and similar to ~25 nm observed for films prepared *via* the CVD route.<sup>11</sup>

$$d = \frac{0.94\lambda}{\beta \cos \theta} \quad (1)$$

### Mott–Schottky impedance spectroscopy

The flat band potential of the semiconductor was calculated from the Mott–Schottky plot recorded using impedance spectroscopy. In a typical measurement the semiconductor–electrolyte junction capacity was measured as a function of applied potential (*vs.* SCE) at 1 kHz.<sup>31</sup> In order to prevent the CdS film from deterioration 0.1 M Na<sub>2</sub>S and 0.1 M NaOH were used in the electrolyte solution.<sup>31</sup> A typical Mott–Schottky plot of  $1/C_{SC}^2$  versus applied potential is shown in Fig. 8, as suggested by the form of eqn (2)

$$\frac{1}{C_{SC}^2} = \frac{2}{A^2 R^2 q N_d \epsilon \epsilon_0} \left( E - E_{fb} - \frac{kT}{q} \right) \quad (2)$$

where  $A$  is the surface area,  $R$  the roughness,  $q$  the electronic charge,  $N_D$  the concentration of donors,  $\epsilon$  and  $\epsilon_0$  the relative and vacuum dielectric permittivities,  $k$  the Boltzmann constant,  $T$  the temperature, and  $E$  the potential. By extrapolating the linear part of the plot, one can find the condition when  $1/C_{SC}^2 = 0$  at which the flat band potential is equal to the electrode potential.

The flat band potentials of films deposited on plasma treated FTO were found to be in the range of  $-0.88 \pm 0.08$  V (statistics of 5 films) (*vs.* SCE). This value coincides very well with those reported in the literature for CdS thin films measured under the same conditions ( $-0.92$  V *vs.* SCE).<sup>31,32</sup> The flat band potential is known to be sensitive to preparation conditions ranging from  $-1.3$  to  $-0.8$  V (*vs.* SCE). The more negative values in this range are close to those reported for single crystal CdS.<sup>31</sup>

The determination of transition voltage for CdS (voltage at which saturation of the semiconductor layer occurs) is shown in Fig. 8. In our experiments the transition voltage was  $-0.09$  V. This is also in agreement with literature values.<sup>31,32</sup>

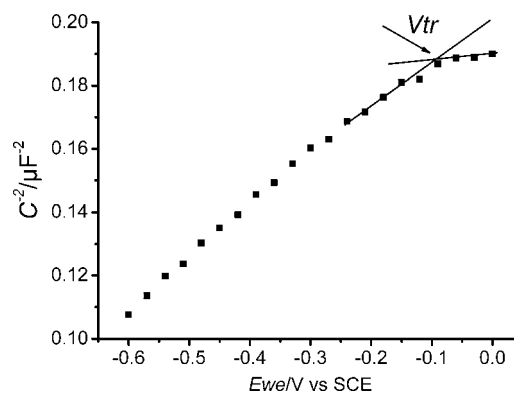


Fig. 8 Typical Mott–Schottky plot of electrodeposited CdS films on bare FTO in 0.1 M Na<sub>2</sub>S and 0.1 M NaOH at 1 kHz, and determination of transition voltage.

## UV-Vis spectroscopy

UV-Vis spectra were used to calculate the band gap energies from eqn (3) in the usual way as described elsewhere.<sup>7,33</sup>

$$\alpha = k \frac{(h\nu - E_g)^m}{h\nu} \quad (3)$$

where  $k$  is a constant,  $h\nu$  the photon energy,  $E_g$  the band gap energy and  $m = 1/2$  for a direct band gap material. Here, the plot of  $(\alpha h\nu)^2$  versus  $h\nu$  yields the band gap energy at the point where linear parts of the curve intersect. The band gap of CdS films prepared in this work was thus found to be  $2.59 \pm 0.02$  eV (Fig. 9a). A similar result ( $E_g = 2.61$  eV) was measured for CdS films prepared by chemical bath deposition on plasma treated FTO substrate.

The reported values of band gap for CdS thin films vary greatly from  $2.58^{11,34,35}$  to  $2.38$  eV.<sup>36</sup> There may be multiple reasons for such differences including quantum confinement effects, observed due to the polycrystalline nature of the film in some literature cases. It was shown that the value of band gap for such films normally reduces with an increase in film thickness, because the probability of formation of bigger crystals increases at longer deposition times/film thickness.<sup>15</sup> In our work, however, the band gap of samples appeared to be independent of film thickness (Table 1) except at very low film thickness ( $\sim 10$  nm). A classical quantum confinement effect with an increase in value of  $E_g$  to  $2.72$  eV was observed for the  $\sim 10$  nm film (Fig. 9b). Although the crystal structure of the semiconductor has a major influence on the value of band gap, the strain and imperfections that appear during deposition may also have a tremendous effect on electric properties producing a wide range of data from different deposition techniques.<sup>11</sup>

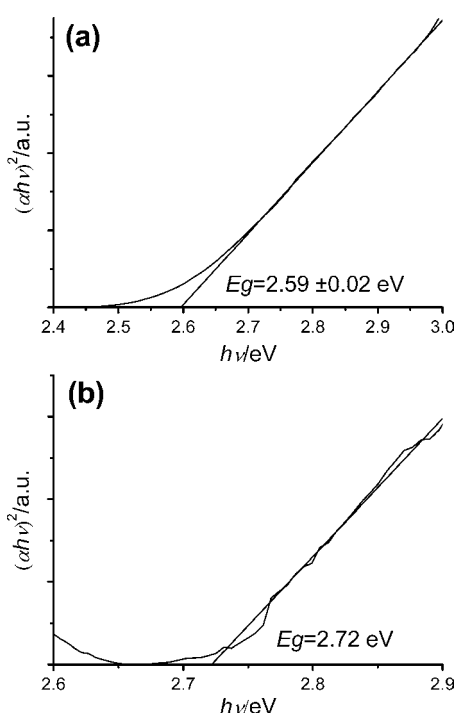


Fig. 9  $(\alpha h\nu)^2$  versus  $h\nu$  plot derived from UV-Vis spectra: (a) thickness  $> 10$  nm; (b) thickness  $\sim 10$  nm.

## Annealing of the films

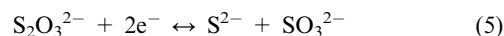
In order to study the influence of temperature on the optical and electrical properties of the deposits, some of the films were annealed in a nitrogen atmosphere for 1 hour at  $350$  °C. Such a low temperature compared to other reports was chosen to prevent sulfur evaporation from the surface (which occurs at  $T > 375$  °C).<sup>19</sup> The band gap was reduced from  $2.59 \pm 0.02$  eV to  $2.52 \pm 0.01$  eV during annealing. This decrease in band gap value is well known in the literature<sup>19,31</sup> and can be attributed to either annealing of defects including the size of the crystals increasing<sup>13</sup> or to changes in the crystal structure of the films (formation of the cubic phase).<sup>19</sup> Most importantly, no deterioration in optical and electrical properties of the films was observed. Such deterioration is common for the films prepared *via* aqueous methods, where presence of incorporated Cd(OH)<sub>2</sub> and H<sub>2</sub>O leads to self-oxidation of the sample.<sup>19</sup>

## Mechanism of growth

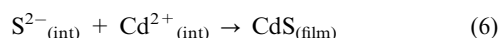
It was shown previously that reduction of thiosulfate in aqueous solutions may proceed in several ways. Either disproportionation of thiosulfate to produce sulfur:



then reduction of S to H<sub>2</sub>S.<sup>16</sup> Alternatively, direct reduction of thiosulfate can take place:<sup>27</sup>



Negligible amounts of H<sup>+</sup> present in the electrolyte make formation of elemental sulfur unlikely. The comparison between the CVs of S<sup>0</sup> and S<sub>2</sub>O<sub>3</sub><sup>2-</sup> shown in Fig. 1c reveals that a more negative potential is needed to reduce elemental sulfur. No film was grown when elemental sulfur was used instead of thiosulfate as the source of S<sup>2-</sup> in this work. Thus eqn (4) appears not to be operative in the ionic liquid medium used in this work. Once S<sup>2-</sup> production is established at the interface (denoted as “int” below) two subsequent processes can take place:



The second process may lead to precipitation of CdS in the bulk solution and therefore be a source of inefficiency in the process. S<sup>2-</sup> may also migrate to the positive electrode in the present cell arrangement and be reoxidized. The growth of the film is therefore ultimately limited by the lower of the rates at which S<sup>2-</sup> is formed and Cd<sup>2+</sup> diffuses to the surface. The rate of thiosulfate reduction is controlled by the current, while deposition temperature and cadmium concentration in the IL determine the rate of Cd<sup>2+</sup> diffusion to the surface. By controlling the rate of sulfur reduction as well as the temperature of deposition we therefore have a means to control the deposition and hence potentially achieve high efficiency atom by atom growth of the films.

## Experimental

Cadmium chloride ( $\text{CdCl}_2$ ) and sodium thiosulfate pentahydrate ( $\text{Na}_2\text{S}_2\text{O}_3 \cdot 5\text{H}_2\text{O}$ ) have been purchased from Merck Pty. Limited;  $\text{P}_{1,4,4,4}$  tosylate was obtained from CYTEC Inc. In all cases, deionized water has been used to assist with dissolution of  $\text{CdCl}_2$  and  $\text{Na}_2\text{S}_2\text{O}_3 \cdot 5\text{H}_2\text{O}$  in the IL.

The electrochemical experiments were performed on a VMP-2 multichannel potentiostat, using a standard three electrode configuration. Platinum wire and a 66-EE009 ("no-leak") Ag/AgCl electrode (Cypress Systems) were used as a counter and reference electrode, respectively.

The chemical bath deposition of CdS on plasma treated FTO film was performed following the procedure reported elsewhere.<sup>14</sup> UV-Vis transmission spectra were recorded at room temperature using a Cary 1E UV-visible spectrophotometer. A Nikon ME600L microscope and a Dektak 150 surface profiler were used for visible inspection of the deposits and characterization of the surface roughness as well as thickness of the film. SEM images and chemical composition measurements (by energy dispersive X-ray analysis, EDX) have been performed on a JEOL 6300F field emission gun scanning electron microscope.

Fluorine-doped tin oxide (sheet resistance  $15 \Omega \square^{-1}$ ) glass slides were used as a substrate. Before the deposition the surface of the FTO was masked, leaving an area equal to  $0.25 \text{ cm}^2$ . Prior to use, the glass slides were sonicated in water solution of DOBATEC detergent, washed several times in deionized water, and sonicated in ethanol to remove traces of detergent. Some FTO samples were also treated with an AC plasma discharge in an Ar– $\text{H}_2$  mixture to remove organic residues from the substrates and then subjected to a plasma polymerization treatment using maleic anhydride following the procedure reported elsewhere.<sup>37</sup>

The as-prepared samples were immediately washed in water at room temperature. Adhesion properties were evaluated using a sellotape test.

XRD measurements were performed on a Philips powder diffractometer with Cu radiation.

## Conclusions

We have successfully electrodeposited CdS films of different thicknesses  $< 200 \text{ nm}$ , which are well adherent to the surface, homogeneous and crack free. The key to this process is the use of an ionic liquid electrolyte at elevated temperatures ( $130\text{--}150 \text{ }^\circ\text{C}$ ) and a sulfide source which is reducible in a potential range where  $\text{Cd}^{2+}$  is not reduced. The work thus presents a substitute for low yield CBD processes that are widely used for solar cell applications with a cheap and effective technique for CdS deposition.

## Acknowledgements

The authors would like to acknowledge Monash University Centre for Electron Microscopy for providing electron microscopic facilities. DRM is grateful to the Australian Research Council for his Federation Fellowship.

## References

- O. Savadogo, *Sol. Energy Mater. Sol. Cells*, 1998, **52**, 361–388.
- P. J. Sebastian, R. Castaneda, L. Ixtlilco, R. Mejia, J. Pantoja, A. Olea, *Solar Hydrogen and Nanotechnology III*, ed. Gunnar Westin, Proceedings of the SPIE, 2008, vol. 7044, p. 4405.
- P. O. Anikeeva, J. E. Halpert, M. G. Bawendi and V. Bulovic, *Nano Lett.*, 2007, **7**, 2196–2200.
- M. Tsuji, T. Aramoto, H. Ohyama, T. Hibino and K. Omura, *J. Cryst. Growth*, 2000, **214**, 1142–1147.
- L. P. Colletti, B. H. Flowers and J. L. Stickney, *J. Electrochem. Soc.*, 1998, **145**, 1442–1449.
- D. B. Fraser and H. Melchior, *J. Appl. Phys.*, 1972, **43**, 3120–3127.
- M. C. Baykul and A. Balcioğlu, *Microelectron. Eng.*, 2000, **51–52**, 703–713.
- M. Ichimura, F. Goto and E. Arai, *J. Appl. Phys.*, 1999, **85**, 7411–7417.
- K. Senthil, D. Mangalaraj and S. K. Narayandass, *Appl. Surf. Sci.*, 2001, **169**, 476–479.
- U. Pal, R. SilvaGonzalez, G. MartinezMontes, M. GraciaJimenez, M. A. Vidal and S. Torres, *Thin Solid Films*, 1997, **305**, 345–350.
- D. Barreca, A. Gasparotto, C. Maragno and E. Tondello, *J. Electrochem. Soc.*, 2004, **151**, G428–G435.
- M. Innocenti, S. Cattarin, F. Loglio, T. Cecconi, G. Seravalli and M. L. Foresti, *Electrochim. Acta*, 2004, **49**, 1327–1337.
- A. Cortes, H. Gomez, R. E. Marotti, G. Riveros and E. A. Dalchiale, *Sol. Energy Mater. Sol. Cells*, 2004, **82**, 21–34.
- M. B. Ortuno-Lopez, M. Sotelo-Lerma, A. Mendoza-Galvan and R. Ramirez-Bon, *Thin Solid Films*, 2004, **457**, 278–284.
- I. Sisman, M. Alanyalioglu and U. Demir, *J. Phys. Chem. C*, 2007, **111**, 2670–2674.
- J. Nishino, S. Chatani, Y. Uotani and Y. Nosaka, *J. Electroanal. Chem.*, 1999, **473**, 217–222.
- K. Premaratne, S. N. Akuranthilaka, I. M. Dharmadasa and A. P. Samantilleka, *Renewable Energy*, 2003, **29**, 549–557.
- P. J. Dale, A. P. Samantilleke, D. D. Shivagan and L. M. Peter, *Thin Solid Films*, 2007, **515**, 5751–5754.
- H. Metin and R. Esen, *Semicond. Sci. Technol.*, 2003, **18**, 647–654.
- S. Z. El Abedin and F. Endres, *ChemPhysChem*, 2006, **7**, 58–61.
- F. Endres, D. MacFarlane and A. Abbott, *Electrodeposition from ionic liquids*, Wiley-VCH, Weinheim, Chichester, 2008, vol. 2008, p. 387.
- W. Lu, A. G. Fadeev, B. H. Qi, E. Smela, B. R. Mattes, J. Ding, G. M. Spinks, J. Mazurkiewicz, D. Z. Zhou, G. G. Wallace, D. R. MacFarlane, S. A. Forsyth and M. Forsyth, *Science*, 2002, **297**, 983–987.
- F. Endres and S. Z. El Abedin, *Phys. Chem. Chem. Phys.*, 2006, **8**, 2101–2116.
- O. Mann, G. B. Pan and W. Freyland, *Electrochim. Acta*, 2009, **54**, 2487–2490.
- S. Z. El Abedin, A. Y. Saad, H. K. Farag, N. Borisenko, Q. X. Liu and F. Endres, *Electrochim. Acta*, 2007, **52**, 2746–2754.
- D. D. Shivagan, P. J. Dale, A. P. Samantilleke and L. M. Peter, *Thin Solid Films*, 2007, **515**, 5899–5903.
- M. Rami, E. Benamar, M. Fahoume and A. Ennaoui, *Phys. Status Solidi A*, 1999, **172**, 137–147.
- Encyclopedia of electrochemistry*, ed. A. J. Bard and M. Stratmann, Wiley-VCH, Weinheim, Cambridge, 2001–2007, vol. 11, p. 48.
- P. K. Nair, O. G. Daza, A. A. C. Readigos, J. Campos and M. T. S. Nair, *Semicond. Sci. Technol.*, 2001, **16**, 651–656.
- B. D. Cullity, *Elements of X-Ray Diffraction*, Addison-Wesley Pub. Co., Reading, MA, Second Edn, 1978.
- M. E. Ozsan, D. R. Johnson, M. Sadeghi, D. Sivapathasundaram, G. Goodlet, M. J. Furlong, L. M. Peter and A. A. Shingleton, *J. Mater. Sci.: Mater. Electron.*, 1996, **7**, 119–125.
- T. Watanabe, A. Fujishim and K. I. Honda, *Chem. Lett.*, 1974, 897–900.
- N. B. Chaure, S. Chaure and R. K. Pandey, *Sol. Energy Mater. Sol. Cells*, 2004, **81**, 39–60.
- M. Z. Huang and W. Y. Ching, *Phys. Rev. B*, 1993, **47**, 9449–9463.
- S. Adachi, *Handbook on physical properties of semiconductors*, Kluwer Academic Publishers, Boston, 2004, p. 1431.
- D. J. Kim, Y. M. Yu, J. W. Lee and Y. D. Choi, *Appl. Surf. Sci.*, 2008, **254**, 7522–7526.
- Z. Ademovic, J. Wei, B. Winther-Jensen, X. L. Hou and P. Kingshott, *Plasma Processes Polym.*, 2005, **2**, 53–63.